

UNCLASSIFIED

AD NUMBER: AD0857474

LIMITATION CHANGES

TO:

Approved for public release; distribution is unlimited.

FROM:

Distribution authorized to U.S. Gov't. agencies and their contractors; Administrative/Operational Use; 1 Jun 1969. Other requests shall be referred to Naval Weapons Center, China Lake, CA

AUTHORITY

USNWC ltr 30 Aug 1977 - c/2 to a/1

AD857474



PROCEEDINGS OF THE  
8TH NAVY SYMPOSIUM  
ON AEROBALLISTICS

VOLUME 2

6, 7, 8 MAY 1969

NAVAL WEAPONS CENTER • Corona Laboratories • Corona, California

SEP 2 1969



SPONSORED BY THE NAVAL AEROBALLISTICS ADVISORY COMMITTEE  
FOR THE  
NAVAL AIR SYSTEMS COMMAND • NAVAL ORDNANCE SYSTEMS COMMAND

DISTRIBUTION STATEMENT

THIS DOCUMENT IS SUBJECT TO SPECIAL EXPORT CONTROLS AND EACH TRANSMITTAL  
TO FOREIGN GOVERNMENTS OR FOREIGN NATIONALS MAY BE MADE ONLY WITH  
PRIOR APPROVAL OF THE NAVAL WEAPONS CENTER.

312

## 50TH ANNIVERSARY COMMEMORATED

Appropriately, the closing date of the Symposium marked the 50th anniversary of a significant milestone in aviation. On 8 May 1919, three naval aircraft left Long Island to attempt the first crossing of the Atlantic. Of the three Curtiss flying boats that started that historic 3,925-nautical-mile flight, the NC-4 (shown on cover), commanded by LCDR A. C. Read, was successful, making the first Atlantic crossing via Newfoundland, the Azores, and Portugal, finally arriving at Plymouth, England.

The Secretary of the Navy designated May 1969 a commemorative period, and it was especially appropriate that the Symposium salute the aeronautical pioneers who made history in May 1919.

ACQUISITION NO.	
OFFICE	WRITE SERIAL <input type="checkbox"/>
DDC	DATE ACQ. <input checked="" type="checkbox"/>
UNANIMOUS	
JUSTIFICATION	
BY _____	
DISTRIBUTION/AVAILABILITY STATE	
DIST.	AVAIL. W/ W/ SERIAL
2	

**PROCEEDINGS OF THE  
8TH NAVY SYMPOSIUM  
ON AEROBALLISTICS**

**VOLUME 2**

**6, 7, 8 MAY 1969**

**NAVAL WEAPONS CENTER • Corona Laboratories • Corona, California**



**SPONSORED BY THE NAVAL AEROBALLISTICS ADVISORY COMMITTEE  
FOR THE  
NAVAL AIR SYSTEMS COMMAND • NAVAL ORDNANCE SYSTEMS COMMAND**

**DISTRIBUTION STATEMENT**

**THIS DOCUMENT IS SUBJECT TO SPECIAL EXPORT CONTROLS  
AND EACH TRANSMITTAL TO FOREIGN GOVERNMENTS OR  
FOREIGN NATIONALS MAY BE MADE ONLY WITH PRIOR  
APPROVAL OF THE NAVAL WEAPONS CENTER.**

**NAVAL WEAPONS CENTER • CHINA LAKE, CALIFORNIA  
JUNE 1969**

## FOREWORD

These *Proceedings*, published in five volumes, comprise the 49 papers presented at the Eighth Navy Symposium on Aeroballistics held at the Naval Weapons Center Corona Laboratories, Corona, Calif., 6, 7, and 8 May 1969.

This symposium was the eighth in a series begun in 1950 under the sponsorship of the then Bureau of Ordnance Committee on Aeroballistics, and currently conducted by the Naval Aeroballistics Advisory Committee as sponsoring committee for the Naval Air Systems Command and the Naval Ordnance Systems Command. The continuing purpose of the symposiums has been to disseminate the results of aeroballistics research and to bring the research findings of industry, the universities, and government laboratories to bear upon the Navy's aeroballistics research and development programs.

Over 200 research scientists representing more than 72 organizations attended this eighth symposium. Sessions 1 and 2 covered the subjects of heat transfer and aerophysics, nozzles and jet effects; Sessions 3 and 4 were concerned with aerodynamics and missile stability; and Session 5 dealt with structures and aeroelasticity, and external carriage and store separation.

The papers in these *Proceedings* have been reproduced in facsimile. They appear in the order of presentation except that all classified papers have been taken out of sequence and grouped together as Volume 5, a confidential volume. Volumes 1 through 4 are unclassified. This is Volume 2.

Requests for or comments on individual papers should be addressed to the respective authors.

RAY W. VAN AKEN  
*General Chairman*  
Symposium Committee

Published by the Publishing Division of the Technical Information Department, NWC; first printing, June 1969, 250 copies.

**BLANK PAGE**

## CONTENTS

## Volume 1

Paper	Page
Authors .....	viii
Greetings .....	ix
Welcome .....	x
Introductory Remarks, Rear Admiral R. J. Schneider, USN .....	xi
U.S. Navy Symposia on Aeroballistics .....	xiii
Naval Aeroballistics Advisory Committee .....	xiv
Paper Selection Committee .....	xv
Attendees .....	xvi
1 Base and Lee Side Flow Studies of Slender Bodies at High Angles of Attack by George S. Pick .....	1
2 An Experimental Investigation of the Hypersonic Aerodynamic Characteristics of Slender Bodies of Revolution at High Angles of Attack by Robert Feldhuhn, Allen Winkelmann and Lionel Pasiuk .....	29
3 Analytical Investigation on Laminar Flow Field and Heat Transfer on Leeward Side of a Sharp Nosed Hypersonic Cone at Large Angle of Attack by Paul K. Chang, Mario J. Casarella, and Russell A. Smith .....	95
4 Pressure Distribution on Bodies at Large Angle of Attack by Howard R. Kelly .....	129
5 Compact Gas-Transpiration Cooling System Analysis by R. W. Allen and R. W. Newman .....	153
6 Experimental Investigation of Transpiration Cooling Near the Stagnation Point of a Cylinder by Richard L. Humphrey .....	181
7 Ballistics Range Experiments on the Effect of Unit Reynolds Number on Boundary-Layer Transition by Norman W. Sheetz, Jr. ....	201
8 Calculation of Blunt Body Flows Using Pade' Fractions and the Method of Characteristics by Andrew H. Van Tuyl .....	215

→ Contents

 Volume 2

9 Applications of the Time-Dependent Technique for the Computation of Compressible Flows by John D. Anderson, Jr., Lorenzo M. Albacete and Allen E. Winkelmann ..	239
10 Nonequilibrium Flow Over Blunt Bodies Using Method of Integral Relations by T. C. Tai .....	267
11 Supersonic Laminar and Turbulent Ablation Studies With Teflon by E. M. Winkler, R. L. Humphrey, J. A. Koehnig, and M. T. Madden .....	311
12 Recent Progress in the Calculation of Turbulent Boundary Layers by Tuncer Cebeci, A.M.O. Smith, and G. Mosinskis .....	351
13 An Experimental Investigation of the Compressible Turbulent Boundary Layer With a Favorable Pressure Gradient by William J. Yanta, David L. Brott, Robert L. Voisinet, and Roland E. Lee .	389
14 An Experimental Reynolds Analogy for the Highly Cooled Turbulent Boundary Layer by Donald M. Wilson .....	411
15 The Effect of Flow Field Irregularities on Swept Leading Edge Heat Transfer by Albert F. Gollnick .....	441
16 An Experimental Study of Mass Addition Effects in the Near Wake by Norman G. Paul, H. J. Unger, F. K. Hill, and J. M. Cameron .....	473
17 Isothermal Leading Edges by Bertram K. Ellis .....	507

## 8th Navy Symposium on Aeroballistics

### Vol. 2

Paper	Page
18 Spikes as a Means of Reducing Drag and Rain Erosion of Blunt Bodies at Supersonic Speeds by Isidor C. Patapis	531

### Volume 3

21 Research on an Asymmetric Glide Reentry Vehicle by Herbert R. Little, Robert H. Burt, and Jerry Coble	545
24 An Analysis of a Slewed-Launch Technique for Air-Launched Missiles by Eugene E. Kluth	587
26 Stabilization of a Liquid-Filled Shell by Inserting a Cylindrical Partition in the Liquid Cavity by John T. Frasier and William P. D'Amico	629
27 Effects of Roll on the Free-Flight Motion of Bodies by C. J. Welsh and R. M. Watt	651
28 Dynamic Stability of the 5-Inch/54 Rocket Assisted Projectile (The Influence of a Non-Linear Magnus Moment) for Eighth United States Navy Symposium on Aeroballistics by W. R. Chadwick	671
29 The University of Virginia Cold Magnetic Wind Tunnel Balance by Hermon M. Parker and Ricardo N. Zapata	695
30 Wind Tunnel Measurements of the Aerodynamic Characteristics of the 2.75 Wraparound Fin Rocket Using a Magnetic Suspension System by Milan Vlajinac	717
31 Nonlinear Aerodynamic Stability Characteristics of the 2.75 Wrap-Around Fin Configuration by John D. Nicolaidis, Charles W. Ingram, James M. Martin, and Alfred M. Morrison	751
32 A Study to Eliminate Flight Instabilities on a High-Drag Air Delivered Mine by Jack C. Hopps	833
34 Two-Dimensional Jet-Interaction Experiments Results of Flow-Field and Scale Effect Studies by Michael J. Werle, Richard T. Driftmyer, and David G. Shaffer	865
35 Interaction Between High Speed Flows and Transverse Jets: A Method for Predicting the Resultant Surface Pressure Distribution by Louis G. Kaufman II	885
36 Aerodynamic and Heat Transfer Effects of Saturn V Plume-Induced Flow Separation by Calvin L. Wilkinson	921

### Volume 4

38 Structural Qualification of the Low Speed FAE Weapon Dispenser by Jack D. Brannan and Wallace W. Parmenter	941
40 Stiffness Matrix for Missile Structures Using Thin Shell Theory by Pao C. Huang	981
41 An Experimental Investigation of Aircraft/Missile Interference Effects by C. Franklyn Markarian	1005
42 Store Separation From the McDonnell Douglas F-4 Aircraft by David L. Schoch	1025
43 Aircraft/Munitions Compatibility—U.S. Air Force Project "Seek Eagle" by Charles S. Epstein	1077
44 Prediction of Store Launch Characteristics Through Statistical Methods by Michael A. Sekellick	1103
45 External Store Airloads Prediction by R. D. Gallagher and P. E. Browne	1131

Paper		Page
46	Estimation of Aircraft Store Separation Behavior on the Basis of Captive Load Data by D. A. Jones .....	1159
47	Prediction of Store Separation Trajectories at the Naval Weapons Center by J. V. Netzer .....	1185
49	An Analytical, Numerical Program for Calculating the Aerodynamic Forces External to Aircraft by Hyman Serbin .....	1205

**Volume 5**  
**(Classified Papers)**

19	The Simulation of Ramjet Configurations With Pod Inlets for Stability and Control Wind Tunnel Testing by James C. Hagan .....	1213
20	Pitch Control Effectiveness of Flap Controls Mounted on a Body of Revolution by E. F. Lucero .....	1229
22	Wing-Tail Interference in Hypersonic Missile Configurations by H. H. Hart .....	1243
23	An Investigation of the Aerodynamic Behavior of Submissiles During Ejection from a High-Speed Rocket by Chris A. Kalivretenos and David N. Bixler .....	1257
25	Feasibility of Increasing Sidewinder Maneuverability by Means of Enlarged Canards by R. E. Meeker .....	1277
33	A Summary of the Sonic Lateral Jet Studies With 9-Degree Cones at Mach Numbers 6 to 20 by W. T. Strike .....	1297
37	Aerodynamic Design of Reaction Jet Controlled Tactical Missiles by L. A. Cassel, D. P. Engh and L. Y. Lam .....	1337
39	Evaluation of Radomes for Hypersonic Flight by L. B. Weckesser and R. K. Frazer .....	1371
48	Weapon-Aircraft Separation: A Review of a Particular Weapon Problem by R. E. Smith .....	1401

AUTHORS

Albacete, Lorenzo M., Paper No. 9	239	Lucero, E. F., Paper No. 20	1229
Allen, R. W., Paper No. 5	153	Madden, M. T., Paper No. 11	311
Anderson, John D., Jr., Paper No. 9	239	Markarian, C. Franklyn, Paper No. 41	1005
Bixler, David N., Paper No. 23	1257	Martin, James M., Paper No. 31	751
Brannan, Jack D., Paper No. 38	941	Meeker, R. E., Paper No. 25	1277
Brott, David L., Paper No. 13	389	Morrison, Alfred M., Paper No. 31	751
Browne, P. E., Paper No. 45	1131	Mosinskis, Gediminas J., Paper No. 12	351
Burt, Robert H., Paper No. 21	545	Netzer, J. V., Paper No. 47	1185
Cameron, J. M., Paper No. 16	473	Newman, R. W., Paper No. 5	153
Casarella, Mario J., Paper No. 3	95	Nicolaides, John D., Paper No. 31	751
Cassel, L. A., Paper No. 37	1337	Parker, Hermon M., Paper No. 29	695
Cebeci, Tuncer, Paper No. 12	351	Parmenter, Wallace W., Paper No. 38	941
Chadwick, William R., Paper No. 28	671	Pasiuk, Lionel, Paper No. 2	29
Chang, Paul K., Paper No. 3	95	Patapis, Isidor, Paper No. 18	531
Coble, Jerry G., Paper No. 21	545	Paul, N. G., Paper No. 16	473
D'Amico, W. P., Paper No. 26	629	Pick, George S., Paper No. 1	1
Driftmyer, Richard T., Paper No. 34	865	Schoch, David L., Paper No. 42	1025
Ellis, Bertram K., Paper No. 17	507	Sekellick, Michael A., Paper No. 44	1103
Engh, D. P., Paper No. 37	1337	Serbin, Hyman, Paper No. 49	1205
Epstein, Charles S., Paper No. 43	1077	Shaffer, David G., Paper No. 34	865
Feldhuhn, Robert, Paper No. 2	29	Sheetz, Norman W., Jr., Paper No. 7	201
Frasier, J. T., Paper No. 26	629	Smith, A. M. O., Paper No. 12	351
Frazer, R. K., Paper No. 39	1371	Smith, R. E., Paper No. 48	1401
Gallagher, R. D., Paper No. 45	1131	Smith, Russell A., Paper No. 3	95
Gollnick, Albert F., Jr., Paper No. 15	441	Strike, William T., Jr., Paper No. 33	1297
Hagan, J. C., Paper No. 19	1213	Tai, T. C., Paper No. 10	267
Hart, H. H., Paper No. 22	1243	Unger, H. J., Paper No. 16	473
Hill, F. K., Paper No. 16	473	Van Tuyl, Andrew H., Paper No. 8	215
Hopps, J. C., Paper No. 32	833	Vlajinac, Milan, Paper No. 30	717
Huang, Pao C., Paper No. 40	981	Voisinet, Robert L. P., Paper No. 13	389
Humphrey, Richard L., Paper No. 6, 11, 181, 311		Watt, R. M., Paper No. 27	651
Ingram, Charles W., Paper No. 31	751	Weckesser, L. B., Paper No. 39	1371
Jones, D. A., Paper No. 46	1159	Welsh, C. J., Paper No. 27	651
Kalivretenos, Chris A., Paper No. 23	1257	Werle, Michael J., Paper No. 34	865
Kaufman, Louis G., II, Paper No. 35	885	Wilkinson, Calvin L., Paper No. 36	921
Kelly, Howard R., Paper No. 4	129	Wilson, Donald M., Paper No. 14	411
Kluth, Eugene E., Paper No. 24	587	Winkelmann, Allen E., Paper No. 2, 9	29, 239
Koenig, J. A., Paper No. 11	311	Winkler, Eva M., Paper No. 11	311
Lam, L. Y., Paper No. 37	1337	Yanta, William J., Paper No. 13	389
Lee, Roland E., Paper No. 13	389	Zapata, Ricardo N., Paper No. 29	695
Little, Herbert R., Paper No. 21	545		

Paper No. 9

**APPLICATIONS OF THE TIME-DEPENDENT TECHNIQUE  
FOR THE COMPUTATION OF COMPRESSIBLE FLOWS  
(U)**

(Paper UNCLASSIFIED)

by

John D. Anderson, Jr., Lorenzo M. Albacete,  
and Allen E. Winkelmann  
U.S. Naval Ordnance Laboratory  
White Oak, Silver Spring, Md. 20910

**ABSTRACT.** (U) A survey is made of some recent Naval Ordnance Laboratory (NOL) numerical calculations of steady, inviscid compressible flows obtained with a time-dependent technique; this technique is particularly advantageous for the analysis of mixed subsonic-supersonic flow fields where steady-flow methods usually encounter difficulties. The time-dependent technique entails the finite-difference solution of the governing unsteady conservation equations in steps of time, starting with assumed initial distributions throughout the flow field. The steady-state flow field, which is the desired result, is approached at large values of time. The technique is exemplified by application to the following cases:

- (1) Flow fields about supersonic and hypersonic blunt bodies, assuming a nonreacting calorically perfect gas, and
- (2) quasi-one-dimensional, convergent-divergent nozzle expansions of a high temperature gas including vibrational and chemical nonequilibrium conditions both upstream and downstream of the throat. In each case, the advantages of the time-dependent technique over a steady-flow analysis are delineated.

## INTRODUCTION

(U) This paper is a survey of some recent numerical calculations, made at NOL, of steady, inviscid, compressible gas flows. The distinguishing aspect of these calculations is that a time-dependent approach is used to obtain the steady-state flow field. The purpose of the present paper is to discuss the philosophy and advantages of the numerical time-dependent technique, and to present results obtained from the application of this technique to the cases of (1) the flow field about supersonic and hypersonic blunt bodies, assuming a calorically perfect gas, and (2) the expansion of a high temperature gas through a convergent-divergent nozzle where vibrational and chemical nonequilibrium prevail within the gas both upstream and downstream of the throat. In both of these cases, the time-dependent technique has some distinct and convincing advantages over more conventional steady-state analysis; these advantages will be delineated in subsequent sections.

(U) The present numerical studies are motivated by the general belief that engineering numerical analysis is rapidly taking its place as a new "third dimension" in fluid dynamics, and that this new dimension complements the other classical dimensions of experiment and theory. The advent of high speed digital computers has prompted this growth, and as a result a fertile field exists for the development and application of new and improved techniques for numerical flow-field analysis; indeed, the time-dependent analysis discussed in the present paper is such a case.

### QUALITATIVE DISCUSSION OF THE TIME-DEPENDENT TECHNIQUE

(U) The time-dependent technique entails the finite-difference solution of the unsteady conservation equations in steps of time. For a given problem (such as the flow field about a specified body with fixed free-stream conditions), the gas-dynamic variables are obtained in steps of time, starting from initially assumed distributions throughout the flow field. The steady-state solution, which is the desired result, is approached at large values of time.

A virtue of this technique is that it is relatively straightforward, and in principle it represents an exact solution for the steady-state flow field in the limit of infinite time. In practice, the steady state is obtained for all practical purposes in a reasonably finite length of time. A second virtue is mathematical, i.e., the unsteady conservation equations are hyperbolic with respect to time regardless of whether the flow is locally subsonic or supersonic; this characteristic allows a well-posed initial value problem throughout the entire flow field. This is in contrast to the steady conservation equations which, in the case of inviscid flows, change their nature from elliptic in the steady subsonic region to hyperbolic in the steady supersonic region; consequently, a stable, unified steady-state solution throughout both regions is difficult to obtain. As a result, the time-dependent method appears to be admirably suited for the unified analysis of mixed subsonic-supersonic flow fields. Indeed, this suitability is exemplified in the present paper by applications to the flow about a supersonic blunt body and the critical flow through a convergent-divergent nozzle.

(U) With regard to the precise numerical finite-difference scheme by which the above time-dependent technique can be implemented, several procedures have appeared in the literature (see for example ref. 1-8). The majority of these schemes involve the introduction of "artificial viscosity" into the inviscid flow problem, either directly in the governing physical conservation equations or indirectly in the numerical finite-difference equations. This concept of artificial viscosity, first suggested by VonNeumann and Richtmyer,<sup>6</sup> allows the calculation and appearance of shock waves with finite thickness as a unified part of the finite-difference scheme; however, the artificial viscosity is a mathematical artifice and its value has no relation to the actual coefficient of viscosity of the gas. Hence, the computed shock thickness has no relation to reality. Indeed, Moretti<sup>7</sup> has made the argument that, in addition to being physically unrealistic as well as requiring a large number of mesh points (and thus excessive computer times), the introduction of artificial viscosity may even mask other inconsistencies in a given application, and hence is generally unsatisfactory. The calculations and results given in the present paper employ a finite-difference scheme first suggested by Moretti and Abbett<sup>8</sup> which does not explicitly introduce an artificial viscosity and which treats shock waves as separate discontinuities. The appealing virtues of this approach are its physical consistency and the rather coarse

computational grid which can be used. This approach is discussed in the following section.

## ANALYSIS

(II) The crux of the present analysis is as follows: For specified conditions, such as (a) a fixed-body shape and specified supersonic free stream, or (b) fixed-nozzle shape and specified equilibrium reservoir conditions, initial values of the flow-field variables  $\rho$ ,  $u$ ,  $v$ ,  $T$ ,  $e_{vib}$  and chemical composition are assumed at regularly spaced grid points throughout the flow field. If all flow variables are known at time  $t$ , then at each grid point new values can be obtained at time  $(t+\Delta t)$  from the first three terms of a Taylor's series expansion in time,

$$g(t+\Delta t) = g(t) + \left(\frac{\partial g}{\partial t}\right)_t \Delta t + \left(\frac{\partial^2 g}{\partial t^2}\right)_t \frac{\Delta t^2}{2} \quad (1)$$

where  $g$  signifies  $\ln \rho$ ,  $\ln u$ ,  $\ln v$ ,  $\ln T$ ,  $\ln(e_{vib})$  and  $\ln \eta_i$  ( $\eta_i$  is the chemical species mole-mass ratio), and  $\Delta t$  is a small increment in time chosen to satisfy certain stability criteria.<sup>10</sup> (For the present numerical computations, the natural logarithms of the nondimensional flow-field variables are employed as the dependent variables in order to improve numerical stability, and a nondimensional time is employed in lieu of  $t$  in equation (1).) Starting with the initially assumed gas-dynamic variables at  $t = 0$ , the flow field is subsequently obtained in steps of time from equation (1). At large values of time (after many time steps, usually on the order of 700 or more) the steady-state flow field is obtained, where  $\left(\frac{\partial g}{\partial t}\right)_t$  and  $\left(\frac{\partial^2 g}{\partial t^2}\right)_t$  both approach zero. For the present investigation, this steady-state solution is the desired result; indeed, one purpose of the present paper is to show that the time-dependent approach is simply an advantageous means to the end. The time derivatives  $\left(\frac{\partial g}{\partial t}\right)_t$  and  $\left(\frac{\partial^2 g}{\partial t^2}\right)_t$  which appear in equation (1) are obtained from the unsteady conservation equations along with the proper boundary conditions; these equations and boundary conditions depend on the particular flow problem at hand.

## BLUNT BODY FLOW FIELDS

(U) The physical problem treated here is the mixed subsonic-supersonic flow field about a blunt body of fixed shape immersed in a specified uniform supersonic or hypersonic free stream, i.e., the "direct" supersonic blunt-body problem. A solution is sought for the steady-flow distribution of  $\rho$ ,  $u$ ,  $v$ ,  $T$ , etc., throughout the flow field between the shock wave and the body surface. The distinguishing aspect of the present analysis is that a time-dependent approach is used to obtain the steady-state flow field. The present blunt-body solution is patterned after that of Moretti and Abbett,<sup>8</sup> and is described in detail in references 8 and 9. Consequently, only a brief outline will be given here.

(U) A rectangular x-y coordinate system is employed for the blunt-body flow field as shown in Figure 1a. Nondimensionalizing by the local shock-layer thickness,  $s-b$ , the flow field is transformed into a rectangle as shown in Figure 1b, where  $\zeta = (x-b)/(s-b)$ . This rectangle is subsequently divided into a number of equally spaced grid points at each of which initial values (at  $t = 0$ ) for the flow variables are assumed. The initial bow-shock shape and detachment distance are also assumed. At all internal grid points, new values of the flow-field variables (at  $t = \Delta t$ ) are then computed from equation (1). The time derivatives,  $(\frac{\partial g}{\partial t})$  and  $(\frac{\partial^2 g}{\partial t^2})$ , in equation (1) are obtained from the unsteady conservation equations, which, for the calorically perfect inviscid blunt-body flow field, are as follows:

$$\text{continuity} \quad \frac{\partial \rho}{\partial t} = - \left[ \frac{\partial (\rho u)}{\partial x} + \frac{\partial (\rho v)}{\partial y} + k \frac{\rho v}{y} \right] \quad (2)$$

$$\text{x-momentum} \quad \frac{\partial u}{\partial t} = - \left( u \frac{\partial u}{\partial x} + v \frac{\partial u}{\partial y} + \frac{1}{\rho} \frac{\partial p}{\partial x} \right) \quad (3)$$

$$\text{y-momentum} \quad \frac{\partial v}{\partial t} = - \left( u \frac{\partial v}{\partial x} + v \frac{\partial v}{\partial y} + \frac{1}{\rho} \frac{\partial p}{\partial y} \right) \quad (4)$$

$$\text{energy} \quad \frac{\partial \phi}{\partial t} = - \left( u \frac{\partial \phi}{\partial x} + v \frac{\partial \phi}{\partial y} \right) \quad (5)$$

$$\text{state} \quad p = \rho RT \quad (6)$$

where  $k = 0$  and  $1$  for two-dimensional and axisymmetric bodies respectively, and  $\phi = \ln p - \gamma \ln \rho$ . The spatial derivatives on the right hand side of equations (2) to (5) are evaluated by means of central finite-differences obtained from the known flow field at the previous time step. Consequently, equations (2) to (5) ultimately yield values for  $\left(\frac{\partial g}{\partial t}\right)_t$  in equation (1), where  $g = \ln \rho, \ln u, \ln v$  and  $\phi$ . Values of  $\left(\frac{\partial^2 g}{\partial t^2}\right)_t$  in equation (1) are obtained by differentiation of equations (2) to (5) with respect to  $t$ . However, these subsequent differentiations introduce cross-derivatives,  $\frac{\partial^2 g}{\partial x \partial t}$ , which are obtained by differentiation of equations (2) to (5) with respect to  $x$ .

(U) The above procedure yields the calculation of flow-field properties in steps of time at the internal points of the rectangle and along the centerline (with the aid of symmetry conditions) in Figure 1b. Concurrently, at each time step, conditions immediately behind the discontinuous shock (boundary AD in Figures 1a and 1b) as well as the local shock wave velocity are obtained from an iterative method which requires the simultaneous satisfaction of the Rankine-Hugoniot jump relations for a moving shock wave and an unsteady, one-dimensional characteristics calculation utilizing the internal flow variables near the shock wave. A similar characteristics calculation yields conditions along the body (boundary BC). The flow field is bounded above by a horizontal line DC, along which properties are simply obtained by linear extrapolation from the internal points. The upper boundary DC must be completely in the supersonic region in order to minimize the effect of this extrapolation on the upstream flow field. Some practical numerical ramifications of this extrapolation as well as pertinent aspects of the technique are discussed in detail in reference 9.

#### NONEQUILIBRIUM NOZZLE FLOWS

(U) The physical problem treated here is that of the quasi-one-dimensional motion of a high-temperature gas expanding from equilibrium reservoir conditions through a convergent-divergent nozzle, where the expansion is rapid enough such that vibrational and chemical nonequilibrium prevail locally in both the subsonic and supersonic portions of the flow. (The term "quasi-one-dimensional" implies

that flow properties in the nozzle are functions of only  $x$  and  $t$ , whereas the local cross-sectional areas are allowed to vary, i.e., the flow is not constant area flow.) Vibrational and chemical nonequilibrium are the only dissipative mechanisms assumed in the flow; the effects of thermal conduction, diffusion and viscous dissipation are assumed to be negligibly small. The equilibrium reservoir conditions and nozzle shape are specified, and a solution is sought for the steady-flow distribution of  $\rho$ ,  $u$ ,  $T$ ,  $p$ ,  $e_{vib}$  and chemical composition in the  $x$ -direction along the nozzle (see Fig. 2). The unique aspect of the present analysis is that a time-dependent approach is used to obtain the steady-state nonequilibrium nozzle flow variables.

(U) For this problem, the time-derivatives,  $(\frac{\partial g}{\partial t})$  and  $(\frac{\partial^2 g}{\partial t^2})$ , which appear in equation (1) are obtained from the unsteady quasi-one-dimensional conservation equations (the independent variables are  $x$  and  $t$ ).

$$\text{continuity} \quad \frac{\partial \rho}{\partial t} = - \frac{1}{A} \frac{\partial (\rho u A)}{\partial x} \quad (7)$$

$$\text{momentum} \quad \frac{\partial u}{\partial t} = - \left( \frac{1}{\rho} \frac{\partial p}{\partial x} + u \frac{\partial u}{\partial x} \right) \quad (8)$$

$$\text{energy} \quad \frac{\partial e}{\partial t} = - \left[ \frac{p}{\rho} \frac{\partial u}{\partial x} + \frac{p}{\rho} u \frac{\partial (\ln A)}{\partial x} + u \frac{\partial e}{\partial x} \right] \quad (9)$$

$$\text{rate} \quad \frac{\partial q}{\partial t} = - u \frac{\partial q}{\partial x} + w(\rho, T, q) \quad (10)$$

$$\text{state} \quad p = \rho R T$$

where  $A = A(x)$ ,  $q$  denotes a nonequilibrium quantity such as  $e_{vib}$  or chemical composition, and  $w$  is a function which depends on the type of rate process under consideration. Equations (7) to (10), along with their subsequent  $t$  and  $x$  differentiations, allow the calculation of the nonequilibrium nozzle flow variables in steps of time, starting with assumed initial distributions throughout the nozzle. This analysis is presented in considerable detail in references 10 and 11; therefore, no further discussion will be made here.

RESULTS

(U) The results illustrated in the present survey are not intended to be a complete documentation of the current numerical calculations; such documentations are available in references 9-11. Rather, the present purpose is to give a sample of the results which clearly illustrate the nature and advantages of the time-dependent technique.

BLUNT BODY RESULTS

(U) Figure 3 illustrates the time-dependent motion of the bow shock wave as it begins from the initially assumed shape and position, and as it subsequently converges to its steady-flow configuration. The body is a two-dimensional parabolic cylinder with a cross-section given by  $b = 0.769 y^2 - 1.0$ . Note that, at early times, the shock wave moves away very rapidly from its initially assumed shape and inexorably approaches its steady-state position. Practically no change can be observed between the 300th and 500th time step. This rapid movement is further demonstrated in Figure 4, which shows the time variation of the nondimensional bow shock wave velocity,  $w/(p_\infty/\rho_\infty)^{1/2}$ , along the centerline. Again, Figure 4 indicates that the strongest transients occur at early values of time. The final steady-state shock wave and sonic line shapes are illustrated in Figure 5 for  $M_\infty = 4$  and 8.

(U) Similar results for a cylinder-wedge are shown in Figure 6, where the time-dependent shock wave motion is again illustrated. The body is composed of a cylindrical nose, a 14-degree half-angle wedge afterbody, and a short, graphically determined and practically indistinguishable transition section which serves to smooth the discontinuous body curvature at the shoulder. (The need for and behavior of such a transition section is discussed in reference 9.) Also in Figure 6, the final steady-state shock wave obtained from the present calculations is compared with the empirical correlation of Billig.<sup>12</sup> This correlation is accurate and simple to apply, as verified in reference 13. Figure 6 shows very good agreement between the present exact numerical results and Billig's correlation. Finally, Figure 7 presents the time variation of the stagnation point pressure, showing its approach to the proper steady-state value, and Figure 8 shows the final, steady-state pressure distribution along the surface of the blunted wedge as a function of the vertical coordinate,  $y$ . Figure 8 shows that: (1) the proper supersonic wedge pressure is achieved asymptotically

and monotonically far downstream of the blunt nose, and (2) the pressure distribution over the cylindrical portion compares favorably with infinite Mach number circular cylinder results obtained by Fuller<sup>14</sup> using an inverse method. At hypersonic speeds, the pressure distribution is somewhat insensitive to  $M_\infty$ ; consequently, an infinite Mach number comparison is reasonably valid.

(U) Two points concerning the nature of the present time-dependent blunt-body calculations can now be summarized from Figures 3-8: (1) the most extreme variations in the flow field occur at early times where the "driving potential" towards the steady state is the strongest, and (2) the proper steady state is approached (and for practical purposes, is achieved) at large values of time.

(U) The previous results have dealt with two-dimensional bodies; the results for axisymmetric shapes are similar, as represented in Figures 9-11. Steady-state shock-wave shapes for a sphere-cone are shown in Figure 9 and compared with Billig's correlation.<sup>12</sup> The body is composed of a spherical nose, a 14 degree half-angle cone afterbody, and a short transition section at the shoulder (similar to the aforementioned cylinder-wedge). In addition, the steady-state surface-pressure distributions are shown in Figures 10 and 11, and are compared with modified Newtonian predictions as well as the combined inverse blunt body and characteristics calculations of Roberts et al.<sup>15</sup> Note that, along the conical surface downstream from the nose, the present time-dependent results qualitatively predict the over-expansion and subsequent approach to the sharp cone pressure value,  $P_c$ . However, the quantitative values for this overexpansion (as well as the sonic line shape) may be influenced by the presence of the body transition section between the spherical nose and conical afterbody (in comparison to a pure sphere-cone shape); this matter is discussed in more detail in reference 9.

(U) The previous figures demonstrate an inherent advantage of the time-dependent approach over more conventional steady-state blunt-body techniques, namely, that by one unified solution, the flow field can be computed not only for just the blunt-nose region, but also for large distances downstream of the nose. In principle, no restriction is put on the extent of the flow field that can be treated; in practice, the flow field extent is limited by requirements for reasonable computer execution times. Incidentally, the computer time for the present blunt-body flow-field calculations for one body shape at one free-stream Mach number averaged 25 minutes on an IBM 7090; however, the

Vol. 2

computer programing was done by the present authors themselves with no effort made for optimization, hence the quoted computer time is misleading and by no means reflects a lower limit.

(U) Many additional results obtained during the present investigation plus some pertinent numerical experiments regarding the nature of the time-dependent blunt-body method are presented in reference 9.

NONEQUILIBRIUM NOZZLE FLOWS

(U) An entirely separate application of the time-dependent technique has been made to the problem of the expansion of a high temperature gas through a convergent-divergent nozzle when vibrational or chemical nonequilibrium conditions prevail within the gas both upstream and downstream of the throat. The present time-dependent analysis circumvents several problems encountered with steady-state analyses, and has the virtue of being a more natural and straightforward approach to the problem. These advantages are discussed at length in references 10 and 11. The practical motivation for nonequilibrium nozzle calculations stems from the importance of high-temperature flows through rocket nozzles and high-enthalpy aerodynamic testing facilities, and the present time-dependent analysis appears to warrant serious consideration for future applications to such flows.

(U) The following results are chosen as demonstrative samples of the present nozzle calculations; a complete discussion and presentation of results can be found in references 10 and 11.

(U) In order to examine the purely fluid dynamic behavior of the present time-dependent nozzle analysis, results were obtained for the case of a calorically perfect (nonreacting, constant  $\gamma$ ) gas; some of these results are illustrated in Figures 12 and 13. Starting with an initial linear distribution, the transient temperature profiles through the nozzle are shown at various time steps in Figure 12. Two important points are noted from Figure 12: (1) at early values of time, the profiles relax very rapidly to a steady-state distribution, and (2) the resulting steady-state distribution shows excellent agreement with known steady-state results obtained from reference 16. These results are complemented by the transient profiles of local-mass flow,  $\rho uA$ , through the nozzle, as shown in Figure 13. The somewhat wavy initial distribution for  $\rho uA$

is a consequence of the arbitrarily assumed initial distributions for  $\rho$  and  $u$ . Figure 13 markedly illustrates that the transient solution rapidly proceeds to the proper steady mass flow,  $\rho u A = \text{constant}$ . This aspect of the present analysis is an important virtue when applied to nonequilibrium flows, where the nonequilibrium critical mass flow can not be calculated in advance and must be obtained as part of the complete nozzle solution.

(U) Figures 14 and 15 illustrate the time-dependent behavior of the vibrational and chemical nonequilibrium solutions respectively. Figure 14 shows the transient distributions of vibrational energy throughout the nozzle for the expansion of pure diatomic nitrogen. Note the rapid approach to the steady-state distribution. This steady-state distribution agrees with the results of a recent steady-flow analysis by Wilson et al<sup>17</sup>; however, the time-dependent results were obtained in a more straightforward fashion.<sup>10,11</sup> Similar comments can be made for the case of the chemical nonequilibrium expansion of partially dissociated oxygen, as shown in Figure 15. Here, the transient profiles of atom mass fraction,  $\alpha$ , are shown at various time steps, and the final steady-state distribution is seen to agree favorably with the steady-state analysis of Hall and Russo.<sup>18</sup>

#### CONCLUDING DISCUSSION

(U) This paper has been a relatively brief survey of numerical, time-dependent, inviscid flow-field calculations made at the U. S. Naval Ordnance Laboratory. In the interest of conciseness, no effort has been made to discuss all the results and details involved with these calculations; the interested reader is urged to consult the cited references for more complete and self-contained discussions. However, the intention of the present survey has been to inculcate some appreciation for the advantages and straightforward nature of the time-dependent technique, and to present some results which are representative of the time-dependent numerical solutions for the flow about supersonic blunt bodies and the high-temperature nonequilibrium expansion through convergent-divergent nozzles.

#### REFERENCES

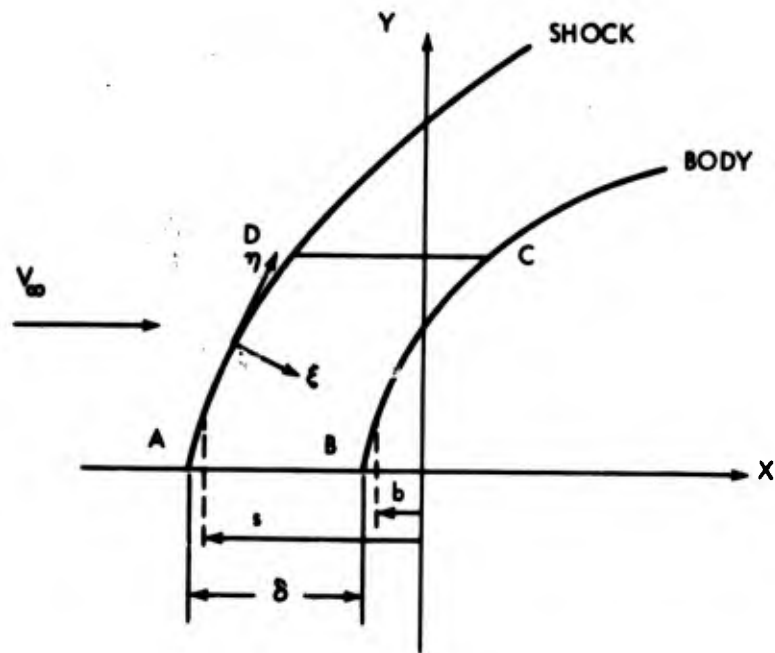
1. Lax, P. D., "Weak Solutions of Nonlinear Hyperbolic Equations and their Numerical Computations," Commun. Pure Appl. Math., Vol. 7, 1954, pp 159-193

**8th Navy Symposium on Aeroballistics**

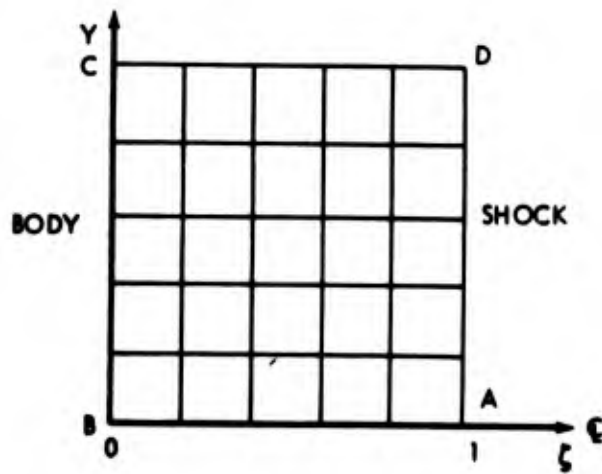
**Vol. 2**

2. Lax, P. D. and Wendroff, B., "Systems of Conservation Laws," Commun. Pure Appl. Math., Vol. 13, 1960, pp 217-237
3. Bohachevsky, I. O. and Rubin, E. L., "A Direct Method for Computation of Nonequilibrium Flows with Detached Shock Waves," AIAA Journal, Vol. 4, No. 4, April 1966, pp 600-607
4. Rubin, E. L. and Burstein, S. Z., "Difference Methods for the Inviscid and Viscous Equations of a Compressible Gas," PIBAL Report No. 989, June 1967, Polytechnic Institute of Brooklyn
5. Masson, B. S., "Two-Dimensional Flow Field Calculations by the Godunov Method," Picatinny Arsenal Technical Report 3575, July 1967
6. VonNeumann, J. and Richtmyer, R. D., "A Method for the Numerical Calculation of Hydrodynamic Shocks," Journal of Applied Physics, Vol. 21, No. 3, March 1950, pp 232-237
7. Moretti, G., "The Importance of Boundary Conditions in the Numerical Treatment of Hyperbolic Equations," PIBAL Report No. 68-34, November 1968
8. Moretti, G. and Abbett, M., "A Time Dependent Computational Method for Blunt Body Flows," AIAA Journal, Vol. 4, No. 12, December 1966, pp 2136-2141
9. Anderson, J. D., Jr., Albacete, L. M. and Winkelmann, A. E., "On Hypersonic Blunt Body Flow Fields Obtained with a Time-Dependent Technique," NOLTR 68-129, August 1968, U. S. Naval Ordnance Laboratory, White Oak, Maryland
10. Anderson, J. D., Jr., "A Time-Dependent Analysis for Vibrational and Chemical Nonequilibrium Nozzle Flows," to be presented at the AIAA 2nd Fluid and Plasma Dynamics Conference, San Francisco, June 1969
11. Anderson, J. D., Jr., "A Time-Dependent Analysis for Quasi-One-Dimensional Nozzle Flows with Vibrational and Chemical Nonequilibrium," NOLTR 69-52 (to be published)
12. Billig, F. S., "Shock Wave Shapes Around Spherical and Cylindrical Nosed Bodies," Journal of Spacecraft and Rockets, Vol. 4, No. 4, June 1967, pp 822-823
13. Anderson, J. D., Jr., Albacete, L. M. and Winkelmann, A. E., "Comment on Shock Wave Shapes Around Spherical and Cylindrical Nosed Bodies," Journal of Spacecraft and Rockets, Vol. 5, No. 10, October 1968, pp 1247-1248

14. Fuller, F. B., "Numerical Solutions for Supersonic Flow of an Ideal Gas Around Blunt Two-Dimensional Bodies," NASA TN-D-791, 1961
15. Roberts, J. F., Lewis, C. H. and Reed, M., "Ideal Gas Spherically Blunted Cone Flow Field Solutions at Hypersonic Conditions," AEDC-TR-66-121, August 1966
16. Ames Research Staff, "Equations Tables, and Charts for Compressible Flow," NACA Report 1135, 1953
17. Wilson, J. L., Schofield, D. and Lapworth, K. C., "A Computer Program for Non-Equilibrium Convergent-Divergent Nozzle Flow," National Physical Laboratory Report 1250, Aeronautical Research Council No. A.R.C. 29246, October 1967
18. Hall, J. G. and Russo, A. L., "Studies of Chemical Nonequilibrium in Hypersonic Nozzle Flows," AFOSR TN 59-1090, CAL Report AD-1118-A-6, November 1959.



1a.



1b.

FIG. 1: Coordinate system and grid points for blunt-body flow field

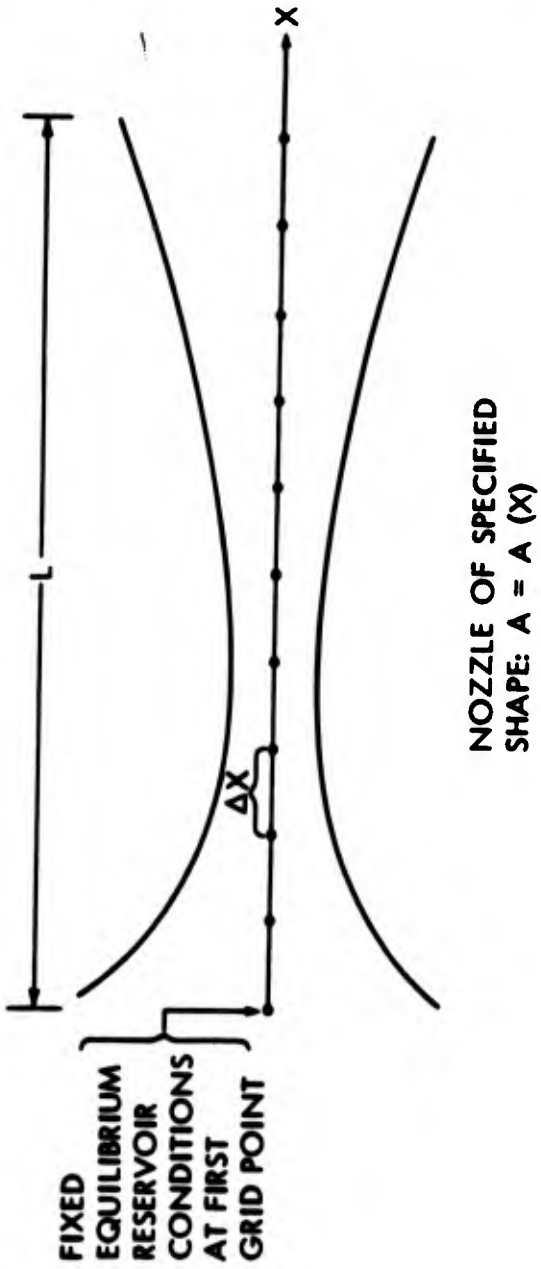


FIG. 2: Coordinate system and grid points for quasi-one-dimensional nozzle flows

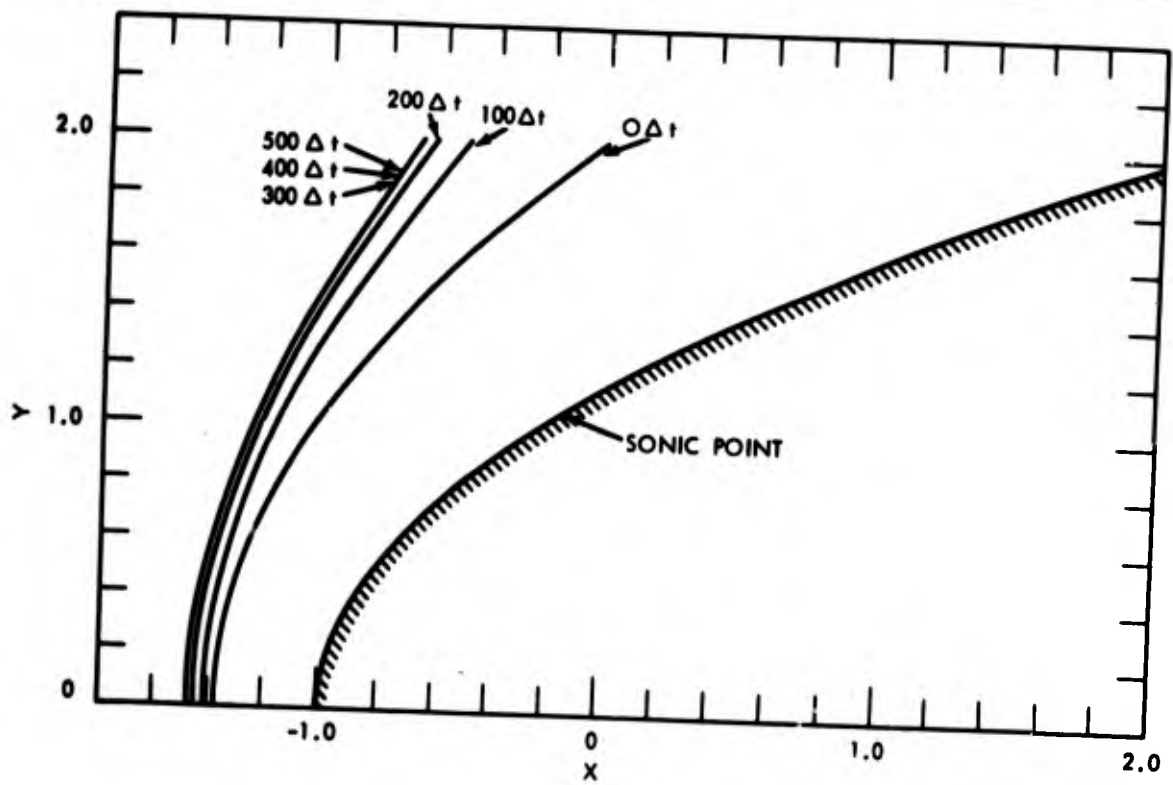


FIG. 3: Time-dependent shock wave motion, parabolic cylinder,  $M_\infty = 4$

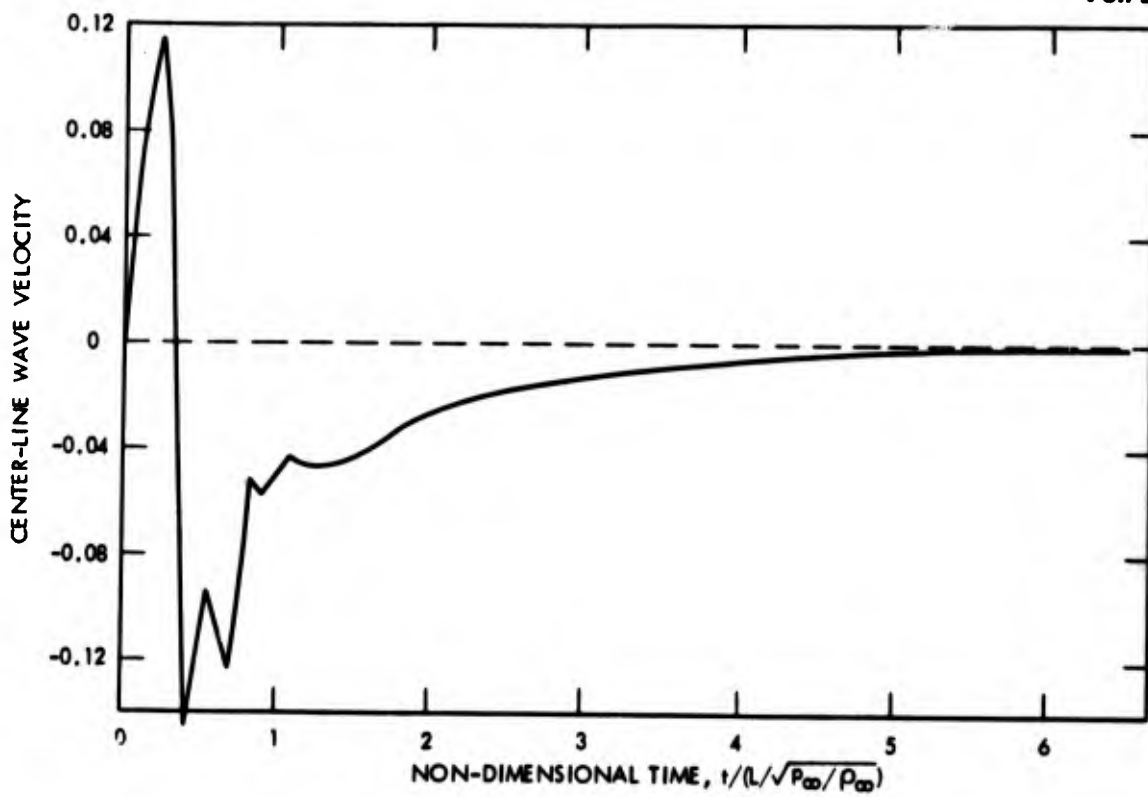


FIG. 4: Time variation of wave velocity, parabolic cylinder,  $M_\infty = 4$

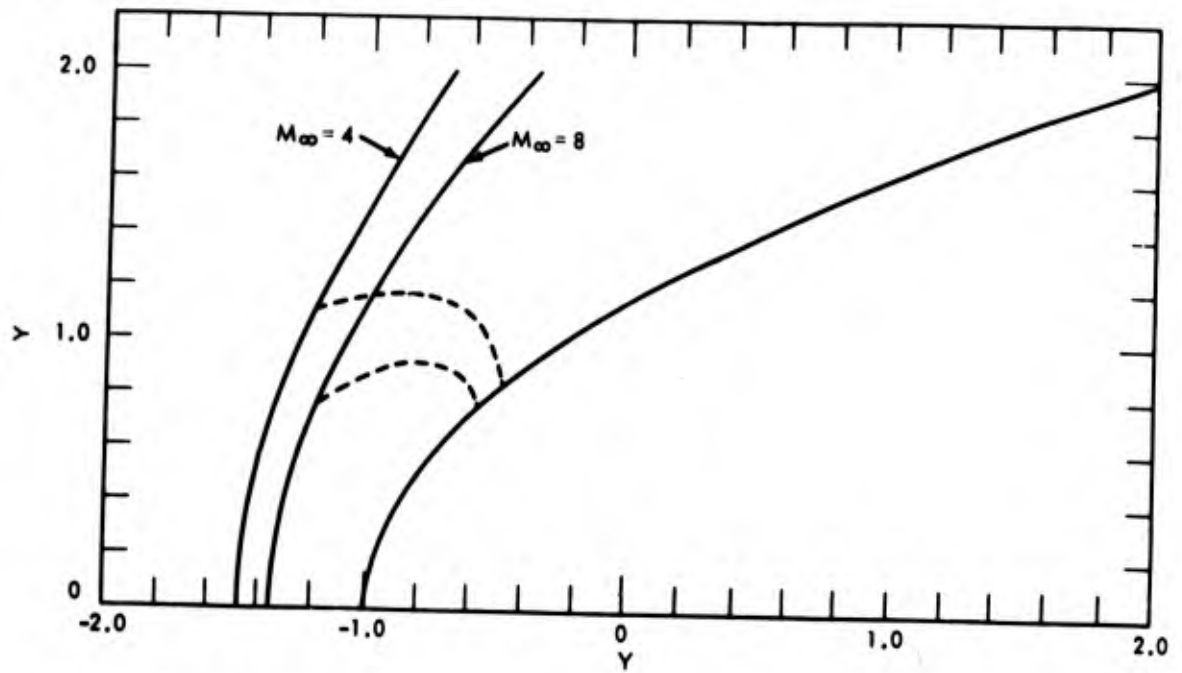


FIG. 5: Steady-state shock shapes and sonic lines obtained with the present time-dependent analysis, parabolic cylinder

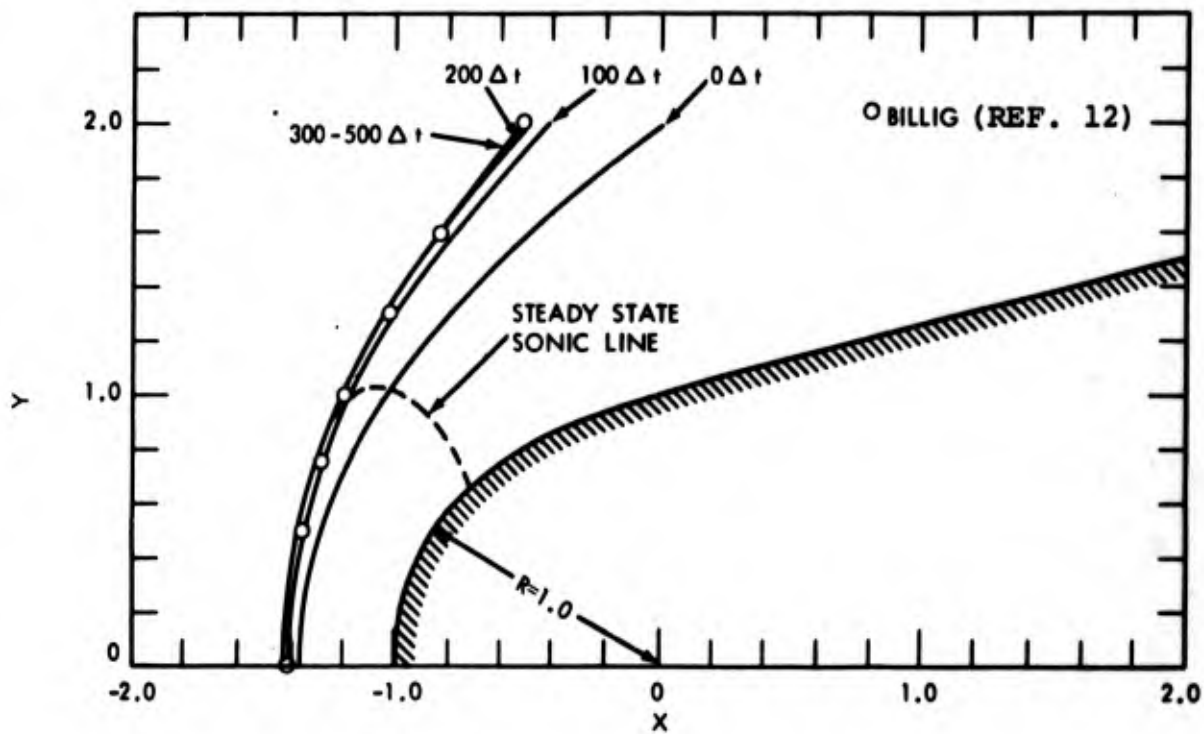


FIG. 6: Time-dependent shock wave motion, blunted wedge,  
 $M_{\infty} = 8$

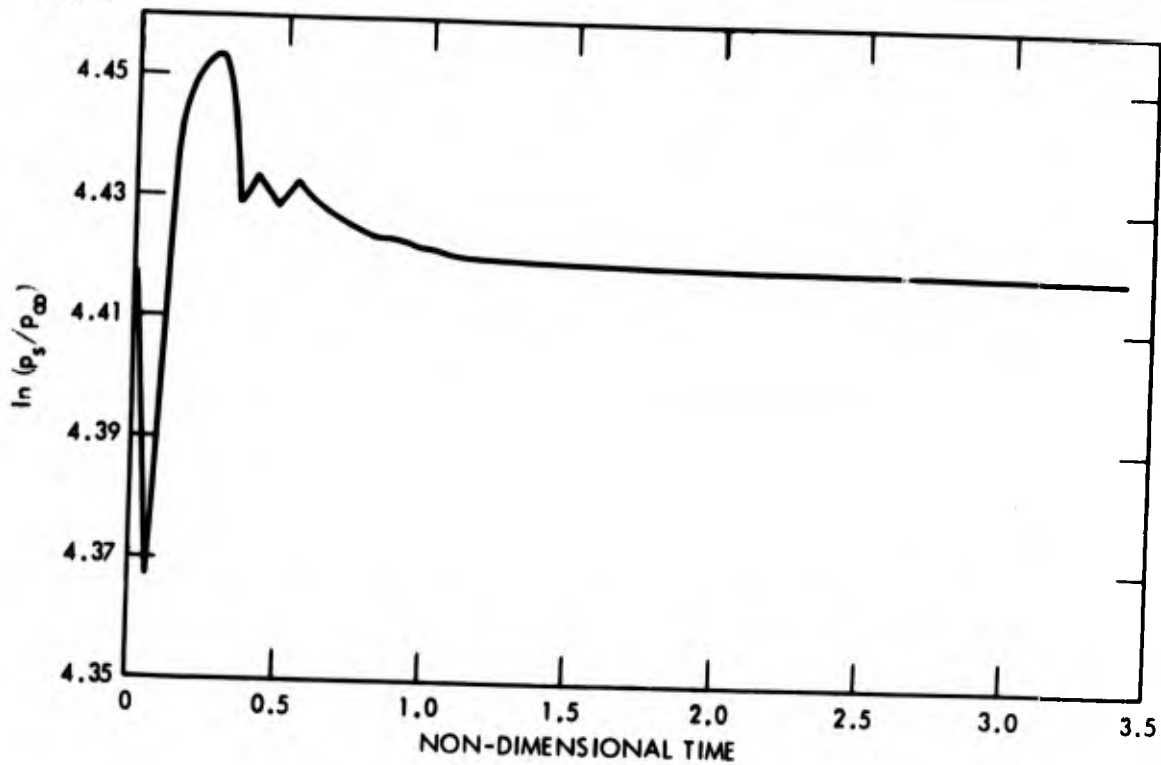


FIG. 7: Time variation of stagnation point pressure, blunted wedge,  $M_\infty = 8$

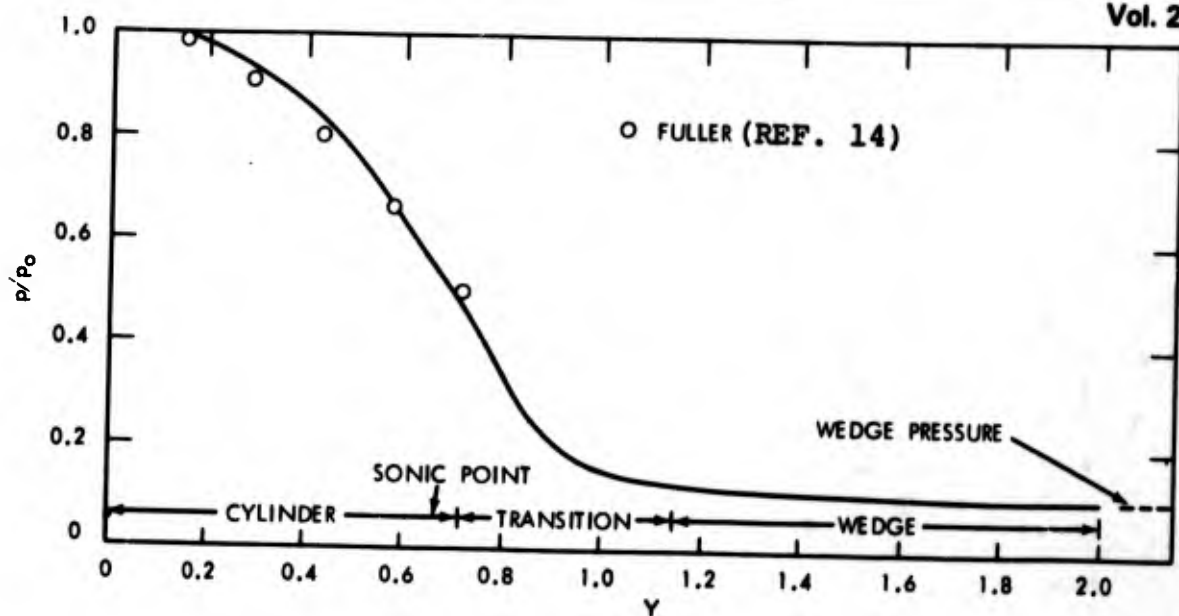


FIG. 8: Steady-state surface-pressure distribution obtained with the present time-dependent analysis; blunted wedge,  $M_\infty = 8.0$

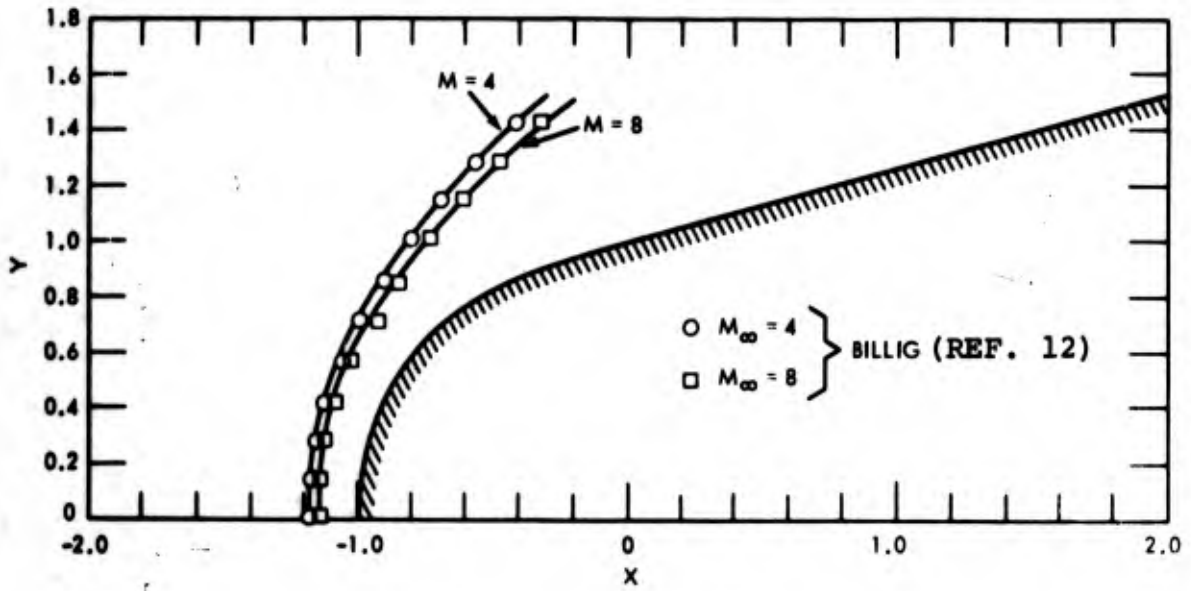


FIG. 9: Steady-state shock-wave shapes obtained with the present time-dependent analysis, sphere-cone

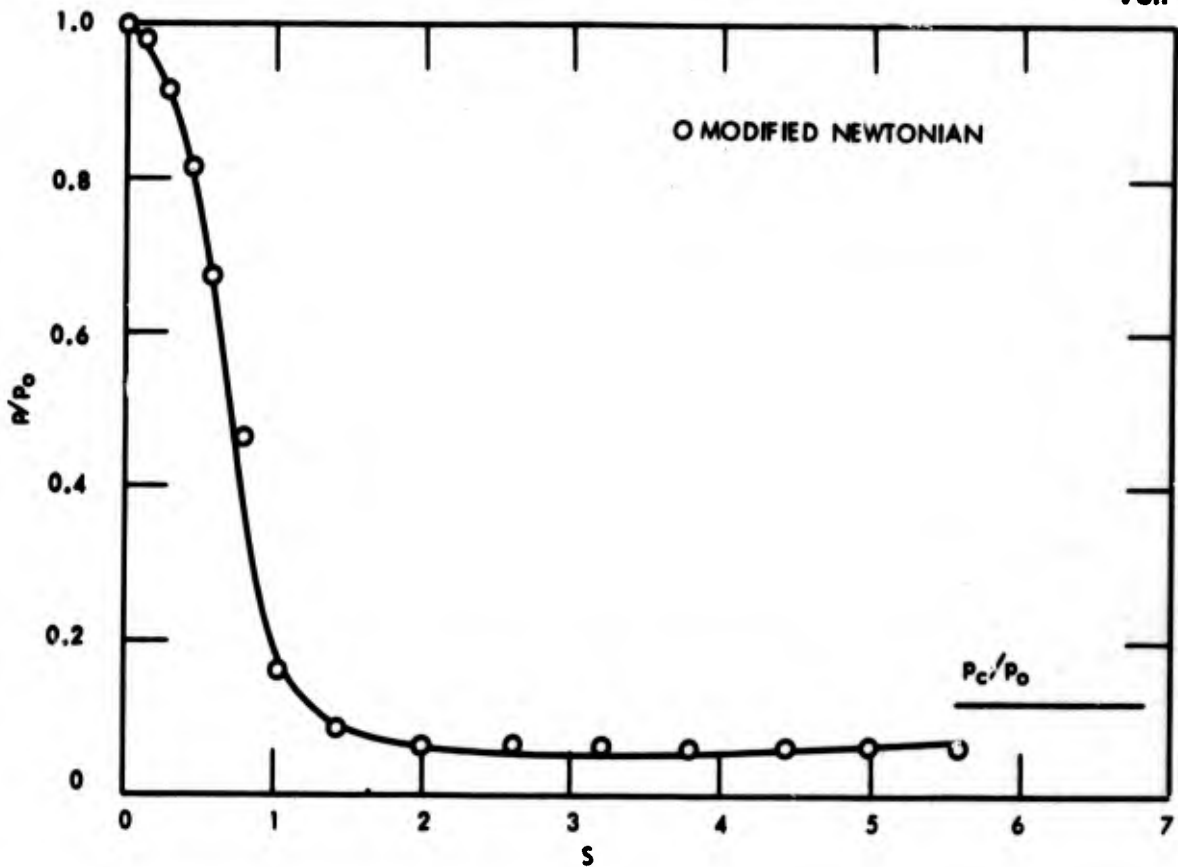


FIG. 10: Steady-state surface-pressure distribution obtained with the present time-dependent analysis, sphere-cone,  $M_\infty = 4$

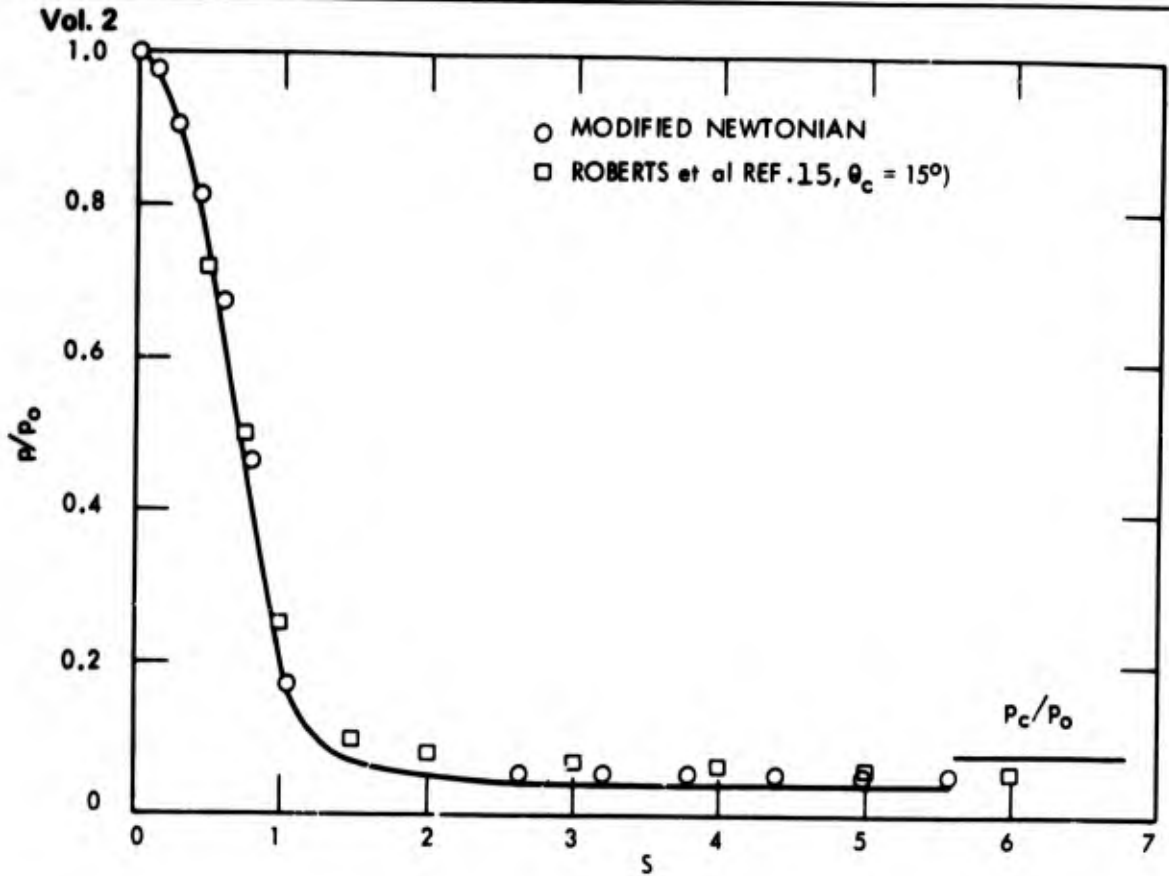


FIG. 11: Steady-state surface-pressure distribution obtained with the present time-dependent analysis, sphere-cone,  $M_\infty = 8$

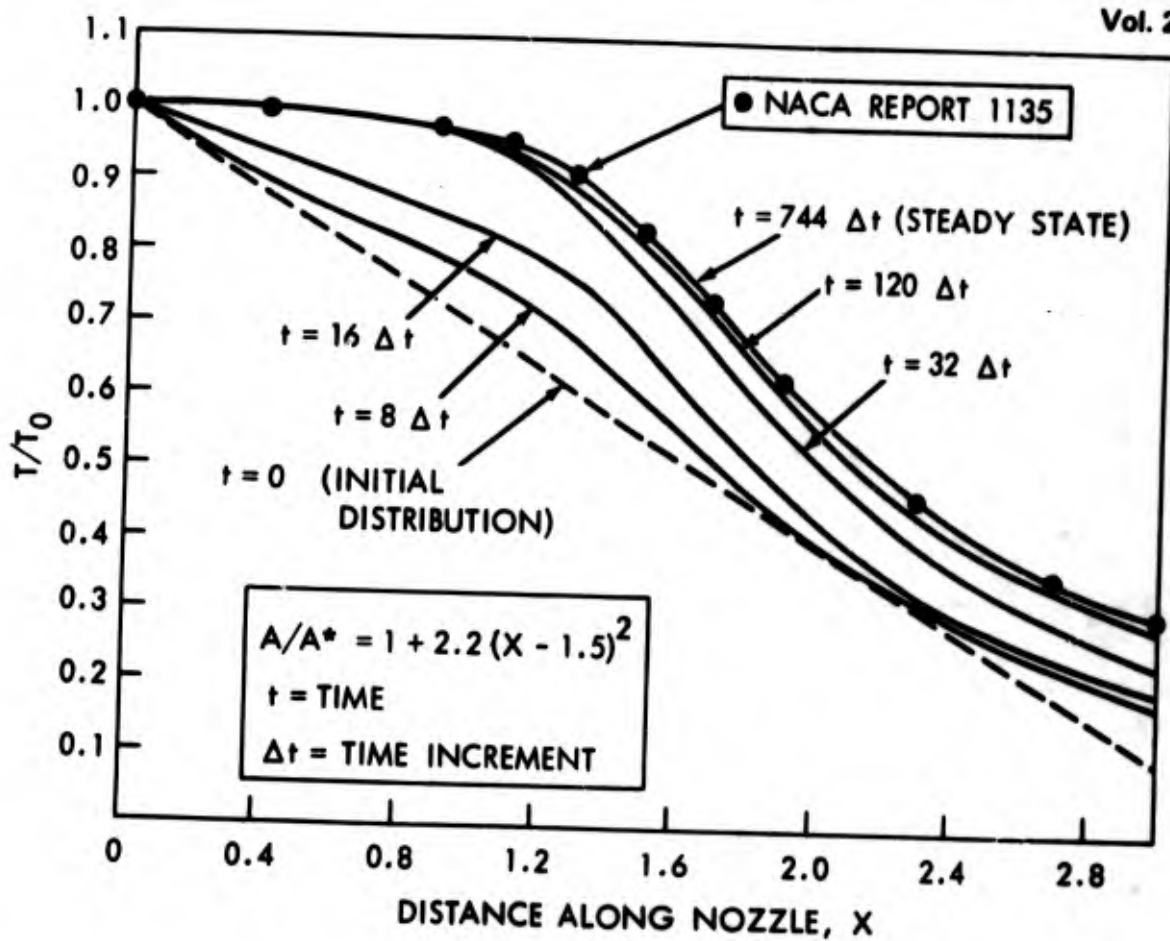


FIG. 12: Transient and final steady-state temperature distributions for a calorically perfect gas obtained from the present time-dependent analysis;  $\gamma = 1.4$

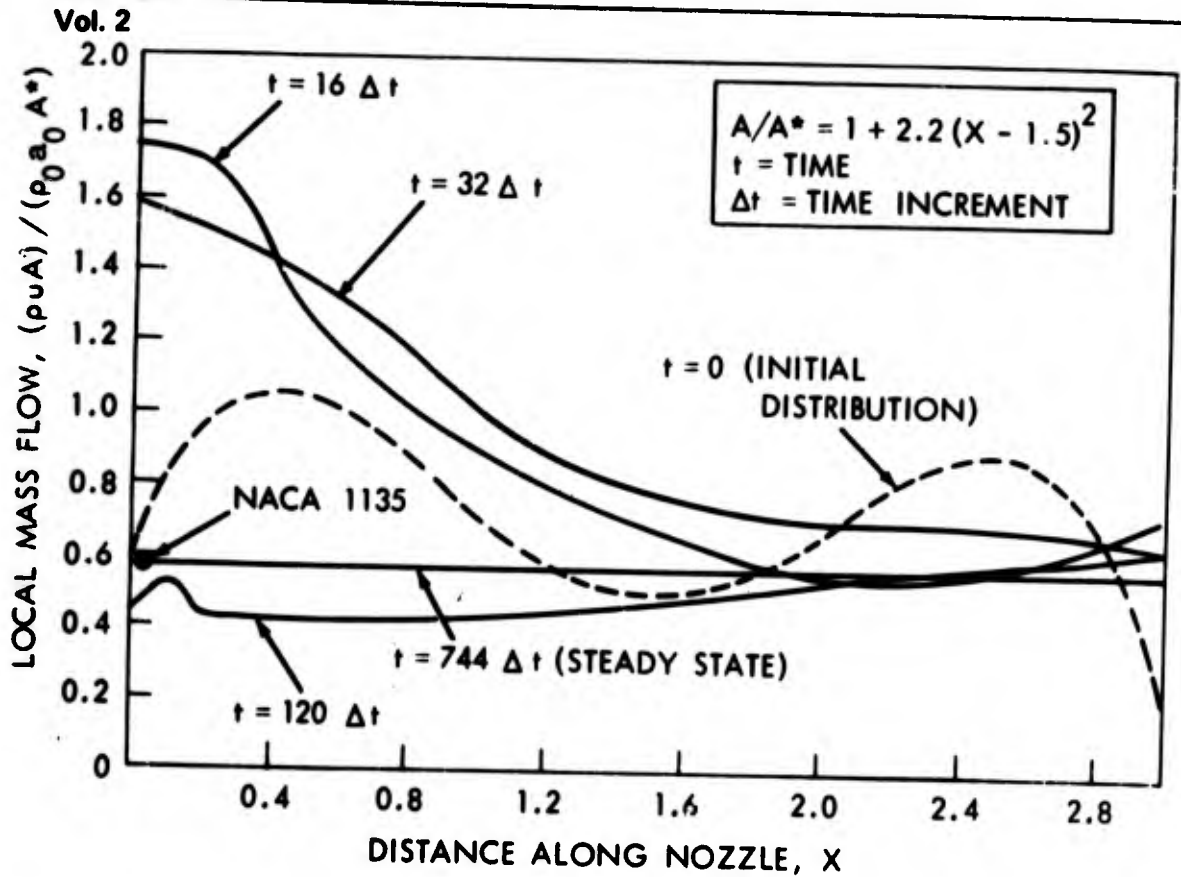


FIG. 13: Transient and final steady-state mass-flow distributions for a calorically perfect gas obtained from the present time-dependent analysis;  $\gamma = 1.4$

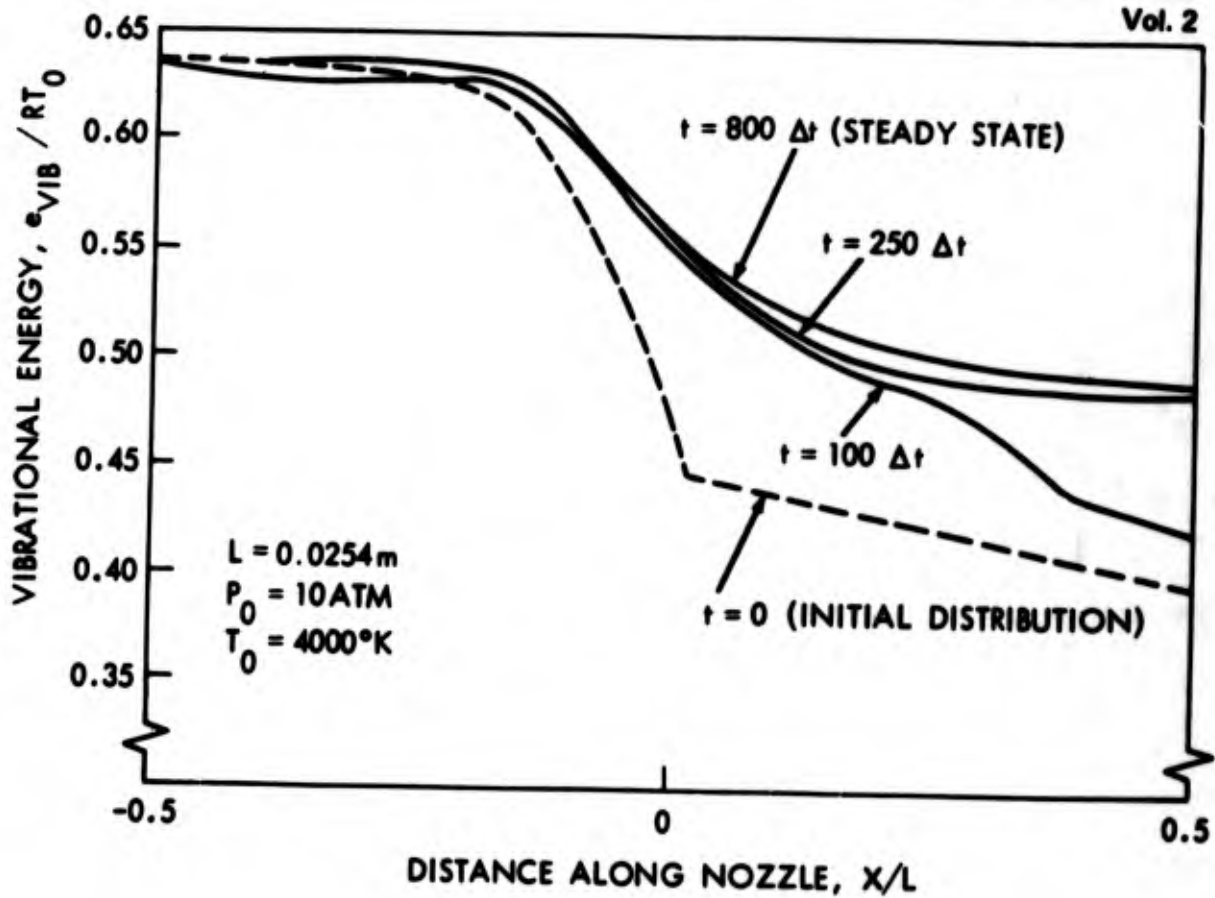


FIG. 14: Transient and final steady-state  $e_{\text{vib}}$  distributions for the nonequilibrium expansion of  $\text{N}_2$  obtained from the present time-dependent analysis

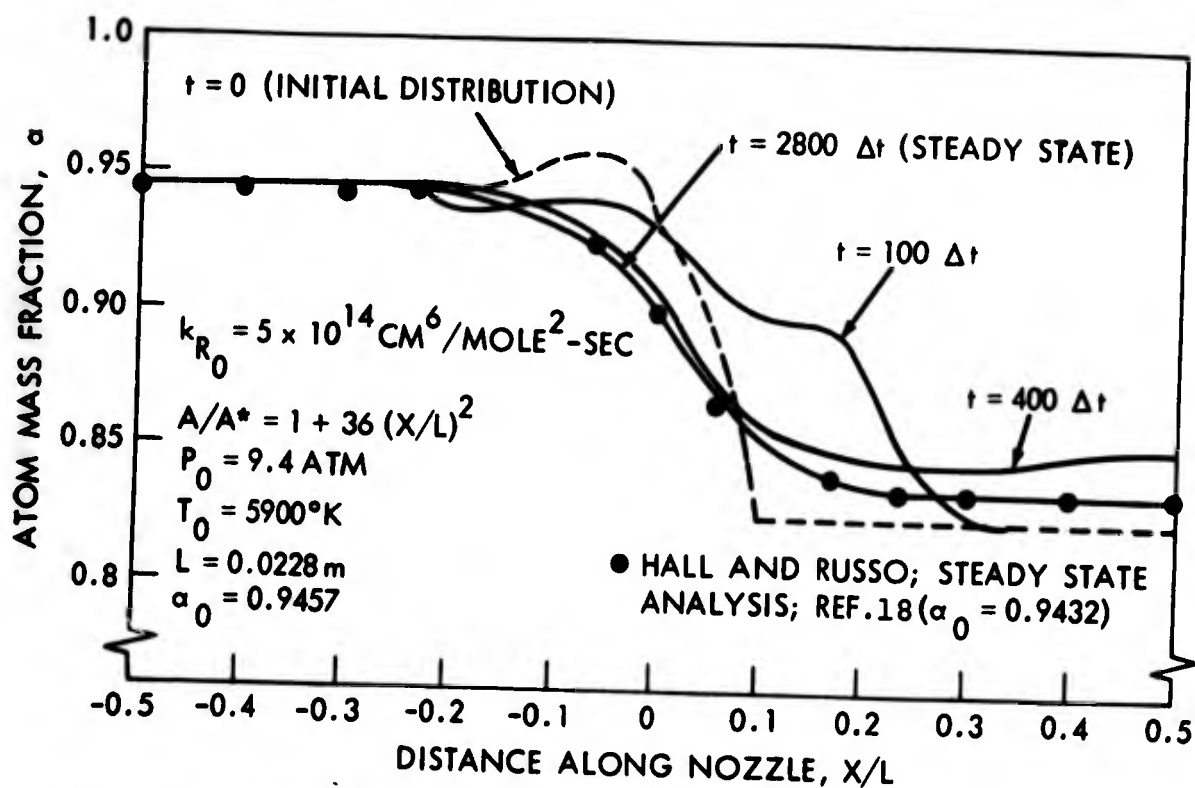


FIG. 15: Transient and final steady-state atom mass fraction distributions for the nonequilibrium expansion of dissociating oxygen obtained from the present time-dependent method

Paper No. 10

**NONEQUILIBRIUM FLOW OVER BLUNT BODIES USING  
METHOD OF INTEGRAL RELATIONS**

(U)

(Paper UNCLASSIFIED)

by

T. C. Tai

Naval Ship Research and Development Center  
Washington, D.C. 20007

**ABSTRACT.** The method of integral relations is employed for calculating the fluid properties of a chemically nonequilibrium flow over blunt bodies traveling at hypersonic speeds. A five-component gas model composed of  $O_2$ ,  $N_2$ ,  $O$ ,  $N$  and  $NO$  is postulated for a reasonable description of the chemical reaction process.

The one-strip integration is considered along with a linear integrand approximation. The flow governing equations are then reduced to a system of ordinary differential equations for integration along the body surface. The fourth-order Runge-Kutta method is used in numerical computation. In order to establish the upper and lower flow boundaries, the frozen and equilibrium flows are also considered using the same technique.

The numerical results compare closely with existing theoretical data. It is found that the "real gas" effect on the pressure is much smaller than on the density and temperature distributions. The nonequilibrium flow results generally fall between those of the frozen and equilibrium cases but tend toward the equilibrium one. However, for  $M_\infty = 8.0$ , the nonequilibrium data, with assumption of vibration being unexcited at the shock, approach those of frozen flow.

SYMBOLS

A	a function defined Equation (B20)
a	functional constant
$C_i$	mass fraction of i-th species, $C_i = \rho_i/\rho$
e	specific internal energy
$F_1$ thru $F_8$	functions defined in Equations (B1) through (B8)
$G_1$ thru $G_6$	functions defined in Equations (B13) through (B18)
h	static enthalpy normalized by its stagnation value
j	number of reactions
K	$K = (\gamma_\infty - 1)/2\gamma_\infty$
$K_c$	equilibrium constant for a chemical reaction
$K_f$	forward reaction rate coefficient
$K_r$	reverse reaction rate coefficient
k	index in Equations (25) and (27)
M	Mach number
m	number of species
N	number of strips divided in shock layer
P	static pressure normalized by its freestream stagnation value
Q	catalytic body
R	local body radius of curvature normalized by the nose radius
$R'_o$	body nose radius
r	radial distance measured from the body axis of symmetry and normalized by the nose radius
s, n	orthogonal curvilinear coordinates measured along and normal to the body surface normalized by the nose radius
T	static temperature normalized by its freestream stagnation value
u, v	normalized velocity components tangent and normal to the shock wave

V	velocity normalized by its maximum value
W	molecular weight
$\alpha$	a function in Equation (26)
$\beta$	a function in Equation (26)
$\gamma$	specific heat ratio
$\delta$	shock layer thickness
$\epsilon$	$\epsilon = \rho_{\infty} / \rho$
$\Theta_d$	characteristic temperature for dissociation
$\Theta_v$	characteristic temperature for vibration
$\theta$	angle between body tangent and axis of symmetry
$\lambda$	a function in Equation (26)
$\nu, \bar{\nu}$	Stoichiometric coefficients
$\rho$	static density normalized by its freestream stagnation value
$\chi$	angle between shock tangent and normal to body axis of symmetry
$w'$	rate of production by chemical reaction

## Subscripts

b	conditions on body surface
i	i-th species
j	j-th chemical reaction
n	component along n-coordinate
s	component along s-coordinate
t	total (freestream stagnation quantities)
$\delta$	conditions at shock
o	at $s = 0$
$\infty$	conditions at freestream

Superscripts

- $\sigma$       { 0, for two-dimensional flow  
          { 1, for axisymmetric flow
- '            (primed) dimensional quantities
- \*           conditions at singular point (sonic point for frozen and  
              equilibrium flows)

## INTRODUCTION

In recent studies of hypersonic flow, a considerable effort has been expended on the problems of predicting aerodynamic forces and heat transfer over a blunt body. For inviscid flow regions, the problem has mostly dealt with the assumption either of frozen (perfect gas) flow or of chemically equilibrium flow (Refs. 1, 2 and 3). Since a finite reaction time has an appreciable effect on the flow properties, the actual flow will be in chemical nonequilibrium along with partial or full vibration excitation. Analyses on nonequilibrium flows have been treated, for instance, by Lick (Ref. 4), Hall, Eschenroeder and Marrone (Ref. 5) and Shih and Baron (Ref. 6). However, the most difficult part of the solution lies in the numerical technique because of two-boundary-value problems involved. Therefore, a workable method for handling the nonequilibrium, as well as equilibrium and frozen flows, is currently in demand.

In this paper, the method of integral relations is employed for numerical treatment of a chemically nonequilibrium flow over blunt bodies traveling at hypersonic speeds. In order to establish the upper and lower flow boundaries, the frozen and equilibrium flows are also considered using the same technique.

## ANALYSIS

## BASIC FLOW EQUATIONS

As shown in Fig. 1, an orthogonal curvilinear coordinate system  $s$  and  $n$ , which are measured along and normal to the body surface, is used. In these coordinates, the governing equations of a steady, adiabatic, inviscid, nonheat-conducting and chemically nonequilibrium flow are as follows:

Continuity

$$\frac{\partial}{\partial s} (\rho V_s r^\sigma) + \frac{\partial}{\partial n} \left[ \left(1 + \frac{n}{R}\right) \rho V_n r^\sigma \right] = 0 \quad (1)$$

$s$ -Momentum

$$V_s \frac{\partial V_s}{\partial s} + \left(1 + \frac{n}{R}\right) V_n \frac{\partial V_s}{\partial n} + \frac{V_s V_n}{R} + \frac{K}{\rho} \frac{\partial P}{\partial s} = 0 \quad (2)$$

# 8th Navy Symposium on Aeroballistics

## Vol. 2

### n-Momentum

$$V_s \frac{\partial V_n}{\partial s} + \left(1 + \frac{n}{R}\right) V_n \frac{\partial V_n}{\partial n} - \frac{V_s^2}{R} + \left(1 + \frac{n}{R}\right) \frac{K}{\rho} \frac{\partial P}{\partial n} = 0 \quad (3)$$

### Energy

$$h + V^2 = 1 \quad (4)$$

### Reaction-Rate

$$V_s \frac{\partial C_i}{\partial s} + \left(1 + \frac{n}{R}\right) V_n \frac{\partial C_i}{\partial n} = \left(1 + \frac{n}{R}\right) \frac{\omega_i' R_o'}{\rho' V_{\max}'} \quad (5)$$

where lengths are normalized with respect to the nose radius, and pressure, density, enthalpy and velocity components with respect to freestream stagnation values and the maximum speed.  $\omega_i'$  is the rate of production of  $i$ -th species and will be discussed in the next section.

Air will be the working medium which consists mainly of oxygen and nitrogen. For simplicity if one considers only a mixture of reacting gases  $O_2$ ,  $N_2$ ,  $O$ ,  $N$  and  $NO$  as described in next section, then three rate equations are required along with the following two algebraic equations for conservation of oxygen and nitrogen:

$$C_O + C_{O_2} + \frac{W_O C_{NO}}{W_{NO}} = (C_{O_2})_{\infty} \quad (5a)$$

$$C_O + C_{O_2} + C_N + C_{N_2} + C_{NO} = 1 \quad (5b)$$

In addition, the equations of thermodynamic state and enthalpy are needed to completely specify the blunt-body nonequilibrium flow problem.

### State

$$P = \rho T W_{\infty} \sum_i \frac{C_i}{W_i} \quad (6)$$

$i = O_2, N_2, O, N$  and  $NO$

Enthalpy

$$\begin{aligned}
 h = W_{\infty} & \left\{ \left[ \sum_{\substack{i=O_2, N_2, \\ NO}} \frac{C_i}{W_i} + \frac{5}{7} \sum_{i=O, N} \frac{C_i}{W_i} \right] T \right. \\
 & + \frac{2}{7} \left[ \sum_{\substack{i=O_2, N_2, \\ NO}} \frac{C_i}{W_i} \frac{\Theta_{v_i}}{e^{\Theta_{v_i}/T} - 1} + \sum_{i=O_2, N_2} \frac{(C_i)_{\infty} - C_i}{W_i} \Theta_{d_i} \right. \\
 & \left. \left. - \frac{C_{NO}}{W_{NO}} \Theta_{d_{NO}} \right] \right\} \quad (7)
 \end{aligned}$$

where  $T$  is normalized with respect to the freestream stagnation temperature. Equation (7) is written based on the assumption of full vibration excitation. Rigorously, vibration relaxation effects should be considered by including vibration rate equations for  $O_2$ ,  $N_2$  and  $NO$ . However, at temperatures high enough so that dissociation begins to appear, the vibrational relaxation model loses its validity (Ref. 7). The use of simpler vibrational equilibrium will be sufficient to describe the nonequilibrium flow phenomena.

The boundary conditions are:

at the body,

$$V_n = 0 \quad (8)$$

at the shock, the Rankine-Hugoniot relations may be applied.

Continuity

$$\rho_{\infty} V_{\infty} \cos \chi = \rho_{\delta} v \quad (9)$$

Momentum

$$K P_{\infty} + \rho_{\infty} V_{\infty}^2 \cos^2 \chi = K P_{\delta} + \rho_{\delta} v^2 \quad (10)$$

$$V_{\infty} \sin \chi = u \quad (11)$$

Energy

$$h_{\infty} + V_{\infty}^2 \cos^2 \chi = h_{\delta} + v^2 \quad (12)$$

## 8th Navy Symposium on Aeroballistics

Vol. 2

Species

$$(C_O)_\delta = (C_N)_\delta = (C_{NO})_\delta = 0$$

$$(C_{O_2})_\delta = (C_{O_2})_\infty$$

$$(C_{N_2})_\delta = (C_{N_2})_\infty \quad (13)$$

where  $u$  and  $v$  are normalized velocity components tangent and normal to the shock. The relations between  $u$  and  $v$  and velocities in the present coordinates are given by:

$$V_{s_\delta} = u \sin (\chi + \theta) + v \cos (\chi - \theta) \quad (14)$$

$$V_{n_\delta} = u \cos (\chi + \theta) - v \sin (\chi + \theta) \quad (15)$$

The shock angle,  $\chi$ , is geometrically related to the shock layer thickness,  $\delta$ , by the equation:

$$\frac{d\delta}{ds} = \frac{1 + \delta/R}{\tan (\chi + \theta)} \quad (16)$$

In summary, there are twelve independent equations, i.e., Equations (1) through (7) and (16) to solve for twelve unknown variables:  $\delta$ ,  $V_s$ ,  $V_n$ ,  $T$ ,  $P$ ,  $\rho$ ,  $h$ ,  $C_{O_2}$ ,  $C_O$ ,  $C_{N_2}$ ,  $C_N$  and  $C_{NO}$ .

For a fully equilibrium flow, the system of equations and boundary conditions remain identically the same except Equations (5) are replaced by the algebraic equations stating the law of mass action:

$$\prod_i \left( \frac{C_i}{W_i} \right)^{\nu_i} = \frac{K_c(T')}{(\rho') \sum_i \nu_i} \quad (\text{for equilibrium flow}) \quad (17)$$

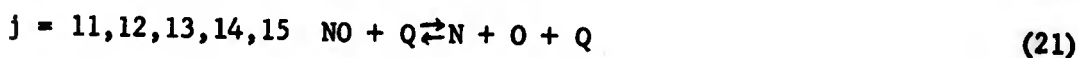
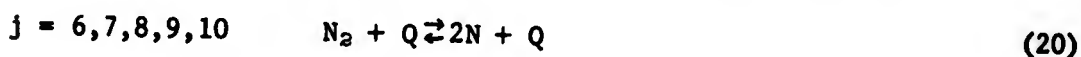
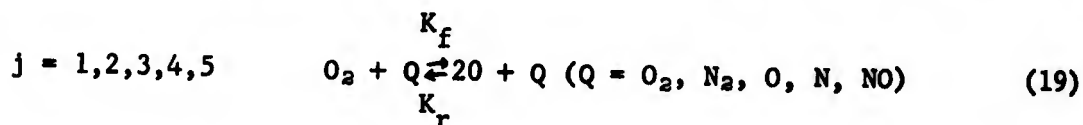
Where  $\nu$  is Stoichiometric coefficient and  $K_c$ , the equilibrium constant for a chemical reaction.

In case of a frozen flow, Equation (5) is dropped and Equation (7) reduces to the simple form.

$$h = T \quad (\text{for frozen flow}) \quad (18)$$

## GAS MODEL AND RATE OF PRODUCTION

For a chemically nonequilibrium flow, the change of various species of the gas mixture towards their thermodynamic equilibrium is governed by dissociation and recombination rate equations. Using air as working medium, a five-component gas model composed of  $O_2$ ,  $N_2$ ,  $O$ ,  $N$  and  $NO$  is postulated for a reasonable description of the chemical reaction process. Species other than oxygen and nitrogen in the air are neglected. Although ionization will normally occur after temperature reaches  $8000^\circ K$ , its effect is small on the energy balance of fluid flow. Thus for gasdynamic purposes, it can be excluded (Ref. 8). The specific reactions describing the high temperature regime for the mixture of five species are, identified by the letter  $j$ ,



The above reactions can be written in a general form



where  $\nu_{ji}$  and  $\bar{\nu}_{ji}$  are Stoichiometric coefficients of  $Q_i$  on the left and right sides, respectively. The factor  $K_{fj}$  and  $K_{rj}$  are the forward and reverse rate coefficients, respectively, of the  $j$ -th reaction. Values of these coefficients can be found in many sources (for instance, Refs. 5 and 8), which differ from one to another. In this paper, those from Ref. 5 are used as listed in Table I.

With reference to Equation (24), the rate of production of  $i$ -th species,  $\omega_i'$ , is given by the following expression:

$$\omega_i' = W_i \sum_j \left[ (\bar{v}_{ji} - v_{ji}) K_{fj} \prod_{k=1}^m \left( \frac{C_k}{W_k} \rho' \right)^{v_{jk}} + (v_{ji} - v_{ji}') K_{rj} \prod_{k=1}^m \left( \frac{C_k}{W_k} \rho' \right)^{v_{jk}} \right] \quad (25)$$

where  $i = 0, N, NO$ . Substituting Equations (25) into (5) completes the desired rate equations.

#### METHOD OF INTEGRAL RELATIONS

A general method of numerical solution for nonlinear aero-hydrodynamic problem is the method of integral relations originally proposed by Dorodnitsyn (Ref. 9). This scheme is directly applicable to the present blunt-body problem. In applying the method, the system of nonlinear partial differential equations (1) through (5) have to be recast in divergence form.

$$\frac{\partial}{\partial s} \alpha(s, n, P, \dots) + \frac{\partial}{\partial n} \beta(s, n, P, \dots) = \lambda(s, n, P, \dots) \quad (26)$$

After dividing the shock layer into strips of equal width, the divergence form of Equations (1) through (5) may be integrated outward from the body surface to each strip boundary successively at some constant value of  $s$ . This procedure reduces the partial differential equations (with independent variables  $s$  and  $n$ ) to ordinary ones (with independent variable  $s$ ). In performing the integration, the distribution of integrand,  $\alpha$ ,  $\beta$  and  $\lambda$ , must be known. A general approach is to approximate the integrands by interpolation polynomials, for example  $\alpha$  by

$$\alpha = \sum_{k=0}^N a_k(s) n^k \quad (27)$$

where  $N$  is the number of strips. In principle, the actual distribution may be represented more closely with an increasing number of strips. However, for a thin shock layer one-strip integration may be approximated to yield fairly accurate results (Refs. 1, 2 and 6). For simplicity, therefore, for  $N = 1$ , Equation (27) assumes the form

$$I = I_b(s) + \frac{n}{\delta} \left[ I_\delta(s) - I_b(s) \right], \quad I = \alpha, \beta, \lambda \quad (28)$$

which implies that the integrands vary linearly between body and shock.

Substituting Equation (28) into (26) and integrating along n-coordinate, there results

$$\frac{1}{2} (\alpha_b - \alpha_\delta) \frac{d\delta}{ds} + \frac{\delta}{2} \frac{d}{ds} (\alpha_\delta + \alpha_b) + \beta_\delta - \beta_b + \frac{\delta}{2} (\lambda_\delta + \lambda_b) = 0 \quad (29)$$

where the subscripts b and  $\delta$  designate at the body and at the shock, respectively. Quantities at the shock are given by Rankine-Hugoniot relations, namely, Equations (9) through (13). Quantities at the body are then dependent variables to be obtained by solving simultaneously the ordinary differential equations which are derived from Equation (29).

#### APPLICATION

The application of the method requires, as mentioned above, that the flow governing equations be recast in divergence form. The resulting forms are given in Appendix A. Upon substituting the corresponding integrands into Equation (29), there results:

$$\frac{dv_{s_b}}{ds} = \frac{F_1}{V_{s_b} - K \frac{dP}{d\rho}} \quad (30a)$$

$$\frac{dX}{ds} = F_2 \quad (30b)$$

$$\frac{dP_b}{ds} = F_3 \quad (30c)$$

$$\frac{d\rho_b}{ds} = F_4 \quad (30d)$$

$$\frac{dT_b}{ds} = F_5 \quad (30e)$$

$$\frac{dC_0}{ds} = F_6 \quad (30f)$$

$$\frac{dC_N}{ds} = F_7 \quad (30g)$$

$$\frac{dC_{NO}}{ds} = F_8 \quad (30h)$$

Where  $F_1$  through  $F_8$  are listed in Appendix B. Note that Eqs. (6) through (15) have been used in deriving Eqs. (30). At this stage, a set of directly integrable equations is completed by adding Eqs. (5) and (16):

$$C_O + C_{O_2} + \frac{W_O C_{NO}}{W_{NO}} = (C_{O_2})_\infty \quad (30i)$$

$$C_O + C_{O_2} + C_N + C_{N_2} + C_{NO} = 1 \quad (30j)$$

$$\frac{d\delta}{ds} = \frac{1 + \delta/R}{\tan(\chi + \theta)} \quad (30k)$$

Equations (30) are good for nonequilibrium flow. For equilibrium flow, Eqs. (30f) through (30h) are replaced by Eq. (17). For frozen flow, Eqs. (30c) through (30e) are eliminated with the aid of isentropic relations while Eqs. (30f) through (30j) are dropped.

## NUMERICAL PROCEDURE

### EVALUATION OF INITIAL VALUES

With known initial values, numerical integration of Eqs. (30) may be carried out along the body surface. The initial values are normally to be evaluated at the stagnation point. The flow properties at the stagnation point are readily found for frozen flow using the isentropic relations with specific heat ratio,  $\gamma = 1.4$ . However, for nonequilibrium and equilibrium flows, they must be obtained by integration along the stagnation streamline from shock to body until the velocity approaches zero. In any case the shock detachment distance (one of initial values) is not obtainable by considering the stagnation streamline alone since it has very little effect on the solution. The equations for this integration are reduced from Eqs. (1) through (7), letting  $V_s = 0$  and  $r^\sigma = 0$ . They are given in Appendix C.

Since at the stagnation point  $V_{s_b} = r^\sigma = 0$ , the derivatives

$dV_{s_b}/ds$  and  $d\chi/ds$  yield the form 0/0. Although this is overcome with the aid of L'Hospital's rules, the numerical integration then has to be started at some point a small distance away from the stagnation point. This is called the "initial point." The initial values at the initial point are then evaluated through a Taylor's expansion from stagnation point remaining first order terms.

#### NUMERICAL METHODS

The standard fourth-order Runge-Kutta method is employed in numerical integration both along the stagnation streamline and along the body surface. In order to avoid divergence of numerical results at the singular point (sonic point for frozen and equilibrium flows), the integration is replaced by a curve fit in the neighborhood of that point. This is accomplished with a fourth-order Lagrangian interpolating polynomial.

In evaluating the flow properties at the shock for equilibrium flow, the Rankine-Hugoniot relations (Equations (9) through (12)), combined with the law of mass action (Equation (17)), result in a fourth-order algebraic equation. This is solved with the aid of Newton's method of iteration. However, for nonequilibrium and frozen flows, no such iteration is required.

#### TWO-BOUNDARY-VALUE PROBLEMS

##### Integration Along Stagnation Streamline

As shown in Appendix C, the values for pressure and density at the stagnation point are needed in the equations for integration along the stagnation streamline. This constitutes a two-boundary-value problem in which the pressure and density values have two boundaries, at the shock and at the body. The former (at the shock) are uniquely determined by the normal shock relations. The latter (at the body) are to be satisfied by repeating the integration; i.e., one uses guessed values for  $P_{stag.pt.}$  and  $\rho_{stag.pt.}$  for the first integration and integrate values for successive integrations until they converge. Convergence is reached generally after two iterations.

##### Integration Along Body Surface

Not as unpopular as the previous one, a two-boundary-value problem involved in the integration along the body surface has been known due to the "feedback" nature of elliptic equations. Here the shock standoff distance has to be guessed at the stagnation point and the resulting solution continues at the "sonic" point. The problem is best illustrated by Equation (30a) along with Fig. 2 where the

derivative of surface velocity is plotted versus s-coordinate. At the sonic point where  $V_{s_b} = \sqrt{KdP/d\rho}$ , the denominator of Equation (30a) goes to zero. A continuous solution exists only if its numerator,  $F_1$ , becomes zero such that the ratio 0/0 still yields a finite quantity. As shown in Fig. 2, a wrong guessed  $\delta_0$  causes  $dV_{s_b}/ds$  to diverge. The adjustment of  $\delta_0$  involves some decision with regard to the smoothness with which the continuity occurs. A typical case requires about 15 iterations.

#### COMPUTATION TIME

Typical run times on an IBM 7090 computer for a complete solution are of the order of four minutes for frozen flow, five minutes for nonequilibrium flow and ten minutes for equilibrium flow. The reason for longer computer time for equilibrium case is due to the iteration involved in determining flow properties at the shock.

#### RESULTS AND DISCUSSION

Numerical results have been computed for a one-foot sphere traveling at 200,000 feet at  $M_\infty = 8.0$  and 14.44. Although the analysis is good for general axisymmetric blunt bodies, the choice of a sphere serves comparison purpose with available data. The frozen and equilibrium flows are also considered as limiting cases. The results along with some previous solutions are presented in Figs. 3 through 15.

#### RESULTS ALONG STAGNATION STREAMLINE

Results for pressure, density, temperature, velocity and mass fraction of oxygen, nitrogen and nitric oxide along the stagnation streamline are shown in Figs. 3 through 7. For nonequilibrium flow, the initial values at the shock are evaluated for both with vibrational energy excited and unexcited. In both cases for  $M_\infty = 14.44$ , the results at the stagnation point all approach those of the equilibrium case. In reality, a finite relaxation time is required for vibrational energy at its fully excited state and thus the actual flow quantities will fall within the above two limiting cases. The integration was terminated when the axial velocity became less than about 0.0005 and the pressure ceased to vary.

The "real gas" effect is best illustrated by the temperature difference between the perfect (frozen) and real (nonequilibrium and equilibrium) gas flows. At  $M_\infty = 14.44$  at 200,000 feet, the temperature at the stagnation point of a sphere for real gases is about one-half that for a perfect gas. This difference becomes smaller when the freestream Mach number decreases as shown in Fig. 5b. Results for

mass fractions, as well as other properties, agree favorably with those of Shih and Baron (Ref. 6) as indicated in Fig. 7. In Ref. 6 the vibration being fully excited at the shock was assumed in non-equilibrium flow calculations.

#### RESULTS ALONG BODY SURFACE

The calculated shock shapes and flow properties along the body surface of a sphere at 200,000 feet are presented in Figs. 8 through 13. As shown in Fig. 8, the shock layer thickness for three types of flows has its value about ten percent of the sphere radius and remains thin up to that point where the local surface Mach number reaches two ( $s \approx 1$ ). This is well past the sonic point beyond which the method of characteristics may be employed.

The frozen, equilibrium and nonequilibrium pressure variations along the body surface are shown in Fig. 9. The nonequilibrium flow results of Ref. 6 are also given. Very good agreement is found. It is seen that the real gas effect on the pressure distribution is small. The calculated pressures can be apparently approximated by the modified Newtonian pressure law with the Busemann centrifugal correction as shown. Since it is generally known that this approximation (modified Newtonian + Busemann) yields lower pressures than experimental data, the presently calculated pressures and those of Ref. 6 are both slightly too low in the downstream region. The discrepancy may be attributed to the use of simplified  $s$ -momentum and rate equations as discussed in Appendix B. The real gas solutions for density, temperature and velocity distributions differ appreciably from those for a perfect gas as shown in Figs. 10 through 12. In general, the nonequilibrium results lie close enough to those equilibrium values for  $M_\infty = 14.44$ . At  $M_\infty = 8.0$ , it is seen in Fig. 11b that the nonequilibrium temperatures with vibration excited at the shock inclines towards equilibrium values, while those with vibration unexcited inclines towards frozen case.

Fig. 13 shows the mass fraction distribution along the body surface at  $M_\infty = 14.44$ . The results compare also favorably with those of Ref. 6. Although not presented, it is found that the results of concentration of species depend directly on the body nose radius  $R'_0$ , as well as the rate of production,  $\omega'_i$ . It can be shown that the overall productive term of rate equations (right side of Equations (5)) may be represented approximately as Reynolds number based on  $R'_0$  times a function of freestream stagnation temperature for a given vehicle speed. The real gas effects become important only if both Mach number and Reynolds number are large.

#### SHOCK DETACHMENT DISTANCE AND SONIC POINT LOCATION

Figs. 14 and 15 show the shock detachment distance and sonic

Vol. 2

point (singular point for nonequilibrium flow) location, respectively, as functions of freestream Mach number. Both results agree excellently with those of Shih and Baron (Ref. 6) and favorably well with that of Traugott (Ref. 1) for detachment distance and those of Kendall (Ref. 11) for sonic point location. Also presented in Fig. 15 are sonic point locations obtained simply from the isentropic expansion using modified Newtonian pressure with centrifugal correction. Different specific heat ratios are used to simulate frozen flow with  $\gamma = 1.4$  or equilibrium flows with  $\gamma = 1.1$  and  $1.2$ . It is found that this simple approach does yield a good approximation to the more sophisticated calculations such as the present method and that of Ref. 6. For high Mach numbers, the results tend to flatten out as in the so-called principle of Mach number independency in hypersonic flow.

CONCLUDING REMARKS

The chemically nonequilibrium flow over axisymmetric blunt bodies using the method of integral relations has been investigated. The frozen and equilibrium flows are also considered, using the same techniques, as limiting cases.

For one-strip integration, the numerical results compare closely with existing theoretical data. The calculated shock layer thickness remains thin enough for one-strip approximation to be valid. It is found that the "real gas" effect on the pressure is much smaller than on the density and temperature distributions. The nonequilibrium flow results generally fall between those of the frozen and equilibrium cases but incline toward the equilibrium one. However, for  $M_\infty = 8.0$  the nonequilibrium data, with assumption of vibration being unexcited at the shock, approach those of frozen flow.

The use of exact s-momentum and reaction rate equations along the body surface might have isolated the influence of flow properties from one streamline to the other in the subsonic region. In this regard, computer programs will be revised as to employ the full s-momentum and reaction rate equations instead of the above exact (along a streamline or body surface) ones. The results will be discussed in the formal report.

REFERENCES

1. Martin Company. An Approximate Solution of the Supersonic Blunt Body Problem for Prescribed Arbitrary Axisymmetric Shapes (U), by Stephen C. Traugott. Baltimore, Md., August 1958. 46 pp. (RR-13, publication UNCLASSIFIED).

2. Douglas Aircraft Company. A Critical Study of the Direct Blunt Body Integral Method (U), by J. Zerikos and W. A. Anderson. Santa Monica, Calif., December 1962. 80 pp. (Douglas Report SM-42603, publication UNCLASSIFIED).
3. Ames Research Center. Numerical Analysis of Flow Properties About Blunt Bodies Moving at Supersonic Speeds in an Equilibrium Gas (U), by Harvard Lamax and Mamorn Inouye. Moffett Field, Calif., July 1964. 79 pp. (NASA TR R-204, publication UNCLASSIFIED).
4. Inviscid Flow of a Reacting Mixture of Gases Around a Blunt Body (U), by Wilbert Lock. J. Fluid Mech. Jan 1960. p. 128 (publication UNCLASSIFIED).
5. Inviscid Hypersonic Air Flows with Coupled Chemical Reactions (U), by J. G. Hall, A. Q. Esehenroeder and P. V. Marrone. J. Aerospace Sci. September 1962. p. 1038 (publication UNCLASSIFIED).
6. Nonequilibrium Blunt-Body Flow Using the Method of Integral Relations (U), by W. C. L. Shih and J. R. Baron. AIAA Journal. June 1964. p. 1062 (publication UNCLASSIFIED).
7. Hypersonic Flow Theory; Vol. 1, Inviscid Flows (U), by Wallace D. Hayes and Ronald F. Probstein. Academic Press. 1966. 602 pp. (publication UNCLASSIFIED).
8. Introduction to Physical Gas Dynamics (U), by Walter G. Vincenti and Charles H. Kruger, Jr. John Wiley and Sons, Inc. 1965. 538 pp. (publication UNCLASSIFIED).
9. Univ. of Brussels. On a Method of Numerical Solution of Some Nonlinear Problems on Aero-Hydrodynamics (U), by A. A. Dorodnitsyn, Brussels. 1957. Proc. 9th Internatl. Congr. Appl. Mech., Vol. 1. p. 485 (publication UNCLASSIFIED).
10. A Similitude for Nonequilibrium Phenomena in Hypersonic Flight (U), by W. E. Gibson and P. V. Marrone. AGARD on High Temperature Aspects of Hypersonic Fluid Dynamics. Brussels, Belgium. March 1962. (publication UNCLASSIFIED).
11. Jet Propulsion Lab. Experiments on Supersonic Blunt-Body Flows (U), by J. M. Kendall, Jr. Pasadena, Calif., February 1962. (Progress Report 20-372, publication UNCLASSIFIED).

## APPENDIX A

## DIVERGENCE FORMS OF BASIC FLOW EQUATIONS

## Continuity

$$\frac{\partial}{\partial s} (\rho V_s r^\sigma) + \frac{\partial}{\partial n} \left[ \left(1 + \frac{n}{R}\right) \rho V_n r^\sigma \right] = 0 \quad (\text{A1})$$

## s-Momendum

$$\begin{aligned} \frac{\partial}{\partial s} \left[ r^\sigma (\rho V_s^2 + KP) \right] + \frac{\partial}{\partial n} \left[ r^\sigma \left(1 + \frac{n}{R}\right) \rho V_s V_n \right] \\ = \left(1 + \frac{n}{R}\right) KP \sin \theta - \frac{r^\sigma \rho V_s V_n}{R} \end{aligned} \quad (\text{A2})$$

## n-Momendum

$$\begin{aligned} \frac{\partial}{\partial s} (r^\sigma \rho V_s V_n) + \frac{\partial}{\partial n} \left[ r^\sigma \left(1 + \frac{n}{R}\right) (\rho V_n^2 + KP) \right] \\ = \left(1 + \frac{n}{R}\right) KP \cos \theta + \frac{r^\sigma (\rho V_s^2 + KP)}{R} \end{aligned} \quad (\text{A3})$$

## Reaction-Rate

$$\begin{aligned} \frac{\partial}{\partial s} (r^\sigma \rho V_s C_i) + \frac{\partial}{\partial n} \left[ r^\sigma \left(1 + \frac{n}{R}\right) \rho V_n C_i \right] \\ = r^\sigma \left(1 + \frac{n}{R}\right) \frac{R'_O \omega'_i}{\rho' V'_{\max}} \end{aligned} \quad (\text{A4})$$

## APPENDIX B

EXPRESSIONS FOR FUNCTIONS APPEARING IN ORDINARY DIFFERENTIAL  
EQUATIONS (30a) THROUGH (30h)

With the use of one-strip approximation in the method of integral relations, the functions  $F_1$  through  $F_8$  in Equations (30a) through (30h) are found as follows:

$$F_1 = \left( \frac{\rho_\delta}{\rho_b} v_{s_\delta} - v_{s_b} \right) \frac{1}{\delta} \frac{d\delta}{ds} - \frac{\sigma \sin \theta}{r_b^\sigma} \left[ \frac{\rho_\delta}{\rho_b} v_{s_\delta} \left( 1 + \frac{\delta}{R} \right) + v_{s_b} \right] \\ - \frac{1}{\rho_b} \left( 1 + \frac{\sigma \delta \cos \theta}{r_b^\sigma} \right) \left[ \left( \frac{2}{\delta} + \frac{1}{R} \right) \rho_\delta v_{n_\delta} + \left( \rho_\delta G_2 + v_{s_\delta} G_1 \right) \frac{d\chi}{ds} \right] \quad (B1)$$

$$F_2 = \left\{ \frac{K r_b^\sigma}{\delta} - (\rho_\delta v_{n_\delta}^2 + K P_\delta) \left( \frac{2}{\delta} + \frac{1}{R} \right) + \left[ r_b^\sigma \rho_\delta v_{s_\delta} v_{n_\delta} \frac{1}{\delta} \frac{d\delta}{ds} \right. \right. \\ \left. \left. + \left( 1 + \frac{\delta}{R} \right) \left( \frac{r_b^\sigma K P_b}{\delta} + \sigma K P_\delta \cos \theta - \sigma \rho_\delta v_{s_\delta} v_{n_\delta} \sin \theta \right) \right] \right\} / \\ \left( r_b^\sigma + \sigma \delta \cos \theta \right) \left( \rho_\delta v_{s_\delta} G_3 + \rho_\delta v_{n_\delta} G_2 + v_{s_\delta} v_{n_\delta} G_1 \right) \quad (B2)$$

$$F_3 = \frac{-1}{K} \left\{ 2 \rho_b v_{s_b} \frac{dv_{s_b}}{ds} + (\rho_b v_{s_b}^2 + K P_b) \frac{1}{\delta} \frac{d\delta}{ds} + \sigma \rho_\delta v_{s_\delta}^2 \left( 1 + \frac{\delta}{R} \right) \frac{\sin \theta}{r_b^\sigma} \right. \\ \left. + \left( 1 + \frac{\sigma \delta \cos \theta}{r_b^\sigma} \right) \left[ \left( 2 \rho_\delta v_{s_\delta} G_2 + v_{s_b}^2 G_1 + K G_4 \right) \frac{d\chi}{ds} + \left( \frac{2}{\delta} + \frac{1}{R} \right) \rho_\delta v_{s_\delta} v_{n_\delta} \right] \right. \\ \left. + \frac{\sin \theta}{r_b^\sigma} \left[ \sigma \rho_b v_{s_b}^2 + (1 + \sigma) K P_b \right] + v_{s_b}^2 \frac{d\rho_b}{ds} \right\} \quad (B3)$$

8th Navy Symposium on Aeroballistics

Vol. 2

$$F_4 = \frac{dP_b}{ds} \left/ \left( T_b W_\infty \sum_i \frac{C_i}{W_i} \right) - \frac{\rho_b}{T_b} \frac{dT_b}{ds} - \rho_b \sum_i \left( \frac{1}{W_i} \frac{dC_i}{ds} \right) \right/ \sum_i \frac{C_i}{W_i} \quad (B4)$$

$$F_5 = \left[ - \frac{2V_{s_b}}{W_\infty} \frac{dV_{s_b}}{ds} - \left[ \sum_{\substack{i=O_2, N_2 \\ NO}} \left( \frac{1}{W_i} \frac{dC_i}{ds} \right) + \frac{5}{7} \sum_{i=O, N} \left( \frac{1}{W_i} \frac{dC_i}{ds} \right) \right] T_b \right.$$

$$\left. - \frac{2}{7} \sum_{\substack{i=O_2, N_2 \\ NO}} \left[ \frac{1}{W_i} \frac{dC_i}{ds} \left( \frac{e^{\Theta_{v_i}}}{e^{\Theta_{v_i}/T_b-1}} - e^{\Theta_{d_i}} \right) \right] \right] \left/ \right.$$

$$\left[ \sum_{\substack{i=O_2, N_2 \\ NO}} \frac{C_i}{W_i} + \frac{5}{7} \sum_{i=O, N} \frac{C_i}{W_i} + \frac{2}{7} \sum_{\substack{i=O_2, N_2 \\ NO}} \frac{C_i}{W_i} \frac{(e^{\Theta_{v_i}/T_b})^2 e^{\Theta_{v_i}/T_b}}{(e^{\Theta_{v_i}/T_b-1})^2} \right] \quad (B5)$$

$$F_6 = \omega'_O G_5 - C_O G_6 \quad (B6)$$

$$F_7 = \omega'_N G_5 - C_N G_6 \quad (B7)$$

$$F_8 = \omega'_{NO} G_5 - C_{NO} G_6 \quad (B8)$$

where

$$\rho_\delta = \rho_\infty / \epsilon \quad (B9)$$

$$P_\delta = P_\infty \left[ 1 + \gamma_\infty M_\infty^2 \cos^2 \chi (1 - \epsilon) \right] \quad (B10)$$

$$V_{s_\delta} = V_\infty \left\{ (1 - \epsilon) \sin \chi \cos \chi \sin \theta + \left[ 1 - (1 - \epsilon) \cos^2 \chi \right] \cos \theta \right\} \quad (B11)$$

$$V_{n_\delta} = V_\infty \left\{ (1 - \epsilon) \sin \chi \cos \chi \cos \theta + \left[ (1 - \epsilon) \cos^2 \chi - 1 \right] \sin \theta \right\} \quad (\text{B12})$$

$$G_1 = \frac{\gamma_\infty M_\infty^2 \sin 2\chi (1 - \epsilon) (A\epsilon - 1)}{\epsilon \left\{ \gamma_\infty M_\infty^2 \cos^2 \chi \left[ A(2\epsilon - 1) - 1 \right] - A - 1 \right\}} \quad (\text{B13})$$

$$G_2 = V_\infty \left\{ \sin \theta + (\cos \chi \cos \theta - \sin \chi \sin \theta) + \left[ (1 - \epsilon) \sin \chi + \epsilon^2 G_1 (\cos \chi) / \rho_\infty \right] \right\} + V_{n_\delta} \quad (\text{B14})$$

$$G_3 = V_\infty \left\{ \cos \theta - (\cos \chi \sin \theta + \sin \chi \cos \theta) + \left[ (1 - \epsilon) \sin \chi + \epsilon^2 G_1 (\cos \chi) / \rho_\infty \right] \right\} - V_{s_\delta} \quad (\text{B15})$$

$$G_4 = P_\infty \gamma_\infty M_\infty^2 \left[ (1 - \epsilon) \sin 2\chi + \epsilon^2 G_1 (\cos^2 \chi) / \rho_\infty \right] \quad (\text{B16})$$

$$G_5 = R'_0 / (\rho'_b V'_{s_b}) \quad (\text{B17})$$

$$G_6 = \frac{\sigma \sin \theta}{r_b^\sigma} + \frac{1}{\delta} \frac{d\delta}{ds} + \frac{1}{\rho_b} \frac{d\rho_b}{ds} + \frac{1}{V_{s_b}} \frac{dV_{s_b}}{ds} \quad (\text{B18})$$

$$\epsilon = \left\{ (1+A)(1 + \gamma_\infty M_\infty^2 \cos^2 \chi) - \left[ (1+A)^2 (1 + \gamma_\infty M_\infty^2 \cos^2 \chi) - 4A \gamma_\infty M_\infty^2 \cos^2 \chi (7 + \gamma_\infty M_\infty^2 \cos^2 \chi) \right]^{1/2} \right\} / (2A \gamma_\infty M_\infty^2 \cos^2 \chi) \quad (\text{B19})$$

and

$$A = (h_\delta + e_\delta) \rho_\delta / P_\delta \quad (\text{B20})$$

Note that from p. 124, Ref. 8

$$A = \begin{cases} 6 & \text{(chemical composition and vibrational energy both frozen)} & \text{(B20a)} \\ 8 & \text{(chemical composition frozen, vibrational energy excited)} & \text{(B20b)} \end{cases}$$

For equilibrium flows, it is found that

$$A = 2 \left[ 3 \sum_{\substack{i=O_2, N_2, NO \\ NO}} \frac{C_i}{W_i} + \sum_{\substack{i=O_2, N_2, NO \\ NO}} \frac{C_i}{W_i} \frac{e^{\Theta_{v_i}/T}}{e^{\Theta_{v_i}/T-1}} + \sum_{i=O_2, N_2} \frac{C_i}{W_i} \frac{e^{\Theta_{d_i}/T}}{T} - \sum_{\substack{i=O_2, N_2, NO \\ NO}} \frac{C_i}{W_i} \frac{e^{\Theta_{d_i}/T}}{T} + 2 \sum_{i=O, N} \frac{C_i}{W_i} \right] / \sum_{\substack{i=O_2, N_2, NO, O, N \\ O, N}} \frac{C_i}{W_i} \quad \text{(B20c)}$$

Since the body surface is also a streamline, the s-momentum and reaction-rate equations may be replaced with their exact forms along a streamline. The corresponding  $F_3$ ,  $F_6$ ,  $F_7$  and  $F_8$  then become

$$F_3 = - \frac{\rho_b V_{s_b}}{K} \frac{dV_{s_b}}{ds} \quad \text{(B21)}$$

$$F_6 = \omega'_O G_5 \quad \text{(B22)}$$

$$F_7 = \omega'_N G_5 \quad \text{(B23)}$$

$$F_8 = \omega'_{NO} G_5 \quad \text{(B24)}$$

The use of above simplified forms is self justifiable within a single streamline. The question arises whether this is an appropriate use in the nose region where the flow is subsonic and its properties

influence from one streamline to the other. In this paper, the numerical results are calculated based on Equations (B21) through (B24) for s-momentum and reaction equations. The programs will be revised as to use Equations (B3), (B6), (B7) and (B8) instead of (B21) through (B24), respectively, and the results will be discussed in the formal report.

## APPENDIX C

## FLOW EQUATIONS ALONG STAGNATION STREAMLINE

Along the stagnation streamline where  $V_s = r^\sigma = 0$ , the basic flow equations are reduced to the following forms.

Continuity

$$\frac{1}{\rho} \frac{d\rho}{dn} + \frac{1}{V_n} \frac{dV_n}{dn} + \frac{1}{1+n} \left[ 1 - \frac{1}{V_n} \left( \frac{\partial V_s}{\partial s} \right)_o \right] = 0 \quad (C1)$$

s-Momentum

$$V_s = 0 \quad (C2)$$

n-Momentum

$$V_n \frac{dV_n}{dn} + \frac{K}{\rho} \frac{dP}{dn} = 0 \quad (C3)$$

Energy

$$h + V_n^2 = 1 \quad (C4)$$

Reaction-Rate

$$V_n \frac{dC_i}{dn} = \frac{R'_o \omega'_i}{\rho' V'_{\max}} \quad (C5)$$

The equations for conservation of species, thermodynamic state and enthalpy assume the same forms as Equations (5) through (7).

The boundary conditions are:

at the body,  $V_n = 0$  (C6)

at the shock,

Continuity  $\rho_\infty V_\infty = -\rho_\delta V_{n_\delta}$  (C7)

Momentum  $KP_\infty + \rho_\infty V_\infty^2 = KP_\delta + \rho_\delta V_{n_\delta}^2$  (C8)

Energy  $h_\infty + V_\infty^2 = h_\delta + V_{n_\delta}^2$  (C9)

Species  $(C_O)_\delta = (C_N)_\delta = (C_{NO})_\delta = 0$  (C10)

$$(C_{O_2})_\delta = (C_{O_2})_\infty$$

$$(C_{N_2})_\delta = (C_{N_2})_\infty$$

The term  $\left(\frac{\partial V_s}{\partial s}\right)$  is a nonzero quantity. It is determined by a linear variation of its values at the shock and at the body; i.e.,

$$\left(\frac{\partial V_s}{\partial s}\right)_o = \left(\frac{\partial V_s}{\partial s}\right)_{o,b} + \frac{n}{\delta_o} \left[ \left(\frac{\partial V_s}{\partial s}\right)_{o,\delta} - \left(\frac{\partial V_s}{\partial s}\right)_{o,b} \right] \quad (C11)$$

The limiting process of L'Hospital's rules applied to Equations (30a) and (30b) gives

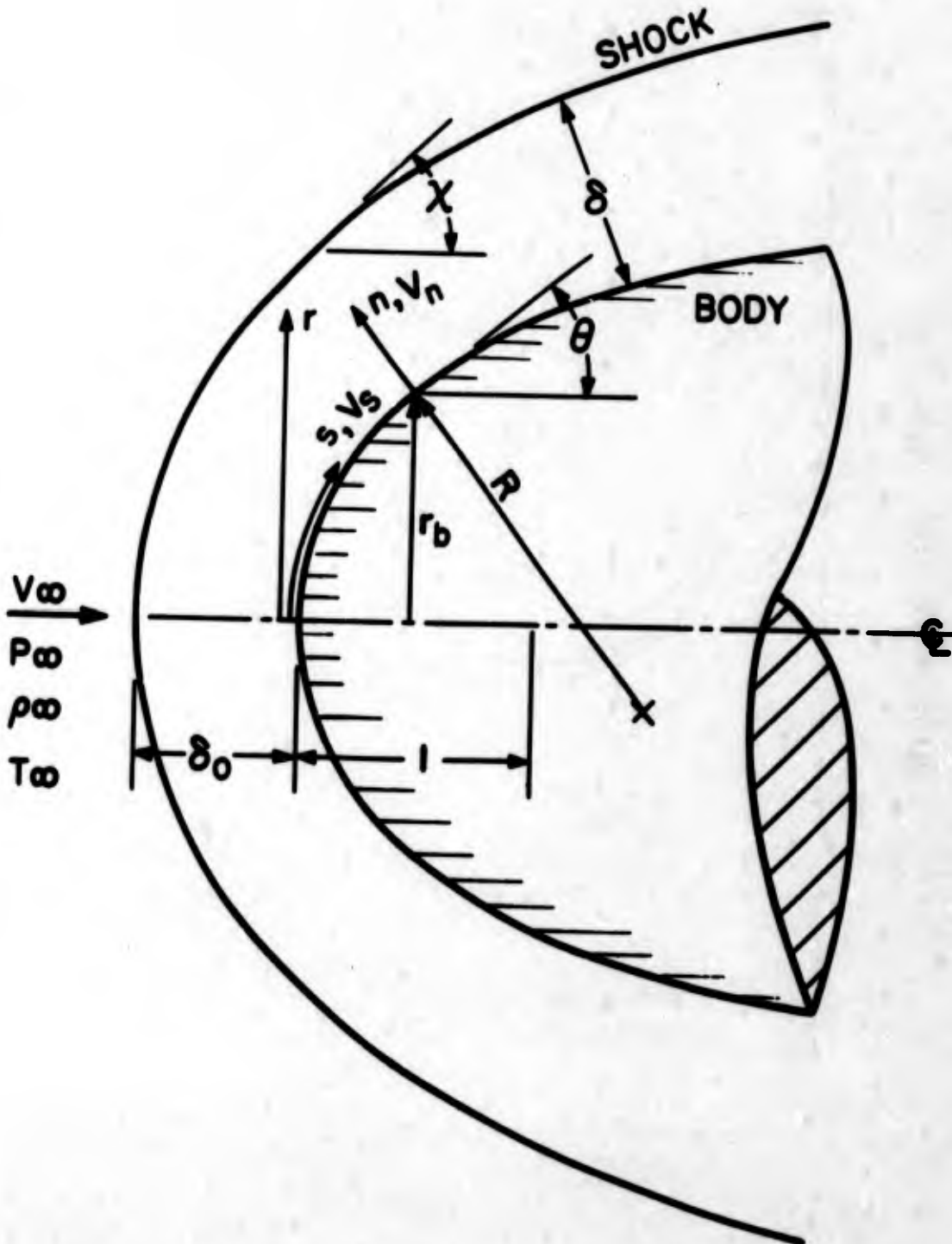
$$\left(\frac{\partial V_s}{\partial s}\right)_{o,b} = \frac{1 + \delta_o}{\delta_o \rho_b V_{n_\delta}} \left[ \rho_\delta V_{n_\delta}^2 \left(1 + \frac{1}{\delta_o}\right) - 2K (P_b - P_\delta) \right] \quad (C12)$$

$$\left(\frac{\partial v_s}{\partial s}\right)_{o,\delta} = \frac{2v_{n\delta}}{\delta_o} \left[ 1 - \frac{K(P_b - P_\delta)}{\rho_\delta v_{n\delta}^2} \right] \quad (C13)$$

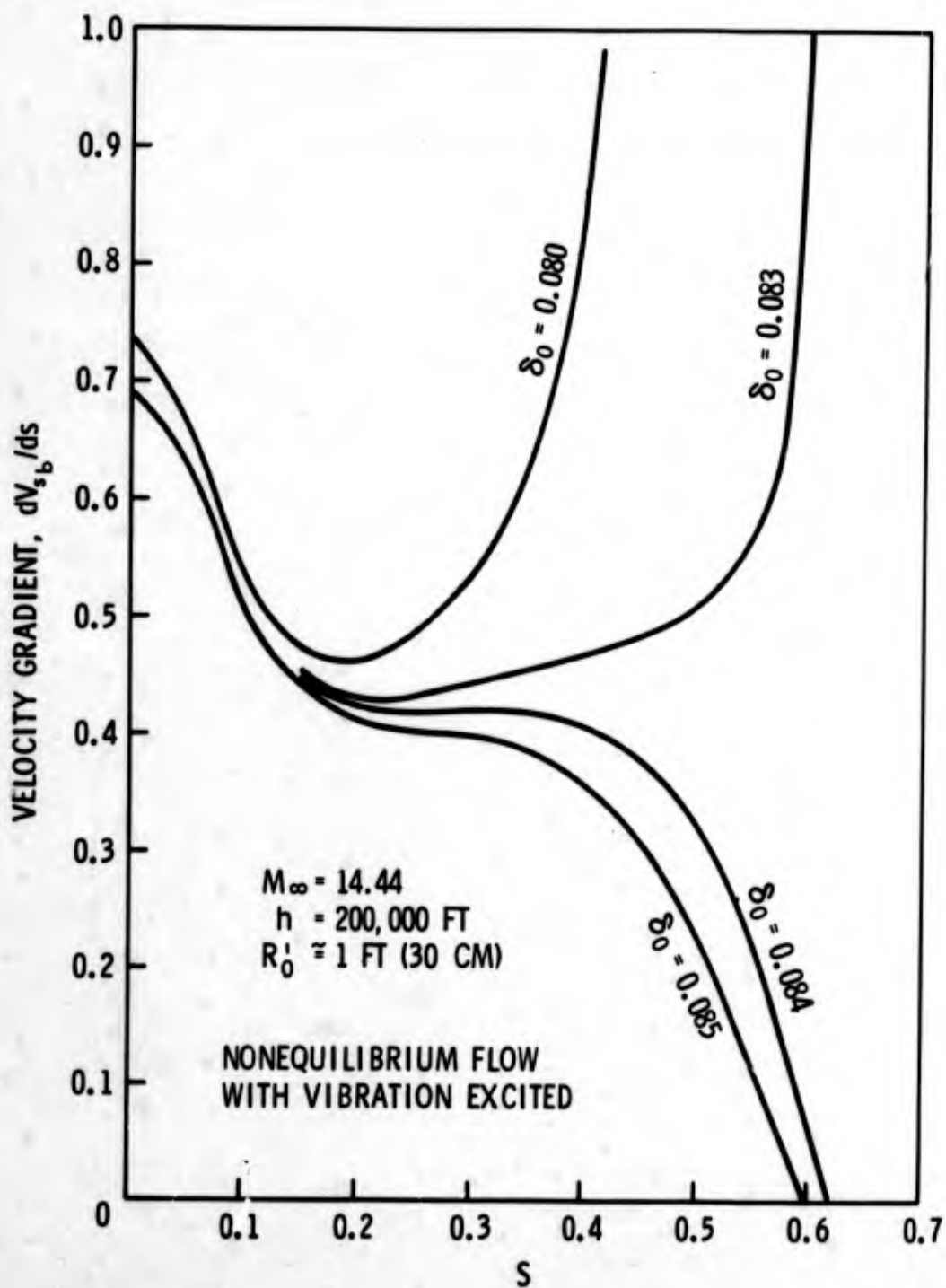
Note that  $P_b$  and  $\rho_b$  are pressure and density at the stagnation point. These values are assumed for the first integration and integrated values are used for successive integrations.

Table I - Forward and Reverse Reaction-Rate Coefficients

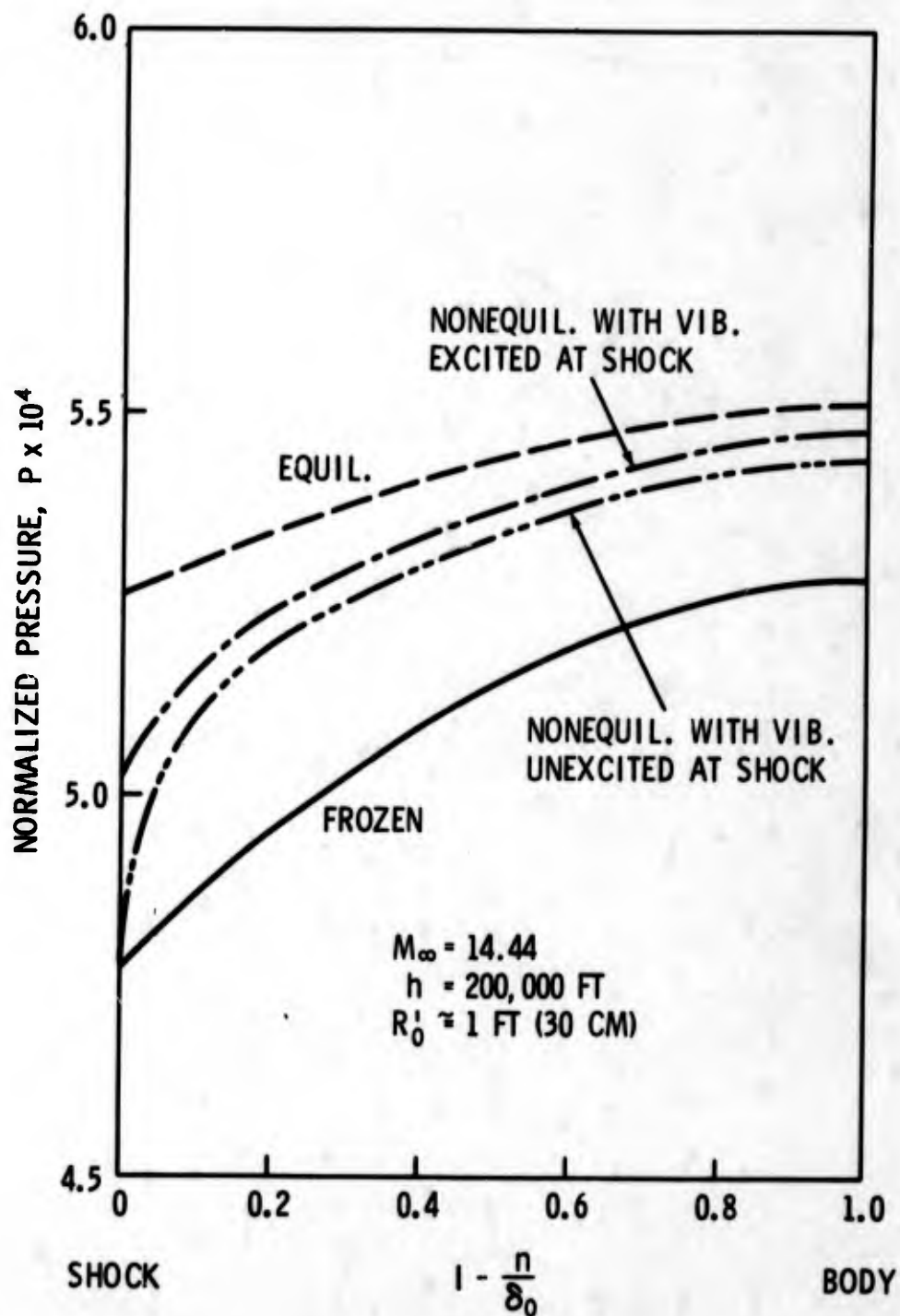
Number	Reaction	Catalytic body Q	$^3 K_f$ (cm <sup>3</sup> /mole sec) T in °K	$K_f/K_r$ (moles/cm <sup>3</sup> )	Source
1	$O_2 + Q \xrightleftharpoons[K_r]{K_f} 2O + Q$	O <sub>2</sub>	$\frac{3.6 \times 10^{21}}{T^{3/2}} \exp \frac{-59380}{T}$	$\frac{1.2 \times 10^3}{P^{1/2}} \exp \frac{-59000}{T}$	Ref. 5
2		0	$\frac{2.1 \times 10^{18}}{T^{1/2}} \exp \frac{-59380}{T}$		
3, 4, 5		N <sub>2</sub> , N, NO	$\frac{1.2 \times 10^{21}}{T^{3/2}} \exp \frac{-59380}{T}$		
6	$N_2 + Q \xrightleftharpoons{K_f} 2N + Q$	N <sub>2</sub>	$\frac{3.0 \times 10^{21}}{T^{3/2}} \exp \frac{-113260}{T}$	$18.0 \exp \frac{-112450}{T}$	Ref. 5
7		N	$\frac{1.5 \times 10^{22}}{T^{3/2}} \exp \frac{-113260}{T}$		
8, 9, 10		O <sub>2</sub> , O, NO	$\frac{9.9 \times 10^{20}}{T^{3/2}} \exp \frac{-113260}{T}$		
11, 12, 13 14, 15	$NO + Q \xrightleftharpoons{K_f} N + O + Q$	O <sub>2</sub> , N <sub>2</sub> , O, N, NO	$\frac{5.2 \times 10^{21}}{T^{3/2}} \exp \frac{-75490}{T}$	$4.0 \exp \frac{-75000}{T}$	Ref. 5
16			$\frac{1.0 \times 10^{12}}{T^{-1/2}} \exp \frac{-3120}{T}$		
17	$N_2 + O \xrightleftharpoons{K_f} NO + N$		$5.0 \times 10^{13} \exp \frac{-38000}{T}$	$4.5 \exp \frac{-37500}{T}$	Ref. 5



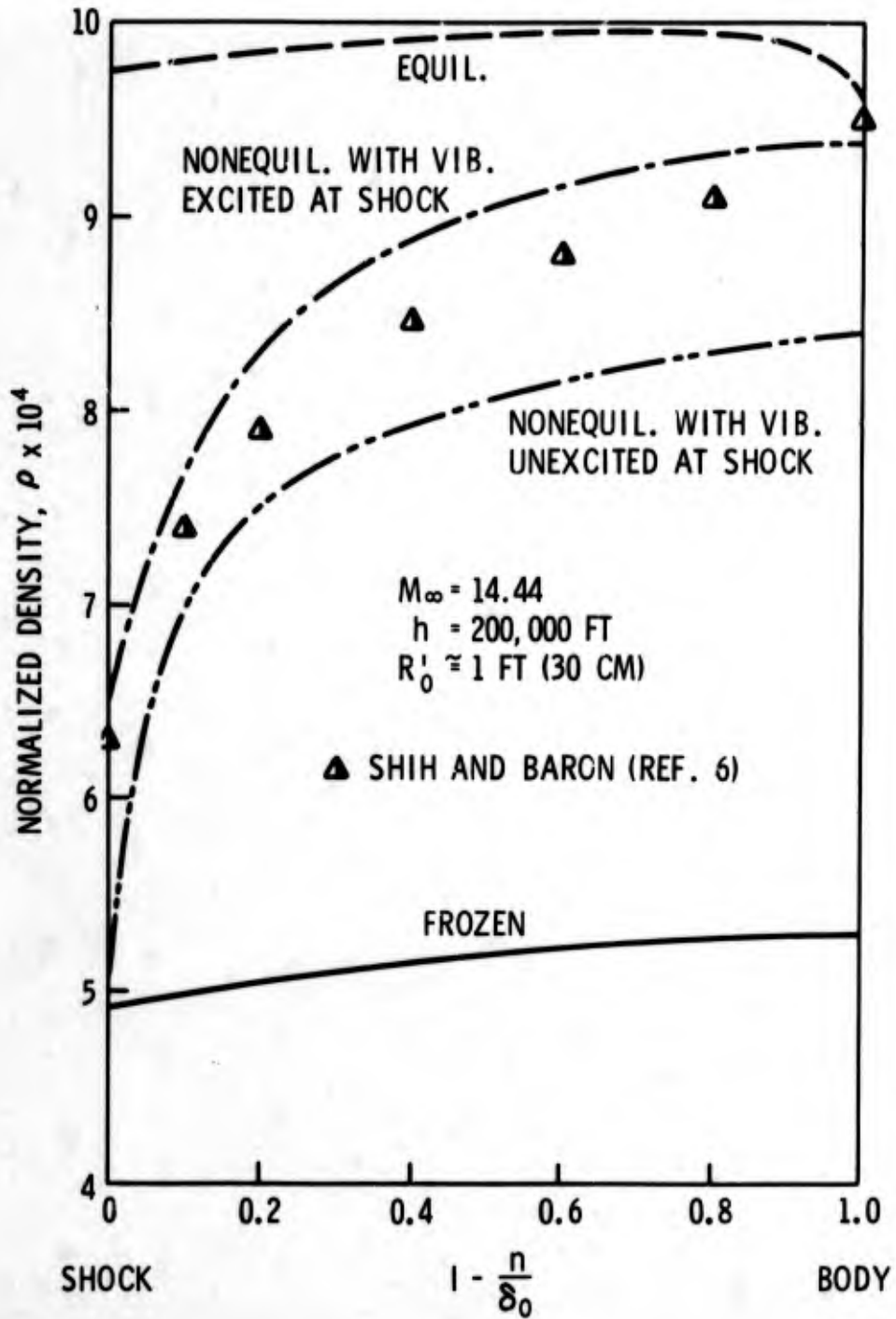
(U) Fig. 1. Coordinate System



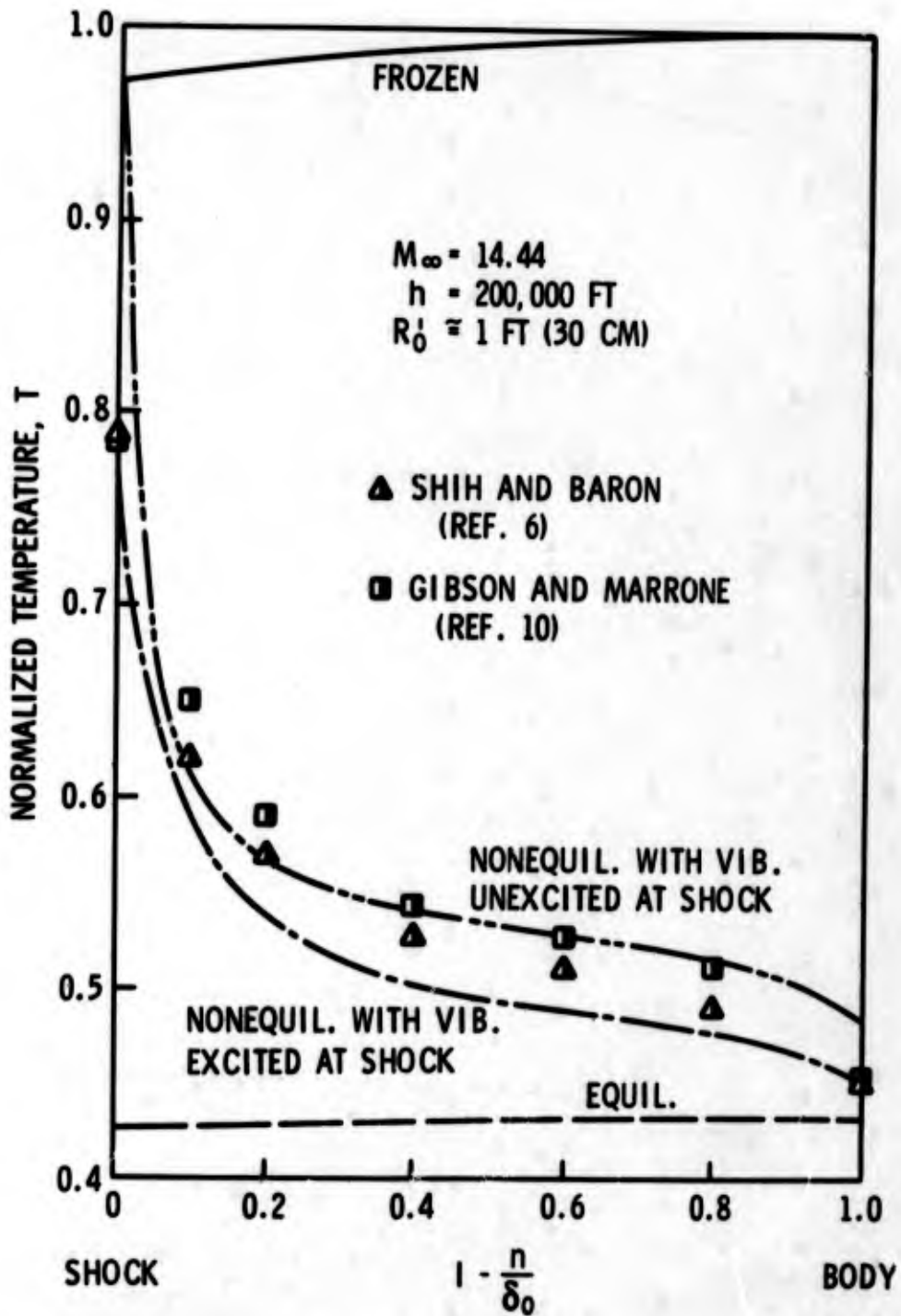
(U) Fig. 2. Velocity Gradients Along Body Surface of a Sphere at  $M_\infty = 14.44$



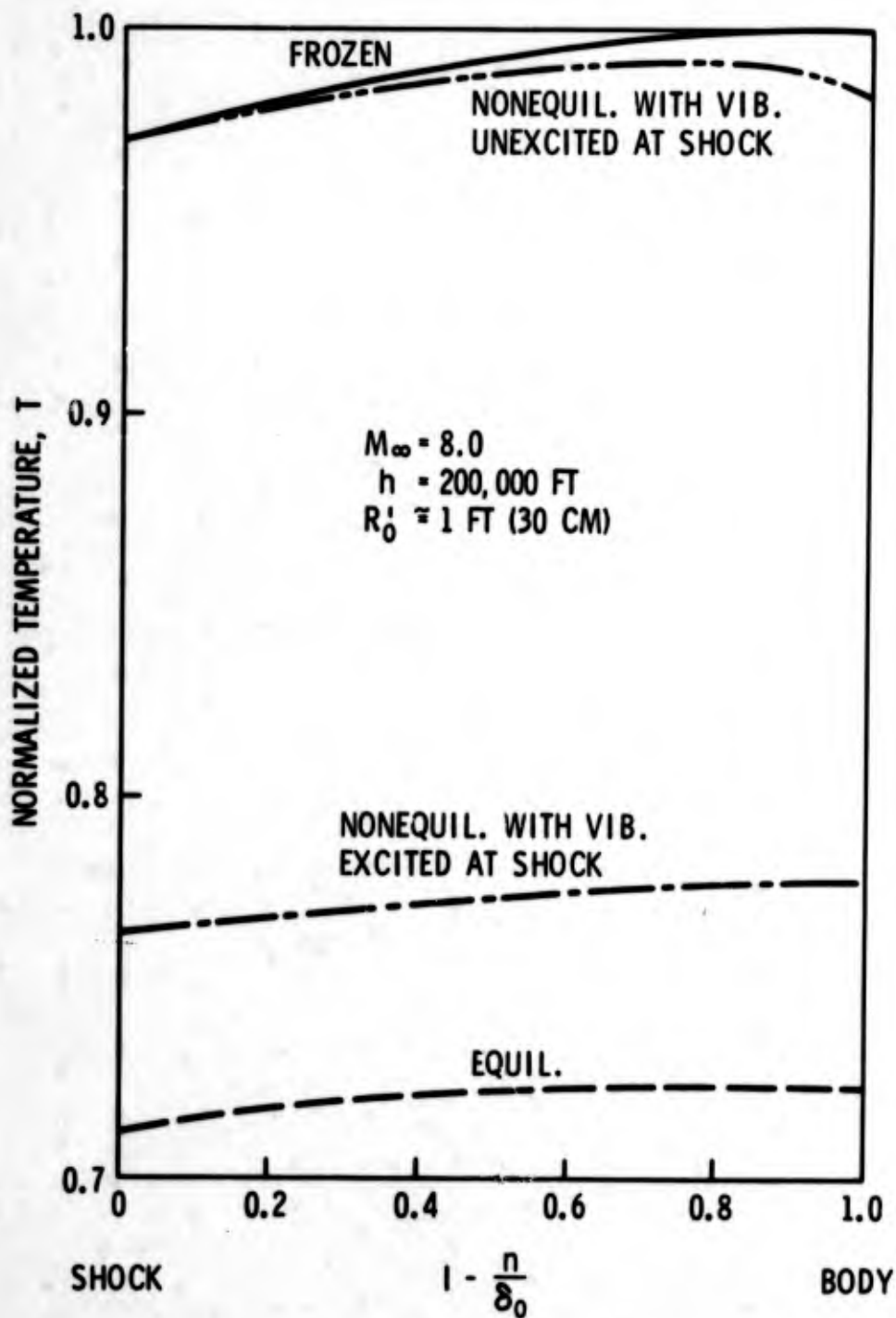
(U) Fig. 3. Pressure Distribution Along Stagnation Streamline for a Sphere at  $M_\infty = 14.44$



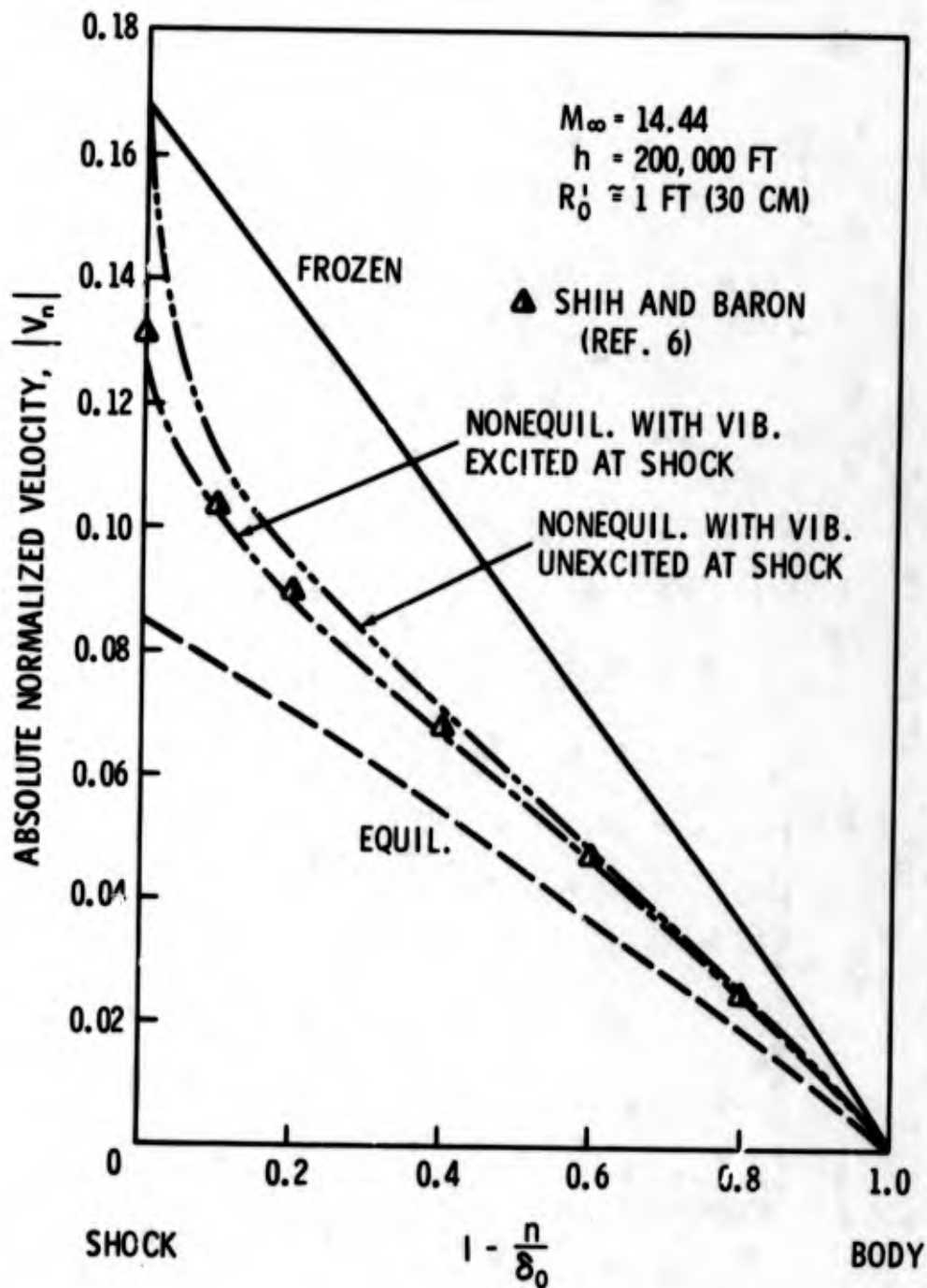
(U) Fig. 4. Density Distribution Along Stagnation Streamline for a Sphere at  $M_\infty = 14.44$



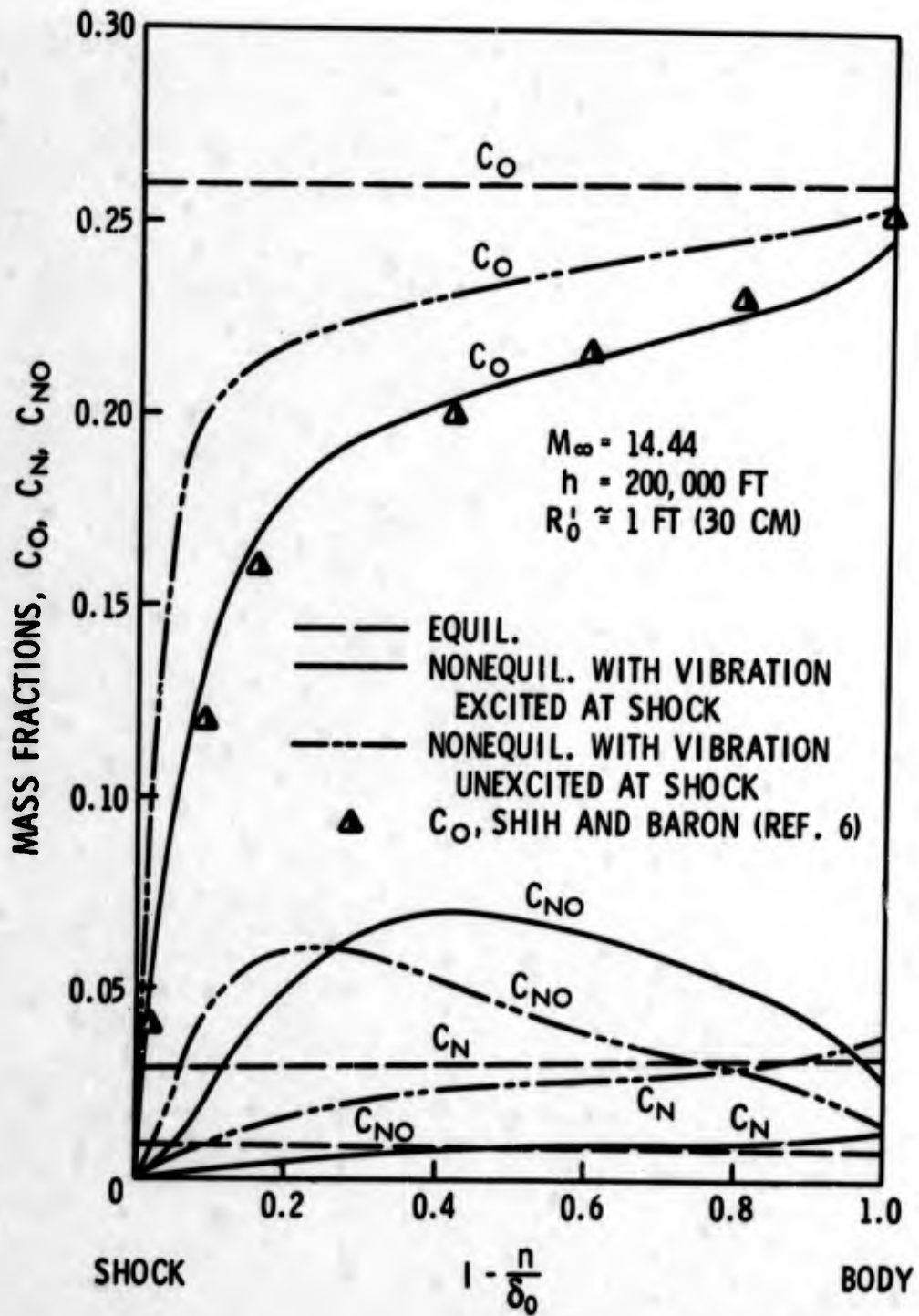
(U) Fig. 5a. Temperature Distribution Along Stagnation Streamline for a Sphere at  $M_\infty = 14.44$



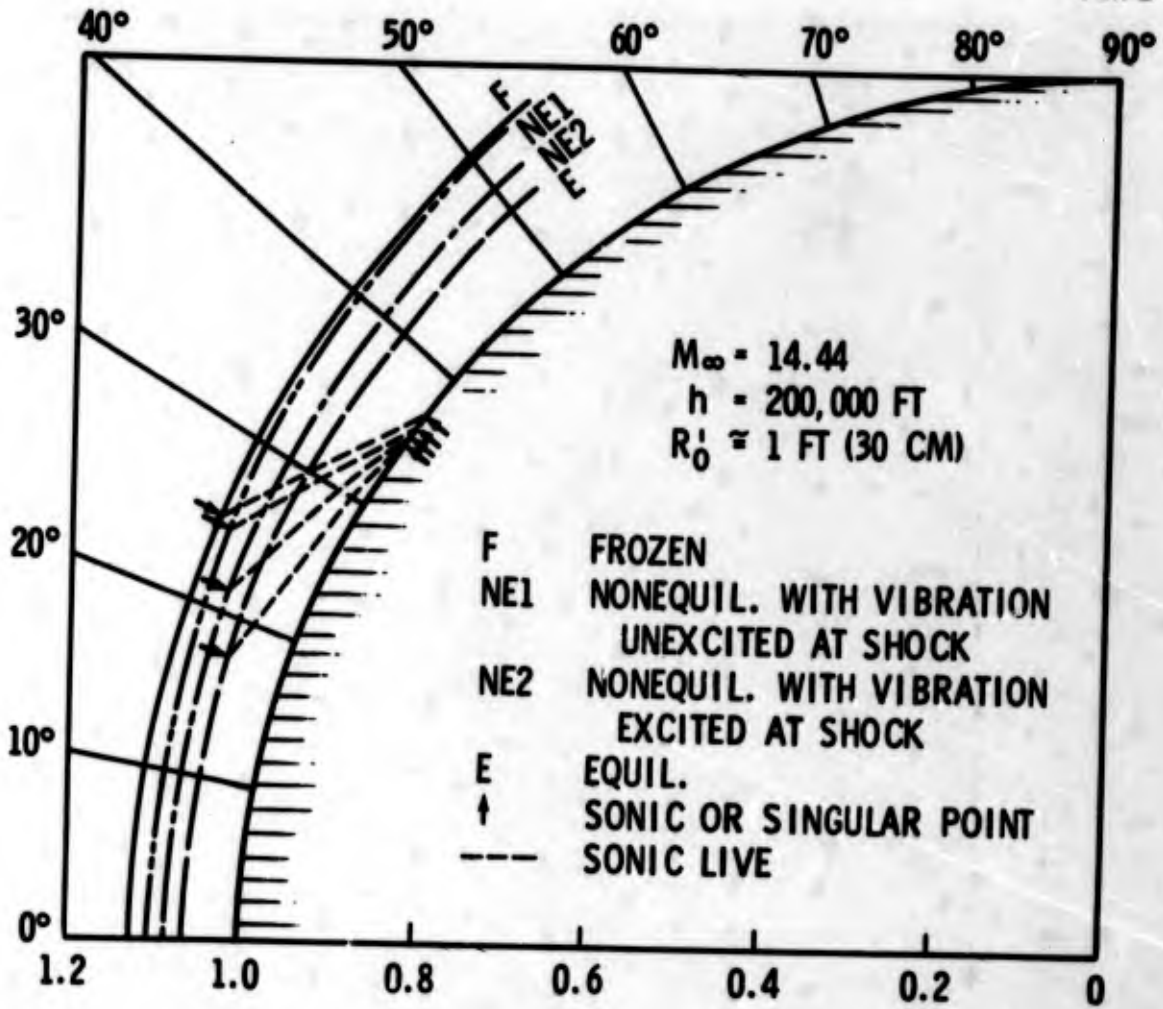
(U) Fig. 5b. Temperature Distribution Along Stagnation Streamline for a Sphere at  $M_\infty = 8.0$



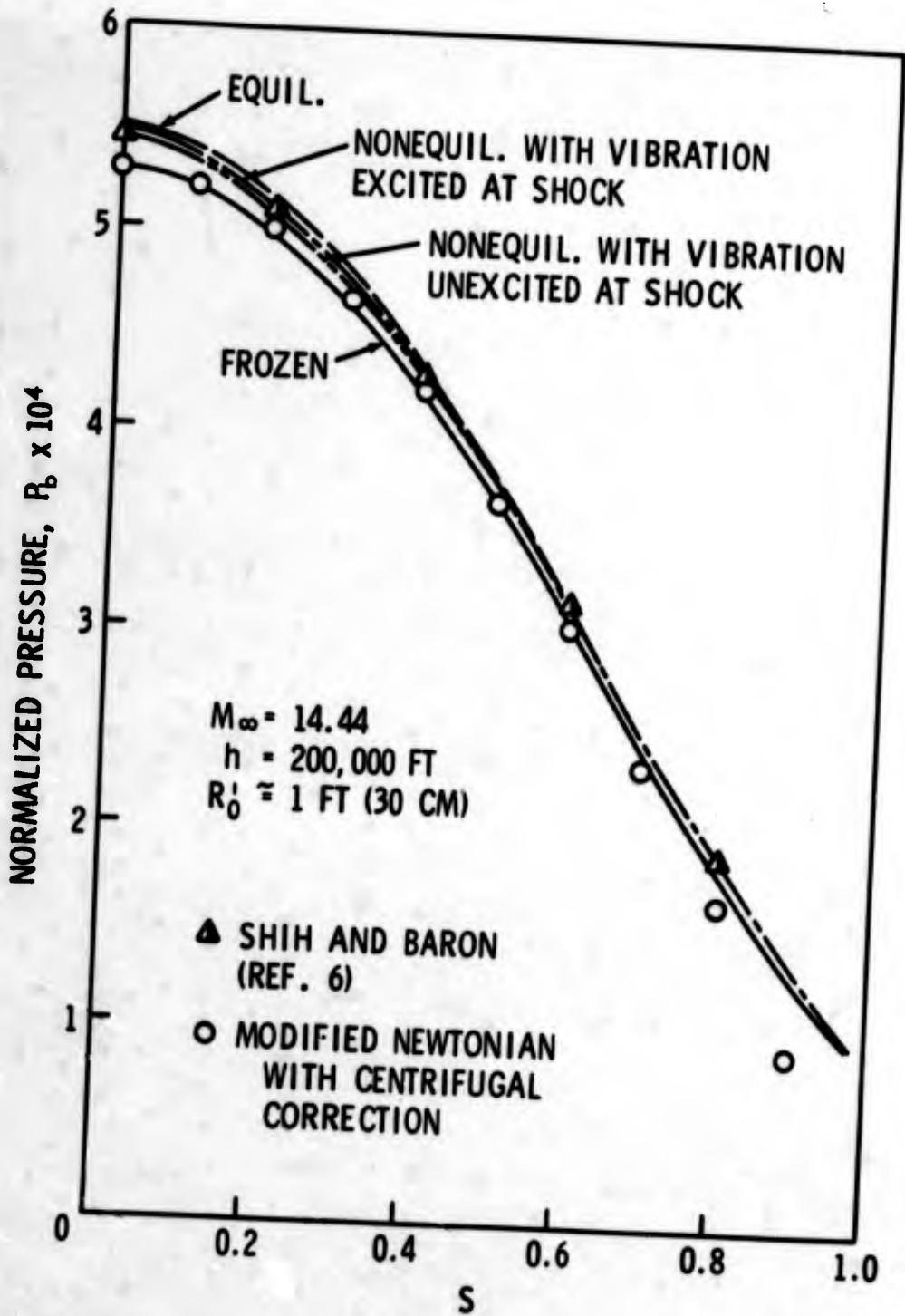
(U) Fig. 6. Velocity Distribution Along Stagnation Streamline for a Sphere at  $M_\infty = 14.44$



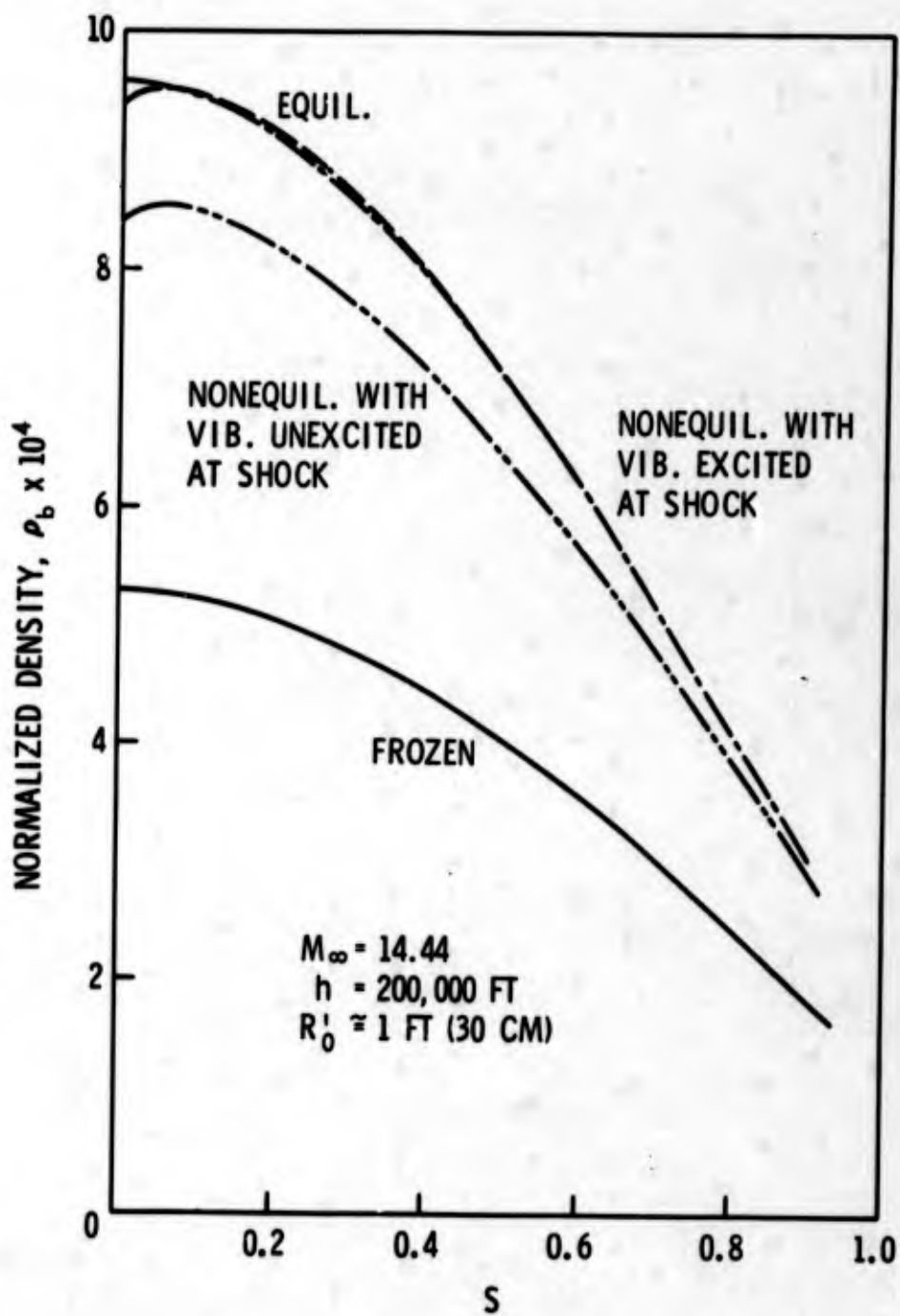
(U) Fig. 7. Mass Fraction Distribution Along Stagnation Streamline for a Sphere at  $M_{\infty} = 14.44$



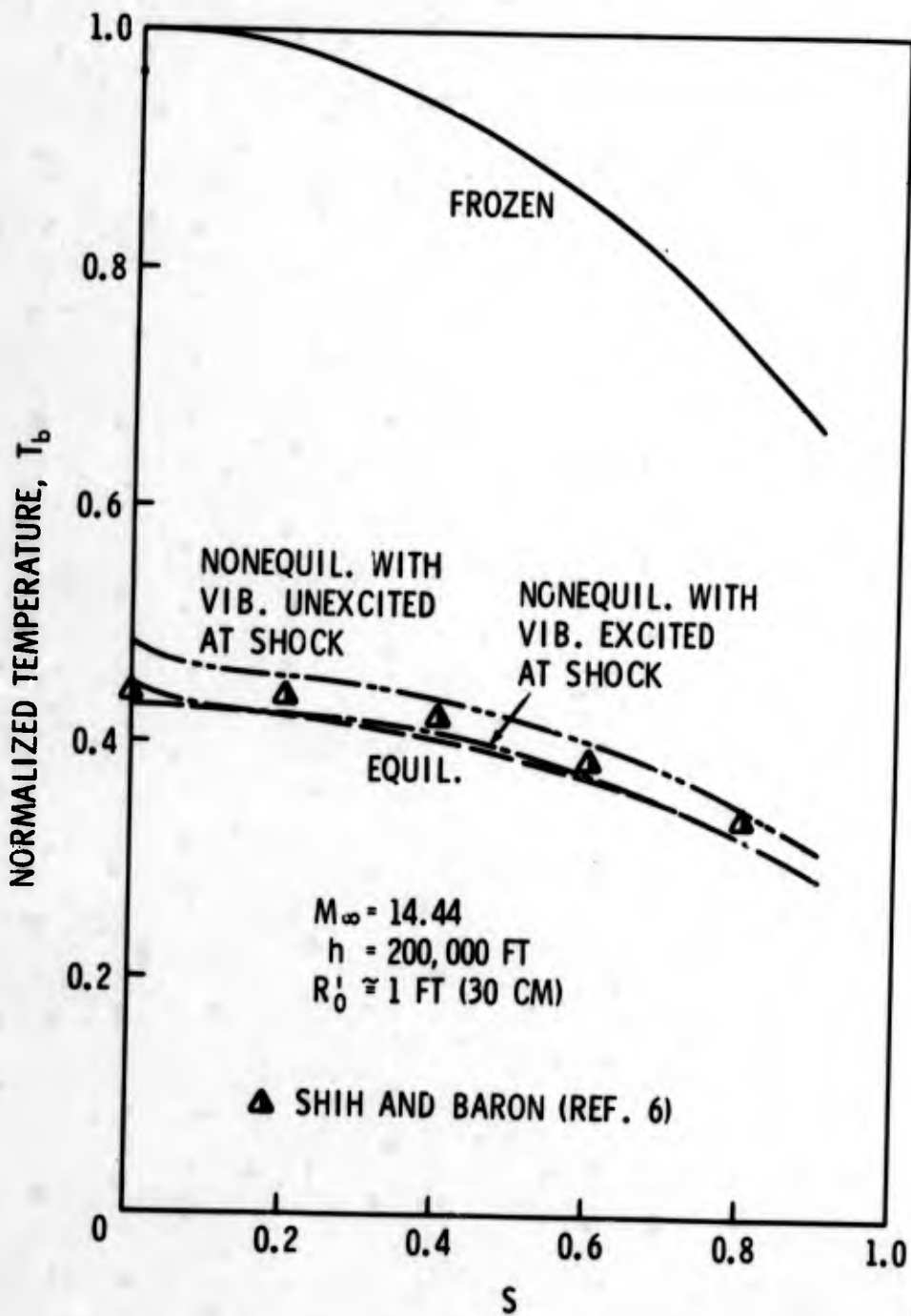
(U) Fig. 8. Shock Shape for a Sphere at  $M_\infty = 14.44$



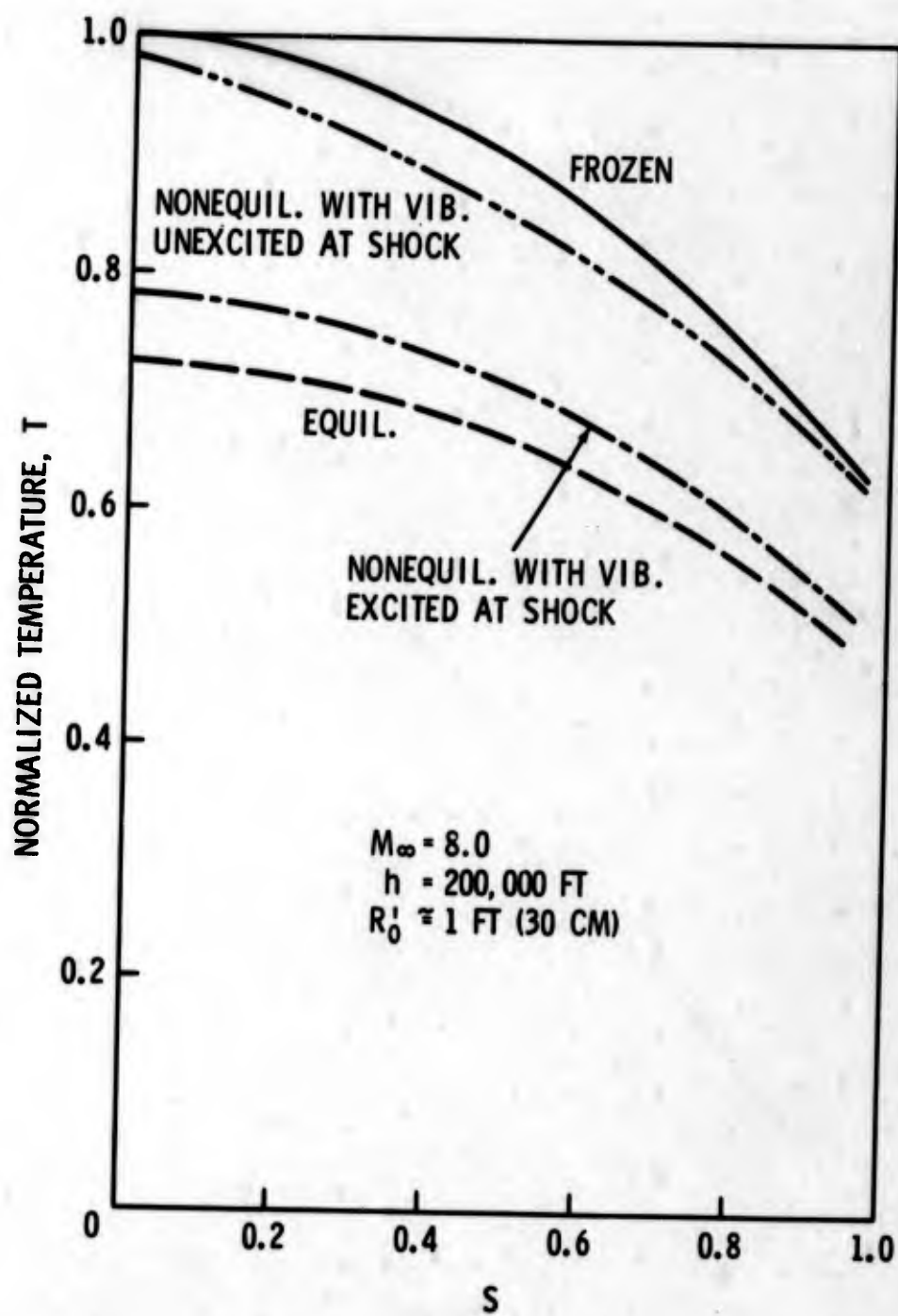
(U) Fig. 9. Pressure Distribution Along Body Surface of a Sphere at  $M_\infty = 14.44$



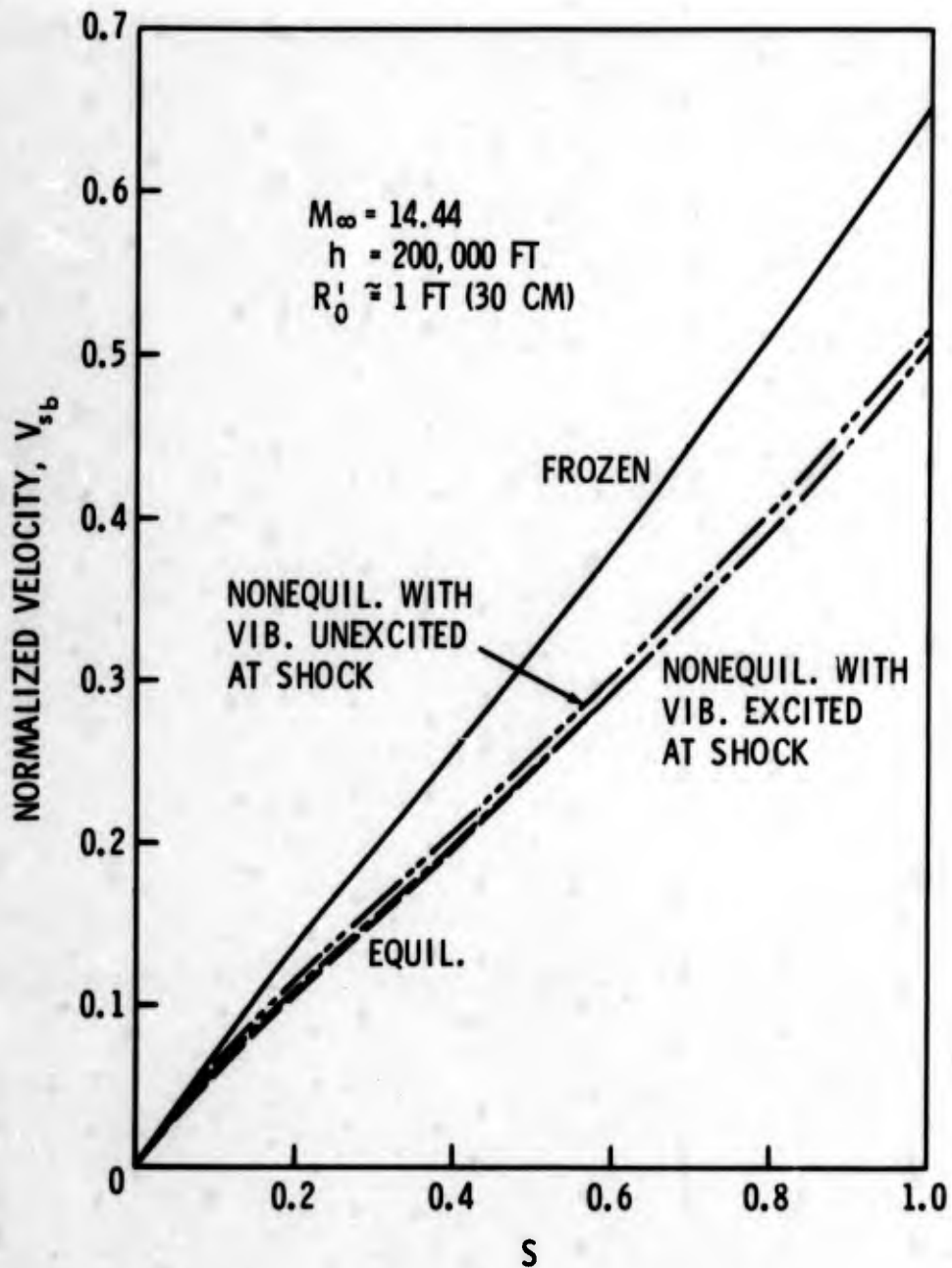
(U) Fig. 10. Density Distribution Along Body Surface of a Sphere at  $M_\infty = 14.44$



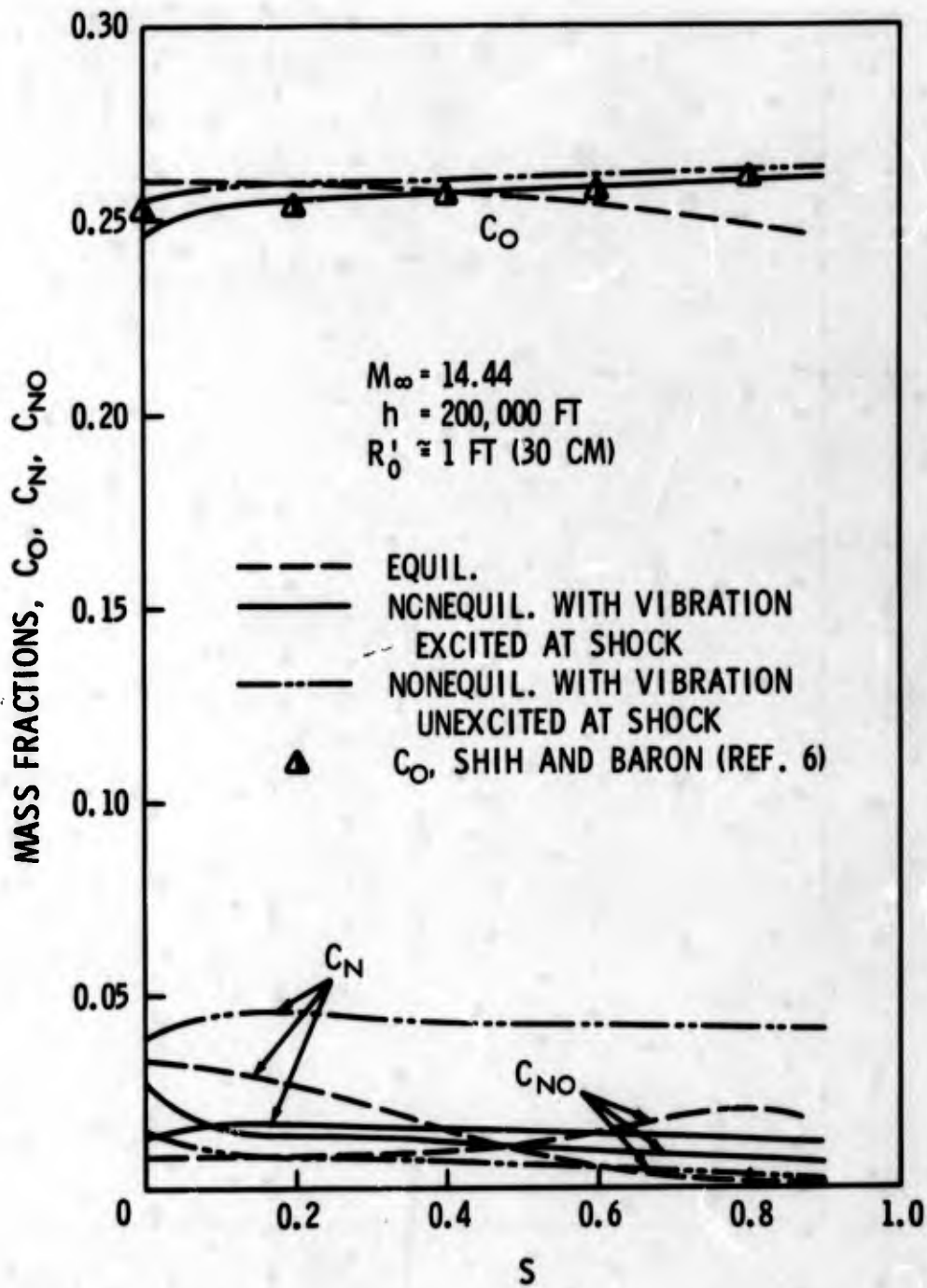
(U) Fig. 11a. Temperature Distribution Along Body Surface of a Sphere at  $M_\infty = 14.44$



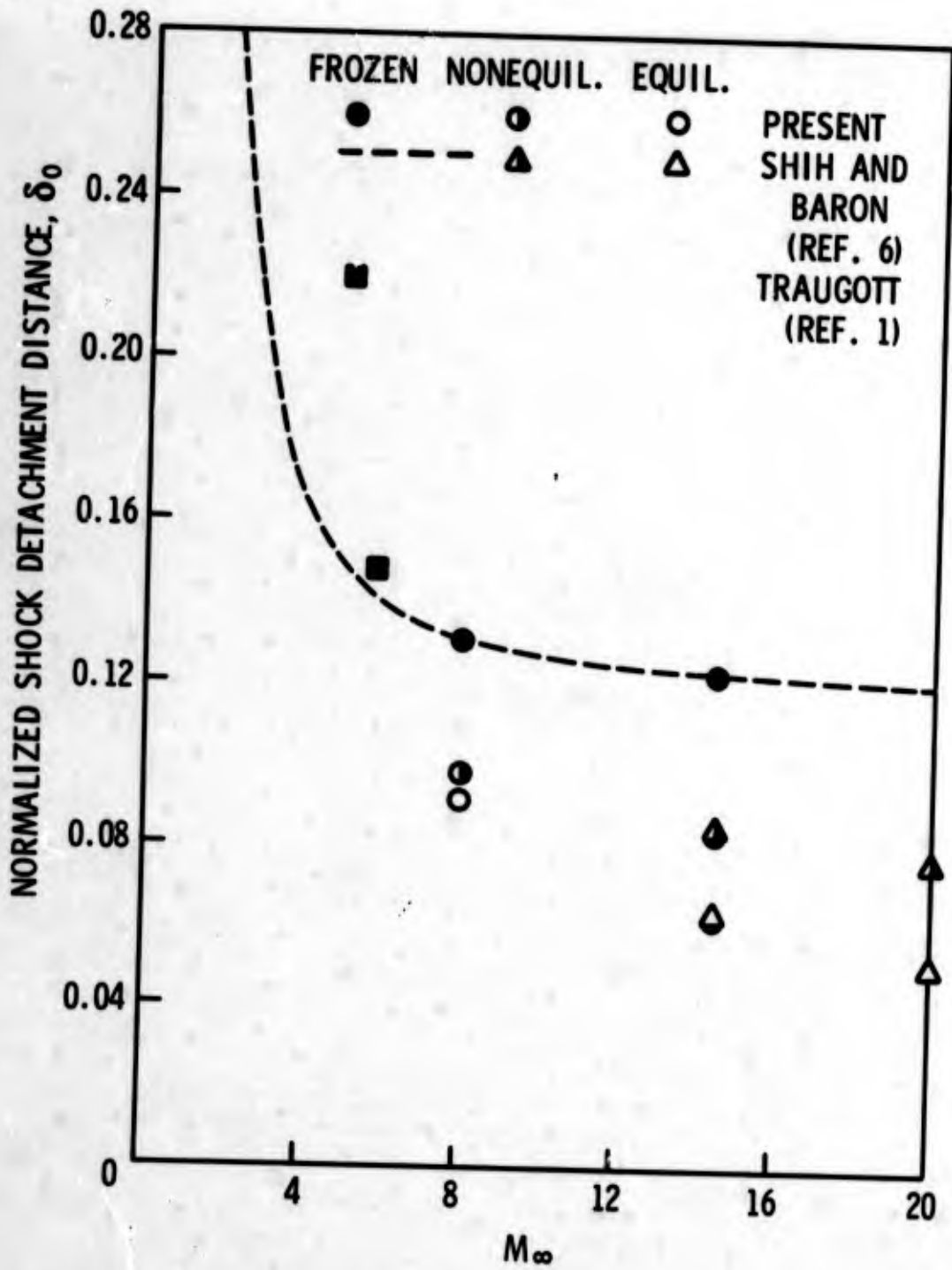
(U) Fig. 11b. Temperature Distribution Along Body Surface of a Sphere at  $M_\infty = 8.0$



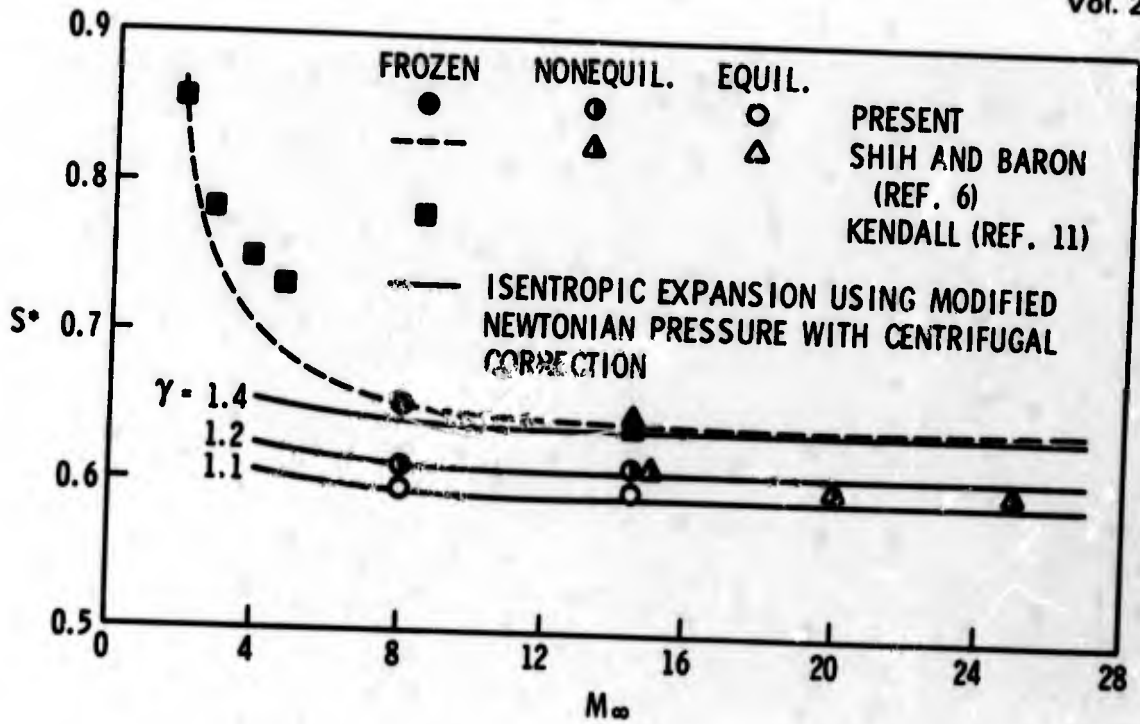
(U) Fig. 12. Velocity Distribution Along Body Surface of a Sphere at  $M_\infty = 14.44$



(U) Fig. 13. Mass Fraction Distribution Along Body Surface of a Sphere at  $M_\infty = 14.44$



(U) Fig. 14. Shock Detachment Distance Along Axis of Symmetry



(U) Fig. 15. Singular Point (Sonic Point for Frozen and Equilibrium Flows) Location

**BLANK PAGE**

Paper No. 11

**SUPERSONIC LAMINAR AND TURBULENT  
ABLATION STUDIES WITH TEFLON\***

(U)

(Paper UNCLASSIFIED)

by

E. M. Winkler, R. L. Humphrey,  
J. A. Koenig, and M. T. Madden  
U.S. Naval Ordnance Laboratory  
White Oak, Silver Spring, Md. 20910

**ABSTRACT.** (U) Experimental programs have been carried out in the U. S. Naval Ordnance Laboratory 3-Megawatt Arc Tunnel to study the interaction of ablation and a vehicle's aerodynamic characteristics. The test conditions involve stagnation pressures of 20 to 30 atmospheres, temperatures of 4000 to 9000°R, and Mach numbers of 2.3 and 3. The test models, made of teflon, were smooth or had cracks machined into the surface. They were instrumented for pressure, temperature, heat-transfer, and skin-friction measurements. The laminar data are compared with the predictions of a numerical procedure known as BLIMP-CMA. Surprisingly close agreements have been found between experimental data and predictions. Ablation-induced transition is observed in all laminar runs. In fully turbulent runs criss-cross striations are observed. Cracks in the ablative models have pronounced effects on the ablative behavior. Substructure heating can be severe depending upon size and direction of the cracks. Ablation reduces the wall-shear stress by about 40 percent.

\* This study was supported by the Naval Ordnance Systems Command, ORDTASK 351-001/092-1/UF 20-322-502, the Independent Exploratory Development Program, Task Number MAT-U3L-000-F008-9812, Problem 027, and the Defense Atomic Support Agency, Contract Number DASA No. 563-68.

NOMENCLATURE

$b$	- width of crack, inch
$h$	- height of crack, inch
$H_w$	- wall enthalpy, BTU/lb
$H_o$	- stagnation enthalpy, BTU/lb
$M$	- Mach number
$p_o$	- supply pressure, atm
$q_{oc}$ or $\dot{q}$	- heat transfer rate to crack wall, BTU/ft <sup>2</sup> sec
$q_o$ or $\dot{q}_o$	- heat transfer rate to duct surface, BTU/ft <sup>2</sup> sec
$Re_\tau$	- friction Reynolds number (on the basis of $b$ )
$T_o$	- supply temperature, °R
$u$	- local flow velocity, ft/sec
$u_\infty$	- free-stream velocity, ft/sec
$x$	- axial distance in flow direction, inch
$y$	- distance into crack, perpendicular to surface, inch
$\delta$	- boundary-layer thickness, inch
$\delta^*$	- boundary-layer displacement thickness, inch
$\tau_w$	- wall-shear stress, lb/ft <sup>2</sup>

## INTRODUCTION

(U) Ablative materials are an accepted means for protecting re-entering vehicles or parts of re-entering vehicles from the intense heating during certain phases of the flight. With their use, problems became apparent or are anticipated to develop which, at present, are inadequately described by analytical approaches. For small vehicles, flight test results have indicated that roll instabilities develop under certain conditions during re-entry. The anomalous forces are significant at altitudes below 100,000 feet. The process is not adequately understood, but it is possibly linked with the interaction of ablation and the vehicle's aerodynamics. There is also concern that cracks in the ablative heat shields, that have developed prior to re-entry, will severely affect the protection of the substructure for which the shields were designed. If cracks have developed in heat shields the ablative behavior may be altered which in turn may affect the aerodynamics of the vehicle. To study these processes, research programs were carried out at the U. S. Naval Ordnance Laboratory (NOL) under the sponsorship of the Naval Ordnance Systems Command and the Defense Atomic Support Agency.

## APPROACH

(U) Because of the lack of an adequate analytical description of the phenomena involved, NOL's approach was primarily experimental. It endeavored to produce actual flight conditions in the 3-Megawatt Arc Tunnel. The experiments were designed to measure boundary-layer parameters and material responses that will assist the development of theory or at least allow an empirical correlation of critical parameters. For a typical IRBM this involves the stagnation conditions shown in Fig. 1, namely pressures of 20 atmospheres and larger and enthalpies of 3000 to 4000 BTU/lb if its flight altitude is lower than 60,000 feet. These supply conditions can be achieved in an arc tunnel. Because of the manner the boundary layer develops on blunted bodies, the proper simulation of flight conditions on a blunted re-entry vehicle can

## Vol. 2

be produced by expanding the gas from a reservoir having the specified stagnation conditions to a relatively low free-stream Mach number. One can either study the flow external or internal to a model with equal validity of the results. NOL selected the latter approach because it is experimentally quite attractive since it allows an easy instrumenting for obtaining pressure, temperature, heat transfer and skin-friction data. For the substructure heating studies, the flight regime to be simulated was approximately the same as shown on Fig. 1. However, in addition to Mach number, supply pressure and enthalpy, a number of other parameters had to be considered to achieve proper simulation of what might occur to a re-entering ICBM with a cracked ablative heat shield. The cracks may be considered as cavities of aspect ratio  $h/b$ . From flow studies in cavities with non-ablating walls one knows that the wall-to-stagnation enthalpy ratio,  $H_w/H_0$ , the friction Reynolds number,  $Re_\tau$ , characteristic sizes as  $b/\delta^*$  and  $h/b$ , as well as the geometry of the cavity influences the heat transfer to the cavity walls. Geometry factors include orientation of the cavity with respect to the flow direction, spacing of the cavities if there are more than one, and the cavity - edge geometry. With ablation present, the blowing rate parameter,  $c_q$ , also has to be considered. It is believed that cracks of 0.01-inch width or larger on the conical part of an ICBM heat shield may present problems. If one considers the point of maximum heating for an ICBM that travels on a trajectory of minimum energy, the following range of parameters are computed for a missile of ballistic factor of 1000, and which has a conical heat shield of 10-degree half angle with a 1/4-inch nose radius:

$$\begin{aligned} 2 &\leq M &\leq 10 \\ 70 &\leq Re_\tau &\leq 2000 \\ 0.05 &\leq b/\delta^* &\leq 10 \\ 0.2 &\leq H_w/H_0 &\leq 0.4 \end{aligned}$$

The blowing rate parameter, essentially an indication of the amount of shielding provided by the ablator, will vary with the material.

## EXPERIMENTAL ARRANGEMENT

(U) The experimental setup is quite simple and is shown in Figs. 2 and 3. The arc heater, in this case a three-phase, four-ring, a.c. arc (Ref. 1), discharges the air into an axially symmetric contoured nozzle. The flow then enters axially symmetric ducts made of the ablative material. The nozzle, as well as the duct contours, have been corrected for the boundary-layer growth. The Mach number 3 nozzle and ducts were designed for laminar flow, while the Mach number 2.3 nozzle and ducts had turbulent boundary-layer corrections applied to them. The flow then discharges into a diffuser and exhaust system.

(U) All but one of the ducts had static-pressure orifices. Some were instrumented for in-depth temperature readings and/or surface temperature readings, heat-transfer and skin-friction measurements (Ref. 2). The Pitot pressure was measured at the exit of the duct in all experiments. Ablation was determined from contour measurements prior to and after the runs. The supply conditions in the arc heater were computed from the measured pressure and mass flow using the method of Ref. 3.

(U) For the substructure heating studies, cracks were machined into the ducts, parallel and transverse to the flow direction. The crack widths and heights were selected to cover a desired range of the parameters listed previously. Heat gauges were installed at the bottom and on the side walls of the cracks.

(U) A total of eleven ducts were tested during this program. The tunnel operating conditions and duct instrumentation are summarized in Table 1.

## ANALYTICAL PROCEDURES

(U) Several analytical programs have been used in the analysis of the experimental data. Test results obtained under conditions where the duct boundary layer was predominantly laminar were compared with the predictions of the Boundary Layer Integral Matrix Program - Charring Material Ablator (BLIMP-CMA) (Ref. 4) which were acquired from the Aerotherm Corporation. These two procedures are fairly versatile and permit calculation of teflon ablation rates, boundary-layer parameters and in-depth material response in non-similar, multicomponent,

chemically-reacting, laminar boundary layers along axisymmetric or planar surfaces. Quasi-steady or transient solutions can be obtained.

(U) The BLIMP program incorporates a modified form of the Scala relation for the ablation of teflon (Refs. 4 and 5) which states that the process is rate controlled over the surface temperature range of interest. Scala had assumed that the ablation of teflon is a quasi-steady depolymerization process according to Ref. 6 where the depolymerization of the teflon polymer is considered of first order with respect to the weight of the solid. He also retained the combustion term in the equation, which greatly improved the agreement between predicted and observed ablation rates. Other assumptions which make the program quite general for various applications are that (a) surface reactions and reactions through the boundary layer and discontinuous wall conditions corresponding to a change in material are allowed, (b) the flow is in equilibrium except that certain species may be considered frozen, or allowed to react at finite rates, (c) there is an option that allows equal or unequal diffusion and thermal diffusion coefficients, (d) the entropy layer, energy balance, or mass balance concepts can be used. For the present application, the options of a reacting surface an equilibrium air boundary layer, unequal diffusion coefficients, and a discontinuous wall condition were used. The latter was required because of the non-ablating cold nozzle wall upstream of the teflon ducts.

(U) The CMA program allows the transient in-depth prediction of wall temperatures. This program is also very flexible. Its basic assumptions are that (a) a maximum of three components are allowed for the ablator - two resins and one reinforcement, (b) the density history follows an Arrhenius-type law, (c) the pyrolysis gases are in equilibrium with the char, (d) the pyrolysis gases pass out of the material immediately, (e) coking cannot occur, (f) the cross-sectional area can vary and (g) the conduction is one-dimensional. The CMA can be run with any one or a combination of three options. These are (a) a specified surface chemistry to define the film coefficient, (b) a specified surface temperature and recession rate and (c) a specified radiation view factor and flux. The program was used with option (b) above. Together with the BLIMP it was used to predict the transient behavior of the teflon ducts. Most of the data, discussed later on, were compared with the transient solution, since it was found that the time for reaching steady state was comparable to the testing time.

(U) Unfortunately, the BLIMP-CMA procedure has as of now, no turbulent boundary-layer option. As a consequence, the data obtained with turbulent boundary layers along the duct wall, could not be compared with predictions. However, numerical procedures were devised to analyze the experimental data to the extent considered essential for the substructure heating studies. It combined a computational program applicable to turbulent boundary layers on non-ablating walls, experimental information, wall species, and temperature data obtained from the use of BLIMP. The computational program (Ref. 7) was first used to calculate the flow and boundary-layer data through the nozzle and duct for the start of the test. The measured time-pressure variation in the duct during the test was then used to correct the boundary-layer edge condition as function of time. The measured wall shear-stress data, together with the BLIMP predicted wall conditions, were used to calculate the wall heating rate, assuming the validity of Reynolds analogy. These were of course quasi-steady state computations. It was felt that this is acceptable, since the experimental shear-stress data indicate that for the turbulent boundary-layer test runs, steady-state conditions were reached in less than one second.

(U) Measured in-depth wall temperatures recorded during the turbulent boundary-layer tests were compared with numerical predictions obtained by using the finite difference technique of Schmidt allowing for the receding surface by the addition of an ablation term.

## RESULTS

### LAMINAR BOUNDARY LAYER TESTS

(U) Six test runs were carried out at a Mach number of 3, a supply pressure of approximately 21 atmospheres and stagnation temperatures of about 9000°R. Test durations were about 11 to 13 seconds. The pressure distribution along the ducts remained essentially unchanged for the duration of the tests. There was a small favorable pressure gradient due to an overcompensation of the boundary-layer growth. The recording of wall temperatures was only partly successful, since the "receding" surface thermocouples failed to recede and showed erratic reading once exposed to the gas flow. The onset of this erratic reading, however, allowed us to fix the onset of ablation to about 4 to 4 1/2 seconds after the start of the tests. The gas-wetted

surfaces of the ducts developed a glossy, waxy surface presumably attributable to one of the teflon degradation species. This has been generally observed by other investigators (Refs. 4 and 7). A yellow to brownish discoloration evidences that combustion has taken place.

(U) Two of the ducts show longitudinal, almost parallel striations over the entire length of the duct as shown in Fig. 4. The cause of the striations is still speculative, there was no recorded difference in operating conditions between the runs where the striations were produced and the others where the surface remained smooth. However, the striations tie in with conclusions reached during the analysis of the experimental data, as will be discussed later on. Increased ablation is observed downstream and upstream of the pressure orifices. Downstream, the increased ablation is plume shaped and extends about eight diameters of the pressure orifice beyond the orifice. The maximum width is about two diameters. On the upstream side, the additional ablation did not occur on all orifices and was confined to a distance of two or three orifice diameters.

(U) For all laminar tests, no ablation was measured at the duct entrance because of the contact with the water-cooled nozzle. Then ablation increased very rapidly and reached a maximum 1 1/2 to 2 inches from the duct entrances. It then decreased, as expected for a laminar boundary layer. But, then an inversion occurred at  $x = 3.5$  inches, and a second maximum appeared at  $x \sim 4.3$  to 4.5 inches. The "normal" behavior was well predicted, though with varying degrees of accuracy, by the BLIMP-CMA programs, as seen from Figs. 5 and 6. There is strong evidence that the observed anomaly was due to boundary-layer transition. The momentum thickness Reynolds number variation along the duct, as predicted by BLIMP, showed that a value of 450 was reached at the point of inversion, which was sufficiently large for transition to occur. The calculated boundary layers exhibited normal laminar velocity profiles prior to the point of inversion, but then showed inflections, see Fig. 8, a strong indication of instability that will lead to transition. The predicted transitional behavior found support in the parallel striations that developed in two of the tests. Other investigators (Refs. 9 and 10) have found parallel striations in the region of laminar instability.

(U) The first shear-stress measurements were made at a location which is now recognized as being the transitional region of the duct. The balance responded very rapidly as

shown in Fig. 9 and appeared to approach the predicted steady-state value in about 13 seconds. The minimum exhibited at  $t = 4.8$  seconds was first erroneously attributed to transients in the ablation process. In a repeat test, carried out to clarify the matter, two balances had been installed in the same duct, one in a definitely laminar region, the other in the transitional region. Readings at the latter location repeated the first data, while in the laminar region, the shear stress was found to decrease uniformly from its non-ablation value, as shown in Fig. 10. The final value is about 36 percent of the predicted cold-wall-shear stress and agrees with the BLIMP-CMA prediction within 22 percent, as shown on Fig. 10.

(U) Steady-state conditions appeared not to be achieved during any of these tests; this was also shown by the CMA calculation. Fig. 11 is a plot of the "heat storage term". It has to vanish for steady-state ablation. At  $\tau = 12$  seconds it was still large in comparison to the surface heating rate for this time, that is,  $\sim 10$  BTU/ft<sup>2</sup>sec as compared to the surface heat transfer of 158 BTU/ft<sup>2</sup>sec.

(U) Predicted and measured in-depth and wall-surface temperatures compared quite well. The in-depth temperature measurements were made with thermocouples installed at various locations along the ducts. Due to the particular thermal characteristics of teflon, the thermocouples had to be installed at depths that would be very close to the surface at the termination of the tests, and the thermocouple location had to be known to within 0.002 inch. This was not quite achieved. It is believed that the experimental data were accurate to not better than 10 percent. The overall agreement with prediction was, however, surprisingly good as seen from Fig. 12. No explanation has been found for the opposite trends of experimental and computed data. Wall-surface temperature data were evaluated from the measured ablation using the Scala relation as given in Ref. 5. Only the data in the definitely laminar portion of duct number 2L were used. The agreement with the BLIMP prediction is within 15°F at a level of 1300°F or 1.2 percent (Fig. 13).

#### TURBULENT BOUNDARY LAYER TESTS

(U) Five test runs were carried out at a Mach number of 2.3, supply pressures approximately 21 and 28 atmospheres and temperatures of 4300 to 4600°R. The boundary layer was fully turbulent, or at least predicted to be fully turbulent, through the entire length of the duct. Ablation was very pronounced under these conditions, and the duct static

pressure decreased very rapidly after the first second of running time as shown in Fig. 14. This pressure variation represented a change in flow Mach number from 2.3 to 2.6. Because of this change in conditions, testing times were kept within 2.7 to 6.5 seconds. Four of the five ducts had longitudinal and transverse cracks instrumented with heat gauges as summarized in Table 1. The values of  $h/b$ ,  $b/\delta^*$  refer to the cold-wall conditions. The fifth duct was used for a reference test for duct number 4T to obtain the needed pressure, temperature, and skin-friction data. Skin-friction data were also obtained with duct number 3T for the 21 atmosphere test series.

(U) The overall ablation behavior of the ducts in this test series was very uniform, increasing from zero at the entrance to a moderate maximum at  $x \approx 1$  inch, and then leveling off to an almost constant value of about 70 percent of the maximum. The total amount of ablation for a given value of wall heat transfer varied linearly with time, allowing the onset of ablation to be deduced. It was determined to be 0.3 second. All ducts exhibited cross-hatched striation patterns as shown in Fig. 16. The patterns started immediately at the duct entrance and formed more regularly if a pressure orifice was not located there. The cracks had a pronounced effect on the striation pattern; they altered the spacings or even caused them to disappear (Fig. 17). At the downstream side of longitudinal cracks, the interference between the crack "wake" and the striations produced a complex pattern (Fig. 18). Analytical studies are under way in connection with this program.

(U) The heat gauges at the bottom and sides of the cracks responded immediately. Some of the temperature readings are shown in Fig. 19. For the longitudinal crack, the center of the downstream wall experienced practically the "cold-wall" surface heating rate. For the bottom of the crack, the heating rate (Fig. 20) varied first almost linearly with time from zero to 0.2 of the surface heating during the first  $1 \frac{1}{4}$  seconds of testing time, and then reached 100 percent of the surface heating within the next  $\frac{3}{4}$  second. The center of the upstream wall showed an erratic behavior probably indicative of changing vortex formation. The transverse crack heating rates showed a more moderate behavior (Fig. 21) reaching at best 8 percent of the surface heating rate.

(U) Unfortunately, the number of runs and the range of variations of parameters was insufficient to draw firm conclusions. The following are the observations: (a) For

aspect ratios of about four, the heat transfer to the bottom of the crack reaches up to 8 percent of the duct surface heat transfer. (b) The value of  $h/b$  does not seem to be a unique correlating parameter, nor does  $b/\delta^*$  or  $Re_\tau$ , as can be seen from Table 2, which contains all data obtained for  $h/b$  of 4. This has not yet been sufficiently analyzed to suggest correlation. (c) With increasing depth of the crack, the heat transfer decreases very sharply and is only 1.0 to 1.8 percent of the surface heating rate. This behavior is consistent with Ref. 11 analytical predictions for this range of  $h/b$  and  $Re_\tau$ , as is shown in Fig. 22.\* (d) The temperature records show some very interesting trends. The short duration run, duct number 1T, shows a uniform rise in temperature. For other runs a periodic behavior is exhibited, or at least suggested, by the temperature traces. After a uniform rise of the crack-bottom temperature for a certain time there follows a period where the temperature remains constant for some time, or even decreases, then the temperature rises again at about the initial rate. This may repeat itself several times in one recording as seen from the temperature traces of Fig. 23. The same periods of temperature rise and constant temperature are not necessarily maintained in two cracks in the same duct. This observation strongly suggests that vortex flow exists in the cracks with the number of the counter-rotating vortices being some multiple of the crack width. Then, as ablation progresses, the crack height is reduced and the width increased to a degree that the vortex at the bottom of the crack can no longer be maintained; the vortex breaks up and the gas becomes more or less stagnant. The bottom temperature remains constant until the next vortex has reached the bottom or a reformation has taken place to fit the changed height and width of the crack. If one adopts the results of Ref. 12, namely, that 30 percent of the heat transferred across the dividing streamline atop of a cavity is transferred at the bottom of the first vortex, and so on, the present results suggest that at the end of the tests two to four vortices existed in the transverse cracks.

#### SUMMARY AND CONCLUSIONS

(U) Supersonic ablation studies with teflon were carried out in the NOL 3-Megawatt Arc Tunnel. The test conditions were selected so that the boundary layer in the teflon ducts was predicted to be either all laminar or all

\*The authors appreciate that ARAP and DASA authorized the use of these unpublished results.

turbulent. Experimental data of wall-static pressure, surface and in-depth temperature, skin friction and heat transfer were obtained. Total ablation was evaluated from the wall recession. The repeatability of test conditions and results was very good with the exception of the so-called surface thermocouples that were inadequately matched to teflon.

(U) The laminar data were compared with the results of two analytical procedures, the BLIMP-CMA. In general, very good agreement was found between experiments and predictions. An observed ablation anomaly in the downstream half of the ducts was analysed to be due to laminar instability which was probably followed by transition.

(U) The ducts tested under turbulent boundary-layer conditions had instrumented transverse and longitudinal cracks to study substructure heating. The non-dimensional heating rate for transverse cracks was found in good agreement with other experimental data and the prediction of an unpublished analytical procedure. The temperature records obtained from gauges on the bottom and side wall of the cracks indicate a changing vortex flow in the cracks.

(U) Parallel striations were found in two of the laminar ducts and cross-hatched striations in all turbulent ducts. Pressure orifices and cracks have a pronounced effect on the striation pattern. Further studies, experimentally and theoretically, are underway.

#### REFERENCES

1. Aerodynamics Department Staff, "The NOL 3 Megawatt Arc Tunnel," NOLTR 66-80, September 1966 (publication unclassified)
2. Bruno, J. R. and Risher, D. B., "Balance for Measuring Skin Friction in the Presence of Ablation," NOLTR 68-163, September 1968 (publication unclassified)
3. Warren, W. R., "Determination of Air Stagnation Properties in a High Enthalpy Test Facility," Journal of the Aerospace Sciences, Volume 26, 835, 1959 (publication unclassified)
4. Scala, S. M., "A Study of Hypersonic Ablation," Proceedings of the 10th International Astronautical Congress, Springer-Verlag, Vienna, 1959 (publication unclassified)

5. Kendall, R. M. and Bartlett, E. P., "A Procedure for Calculating the Non-Similar, Laminar, Chemically Reacting Boundary Layer over an Ablating Teflon Body with Coupled Quasi-Steady or Transient Wall Boundary Conditions," Aerotherm Final Report No. 68-32, April 1968 (publication unclassified)
6. Siegle, J. C. and Muus, L. T., "Pyrolysis of Polytetrafluoroethylene," address to American Chemical Society Meeting, September 1956 (unclassified)
7. Glowacki, W. J., "Fortran IV Program for Calculating the Turbulent Boundary Layer Growth for Contoured Axisymmetric Nozzles Using Air or Nitrogen," (to be published as NOLTR - unclassified)
8. Friedman, H. L., "The Mechanism of Polytetrafluoroethylene Pyrolysis," General Electric, MSVD Technical Information Series R59SD385, June 1959 (publication unclassified)
9. Gregory, N., Stuart, J. T. and Walker, W. S., "On the Stability of Three-Dimensional Boundary Layers with Application to the Flow due to a Rotating Disk". Boundary Layer Effects in Aerodynamics, Philosophical Library, Inc., 1957 (publication unclassified)
10. Knapp, C. F. and Roache, P. J., "A Combined Visual and Hot-Wire Anemometer Investigation of Boundary-Layer Transition," AIAA Journal, Volume 6, 29, 1968 (publication unclassified)
11. Donaldson, Coleman duP. and Dunn J. E., "Final Report on Flow and Heat Transfer Studies in Transverse Cracks," ARAP Report No. 133 (to be published)
12. Haugen, R. L. and Dhanak, A. M., "Heat Transfer in Turbulent Boundary-Layer Separation Over a Surface Cavity," Journal of Heat Transfer, Trans. ASME, Volume 89, Series G, No. 4, 1967 (publication unclassified)

(U) TABLE 1. Operating Conditions and Instrumentation

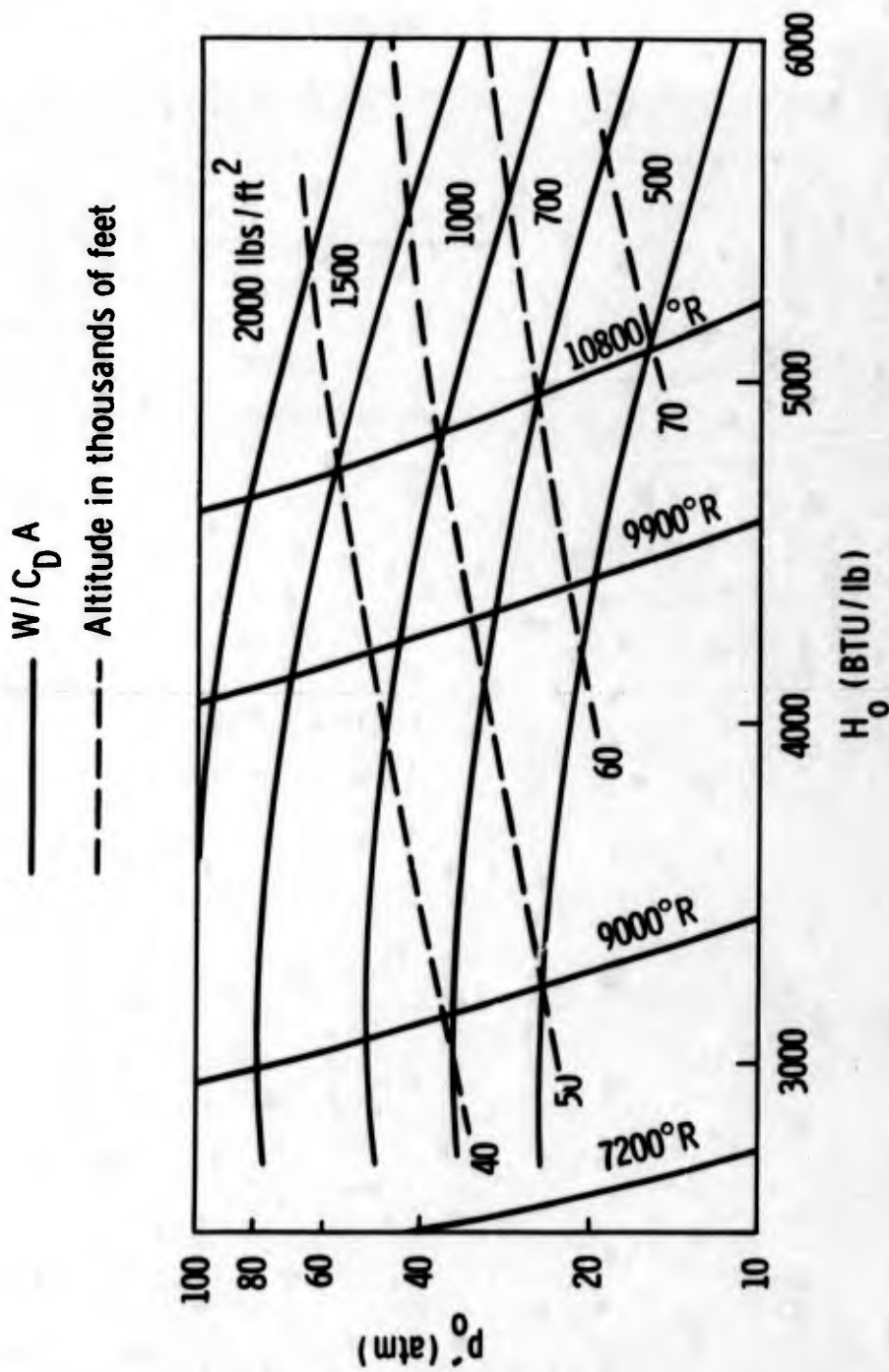
Duct Number	Mach Number	Supply Pressure (atm)	Supply Temperature ( $^{\circ}$ R)	Test Time (sec)	Instrumentation
1L	3.03	20.3	7700	13	6 static-pressure orifices
2L	3.04	21.4	8800	13	4 surface thermocouples - 6 static-pressure orifices
3L	3.03	22.0	7870	13	4 thermocouple plugs with 3 thermocouples per plug - 6 static-pressure orifices
4L	3.06	22.45	6600	13	1 skin-friction balance - 6 static-pressure orifices 4 thermocouple plugs
5L	3.03	22.0	7560	13	6 static-pressure orifices - 1 longitudinal and 1 transverse crack, each with one heat gauge
6L	3.06	22.3	6220	12	2 skin-friction balances
1T	~2.3	20.6	4330	2.7	3 static-pressure orifices - 1 longitudinal and 1 transverse crack, each with one heat gauge
2T	~2.3	20.6	4680	5.7	1 static-pressure orifice - longitudinal crack with three heat gauges 1 transverse crack with one heat gauge
3T	~2.3	21	4320	4.2	1 static-pressure orifice - 2 transverse cracks, each with one heat gauge

(U) TABLE 1. Cont.

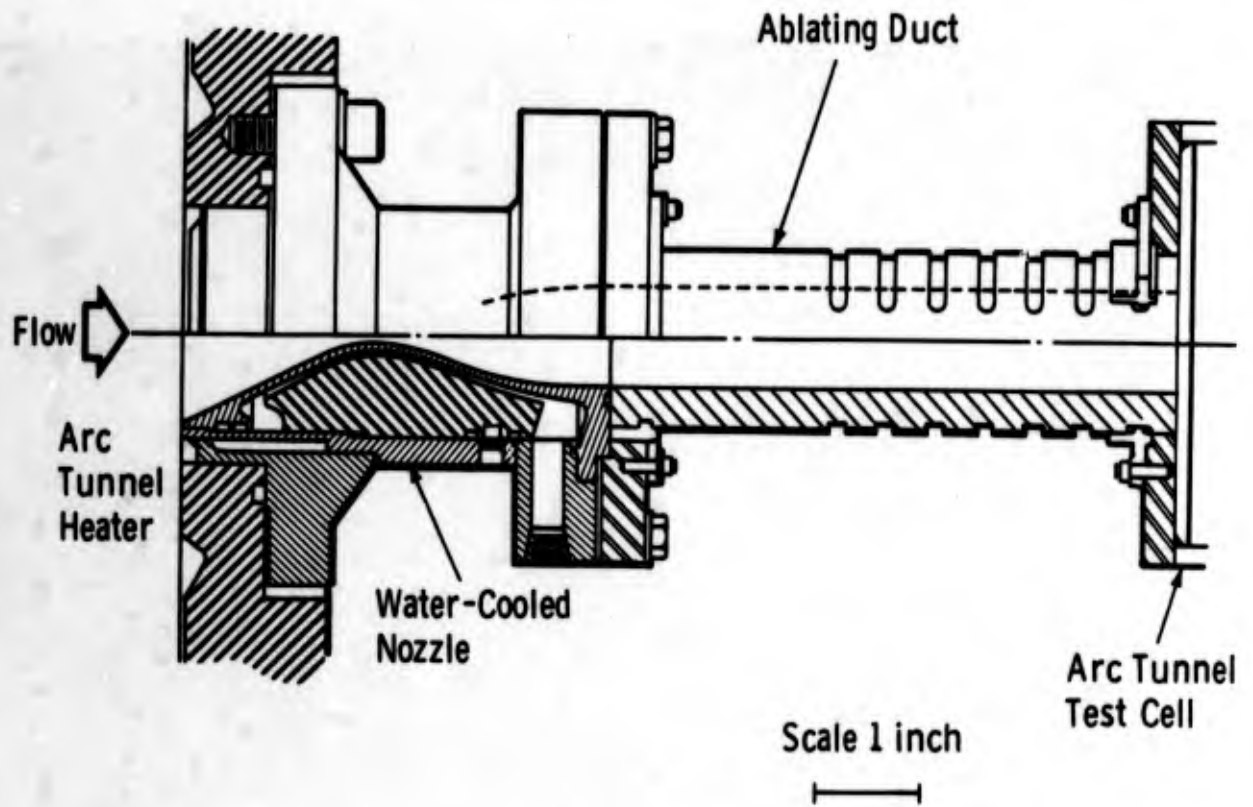
Duct Number	Mach Number	Supply Pressure (atm)	Supply Temperature (°R)	Test Time (sec)	Instrumentation
3AT	~2.3	21	4320	6.4	2 static-pressure orifices - 2 transverse cracks, each with one heat gauge - 1 skin-friction balance
4T	~2.3	28.5	4330	4.4	2 static-pressure orifices - 3 transverse cracks, each with one heat gauge
5T	~2.3	28.5	4330	4.6	3 static-pressure orifices - 3 in-depth thermo-couples - 1 skin-friction balance

(U) TABLE 2. Characteristics of Cracks

Duct Number	Type of Crack	Height h (in.)	Width b (in.)	h/b	b/ $\delta^*$	Re $_{\tau}$
1T	transverse	0.115	0.031	3.7	2.16	1200
	longitudinal (1-inch long)	0.133	0.031	4.3	3.86 to 3.35	1900
2T	transverse	0.200	0.031	6.5	2.28	1200
	longitudinal (1-inch long)	0.226	0.050	4.5	3.95 to 3.43	1900
3T	transverse	0.220	0.031	7.1	3.96	1600
	transverse	0.220	0.031	7.1	3.35	1850
3AT	transverse	0.124	0.031	4	3.96	1600
	transverse	0.125	0.031	4	3.35	1850
4T	transverse	0.124	0.030	4.1	2.52	1300
	transverse	0.400	0.100	4	7.13	4000
	transverse	0.124	0.030	4.1	1.88	1200



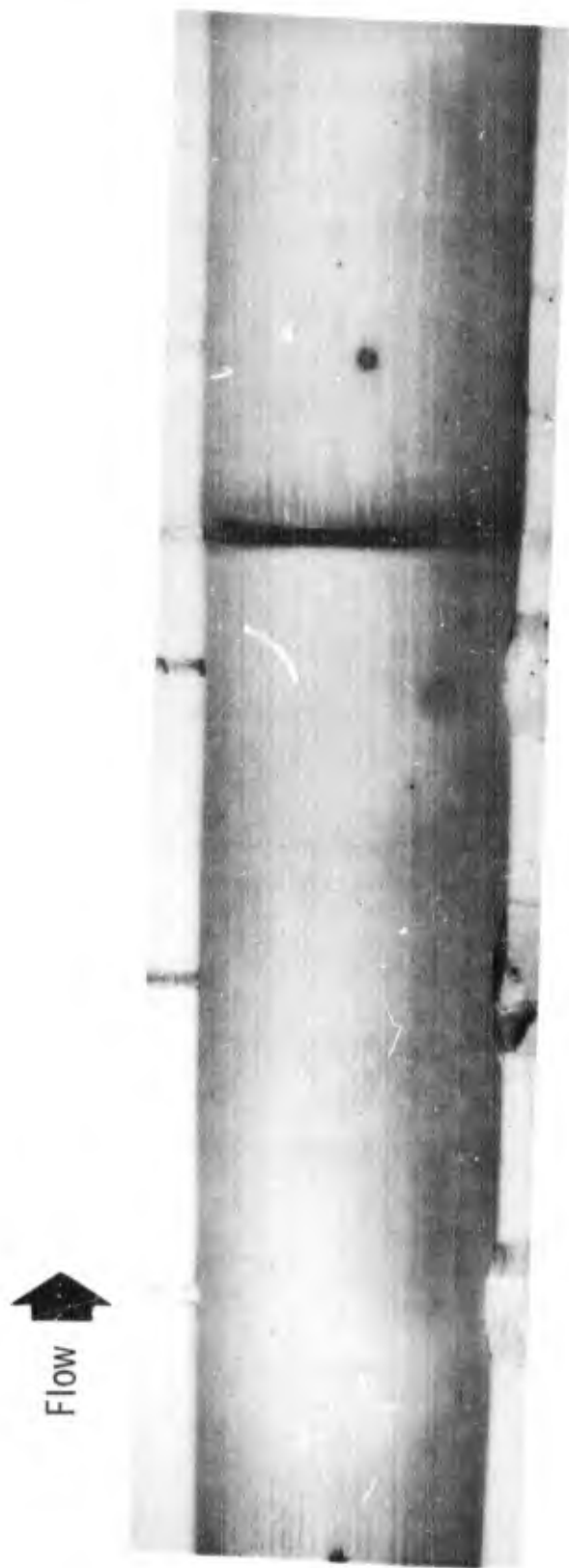
(U) FIG. 1 Stagnation-Point Pressure vs Stagnation Enthalpy for a 2500 Nautical Mile Minimum Energy Trajectory



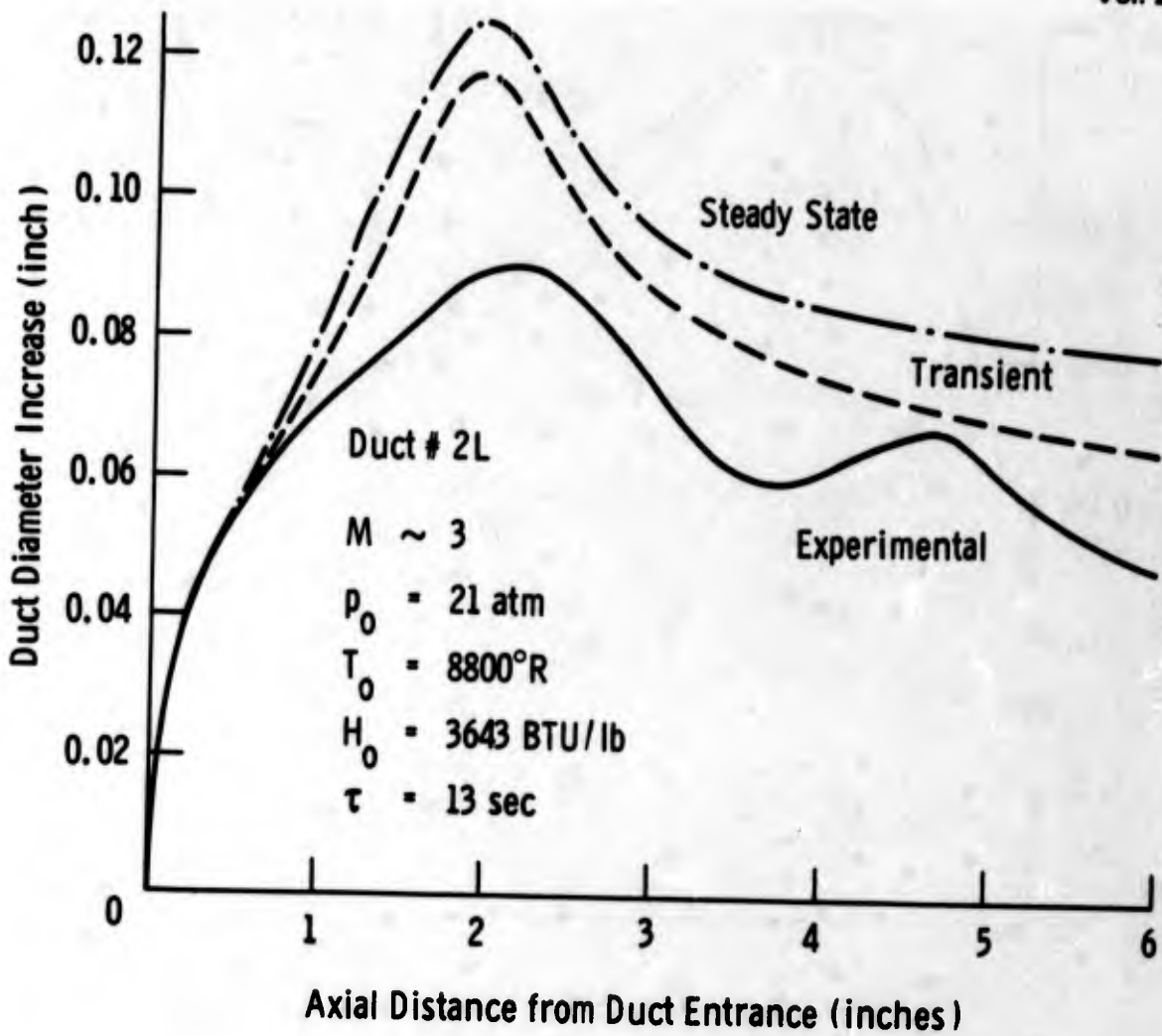
(U) FIG. 2 Nozzle and Ablation Duct Arrangement



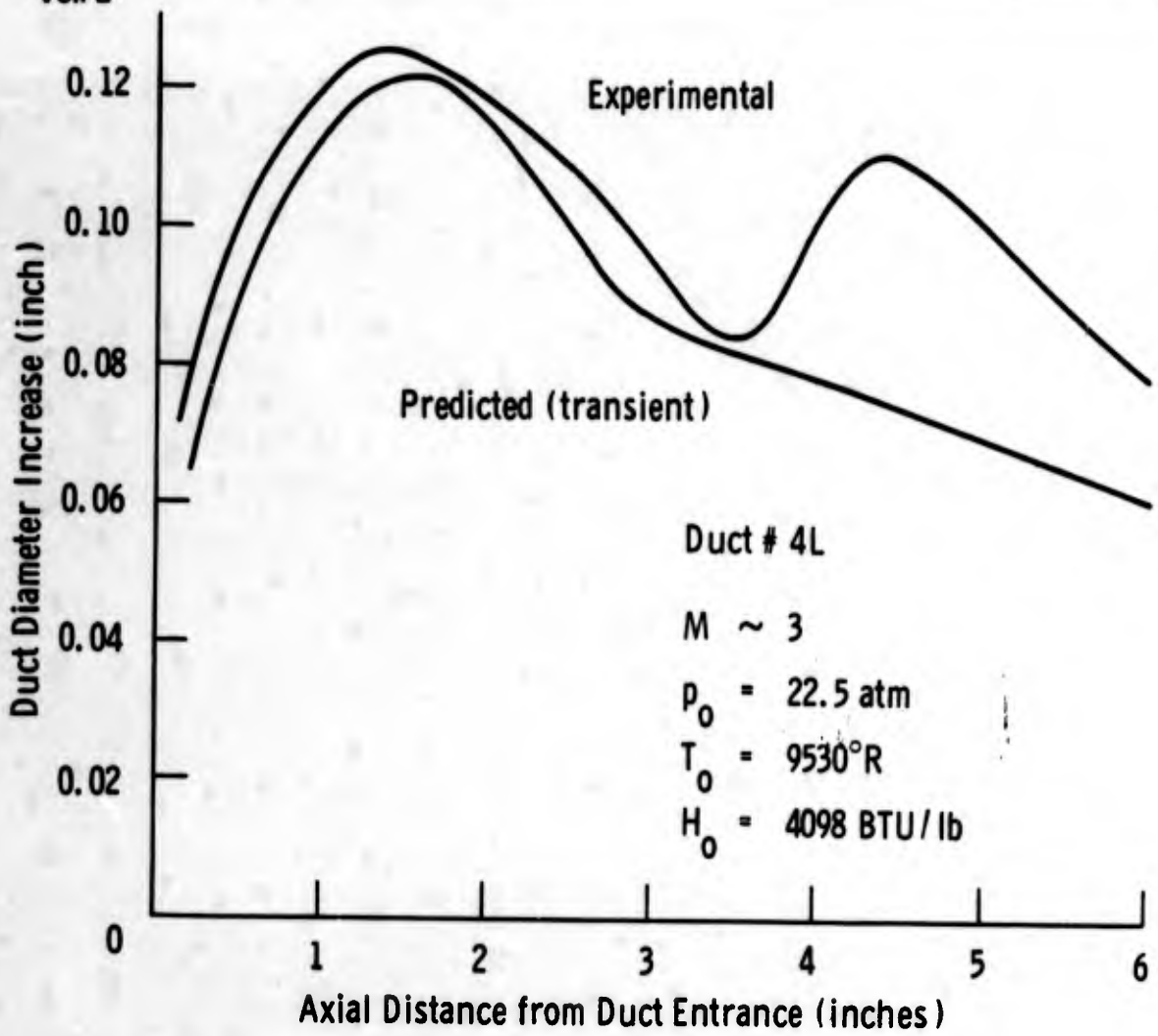
(U) FIG. 3 Experimental Set-up of Teflon Duct



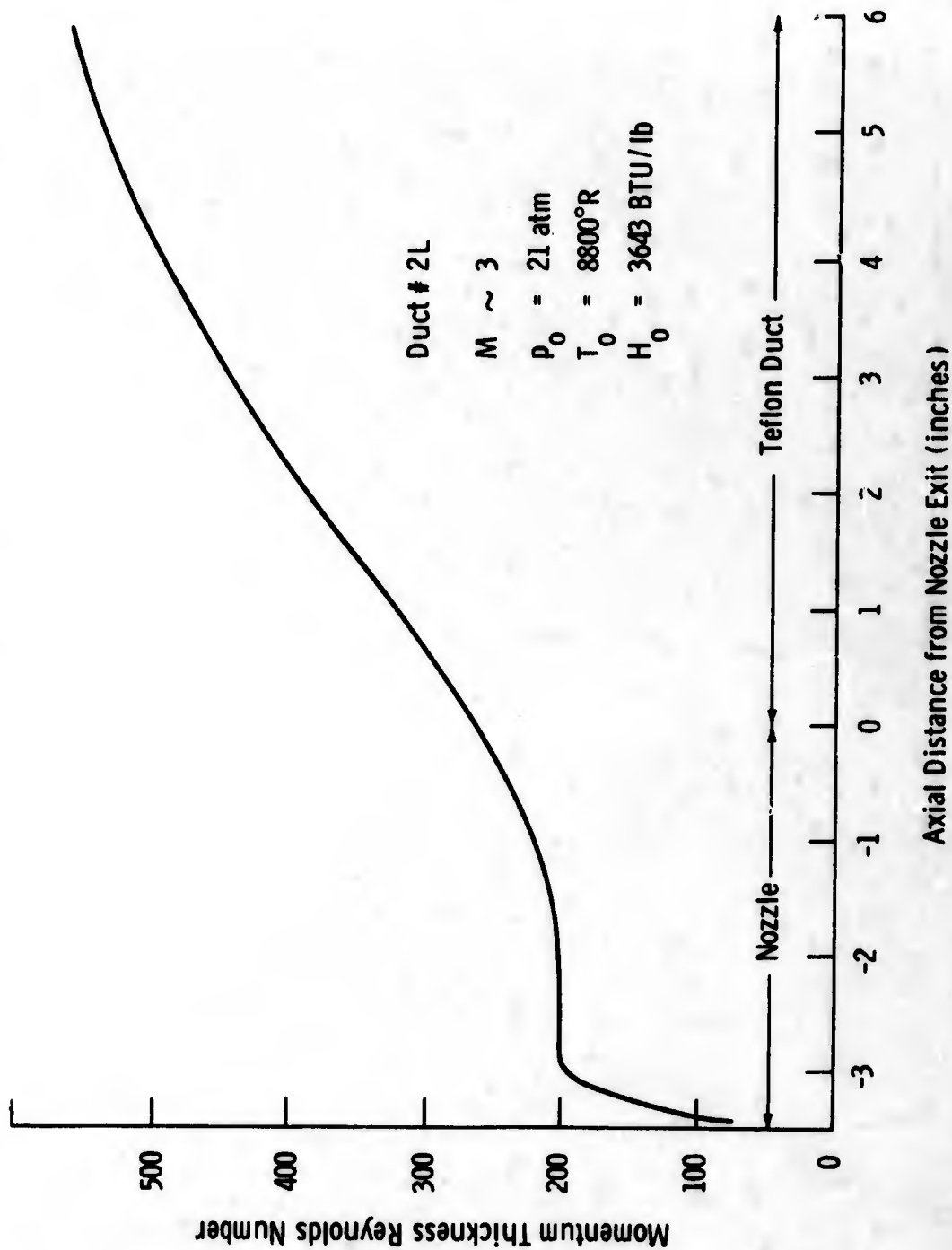
(U) FIG. 4 Inside View of Duct # 5L after Test



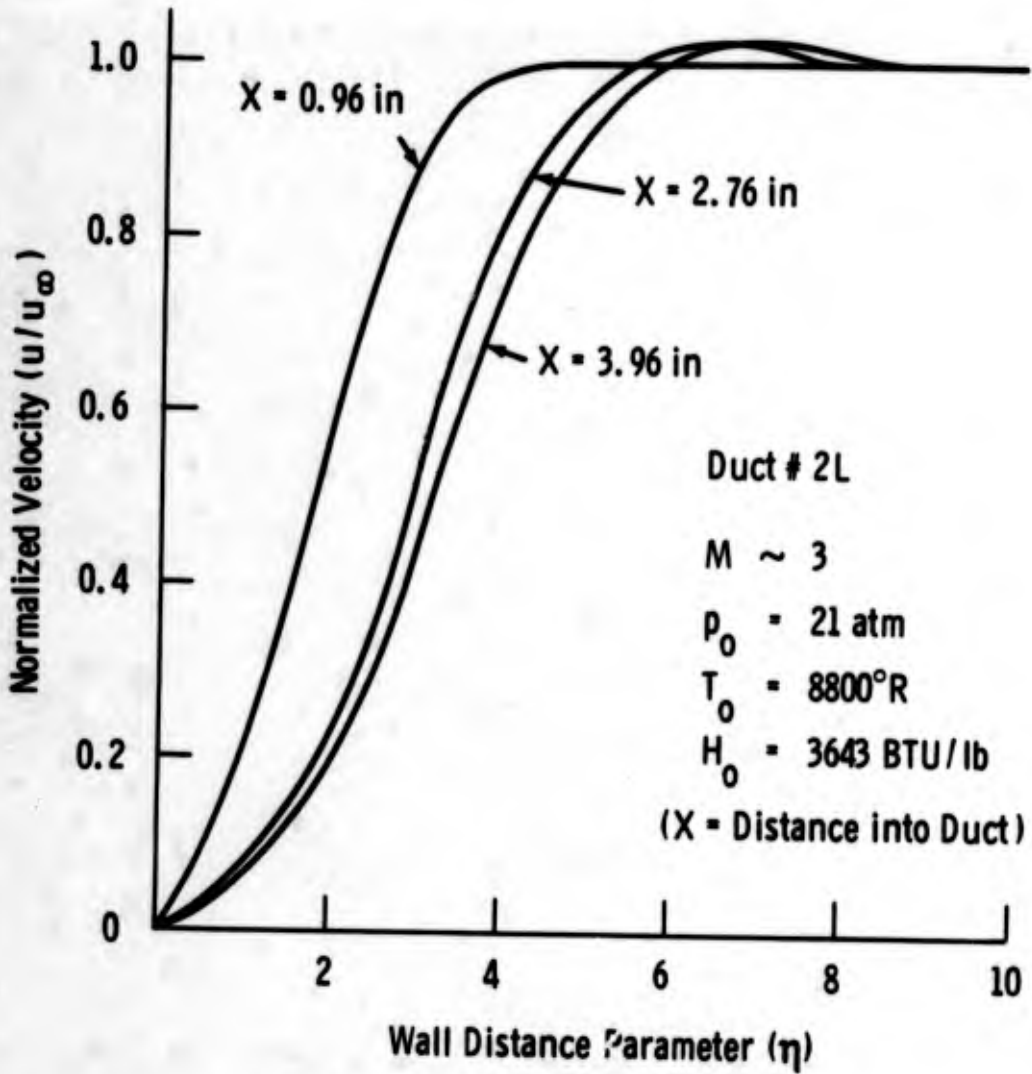
(U) FIG. 5 Predicted and Measured Total Recession



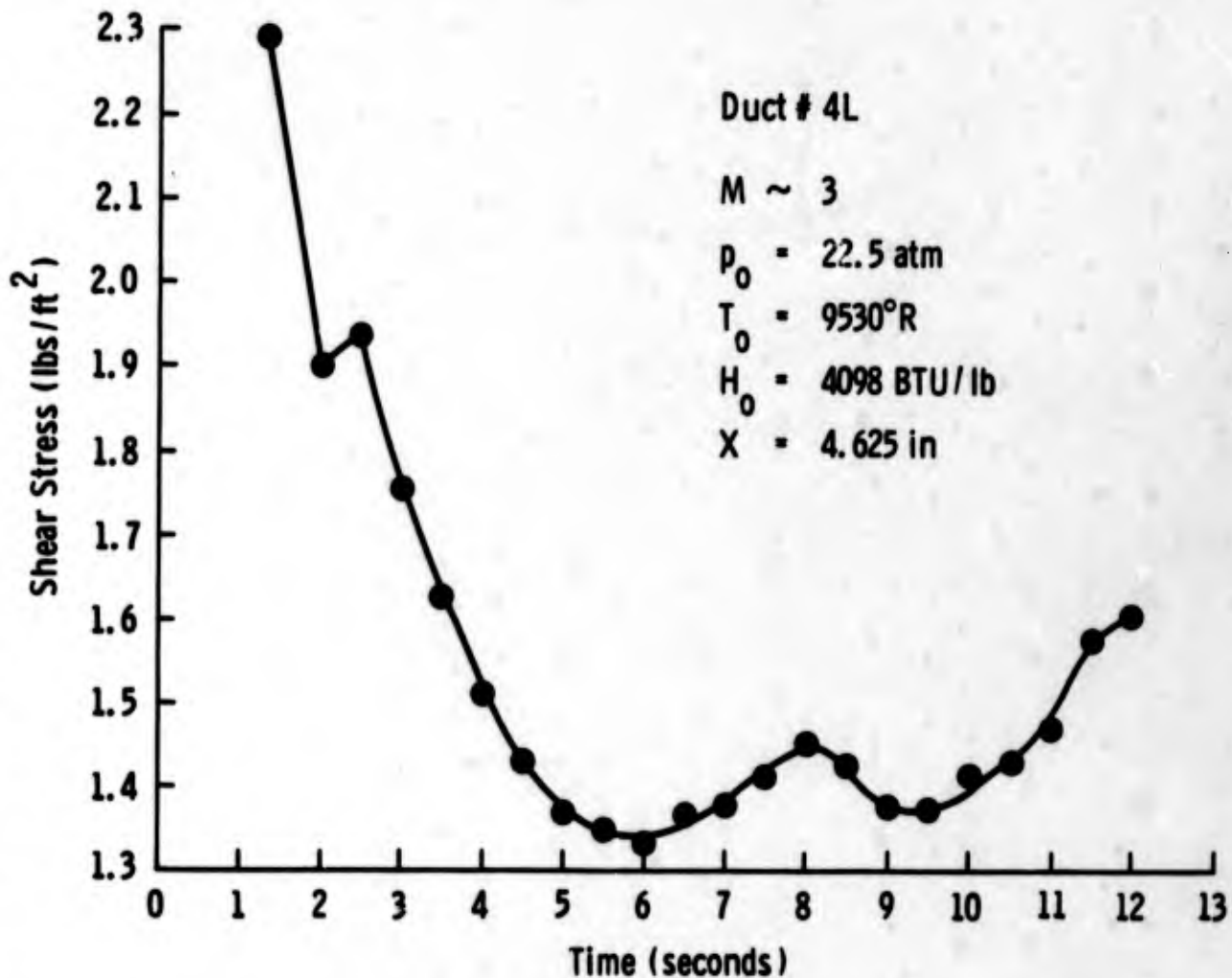
(U) FIG. 6 Predicted and Measured Total Recession



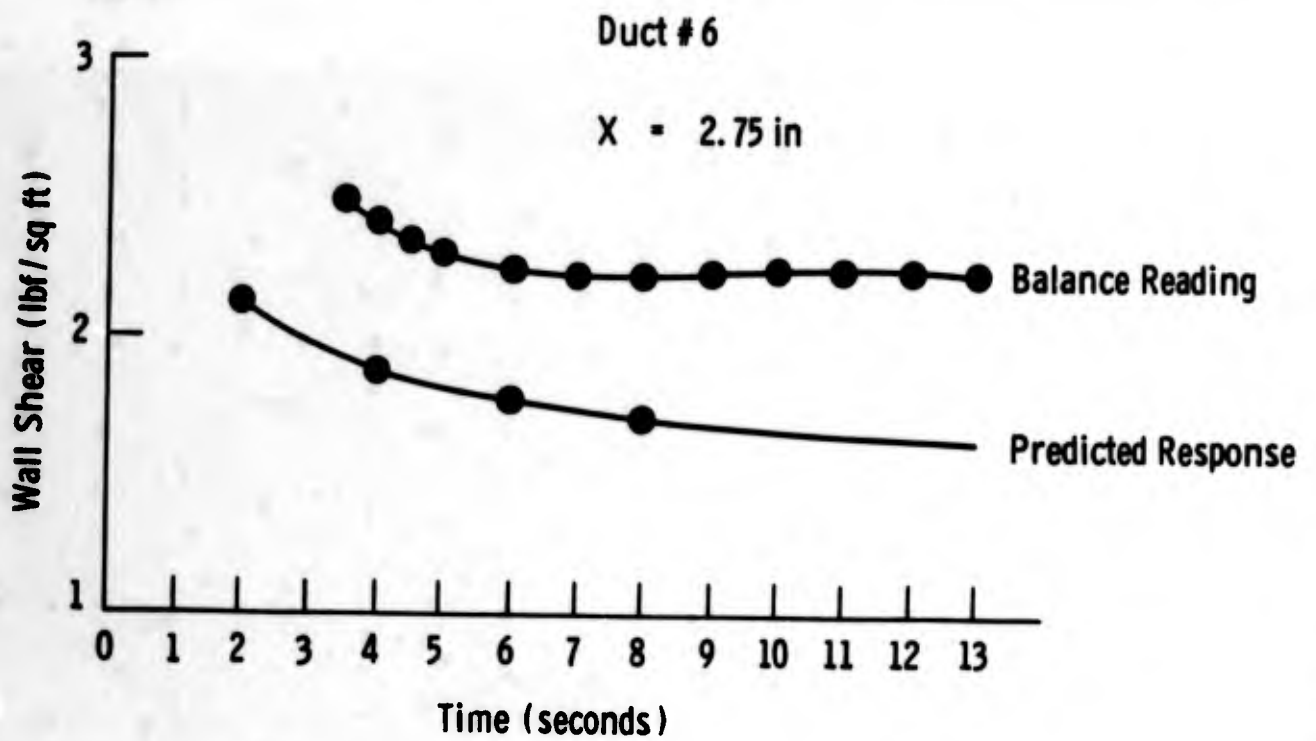
(U) FIG. 7 Calculated Momentum Thickness Reynolds Number Variation



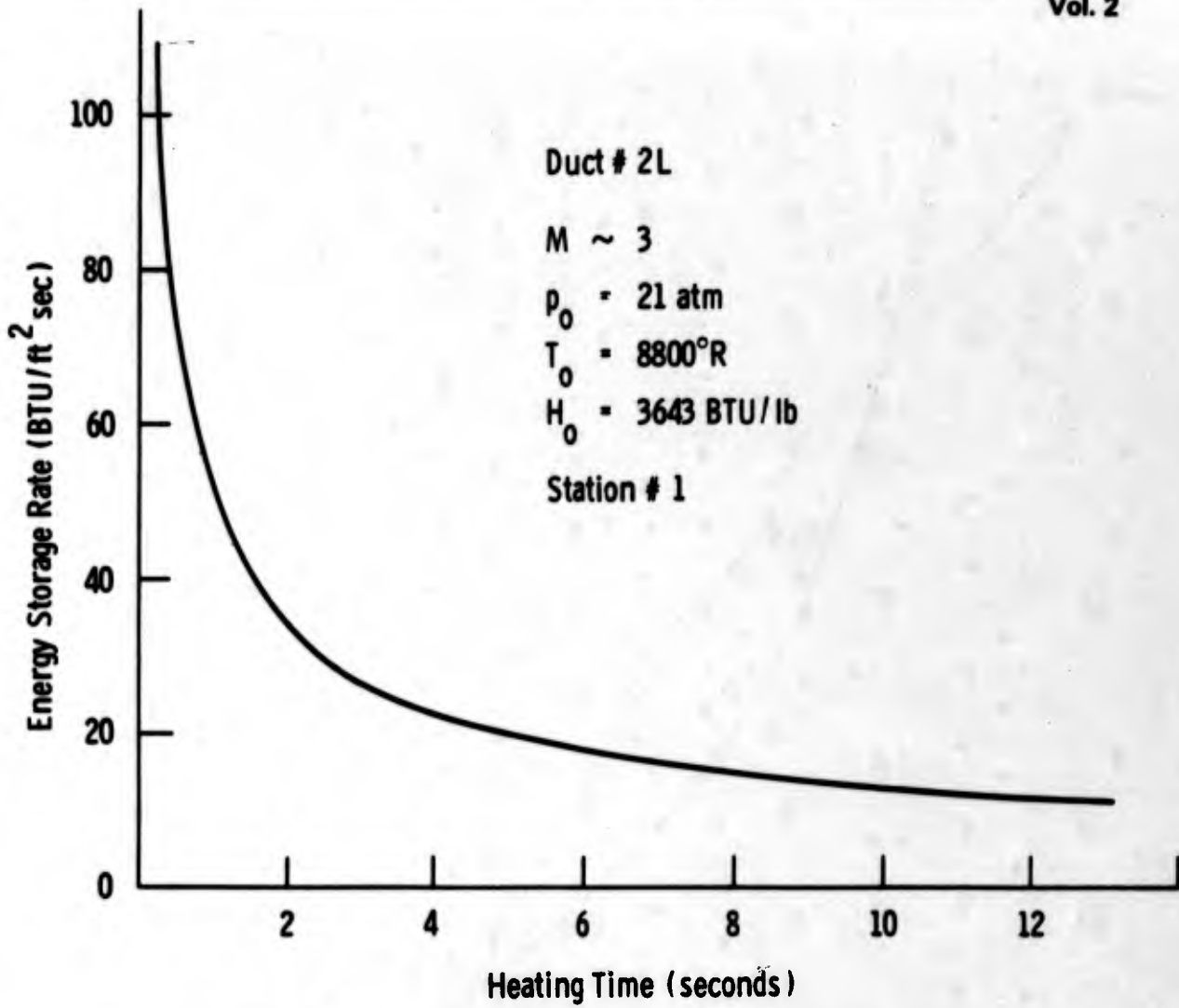
(U) FIG. 8 Calculated Velocity Profiles



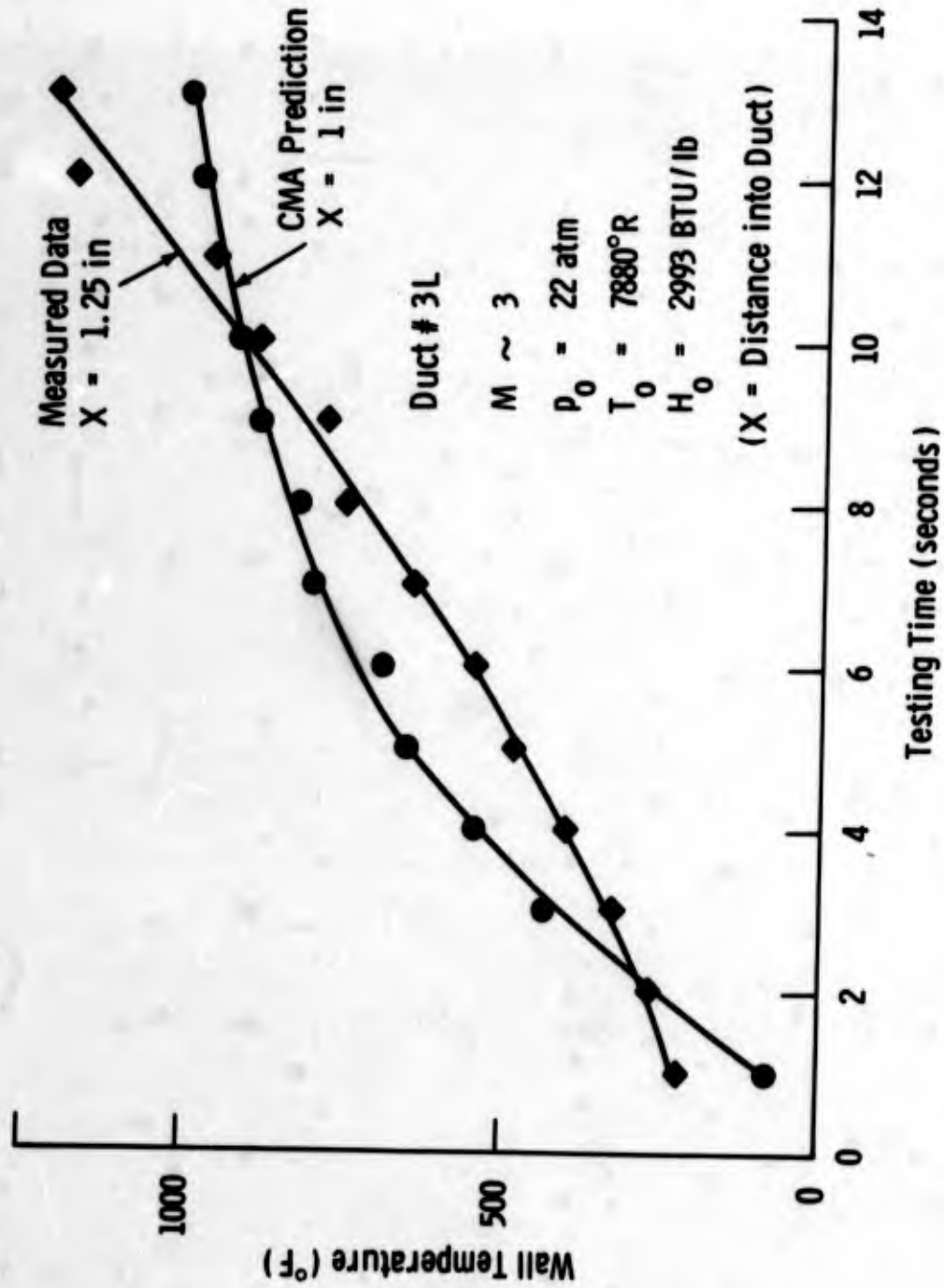
(U) FIG. 9 Shear Stress Variation with Time



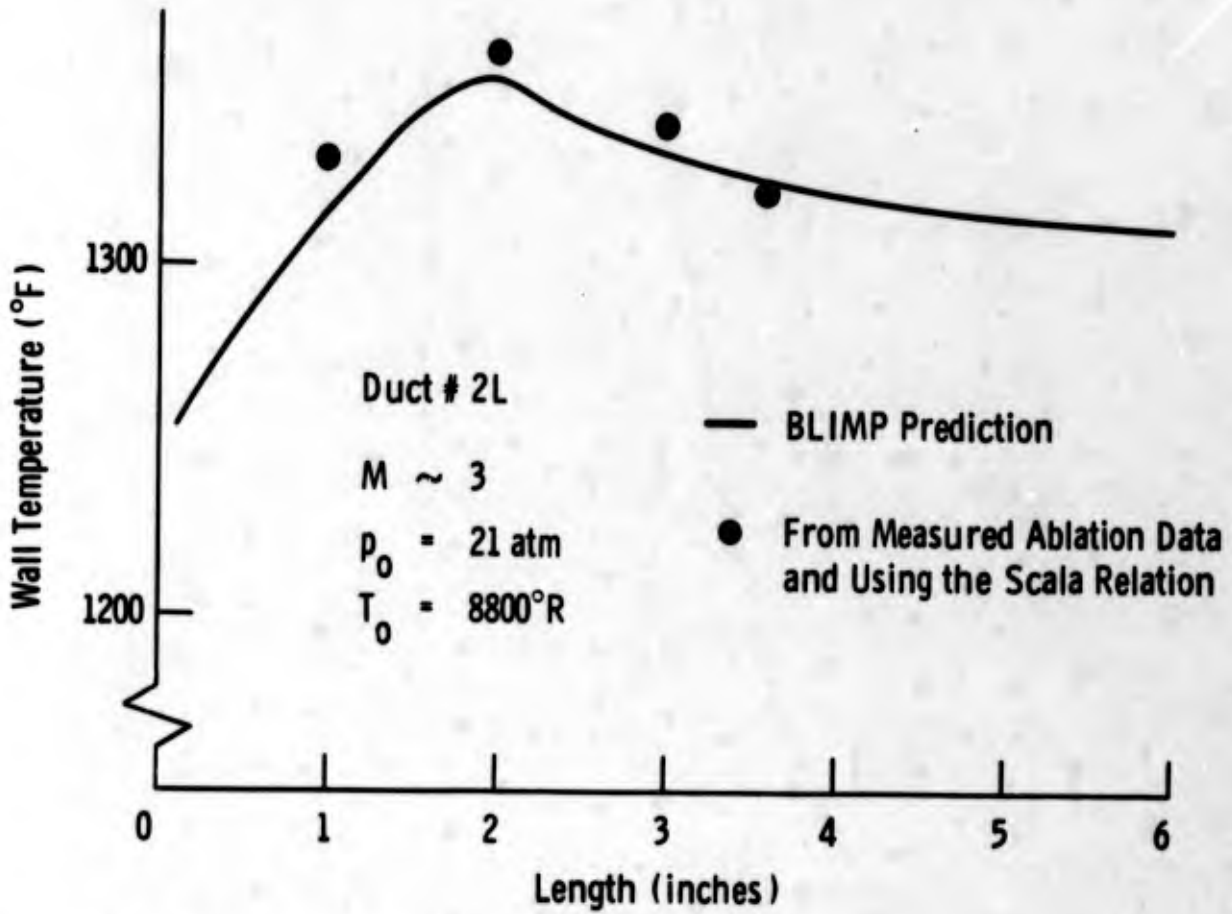
(U) FIG. 10 Wall Shear Response



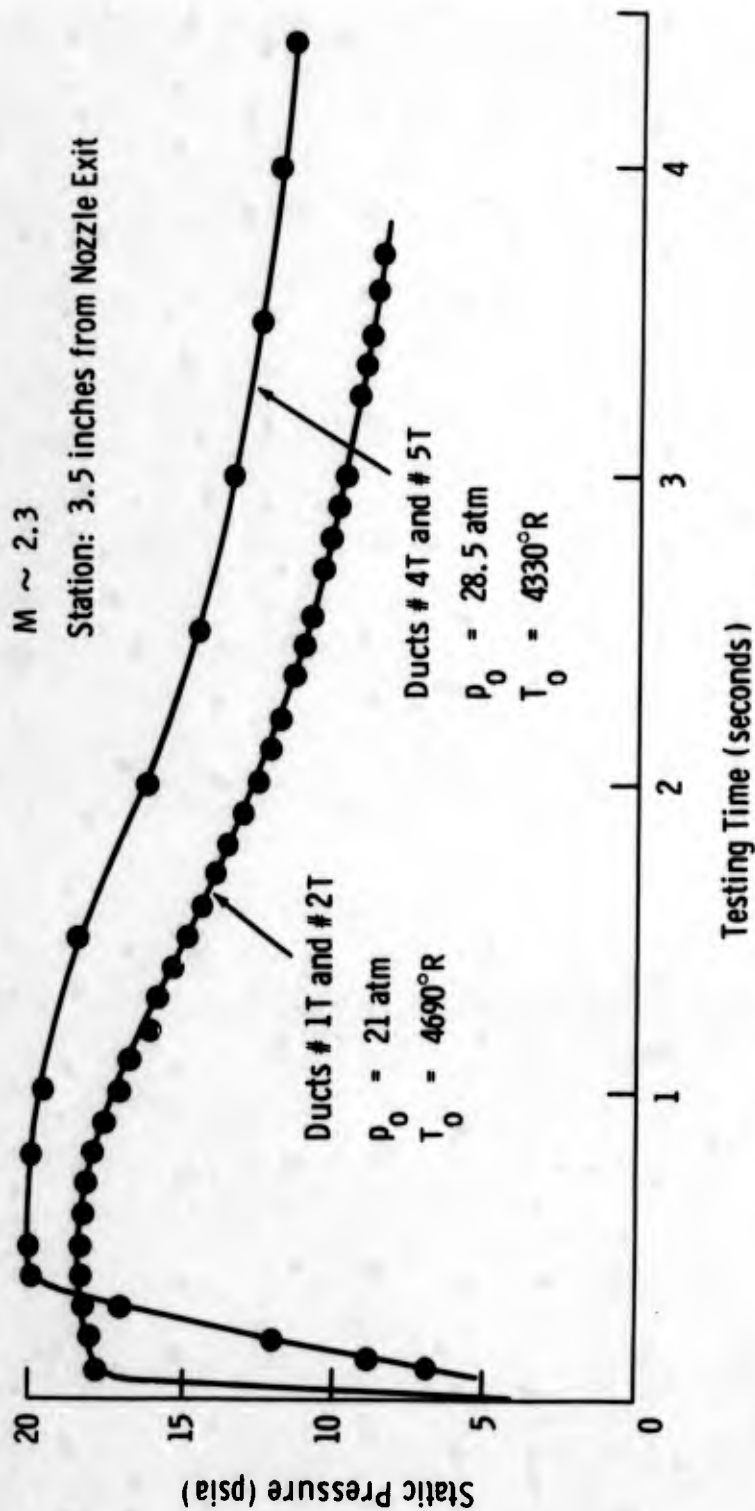
(U) FIG. 11 CMA Predicted Approach to Steady State Ablation



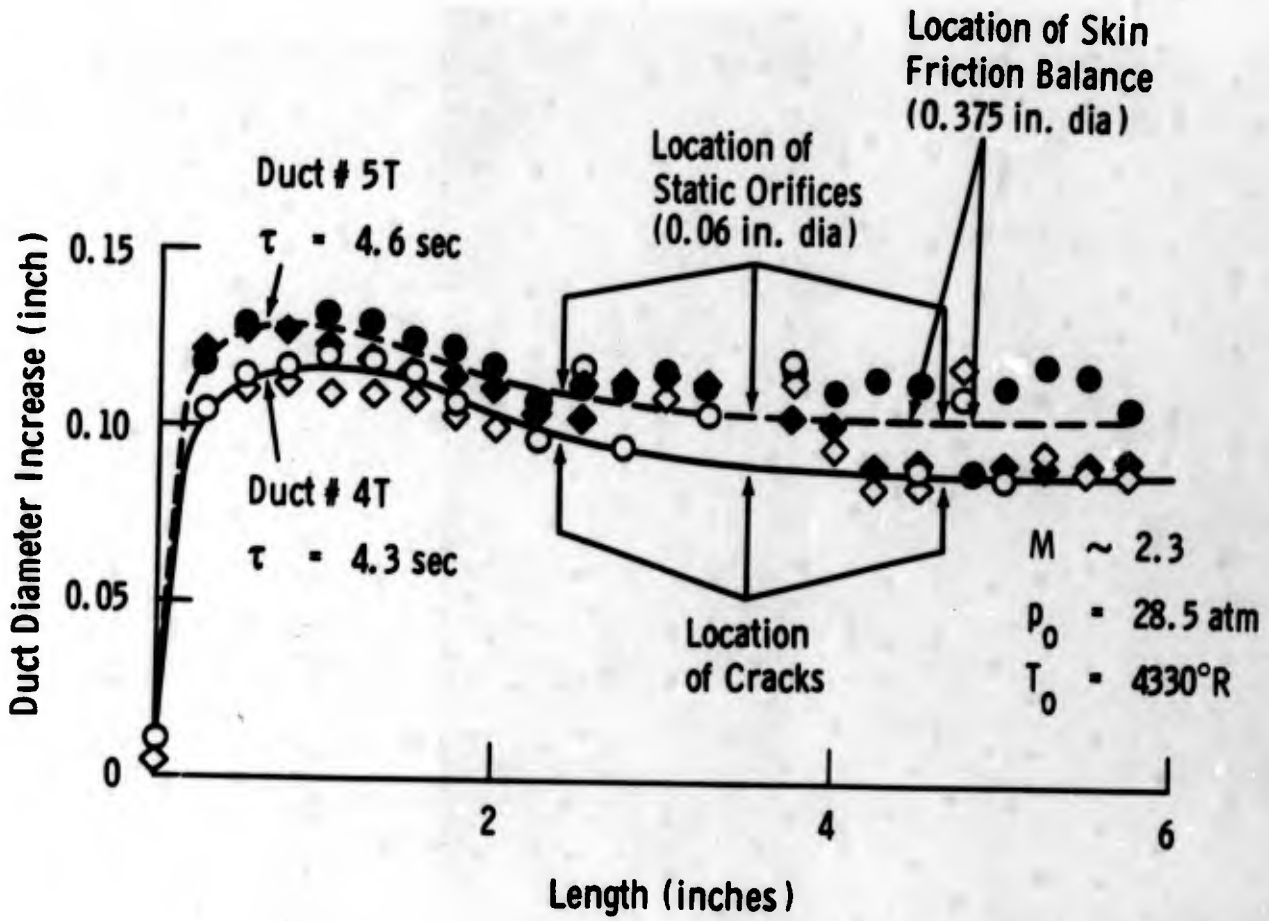
(U) FIG. 12 Predicted and Measured In-Depth Temperatures



(U) FIG. 13 Experimental and Predicted Steady-State Duct Surface Temperature



(U) FIG. 14 Static Pressure Variation with Time (Turbulent Boundary Layers)

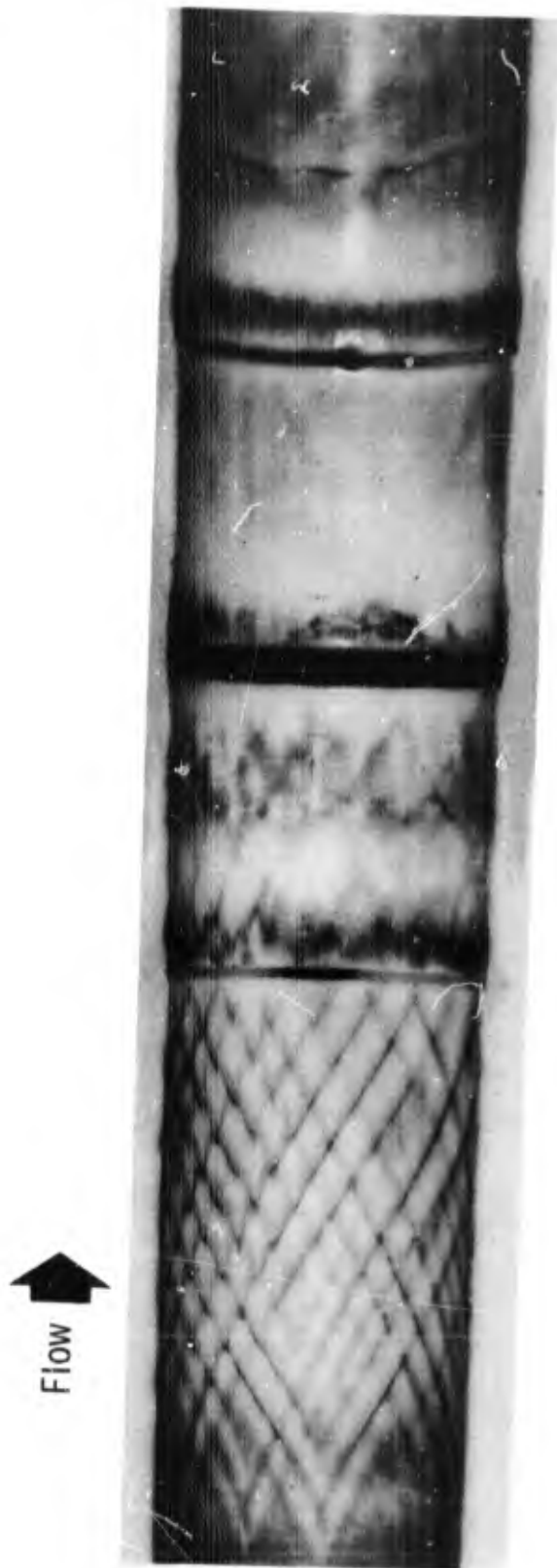


(U) FIG. 15 Total Surface Recession

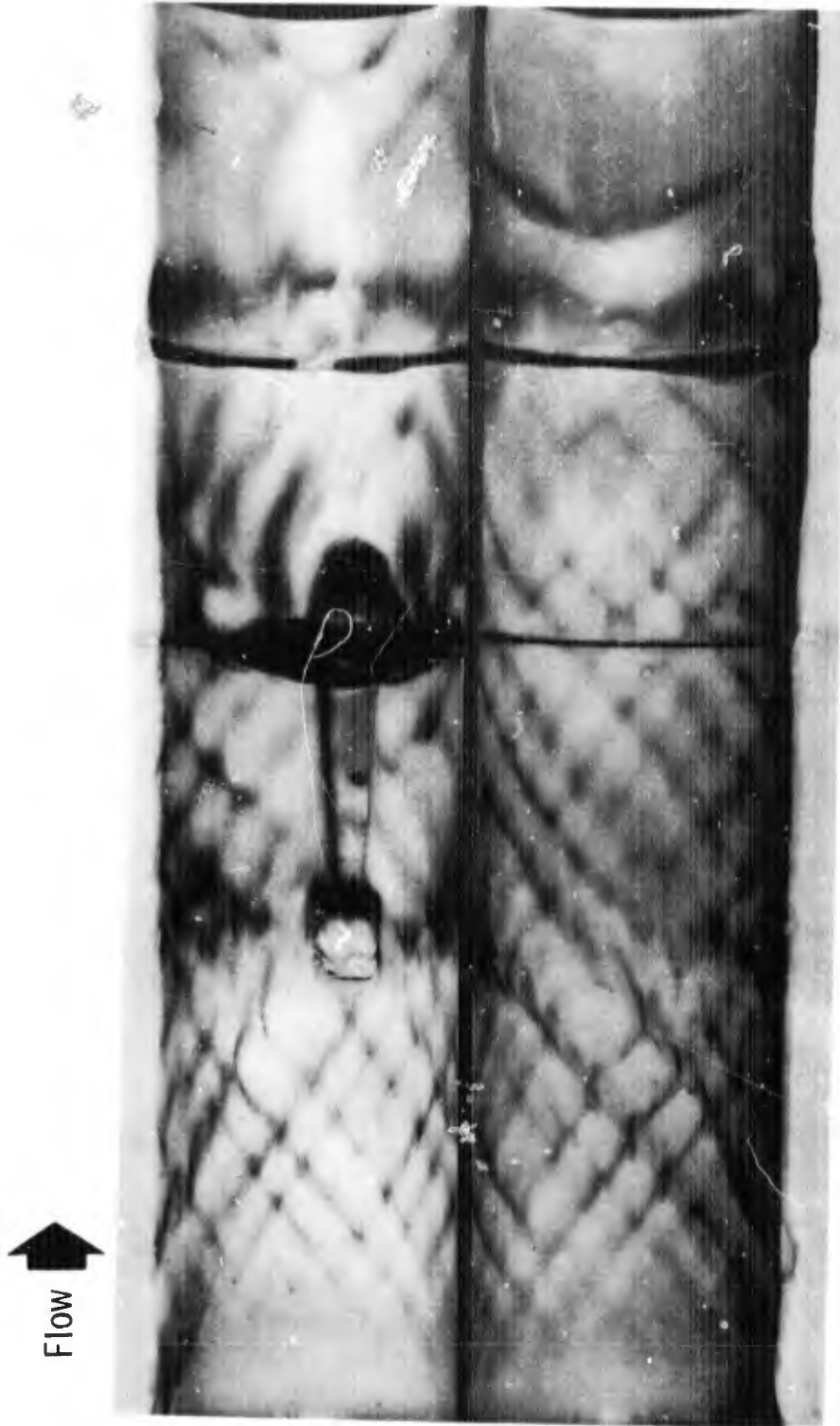
Flow ↑



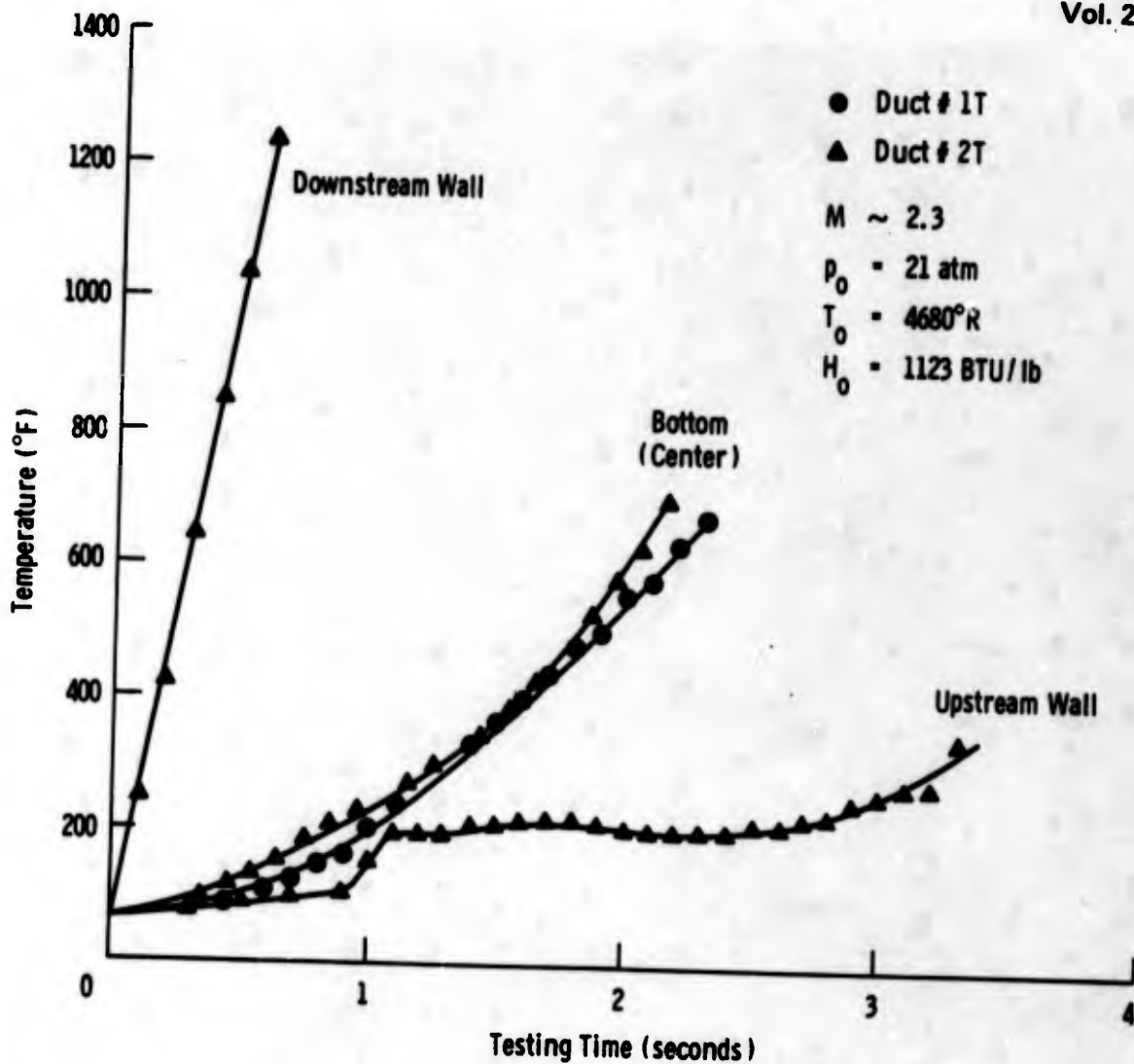
(U) FIG. 16 Cross-Hatched Striation Pattern



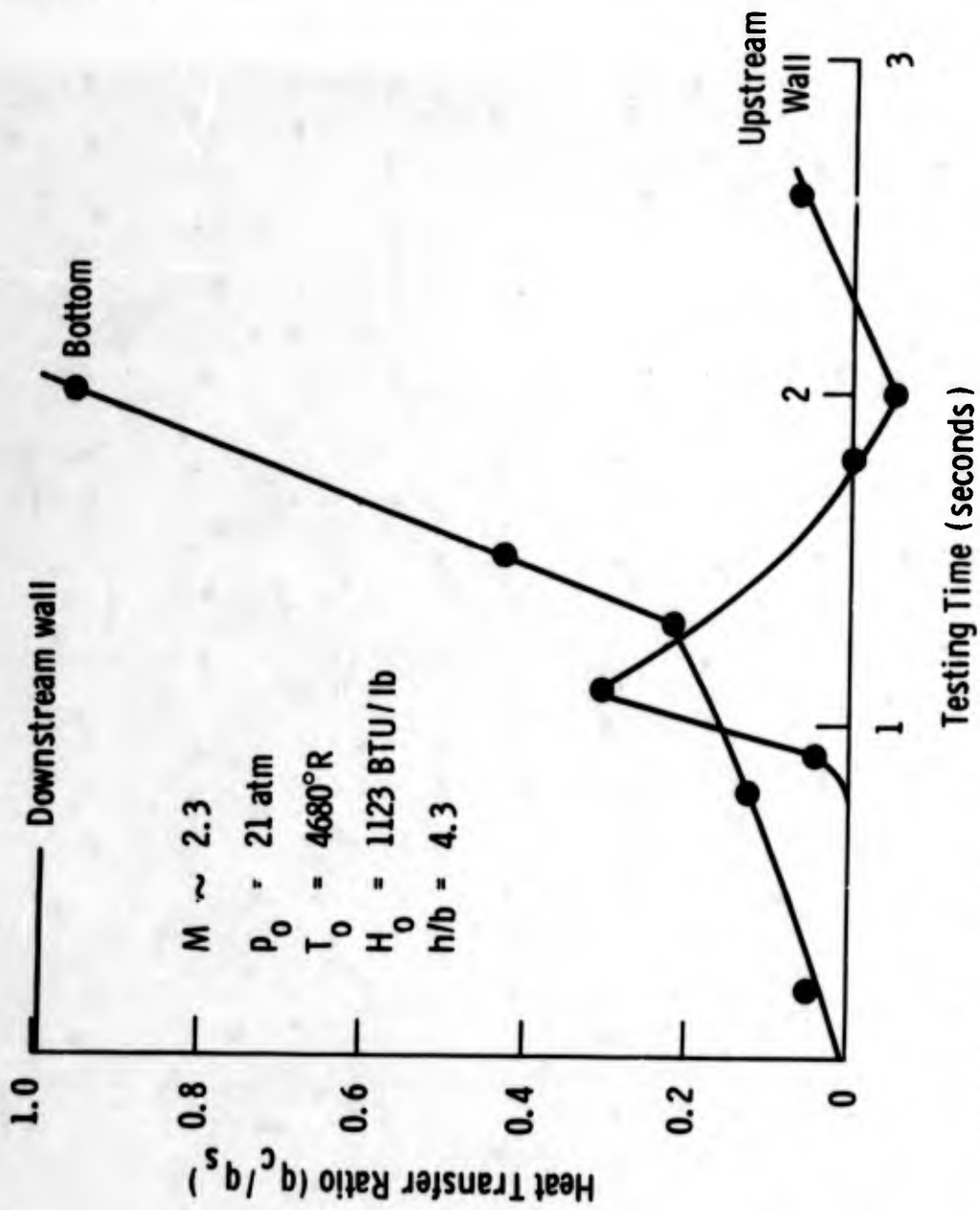
(U) FIG. 17 Modification of Striation Patterns due to Transverse Cracks



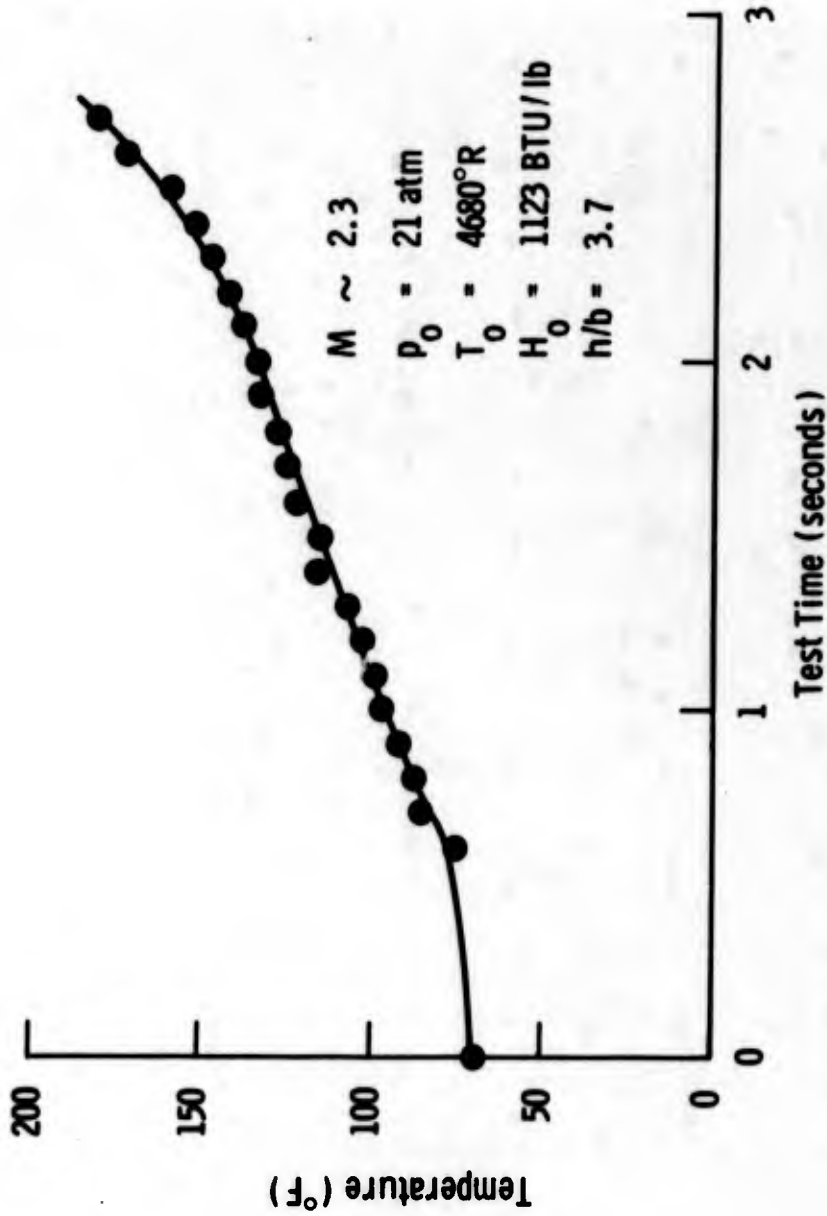
(U) FIG. 18 Modification of Striation Pattern due to a Longitudinal Crack



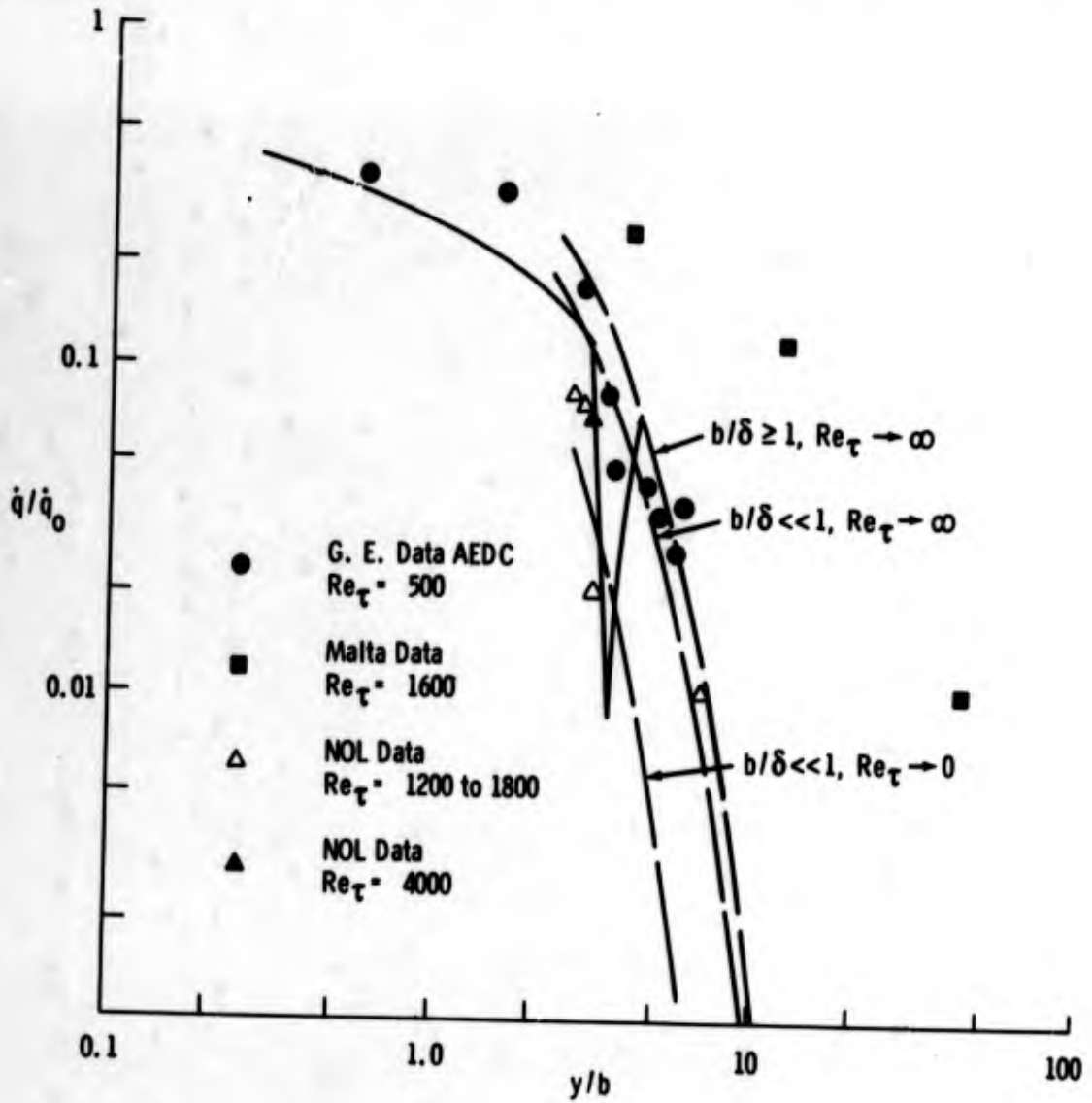
(U) FIG. 19 Temperature Variation for Longitudinal Cracks



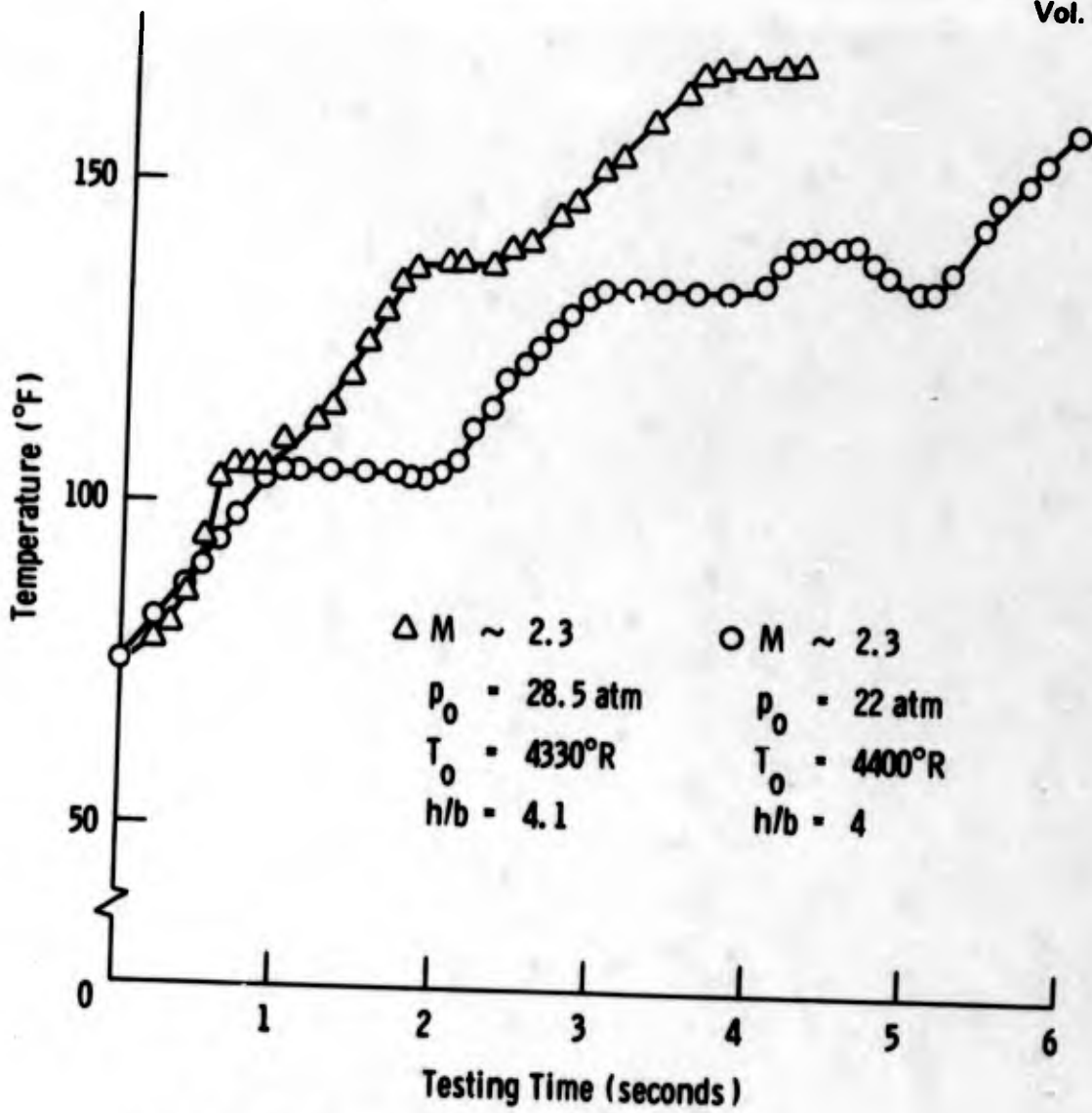
(U) FIG. 20 Heat Transfer to Side Wall's and Bottom of a Longitudinal Crack



(U) FIG. 21 Temperature Variation at the Bottom of a Transverse Crack



(U) FIG. 22 Transverse Crack Heating Summary  
 (Courtesy Aeronautical Research  
 Associates of Princeton)



(U) FIG. 23 Temperature Variation in Transverse Cracks

**BLANK PAGE**

Paper No. 12

**RECENT PROGRESS IN THE CALCULATION OF  
TURBULENT BOUNDARY LAYERS**

(U)

(Paper UNCLASSIFIED)

by

Tuncer Cebeci, A.M.O. Smith, and G. Mosinskis  
McDonnell Douglas Corporation  
Douglas Aircraft Company  
Long Beach, Calif. 90801

**ABSTRACT.** (U) In the seventh BOWACA symposium on aeroballistics held at Point Mugu in June 1966, A.M.O. Smith and his coworkers presented the governing boundary-layer equations for incompressible and compressible turbulent flows and outlined a general method of solution for these equations. Some results were given for the case of incompressible flows.

(U) The present paper reviews our progress in this area since the last meeting and presents a few comparisons of the many calculated and experimental results for incompressible and compressible turbulent flows with and without heat transfer for Mach numbers up to 5. Based on the comparisons made so far, it can be said that the method is quite accurate and fast; a typical compressible turbulent flow can be calculated in less than two minutes on the IBM 360/65 computer.

INTRODUCTION

(U) In the seventh BOWACA symposium on aeroballistics held at Point Mugu in June 1966, A.M.O. Smith and his coworkers presented the governing boundary-layer equations for incompressible and compressible turbulent flows and outlined a general method of solution for these equations [1]. The numerical method was the one that was developed at Douglas under contract NOw 60-0533c for solving laminar boundary-layer equations and was based on the shooting technique. The fluctuation terms in these equations were eliminated by means of eddy-viscosity and eddy-conductivity concepts. Some results were given for the case of incompressible flows.

(U) Since that time much progress has been made and very encouraging results have been obtained in this important area. First, the computation time has been reduced drastically by replacing the shooting method by an implicit finite-difference method without sacrificing accuracy. For example, with the present method a typical incompressible turbulent flow can be calculated approximately in one minute, and a typical compressible one can be calculated in less than two minutes on the IBM 360/65 computer.

(U) Second, the method has been well explored for incompressible turbulent flows with and without heat transfer and good results have been obtained. Out of the twenty-five different turbulent-boundary-layer prediction methods presented at the Stanford Conference held this past summer at Stanford, the Douglas method [2] was evaluated to be one of the methods placed in the top group. Third, the boundary-layer equations that are being solved account for the transverse-curvature effects which become quite important in predicting boundary-layer growth on slender bodies of revolution such as certain missiles or at the tail of a streamlined body of revolution. The present method was used to compare the available experimental data for such cases. The results were quite good.

(U) Fourth, the method has been explored for a good number of adiabatic compressible turbulent flows with and without pressure gradients for a range of Mach numbers up to 5 and again good agreement with experiments was obtained. At present the method is being explored for compressible turbulent flows with heat and mass transfer.

(U) The following sections describe the method and present several comparisons of calculated and experimental results for incompressible and compressible turbulent flows.

## BASIC EQUATIONS

## BOUNDARY-LAYER EQUATIONS

(U) If the normal-stress terms are neglected, the compressible turbulent boundary-layer equations for two-dimensional and axisymmetric flows can be written as in [3]:

Continuity

$$\frac{\partial}{\partial x} (r^k \rho u) + \frac{\partial}{\partial y} [r^k (\rho v + \overline{\rho'v'})] = 0 \quad (1)$$

Momentum

$$\rho u \frac{\partial u}{\partial x} + (\rho v + \overline{\rho'v'}) \frac{\partial u}{\partial y} = \rho_e u_e \frac{du_e}{dx} + \frac{1}{r^k} \frac{\partial}{\partial y} [r^k (\mu \frac{\partial u}{\partial y} - \overline{\rho u'v'})] \quad (2)$$

Energy

$$\rho u \frac{\partial H}{\partial x} + (\rho v + \overline{\rho'v'}) \frac{\partial H}{\partial y} = \frac{1}{r^k} \frac{\partial}{\partial y} \left[ r^k \frac{\lambda}{c_p} \frac{\partial H}{\partial y} - \overline{\rho v'H'} + \mu \left(1 - \frac{1}{Pr}\right) u \frac{\partial u}{\partial y} \right] \quad (3)$$

where  $k = 0$  for two-dimensional flow and  $k = 1$  for axisymmetric flow.

(U) The basic notation and scheme of coordinates are shown in Fig. 1, where  $u_\infty$  is a reference velocity,  $u_e(x)$  is the velocity just outside the boundary layer,  $H_e$  is the total enthalpy outside the boundary layer, and  $h_e$  is the local enthalpy outside the boundary layer. The coordinates are a curvilinear system in which  $x$  is distance along the surface measured from the stagnation point or leading edge. The dimension  $y$  is measured normal to the surface. Within the boundary layer, the velocity components in the  $x$ - and  $y$ -directions are  $u$  and  $v$ , respectively. The body radius is  $r_0$ .

(U) In these equations, the transverse-curvature effect (TVC) is retained because of its importance in predicting boundary-layer growth on slender bodies, such as certain missiles or at the tail of a streamlined body of revolution. In such cases the radius of the body may be of the same order of magnitude as the thickness of the boundary layer, and neglect of this effect could be quite important.

(U) The boundary conditions are:

Momentum

$$\begin{aligned} u(x,0) &= 0 \\ v(x,0) &= 0 \quad \text{or} \quad v(x,0) = v_w \text{ (mass transfer)} \\ \lim_{y \rightarrow \infty} u(x,y) &= u_e(x) \end{aligned}$$

Energy

$$H(x,0) = H_w \quad \text{or} \quad \frac{\partial H}{\partial y}(x,0) = \left(\frac{\partial H}{\partial y}\right)_w, \\ \lim_{y \rightarrow \infty} H(x,y) = H_e(x) \quad (5)$$

## FORMULATION OF EDDY VISCOSITY AND TURBULENT PRANDTL NUMBER

(U) In order to solve Eqs. (1), (2), and (3), it is necessary to relate  $-\overline{u'v'}$ , the Reynolds shear-stress term, and the  $-\overline{v'H'}$  term to the dependent variables  $u$  (or  $v$ ), and  $H$ , respectively. Here we use eddy-viscosity ( $\epsilon$ ) and eddy-conductivity ( $\lambda_t$ ) concepts, and set

$$-\overline{u'v'} = \epsilon \frac{\partial u}{\partial y} \quad (6)$$

and

$$-\overline{v'H'} = \lambda_t \frac{\partial H}{\partial y} \quad (7)$$

Equation (7) can also be written as

$$-\overline{v'H'} = \frac{c_p \epsilon}{Pr_t} \frac{\partial H}{\partial y} \quad (8)$$

by defining the turbulent Prandtl number as  $Pr_t = c_p \epsilon / \lambda_t$ .

(U) The expression for  $\epsilon$  in the inner region is based on Prandtl's mixing-length theory; that is,

$$\epsilon_i = \ell^2 \left| \frac{\partial u}{\partial y} \right| \quad (9)$$

where  $\ell$ , the mixing length, is given by  $\ell = k_1 y$ . A modified expression for  $\ell$  is used in Eq. (9) to account for the viscous sublayer close to the wall. This modification, suggested by Van Driest [4], is

$$\ell = k_1 y \left[ 1 - \exp\left(-\frac{y}{A}\right) \right] \quad (10)$$

where  $A$  is a constant for a given streamwise location in the boundary layer, and is defined as  $26\nu(\tau_w/\rho)^{-1/2}$ , with  $w$  denoting values at the wall. Equation (10) was developed for a flat plate. Here, we modify the constant  $A$  to account for pressure gradient. From the momentum equation it follows that the shear stress close to the wall may be written as

$$\tau = \tau_w + \frac{dp}{dx} y \quad (11)$$

If  $A$  is defined as  $26\nu(\tau/\rho)^{-1/2}$ , the constant becomes

$$26\nu \left( \frac{\tau_w}{\rho} + \frac{dp}{dx} \frac{y}{\rho} \right)^{-1/2} \quad (12)$$

Then the expression for inner eddy viscosity becomes

$$\epsilon_i = k_1^2 y^2 \left\{ 1 - \exp \left[ - \frac{y}{26\nu} \left( \frac{\tau_w}{\rho} + \frac{dp}{dx} \frac{y}{\rho} \right)^{1/2} \right] \right\}^2 \left| \frac{\partial u}{\partial y} \right| \quad (13)$$

(U) The expression for  $\epsilon$  in the outer region is based on a constant eddy viscosity,  $\epsilon_o$ ,

$$\epsilon_o = k_2 u_e \delta_k^* \quad (14)$$

modified by Klebanoff's [5] intermittency factor  $\gamma$ , approximated by the following formula

$$\gamma = \left[ 1 + 5.5 \left( \frac{y}{\delta} \right)^6 \right]^{-1} \quad (15)$$

which is a convenient and sufficiently accurate approximation to the error function.

(U) The choice of constants  $k_1$  and  $k_2$  in the eddy-viscosity formulas depends slightly on the definition of the boundary-layer thickness  $\delta$ . As in several previous studies, for example, Ref. 2,6, the values of the constants  $k_1$  and  $k_2$  are taken to be 0.40 and 0.0168, respectively, and  $\delta$  is defined as the  $y$ -distance for which  $f' = 0.995$ .

(U) The constraint used to define the inner and outer regions is the continuity of the eddy viscosity; from the wall outward, the expression for inner eddy viscosity applied until  $\epsilon_i = \epsilon_o$ . The dividing point is  $y_c$ . Figure 2 shows a typical eddy-viscosity variation across the boundary layer for a flat-plate flow.

#### TRANSFORMATION OF BOUNDARY-LAYER AND EDDY-VISCOSITY EQUATIONS

(U) Equations (1), (2), and (3), which are expressed in the coordinates of the physical plane, require starting profiles, but these equations are singular at  $x = 0$ . For this reason, we first transform them as in previous studies to a coordinate system that removes the singularity at  $x = 0$ , stretches the coordinate normal to the flow direction, and places the equations in an almost two-dimensional form. We use a combination of the Probstein-Elliot [7] and Levy-Lees [8] transformations.

$$d\xi = \rho_e \mu_e u_e \left( \frac{r_o}{L} \right)^{2k} dx, \quad d\tau_1 = \frac{\rho_1 u_e}{(2\xi)^{1/2}} \left( \frac{r}{L} \right)^k dy \quad (16)$$

If a stream function  $\psi$  is introduced such that

$$\frac{\partial \psi}{\partial y} = \left( \frac{r}{L} \right)^k \rho u, \quad \frac{\partial \psi}{\partial x} = - \left( \frac{r}{L} \right)^k (\rho v + \overline{\rho' v'}) \quad (17)$$

## Vol. 2

and if  $\psi$  is related to a dimensionless stream function  $f$  as

$$\psi(x, y) = (2\xi)^{1/2} f(\xi, \eta) \quad (18)$$

then the momentum equation, Eq. (2), and the energy equation, Eq. (3), become:

Momentum

$$\left[ (1+t)^{2k} C(1+\epsilon^+) f'' \right]' + f f'' + \beta \left[ \frac{\rho_e}{\rho} - (f')^2 \right] = 2\xi \left[ f' \frac{\partial f'}{\partial \xi} - f'' \frac{\partial f}{\partial \xi} \right] \quad (19)$$

Energy

$$\left\{ (1+t)^{2k} C \left[ \left( 1 + \epsilon^+ \frac{\text{Pr}}{\text{Pr}_t} \right) \frac{g'}{\text{Pr}} + \frac{u_e^2}{H_e} \left( 1 - \frac{1}{\text{Pr}} \right) f' f'' \right] \right\}' + f g' = 2\xi \left( f' \frac{\partial g}{\partial \xi} - g' \frac{\partial f}{\partial \xi} \right) \quad (20)$$

after the terms  $-\overline{u'v'}$  and  $-\overline{v'H'}$  are replaced by the relations given by Eqs. (6) and (8). In Eqs. (19) and (20),  $t$  is the transverse-curvature term,  $\beta$  is the pressure-gradient term,  $C$  is the viscosity-density term, and  $\epsilon^+$  is the ratio of eddy viscosity to kinematic viscosity. They are defined as follows:

$$t = -1 + \left[ 1 + \frac{2L \cos \alpha}{r_0^2} \frac{(2\xi)^{1/2}}{\rho_e u_e} \int_0^\eta \frac{\rho_e}{\rho} d\eta \right]^{1/2}$$

$$\beta = \frac{2\xi}{u_e} \frac{du_e}{d\xi}, \quad C = \frac{\rho \mu}{\rho_e \mu_e}, \quad \epsilon^+ = \frac{\epsilon}{\nu}$$

The dependent variables  $f'$  and  $g$  in Eqs. (19) and (20) are dimensionless velocity and total-enthalpy ratios, respectively, defined as  $f' = u/u_e$  and  $g = H/H_e$ . It can be seen from Eqs. (19) and (20) that setting  $k = 0$  reduces the boundary-layer equations to two-dimensional form. For axisymmetric flow with no transverse-curvature effect,  $k = 1$  and  $t = 0$ , which indicates that the ratio of  $r$  to  $r_0$  is unity, since

$$r = r_0 + y \cos \alpha$$

and  $t$  in the physical plane is defined as  $t = (y \cos \alpha)/r_0$ . Furthermore, if  $\epsilon^+$  is zero, Eqs. (19) and (20) reduce to a classical form of the compressible laminar boundary-layer equations.

(U) The boundary conditions given by Eqs. (4) and (5) become:

Momentum

$$f(\xi, 0) = f_w = 0 \quad \text{or}$$

$$f_w = - \frac{1}{(2\xi)^{1/2}} \int_0^\xi \left(\frac{L}{r_0}\right)^k \frac{\rho_w v_w}{\rho_e \mu_e u_e} d\xi \quad (\text{mass transfer}) \quad (21a)$$

$$f'(\xi, 0) = 0 \quad \lim_{\eta \rightarrow \infty} f'(\xi, \eta) = 1 \quad (21b)$$

Energy

$$g(\xi, 0) = \frac{H_w}{H_e} = g_w \quad \text{or} \quad g'_w(\xi, 0) = g'_w \quad (22a)$$

$$\lim_{\eta \rightarrow \infty} g(\xi, \eta) = 1 \quad (22b)$$

Similarly, we can transform the eddy-viscosity expressions by using the transformation given by Eqs. (16) and (18). In dimensionless form, the expression for eddy viscosity for the inner region becomes

$$\epsilon_i^+ = k_1^2 \left(\frac{\rho}{\rho_e}\right) A_1 (1+t)^k |f''| Y^2 \left\{ 1 - \exp \left[ - \frac{A_1}{26} \left(\frac{r_0}{L}\right)^{k/2} Y \right. \right. \\ \left. \left. \cdot \left( \left| f_w'' \frac{\rho_w}{\rho} \frac{\mu_w}{(2\xi)^{1/2}} - \frac{\rho_e}{\rho} \frac{\mu_e}{(2\xi)^{1/2}} \beta Y \right| \right)^{1/2} \right] \right\}^2 \quad (23)$$

where

$$A_1 = \frac{\rho}{\rho_e} \frac{(2\xi)^{1/2}}{\mu} \left(\frac{L}{r_0}\right)^k, \quad Y = \int_0^\eta (1+t)^{-k} \left(\frac{\rho_e}{\rho}\right) d\eta$$

For two-dimensional and axisymmetric flows, the definition of displacement thickness,  $\delta_k^*$ , used in the outer eddy-viscosity expression is

$$\delta_k^* = \int_0^\infty \left( 1 - \frac{u}{u_e} \right) dy \quad (24)$$

Vol. 2

which, in terms of the transformation defined by Eqs. (16) and (18), becomes

$$\delta_k^* = \frac{(2\xi)^{1/2}}{\rho_e u_e} \left(\frac{L}{r_o}\right)^k \int_0^\infty (1+t)^{-k} \frac{\rho_e}{\rho} (1-f') d\eta \quad (25)$$

(U) It is to be noted that the definition of  $\delta^*$  for axisymmetric flows with transverse-curvature effect is not the same as the definition of  $\delta^*$  for two-dimensional flows. In the former case, the displacement thickness is defined as

$$\delta^* \left(1 + \frac{\delta^*}{2r_o}\right) = \int_0^\infty \left(\frac{r}{r_o}\right) \left(1 - \frac{u}{u_e}\right) dy$$

which can be related to two-dimensional  $\delta^*$  as follows:

$$\frac{\delta^*}{r_o} = -1 + \sqrt{1 + \frac{2\delta_{\text{two-dim}}^*}{r_o}}$$

In the outer eddy-viscosity expression, however, the  $\delta_k^*$  is used as a characteristic length, and its definition remains unchanged from that given by Eq. (24) for either incompressible, compressible, or axisymmetric flows with transverse-curvature effects.

(U) In dimensionless form, the expression for the outer eddy viscosity then becomes

$$\epsilon_o^+ = k_2 \left(\frac{L}{r_o}\right)^k \frac{\rho}{\rho_e} \frac{(2\xi)^{1/2}}{\mu} \left[ \int_0^{\eta_\infty} (1+t)^{-k} \frac{\rho_e}{\rho} (1-f') d\eta \right] \gamma \quad (26)$$

where  $\gamma$ , as defined by Eq. (15), now becomes

$$\gamma = \left\{ 1 + 5.5 \frac{\left[ \int_0^{\eta} (1+t)^{-k} \frac{\rho_e}{\rho} d\eta \right]^6}{\left[ \int_0^{\eta_\infty} (1+t)^{-k} \frac{\rho_e}{\rho} d\eta \right]^6} \right\}^{-1}$$

## FLUID PROPERTIES

(U) Fluid properties that appear in the momentum and energy equations are density ( $\rho$ ), viscosity ( $\mu$ ), specific heat at constant pressure ( $c_p$ ), and thermal conductivity ( $\lambda_\ell$ ). The latter appears in the energy equation through the laminar Prandtl number,  $Pr$ , defined as  $Pr = \mu c_p / \lambda_\ell$ .

(U) The present method is developed so that arbitrary fluid properties may be used. In other words, the fluid properties are inputs in the computer program in the form of formulas or tables as functions of temperature. In this study, air is treated as a perfect gas, and the fluid properties  $\mu$  and  $\rho$  are assumed to be functions of specific enthalpy only; the specific heat of air at constant pressure,  $c_p$ , is assumed to be constant and equal to  $6035 \text{ ft}^2/\text{sec}^2 \text{ }^\circ\text{R}$ . The viscosity  $\mu$  is obtained from Sutherland's law expressed as

$$\frac{\mu}{\mu_\infty} = \left( \frac{h}{h_\infty} \right)^{3/2} \frac{h_\infty + 1.19493 \times 10^6}{h + 1.19493 \times 10^6} \quad (27)$$

The density-enthalpy relation is obtained from the equation of state and from the assumption that static pressure remains constant within the boundary layer. Prandtl number is an input to the computer program.

## METHOD OF SOLUTION

## SOLUTION OF THE MOMENTUM EQUATION

(U) Before we solve Eqs. (19) and (20) by an implicit finite-difference method, we first linearize Eq. (19). Introducing a translated stream function  $\varphi$  defined by  $\varphi = f - \eta$  and replacing the streamwise derivatives by three-point finite-difference formulas at  $\xi = \xi_n$ , which permits arbitrary spacing in the  $\xi$ -direction, we get

$$\begin{aligned} [(1+t)^{2k} c(1+\epsilon^+) \varphi'']' + (\varphi + \eta) \varphi'' + \beta [(\rho_e/\rho) - (\varphi')^2 - 2\varphi' - 1] \\ = 2\xi [( \varphi' + 1)(A_1 \varphi' + A_2 \varphi'_{n-1} + A_3 \varphi'_{n-2}) \\ - \varphi''(A_1 \varphi + A_2 \varphi_{n-1} + A_3 \varphi_{n-2})] \quad (28) \end{aligned}$$

where for simplicity, the subscript  $n$  is dropped. At  $\xi = \xi_n$ , the quantities  $A_1$ ,  $A_2$ , and  $A_3$  are the usual Lagrangian interpolation formulas and are known, and the quantities having the subscripts  $n-1$  and  $n-2$  are known functions of  $\eta$  from solutions obtained at the two previous stations. Thus, at  $\xi = \xi_n$ , Eq. (28) is an ordinary differential equation in  $\eta$ . There is no problem of starting the solution, because the terms with streamwise derivatives disappear, since  $\xi = 0$ . At the next station,  $\xi_1$ , the three-point formulas are replaced by

two-point formulas; at all stations farther downstream the three-point formulas are used.

(U) To linearize Eq. (28), we assume that certain terms that make the equation nonlinear are known from the previous iteration; that is,

$$\begin{aligned} [(1+t)^{2k} C_o (1+\epsilon^+) \phi''']' + (\phi_o + \eta) \phi'' + \beta[(\rho_e/\rho)_o - \phi_o' \phi' - 2\phi' - 1] \\ = 2\xi[(\phi_o' + 1)(A_1 \phi' + A_2 \phi'_{n-1} + A_3 \phi'_{n-2}) \\ - \phi_o''(A_1 \phi + A_2 \phi_{n-1} + A_3 \phi_{n-2})] \quad (29) \end{aligned}$$

The subscript  $o$  indicates that the function is obtained from a previous iteration.

(U) The solution of Eq. (29) is obtained by an implicit finite-difference method after the dependent variable  $\phi$  has been replaced by the perturbation terms  $\overline{\Delta\phi} = \phi - \phi_o$ ,  $\overline{\Delta\phi}' = \phi' - \phi_o'$ , etc.\* A finite-difference pattern in the shape of a horizontal T involving three points in the  $\xi$ -direction and five points in the  $\eta$ -direction is used. See Fig. 3. The resulting algebraic equations are solved by the Choleski matrix method.

#### SOLUTION OF THE ENERGY EQUATION

(U) The method of solution of the energy equation is similar to that of the momentum equation. Again the  $\xi$ -derivatives are replaced by finite-difference formulas that are identical to those in the momentum equation. The energy equation is solved by an implicit finite-difference method. However, this time the five points in the  $\eta$ -directions are replaced by three points because the energy equation is of second order.

(U) For details of the solutions of both the momentum and the energy equations see Ref. 9.

#### VARIABLE-GRID SPACING IN THE $\eta$ -DIRECTION

(U) The finite-difference formulas used in both the momentum and the energy equations contain a variable grid in the  $\eta$ -direction, which permits shorter steps close to the wall and longer steps away from the wall. The grid has the property that the ratio of lengths of any two adjacent intervals is a constant; that is,  $\Delta\eta_i = K\Delta\eta_{i-1}$ . The distance to the  $i$ -th grid line is given by the following formula:

$$\eta_i = h_1 \frac{K^i - 1}{K - 1} \quad i = 0, 1, 2, 3, \dots N \quad (30)$$

\*The reason for choosing  $\phi$  rather than  $f$ , and  $\overline{\Delta\phi}$  rather than  $\phi$ , is that the round-off errors are reduced.

where  $h_1$  is the length of the first step and  $i = N$  when  $\eta_i = \eta_\infty$ . Figure 4 accurately represents the  $\eta$ -spacing for  $\eta_\infty = 100$ ,  $h_1 = 0.01$  and  $K = 1.07$ .

#### STARTING THE SOLUTION

(U) The present method handles both incompressible and compressible laminar and turbulent flows. The calculations begin at the leading edge or at the stagnation point, where  $\xi = 0$ , and proceed downstream. At station  $\xi = 0$ , the flow is laminar, and it becomes turbulent at any specified station where  $\xi > 0$  allowing  $\epsilon^+$  to become nonzero. A calculation can also be started at any  $\xi$ -location, provided that initial velocity and enthalpy profiles are specified. Of course, for incompressible flows with no heat transfer it is only necessary to specify the velocity profile.

(U) Consider the case when initial velocity and enthalpy profiles are known at  $\xi = \xi_{n-1}$  and we seek a solution to momentum and energy equations at  $\xi = \xi_n$ . We first calculate the fluid properties from the enthalpy profiles at  $\xi = \xi_{n-1}$  and start the computations from the momentum equation. Before the momentum equation can be solved, it is necessary to establish the inner and outer regions for the eddy-viscosity formulas. Since the eddy-viscosity expressions contain terms like  $f''$  and  $\delta^*$ , these two regions are not known until a solution of the momentum equation is generated. Thus, an iteration process is necessary. For the first iteration,  $\delta^*$  and  $f''$  are obtained from the solution at  $\xi_{n-1}$ , and inner and outer regions are established by the continuity of the eddy-viscosity equations. With this information a solution of the momentum equation is obtained and consequently a solution of the energy equation. Then fluid properties are obtained for that particular solution, inner and outer regions for the eddy-viscosity formulas are established and the momentum and energy equations are solved in succession. An iteration procedure based on the convergence of  $\delta^*$  and  $f''_w$  is used\*. Figure 5 shows the flow diagram at  $\xi = \xi_n$ .

(U) It is important to note that as the calculations proceed downstream, the boundary-layer thickness increases. Since at  $\xi = \xi_n$  the initial values of  $f$  and its derivatives are obtained from the values at  $\xi = \xi_{n-1}$ , it is necessary to make an assumption for these values for  $\eta > (\eta_\infty)_{n-1}$ , where  $(\eta_\infty)_{n-1}$  is the transformed boundary-layer thickness at  $\xi = \xi_{n-1}$ . For this reason, at  $\xi = \xi_n$  the values of  $f$  and its derivatives are obtained from  $\xi = \xi_{n-1}$  up to  $\eta = (\eta_\infty)_{n-1}$ . For  $\eta > (\eta_\infty)_{n-1}$ ,  $f$  is obtained from  $f = [\eta - (\eta_\infty)_{n-1} + f_{n-1}(\eta_\infty)]$ ,  $f'$  is assumed to be unity, and  $f''$  and  $f'''$  are assumed to be zero (see Fig. 6). The latter assumption is permissible, since  $f''$  and  $f'''$  approach zero as  $\eta \rightarrow \eta_\infty$ .

\*For laminar flows, the convergence criterion is based only on  $f''_w$ .

ACCURACY OF THE NUMERICAL METHOD

(U) The ultimate test of a numerical method is a comparison of calculated results with exact solutions and with experiments. For laminar flows there are many analytically obtained solutions as well as solutions obtained by well-tested and well-established numerical methods. On the other hand, there are no exact solutions for turbulent flows, and all one can do is to compare the calculated results with experiments. Since the turbulent boundary-layer equations must contain some empiricism in them because of the fluctuation terms, it is necessary to establish the accuracy of a numerical method before one can investigate the validity of the assumptions made for the fluctuation terms. In addition, it is quite useful to study the characteristics of the numerical method, such as computation speed, rate of convergence, etc.

(U) Such a study has been made for the present method in Ref. 9. Various incompressible and compressible laminar flows, and incompressible turbulent flows have been calculated by this method, and comparisons with exact solutions, numerical solutions, as well as experimental flows have been made. In all cases, the method was found to be completely accurate for both laminar and turbulent flows. The investigation showed also that the computation time was very small. In general, a typical flow, either laminar or turbulent, consists of about twenty x-stations. The computation time per station is about one second for an incompressible laminar flow and about two to three seconds for an incompressible turbulent flow on the IBM 360/65. Solution of energy equation in either laminar or turbulent flows increases the computation time about one second per station. For further details, such as effect of  $\Delta\xi$  and  $\Delta\eta$ -spacings on the computation time, accuracy, rate of convergence, see Ref. 9.

COMPARISONS OF CALCULATED AND EXPERIMENTAL RESULTS

(U) In this section we present comparisons of calculated and experimental results for several incompressible and compressible turbulent flows obtained by the present method discussed in the previous sections. It should be pointed out that these comparisons are just a few of the many flows investigated by this method, and the reader should see Refs. 2, 6, 10, 11, and 12 for further comparisons.

## INCOMPRESSIBLE FLOWS WITH NO HEAT TRANSFER

## TWO-DIMENSIONAL FLOWS

(U) A large number of two-dimensional turbulent flows, such as flat-plate flows, equilibrium flows in favorable and in adverse pressure gradients, and nonequilibrium and separating flows, have been calculated by this method. The results were presented at the special symposium held at Stanford in August 1968. In most of these flows, the agreement between calculation and experiment was quite satisfactory (see Refs. 2 and 12). Here we present a comparison of calculated results with experiment for flat-plate flows with and without mass transfer.

(U) Figure 7a shows a comparison of local skin-friction coefficients calculated by the present method and those calculated by the Prandtl-Schlichting formula (Ref. 13) for a flat-plate flow,

$$c_f = (2 \log_{10} R_x - 0.65)^{-2.3} \quad (31)$$

as well as experimental values and Coles' line (Ref. 14). The experimental values are taken from Ref. 14. Figure 7b shows a comparison of calculated results with experiment and with those given by the universal logarithmic velocity

$$\frac{u}{u^*} = 5.75 \log_{10} \frac{yu^*}{\nu} + 5.10 \quad (32)$$

at  $R_x = 10^6$  and  $10^7$ . Figure 7c shows a comparison of calculated results with experiment and with those given by the logarithmic velocity distribution (Ref. 14),

$$\frac{u_e - u}{u^*} = 2.80 - 5.75 \log_{10} \left( 4.05 \frac{y}{\delta^*} \frac{u^*}{u_e} \right) \quad (33)$$

at  $R_x = 10^6$  and  $10^7$ . Figure 7d shows a comparison of calculated and experimental results for Klebanoff's data (Ref. 14) at  $R_\delta = 77,000$ .

(U) The method has also been used to compute flows with mass transfer. Figure 8 shows the results for two uniform blowing rates,  $v_w/u_e = 0.001$  and  $0.002$ , for the boundary layer measured by Mickley and Davis [15], and Fig. 9 shows the results for two uniform suction rates,  $v_w/u_e = -0.00312$  and  $-0.00429$ , for the boundary layer measured by Tennekes [16]. The agreement in both cases is quite satisfactory.

## AXISYMMETRIC FLOWS WITH TRANSVERSE-CURVATURE EFFECTS

(U) When the radius of a body in a viscous flow is of the same order of magnitude as the thickness of the boundary layer, the transverse curvature effect becomes quite important and strongly affects

## Vol. 2

the skin friction and heat transfer. Extensive analytical study of the TVC effect has been made for laminar flows, but not much work has been done for turbulent flows. In Ref. 17, Landweber investigated the TVC effect by using the 1/7th-power-law velocity profile and the Blasius skin-friction law. Using the momentum integral equation, he found that, at a given value of momentum-thickness Reynolds number, skin friction on the cylinder was greater than that on a flat plate and that the boundary-layer thickness was correspondingly smaller. In Ref. 18, Richmond reported an experimental investigation of axisymmetric boundary layers. He measured the velocity profiles on various slender cylinders and estimated the skin friction by the "streamlines hypothesis" of Coles [19]. In Ref. 20, Yasuhara described experiments on an axisymmetric boundary layer along a 20mm-diameter, 1750mm-long cylinder, to investigate the TVC effect on the velocity profile. He measured velocity profiles in laminar, transition, and turbulent regions. His laminar velocity profiles agreed fairly well with theory. When he plotted his turbulent velocity profiles in the law-of-the-wall coordinates used by Richmond, he observed that, as the boundary-layer thickness increased relative to the body radius, the profile near the outer layer tended to bend down relative to the line of the logarithmic-wall law. This was caused by the TVC effect. Recently, Rao [21] extended Coles' law of the wall to thick, axisymmetric turbulent boundary layers in which the sublayer thickness is comparable to the radius of transverse curvature. He showed that the law of the wall very close to the wall can be expressed in the form

$$\frac{u}{u^*} = \frac{u^* a}{\nu} \ln \frac{r}{a} \quad (34)$$

rather than by the linear relation  $u/u^* = yu^*/\nu$  of two-dimensional flow or by the form  $u/u^* = yu^*/\nu (1 + y/2a)$  used by Richmond. He stated that at small values of  $R_a = u_e a/\nu$  there was a 50-percent difference between the value of  $c_f$  obtained by Richmond with the streamline hypothesis and the value obtained by Eq. (34).

(U) The same kind of flow has been computed by the present method [10]. Figures 10 and 11 show a comparison of calculated and experimental velocity profiles for the boundary layer measured by Richmond. Figure 12 shows a comparison of calculated and experimental law-of-the-wall profiles in the axisymmetric turbulent boundary layers. Figure 13 shows a comparison of calculated and experimental velocity profiles for the boundary layer measured by Yasuhara. The results indicate that the present method is quite accurate, as it was in two-dimensional flows.

## INCOMPRESSIBLE FLOWS WITH HEAT AND MASS TRANSFER

(U) The results obtained by the present method for two-dimensional incompressible flows with heat transfer are described in Ref. 2. These flows consist of flat-plate flows with heating and cooling, as well as

flows in both favorable and adverse pressure gradients with cooling. Some of the comparisons are presented here.

(U) The local Stanton number is defined as

$$St = \frac{-q_w}{\rho_e u_e (H_e - H_w)} \quad (35)$$

which, in terms of transformed variables can be written as

$$St = \left(\frac{r_0}{L}\right)^k \left(\frac{C}{Pr}\right)_w \frac{\mu_e}{(2\xi)^{1/2}} \left(\frac{g'_w}{1 - g_w}\right) \quad (36)$$

#### FLAT-PLATE FLOWS

(U) Figure 14 shows a comparison of local Stanton numbers and velocity profiles on an isothermal, heated flat plate measured by Reynolds, Kays, and Kline [22]. In the calculations, the laminar Prandtl number was assumed to be 0.70. Figure 15 shows the computed local Stanton numbers, together with the experimental values obtained by Reynolds, Kays, and Kline [23], for a step variation of wall temperature.

#### ACCELERATING FLOWS

(U) Figures 16 and 17 show the results obtained for two accelerating flows. These flows were measured by Moretti and Kays [24]. In the calculations, the experimental temperature difference between wall and free stream,  $\Delta t(x)$ , and the velocity distribution,  $u_e(x)$ , were used as in Ref. 24. This is the reason for the small oscillations that appear in the calculated values of Stanton number.

#### DECELERATING FLOWS

(U) Figure 18 shows a comparison of computed local Stanton numbers and experimental values for the decelerating flow measured by Moretti and Kays [24], together with the experimental streamwise variations of  $\Delta t(x)$  and  $u_e(x)$ . Again, the agreement is quite satisfactory.

#### FLAT-PLATE FLOWS WITH HEAT AND MASS TRANSFER

(U) Several examples of incompressible turbulent flow with heat and mass transfer (suction and blowing) have been computed by the present method. Figure 19 shows a typical comparison. The experimental data is due to Moffat and Kays [25].

COMPRESSIBLE FLOWS WITH NO HEAT TRANSFER

(U) A large number of two-dimensional compressible turbulent flows with no heat transfer have been calculated by the present method. The results are reported in Ref. 11. Because of the scarcity of experimental data with pressure gradients, most of the experimental data considered in that reference were for flat-plate flows covering a range of Mach numbers up to 5. Only one two-dimensional accelerating flow and one axisymmetric flow with and without transverse-curvature effect were considered.

FLAT-PLATE FLOWS

(U) Figure 20 shows comparisons of calculated and experimental velocity profiles, Mach profiles, and local skin-friction coefficients for the boundary layer measured by Coles [26]. Skin-friction coefficients were measured by the floating-element technique.

(U) Figure 21 shows a comparison of local skin-friction values for the boundary layer measured by Moore and Harkness [27] at a nominal Mach number of 2.8. The results indicate good agreement even for very high Reynolds numbers. The experimental skin friction was obtained by the floating-element technique.

ACCELERATING FLOWS

(U) Figure 22 shows the results for an accelerating flow measured by Pasiuk et al [28]. Calculations were started by assuming an adiabatic flat-plate flow that matched the experimental momentum-thickness value at  $x = 0.94$  feet. Then the experimental Mach number distribution was used to compute the rest of the flow. The edge Mach number varied from  $M_e = 1.69$  at  $x = 0.94$  feet to  $M_e = 2.97$  at  $x = 3.03$  feet. Figure 22a shows a comparison of calculated and experimental values of displacement thickness and momentum thickness, together with a comparison of calculated local skin-friction values with those obtained from the momentum integral equation by using the experimental data. Figures 22b and 22c show a comparison of calculated and experimental velocity and temperature profiles, respectively, for three x-stations. The agreement, except in skin friction, is quite satisfactory.

AXISYMMETRIC FLOWS WITH AND WITHOUT TRANSVERSE-CURVATURE EFFECTS

(U) Figure 23 shows the results for a waisted body of revolution measured by Winter, Smith, and Rotta [29] for two Mach numbers,  $M_e = 0.6$  and 1.4. The experimental skin-friction values were obtained by the "razor blade" technique. The calculations were started by using the experimental velocity profile at  $x/L = 0.4$ . The enthalpy profile at  $x/L = 0.4$  was obtained from the energy equations by using the experimental velocity profile at the same x-location. Calculations were made with and without transverse-curvature effects.

(U) Figures 23a and 23b show that the calculated skin-friction values are in good agreement with experiment. Although the calculated skin-friction values without the TVC effect agree quite satisfactorily with the experimental values, the agreement is even better with the TVC effect. The results also show that the effect of transverse curvature markedly affects the momentum-thickness values. Without this TVC effect, the calculated  $\theta$ -values deviate considerably from the experimental values, especially at locations where the radius of the body is quite small, for example, when  $x/L = 0.6$  to  $0.8$ . With the TVC effect, the agreement in  $\theta$  is much better. It is also interesting to note that the computed  $\theta$ -values without the TVC effect agree quite well with the calculated  $\theta$ -values reported in Ref. 29, which indicates the importance of transverse-curvature effect.

#### SUMMARY OF SKIN-FRICTION RESULTS

(U) Figure 24 shows a comparison of calculated and experimental skin-friction coefficients for the compressible adiabatic turbulent flat-plate flows reported in Ref. 11. The experimental skin-friction values were all measured by the floating-element technique, except for those obtained by Kistler [30], which were obtained from velocity profiles. The calculated values cover a Mach number range of 0.41 to 4.67 and a momentum-thickness Reynolds number range of  $1.6 \times 10^3$  to  $702 \times 10^3$ . The rms error based on the 43 experimental values examined, all obtained by the floating-element technique, is 3.5 percent, which is well within the experimental scatter.

(U) Figure 25 shows a comparison of the ratio of calculated and experimental compressible skin-friction coefficient to its incompressible value at the same  $x$  Reynolds number as a function of Mach number, together with the Spalding-Chi correlation [31]. The incompressible skin-friction values were obtained from Ref. 14. The calculated and experimental skin-friction ratios compare quite well. It is remarkable that when the calculated values deviate from the Spalding-Chi correlation the experimental values also do.

#### COMPRESSIBLE FLOWS WITH HEAT TRANSFER

(U) Although the present method has been well explored for compressible adiabatic flows, it has not been sufficiently explored for compressible flows with heat transfer and mass transfer or both. This is now being done, and the results will be reported later.

(U) Figure 26 shows a comparison of calculated Stanton numbers and average skin-friction values for the flat-plate boundary layer measured by Pappas [32]. The calculations are made for a Mach number of 2.27 and for a wall-to-edge temperature ratio of 2.19. The agreement is quite good.

DISCUSSION

(U) A numerical solution of the turbulent-boundary-layer equations based on a particular eddy-viscosity formulation and the assumption of a constant turbulent Prandtl number is presented for various incompressible and compressible flows with and without heat and mass transfer. Many flows computed by this method show that the method is quite satisfactory for incompressible flows with and without heat transfer and for compressible adiabatic flows. In addition, the computation time is quite small. It is remarkable that a simple eddy-viscosity formulation based on flat-plate data can give such satisfactory results\*.

(U) In principle, the present method is similar to the ones used by Herring and Mellor [33] and by Patankar and Spalding [34]. The main difference between them lies in the eddy-viscosity expression used for each region, as well as the assumptions for the turbulent Prandtl number. Also, the transformations used to stretch the coordinates normal to the flow direction, as well as the numerical method used to solve the boundary-layer equations, are considerably different. The method of Herring and Mellor and the present method can handle mass transfer; the method of Patankar and Spalding can not. This is due to the use of the Couette-flow assumption, which was used to overcome difficulties with solutions in the region near the wall, where the dependent variables and exchange coefficients vary considerably.

(U) The present method has the advantage of being applicable to both laminar and turbulent flows. Since a flow always has a laminar portion if it starts from a stagnation point, such an advantage is particularly useful. The present method utilizes the upstream history as the calculations proceed downstream. At any station, a laminar profile can be obtained by merely setting the eddy-viscosity term in Eq. (19) equal to zero.

(U) Although it is hard to say to what minimum Reynolds numbers the present eddy-viscosity formulation holds true, the results for incompressible flat-plate flows indicate that for  $R_0$ -values as small as 1000 the calculated results agree quite well with experiment. For compressible adiabatic flows, the results have been checked with experiment to  $R_0$ -values as low as 1600 and again the agreement was good.

(U) It is interesting to note that the present eddy-viscosity formulation accounts quite well for the compressibility effect, at least within the Mach number range considered, 0 to 5. Figure 27 shows a comparison of two calculated velocity profiles at the same  $R_0$ , one for incompressible and the other for compressible flow. Because of the compressibility effect, the difference between the two profiles is quite appreciable, and eddy viscosity accounts very well for this effect.

\*It should be pointed out that the present method also has the advantage that various other formulations of eddy-viscosity or turbulent Prandtl number can be used with very little change in the basic method.

(U) On the basis of comparisons involving various flows, the present method appears to be as accurate and as satisfactory as the method of Bradshaw and Ferriss [35]. The latter method differs from the present method in that it involves a solution of the turbulence kinetic energy, the mean momentum equation, the continuity equation and the instantaneous temperature equation by making certain assumptions about the turbulence terms appearing in these equations.

(U) The results also point out several advantages of the present method over the methods that use momentum and/or energy integral equations. Because of their simplicity and their short computation times, the latter methods are quite popular. Some of them can also be quite accurate, at least, for two-dimensional incompressible turbulent flows, as was shown in a special conference on "Prediction Methods for Turbulent Flows" held at Stanford University in August 1968. However, the disadvantages of these methods are that they cannot be readily extended to many important problems such as axisymmetric flows with and without transverse-curvature effects, flows with heat and mass transfer, flows with slip at the wall, etc. On the other hand, the present method eliminates many of the disadvantages of these momentum integral-type methods by proceeding to solve the full partial-differential equations. Although the computation time of the present method is still more than that of an integral method, the difference is small and is not a major factor.

(U) Needless to say, much work remains to be done in this very important area of fluid mechanics. The present method has been explored quite extensively for incompressible flows with and without heat transfer and for compressible adiabatic flows, but it has not been explored enough for compressible flows with heat transfer. Furthermore, the method needs to be explored for flows with heat and mass transfer. It should be pointed out that, although the present method predicts the flow separation quite accurately, it does not calculate the velocity profiles satisfactorily close to separation. This is to be expected from the eddy-viscosity formulation used in the present method, as well as the ones used by Herring and Mellor and by Spalding and Patankar. According to this formulation, the boundary layer is regarded as a composite layer characterized by inner and outer regions. In the inner region, an eddy viscosity based on Prandtl's mixing-length theory is used (see Eq. (10)); in the outer region, a constant eddy viscosity modified by an intermittency factor is used (see Eq. (14)). The latter can also be shown to be equivalent to

$$\epsilon_0 = l_2^2 \left| \frac{\partial u}{\partial y} \right|, \quad (37)$$

where  $l_2$ , the mixing length, can be taken equal to 0.075 $\delta$ , which is recommended in Ref. 36. Since the continuity of eddy viscosity is being used

$$\epsilon_i = \epsilon_0 \quad (38)$$

or

$$k_1^2 = k_2^2 \quad (38)$$

Neglecting the exponential term in the inner eddy-viscosity formula, we can write Eq. (38), as

$$(0.4y)^2 = (0.075\delta)^2$$

or

$$\frac{y}{\delta} = \frac{0.075}{0.40} = 0.1875 \quad (39)$$

This means that the switching point between the inner and outer regions is fixed. Since when the flow approaches separation conditions the outer region moves toward the wall, the  $y/\delta$  ratio should not be a constant and must be decreasing. Keeping it a constant (approximately), as the present eddy-viscosity formulation does, limits the accuracy of calculation of velocity profiles close to separation. Therefore, further work should be done in the eddy-viscosity formulation, to remedy the situation.

## NOMENCLATURE

a	cylinder radius
$c_f$	local skin-friction coefficient, $\tau_w/(1/2)\rho_e u_e^2$
$\bar{c}_f$	average skin-friction coefficient
$c_p$	specific heat at constant pressure
C	viscosity-density parameter, $\rho\mu/\rho_e\mu_e$
f	dimensionless stream function, see Eq. (18)
g	dimensionless total enthalpy ratio, $H/H_e$
h	specific enthalpy
H	total enthalpy, $h + u^2/2$
k	flow index, =0(two-dim. flow) and = 1(axisym. flow)
$k_1, k_2$	constant in eddy-viscosity formulas
K	variable-grid parameter, see Eq. (30)
l	mixing length
L	reference body length
M	Mach number
p	pressure

Pr	Prandtl number, $\mu c_p / \lambda_l$
q	local heat-transfer rate per unit area
r	radial distance from axis of revolution
$r_0$	body radius
R	transverse-curvature parameter, $R_x(r_0/x)^2/4$
$R_x$	Reynolds number, $u_e x / \nu_e$
$R_\delta$	Reynolds number, $u_e \delta / \nu_e$
$R_\theta$	Reynolds number, $u_e \theta / \nu_e$
St	Stanton number
t	transverse curvature term, $(y \cos \alpha) / r_0$
$\Delta t$	temperature difference between wall and free stream, $T_w - T_\infty$
T	absolute temperature
u	x-component of velocity
$u^*$	friction velocity, $(\tau_w / \rho)^{1/2}$
v	y-component of velocity
x	distance along body surface measured from leading edge
y	distance normal to x
$\alpha$	angle between y and r, i.e., slope of body of revolution
$\beta$	velocity-gradient parameter, $2\xi / u_e (du_e / d\xi)$
$\gamma$	intermittency factor
$\delta$	boundary-layer thickness
$\delta^*$	displacement thickness, $\int_0^\infty \left(1 - \frac{\rho u}{\rho_e u_e}\right) dy$
$\epsilon$	kinematic eddy viscosity
$\epsilon^+$	ratio of kinematic eddy viscosity to kinematic viscosity, $\epsilon / \nu$
$\eta$	transformed y-coordinate
$\theta$	momentum thickness, $\int_0^\infty \frac{\rho u}{\rho_e u_e} \left(1 - \frac{u}{u_e}\right) dy$
$\lambda$	thermal conductivity
$\mu$	dynamic viscosity
$\nu$	kinematic viscosity

## 8th Navy Symposium on Aeroballistics

---

### Vol. 2

$\xi$	transformed x-coordinate
$\rho$	mass density
$\tau$	shear stress
$\psi$	stream function

### Subscripts

c	switching point between the inner and outer eddy-viscosity formulas
i	incompressible flow
e	outer edge of boundary layer
l	laminar flow
t	turbulent flow
w	wall
$\infty$	free-stream conditions

primes denote differentiation with respect to  $\eta$

### REFERENCES

1. Douglas Aircraft Company. Progress in Solving the Full Equations of motion of a Compressible Turbulent Boundary Layer, (U), by A.M.O. Smith, N. Jaffe, and R.C. Lind. Long Beach, California, 1966 (Douglas paper No. 3925).
2. Douglas Aircraft Company. A Finite-Difference Solution of the Incompressible Turbulent Boundary-Layer Equations with Heat Transfer, (U), by T. Cebeci and A.M.O. Smith. To be presented at the Eleventh National Heat Transfer Meeting in Minneapolis (August 1969). Long Beach, California, March 1969. (Douglas paper No. 5520).
3. Douglas Aircraft Company. Numerical Solution of the Turbulent Boundary-Layer Equations, (U), by A.M.O. Smith and T. Cebeci. Long Beach, California, May 1967. (Report No. DAC 33735).
4. Journal of Aerospace Science. On Turbulent Flow Near a Wall, (U), by E. R. Van Driest, November 1956. (Vol. 23, No. 11).
5. National Advisory Committee for Aeronautics. Characteristics of Turbulence in a Boundary Layer with Zero Pressure Gradient, (U), by P. S. Klebanoff, July 1954. (NACA TN 3178).
6. Douglas Aircraft Company. Solution of the Boundary-Layer Equations for Incompressible Turbulent Flow, (U), by A.M.O. Smith and T. Cebeci. Long Beach, California, 1968. pages 174-191 (Proceedings of the 1968 Heat Transfer and Fluid Mechanics Institute).

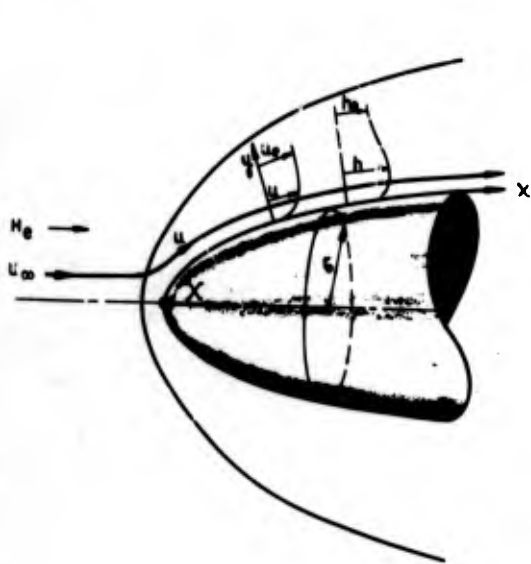
7. Journal of Aero. Sciences. The Transverse-Curvature Effect in Compressible Axially Symmetric Laminar Boundary-Layer Flow, (U), by R.F. Probstein and D. Elliott. March 1956.
8. Academic Press. Hypersonic Flow Theory, (U), by W.D. Hayes and R.F. Probstein. page 290, 1959.
9. Douglas Aircraft Company. A Finite-Difference Method for Calculating Compressible Laminar and Turbulent Boundary Layers. Part I, (U), by T. Cebeci, A.M.O. Smith and L.C. Wang. Long Beach, California, March 1969. (Report No. DAC 67131).
10. Douglas Aircraft Company. Laminar and Turbulent Incompressible Boundary Layers on Slender Bodies of Revolution in Axial Flow, (U), by T. Cebeci, 1968. To be published in the transactions of ASME. (Also Douglas Engineering Paper No. 5524.)
11. Douglas Aircraft Company. Calculation of Compressible Adiabatic Turbulent Boundary Layers, (U), by T. Cebeci, A.M.O. Smith and G. Mosinskis, Long Beach, California. May 1969. To be presented to the AIAA 2nd Fluid and Plasma Dynamics Conference, June 1969. (Also Douglas Engineering Paper No. 5533.)
12. Douglas Aircraft Company. A Finite-Difference Solution of the Incompressible Turbulent Boundary-Layer Equations by an Eddy-Viscosity Concept, (U), by T. Cebeci and A.M.O. Smith. Long Beach, California, October 1968. (Report No. DAC 67130.)
13. McGraw-Hill Company. Boundary-Layer Theory, (U), by H. Schlichting, 1960.
14. Jet Propulsion Laboratory. Measurements in the Boundary Layer on a Smooth Flat Plate in Supersonic Flow. I. The Problem of the Turbulent Boundary Layer, (U), by D. Coles. Pasadena, California, June 1953. (Report No. 20-69.)
15. National Advisory Committee for Aeronautics. Momentum Transfer for Flow Over a Flat Plate with Blowing, (U), by H.S. Mickley and R.S. Davis, November 1957. (NACA TN 4017.)
16. Technological University Delft. Similarity Laws for Turbulent Boundary Layers with Suction or Injection, (U), by H. Tennekes. December 1964. (Report VTH-119.)
17. David Taylor Model Basin. Effect of Transverse Curvature on Frictional Resistance, (U), by L. Landweber. Washington, D.C., 1949. (Report No. 689.)
18. California Institute of Technology. Experimental Investigation of Thick Axially Symmetric Boundary Layers on Cylinders at Subsonic and Hypersonic Speeds, (U), by R. Richmond. Ph.D. Thesis, Pasadena, California, 1957.
19. The Law of the Wall in Turbulent Shear Flow, (U), by D. Coles. 50 Jahre Grenzschichtforschung, 1955. pages 153-163.

## 8th Navy Symposium on Aeroballistics

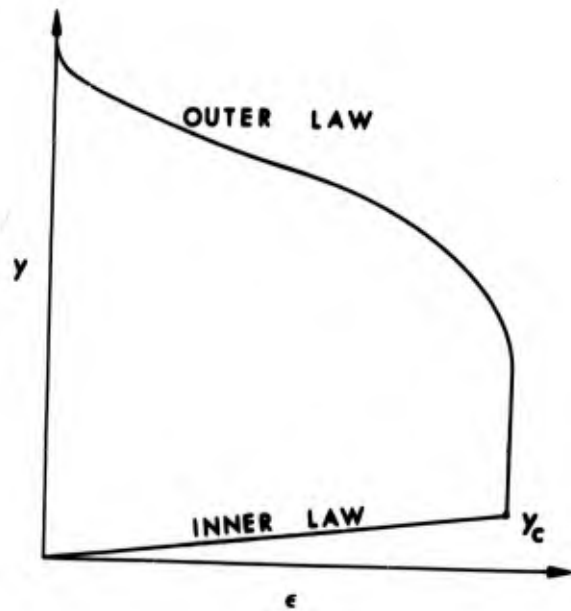
### Vol. 2

20. Experiments of Axisymmetric Boundary Layers Along a Cylinder in Incompressible Flow, (U), by M. Yasuhara. Transactions of the Japan Society of Aerospace Sciences, 1959. Vol. 2, page 33.
21. Journal of Basic Engineering. The Law of the Wall in a Thick Axisymmetric Turbulent Boundary Layer, (U), by G.N.V. Rao. March 1967. pages 237-239.
22. National Aeronautics and Space Administration. Heat Transfer in the Turbulent Incompressible Boundary Layer. I. Constant Wall Temperature, (U), by W.C. Reynolds, W.M. Kays, and S.J. Kline. December 1958. (NASA MEMO 12-1-58W.)
23. National Aeronautics and Space Administration. Heat Transfer in the Turbulent Incompressible Boundary Layer. III. Arbitrary Wall-Temperature Distribution, (U), by W.C. Reynolds, W.M. Kays, and S.J. Kline. December 1958. (NASA MEMO 12-2-58W.)
24. Stanford University. Heat Transfer Through an Incompressible Turbulent Boundary Layer with Varying Free-Stream Velocity and Varying Surface Temperature, (U), by P.M. Moretti and W.M. Kays. (Dept. of Mechanical Engineering Report No. PG-1.)
25. International Journal of Heat and Mass Transfer. The Turbulent Boundary Layer on a Porous Plate: Experimental Heat Transfer with Uniform Blowing and Suction, (U), by R.J. Moffat and W.M. Kays. 1968. Vol. 11, pages 1547-1566.
26. Jet Propulsion Laboratory. Measurements in the Boundary Layer on a Smooth Flat Plate in Supersonic Flow. III. Measurements in a Flat Plate Boundary Layer at the Jet Propulsion Laboratory. California Institute of Technology, Pasadena, Calif., June 1953. (Rept. 20-71.)
27. Ling-Temco-Vought Research Center. Experimental Investigation of the Compressible Turbulent Boundary Layer at Very High Reynolds Numbers. (U), by D.R. Moore and J. Harkness. April 1964. (Rept. O-7100/4R-9.)
28. Experimental Reynolds Analogy Factor for a Compressible Turbulent Boundary Layer with a Pressure Gradient, (U), by L. Pasiuk, S.M. Hastings, and R. Chatham. February 1965. (NOLTR 64-200.)
29. Turbulent Boundary-Layer Studies on a Waisted Body of Revolution in Subsonic and Supersonic Flow, (U), by K.G. Winter, K.G. Smith, and J.C. Rotta. May 1965. (AGARDograph 97, Part I, pages 933-962.)
30. Ballistic Research Labs. Fluctuation Measurements in Supersonic Turbulent Boundary Layers, (U), by A.L. Kistler. Aberdeen Proving Ground, Md., August 1958. (Rept. 1052.)
31. Journal of Fluid Mechanics. The Drag of a Compressible Turbulent Boundary Layer on a Smooth Flat Plate with and Without Heat Transfer, (U), by D.B. Spalding and S.W. Chi. 1964. (Vol. 18, Part I, pages 117-143.)

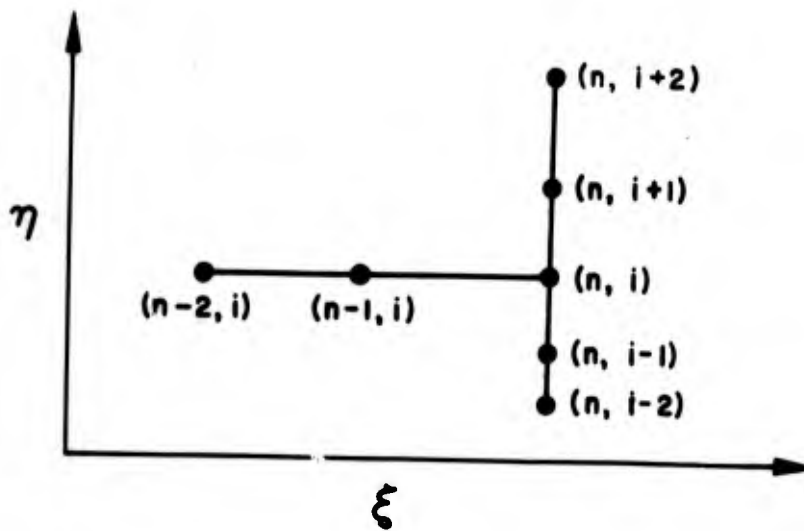
32. National Aeronautics and Space Administration. Measurement of Heat Transfer in the Turbulent Boundary Layer on a Flat Plate in Supersonic Flow and Comparison with Skin-Friction Results, (U), by C.C. Pappas. June 1954. (NASA TN 3222.)
33. National Aeronautics and Space Administration. A Method of Calculating Compressible Turbulent Boundary Layers, (U), by H.J. Herring and G.L. Mellor. September 1968. (NASA CR-1144.)
34. C.R.C. Press. Heat and Mass Transfer in Boundary Layers, (U), S.V. Patankar and D.B. Spalding. Cleveland, Ohio, 1968.
35. National Physical Laboratory. Calculation of Boundary-Layer Development Using the Turbulent Energy Equation. IV. Heat Transfer with Small Temperature Differences, (U), by P. Bradshaw and D.H. Ferriss. Middlesex, England, May 1968. (Aero Rept. 1271.)
36. Imperial College. The Distribution of the Mixing Length in Turbulent Flows Near Walls, (U), M.P. Escoudier. London, 1965. (Mech. Eng. Dept.)



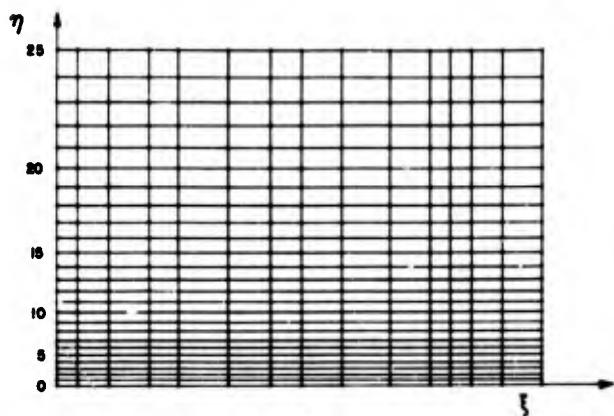
(U) FIG. 1. Coordinate System for the Boundary Layer on a Body of Revolution.



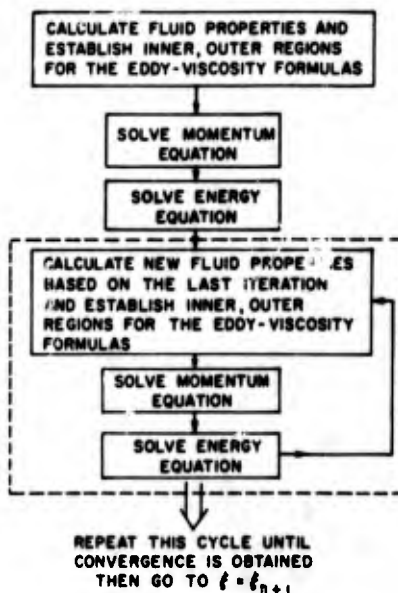
(U) FIG. 2. Typical Eddy-Viscosity Distribution Across a Boundary Layer.



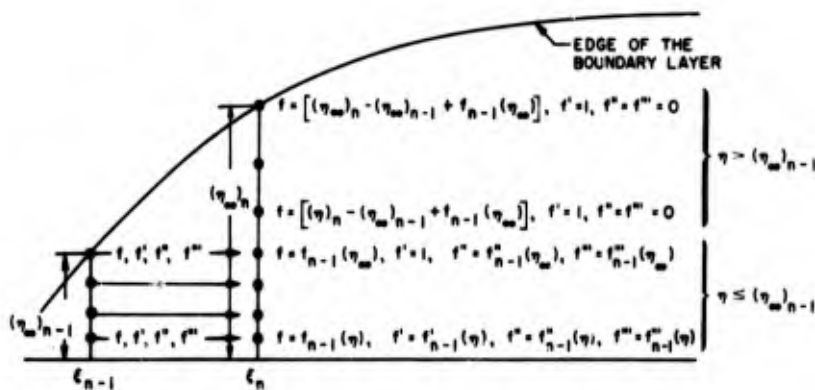
(U) FIG. 3. Finite-Difference Molecule for the Momentum Equation at \$(n, i)\$.



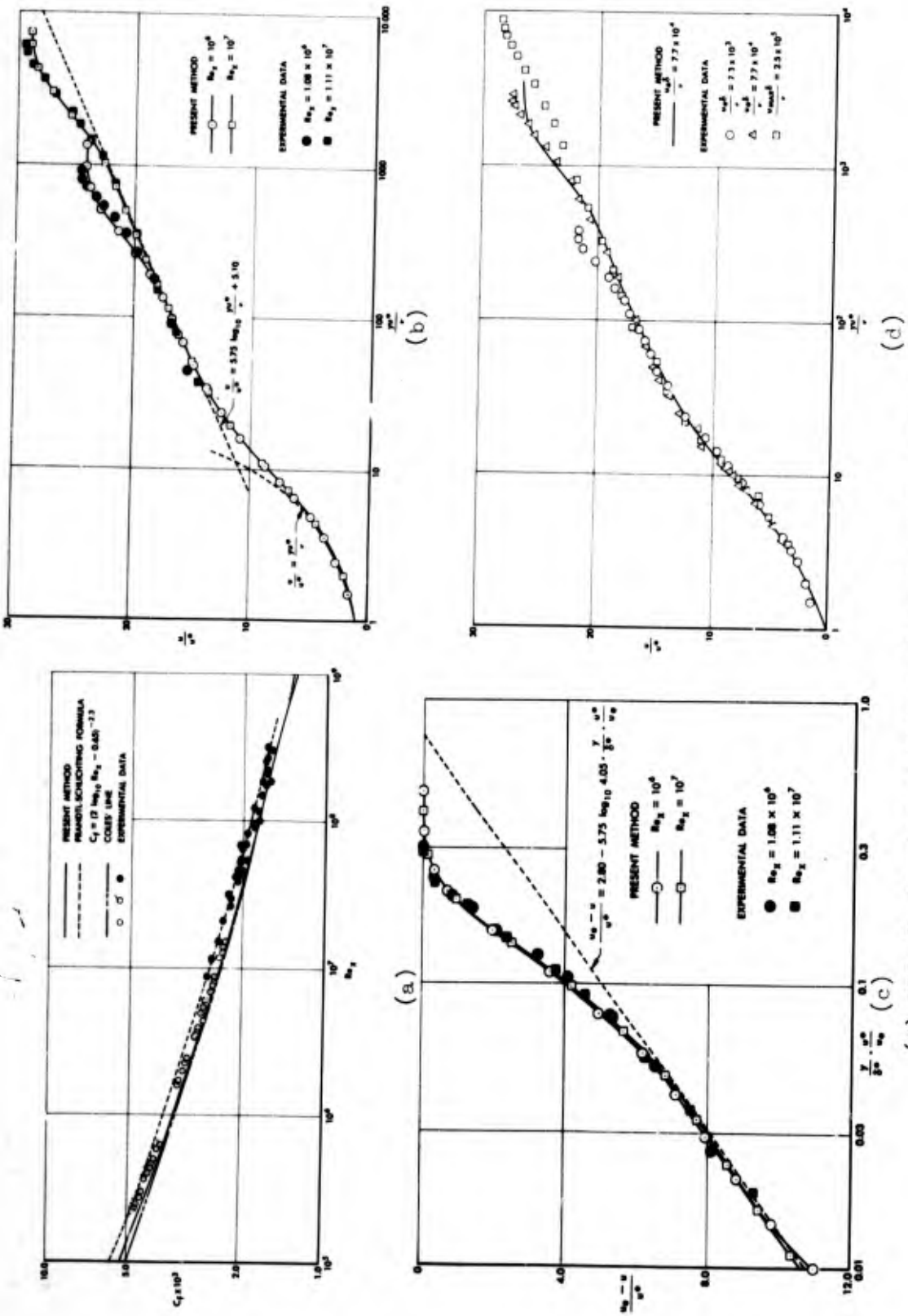
(U) FIG. 4. Finite-Difference Variable-Grid System in the  $\eta$ -Direction.



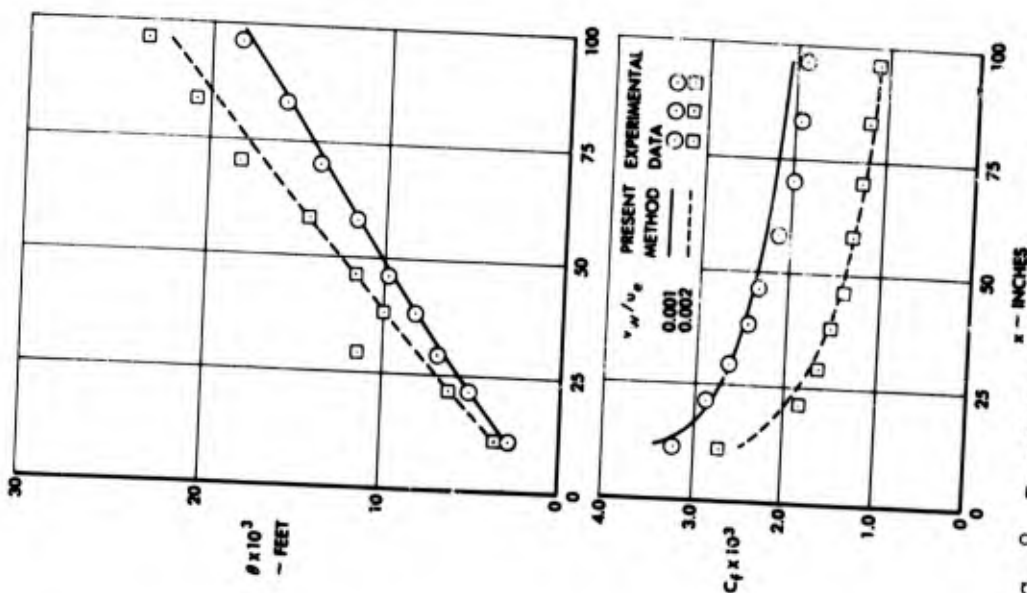
(U) FIG. 5. Flow Diagram for Solving the Boundary-Layer Equations at  $\xi = \xi_n$ .



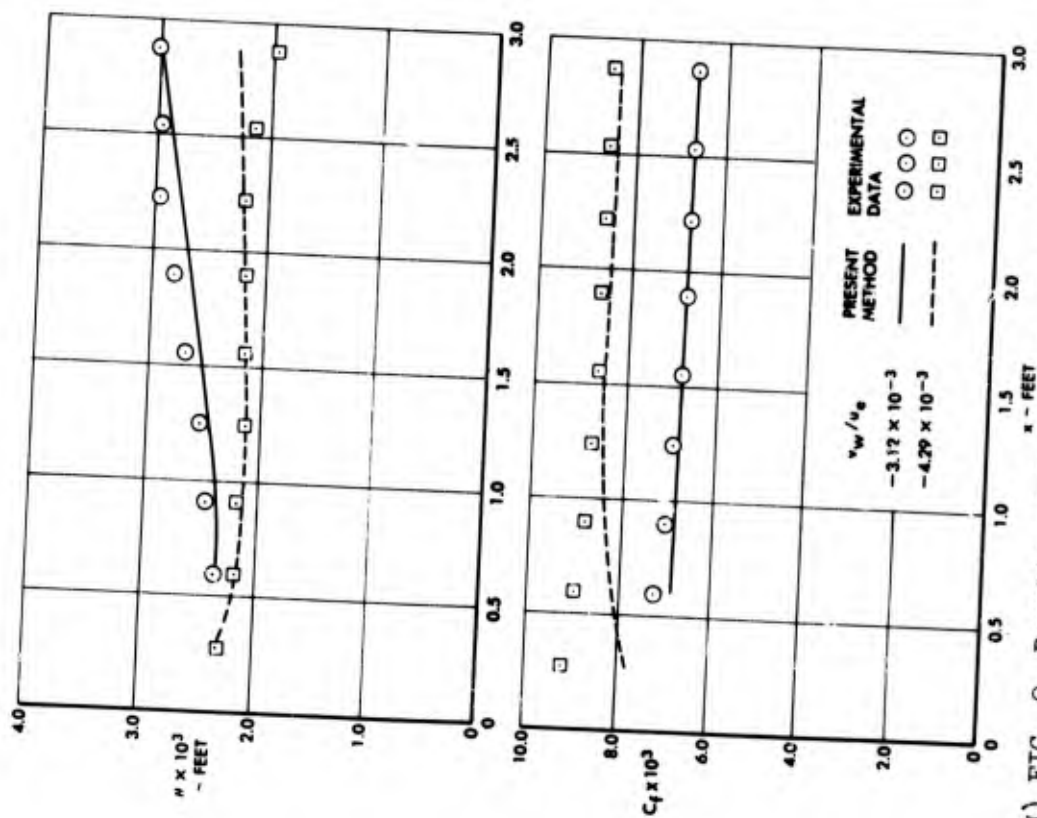
(U) FIG. 6. Diagram Showing the Method of Generating the Initial Coefficients of the Momentum Equation at  $\xi = \xi_n$ .



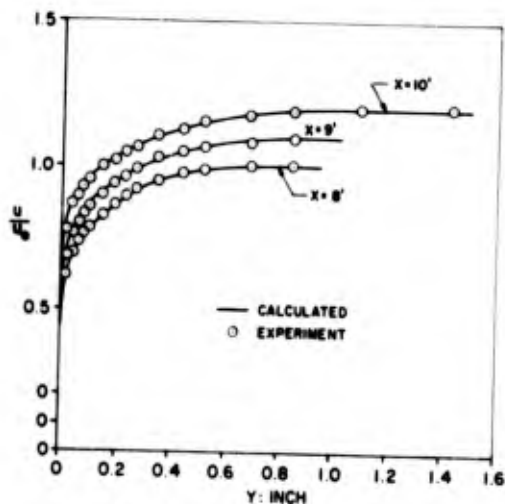
(U) FIG. 7. Results of Calculations for a Flat-Plate Flow.



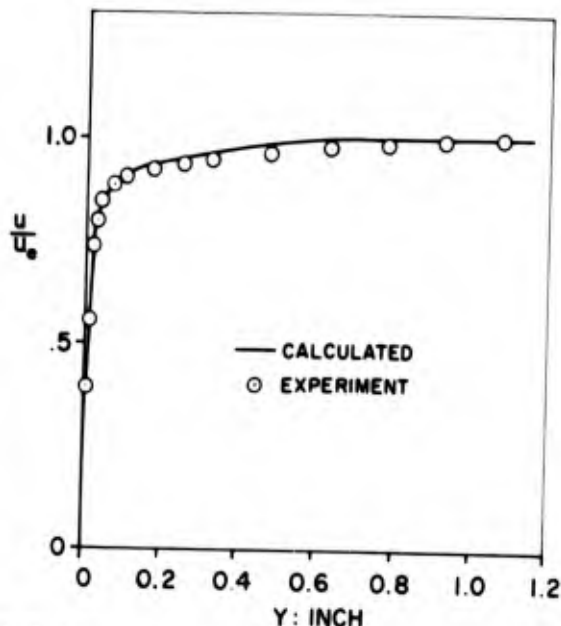
(U) FIG. 8. Results of Calculations for the Flat Plate with Two Uniform Blowing rates,  $v_w/u_e = 0.001$  and  $0.002$ . (Experimental Data of Mickley and Davis).



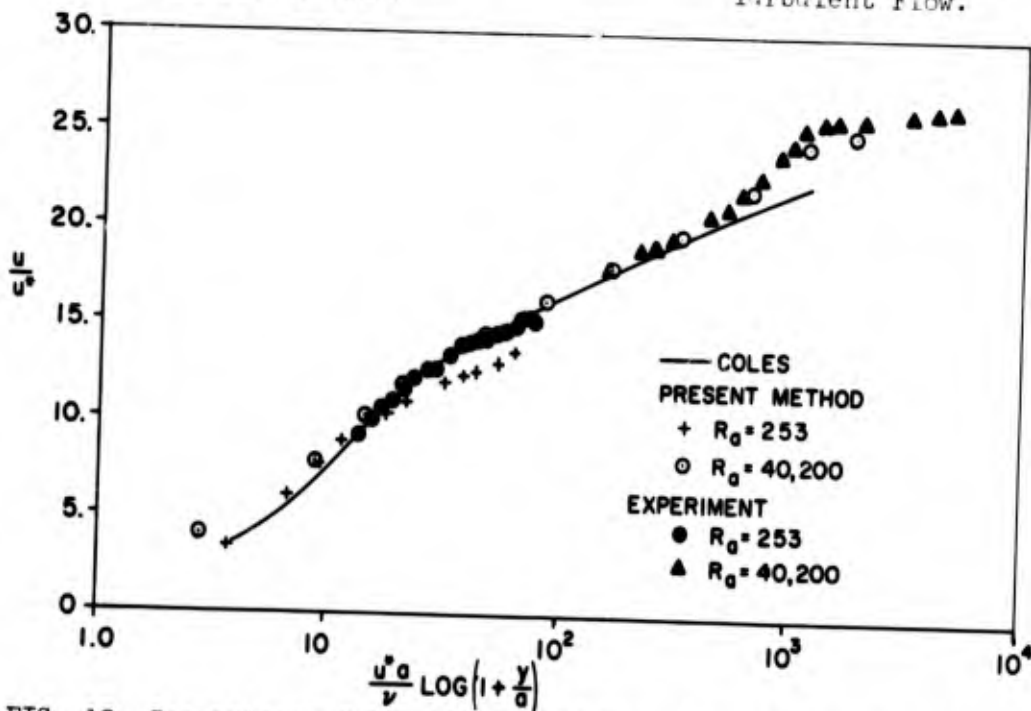
(U) FIG. 9. Results of Calculations for the Flat Plate with Two Uniform Suction Rates.  $v_w/u_e = -0.00312$  and  $-0.00429$ . (Experimental Data of Tennekes).



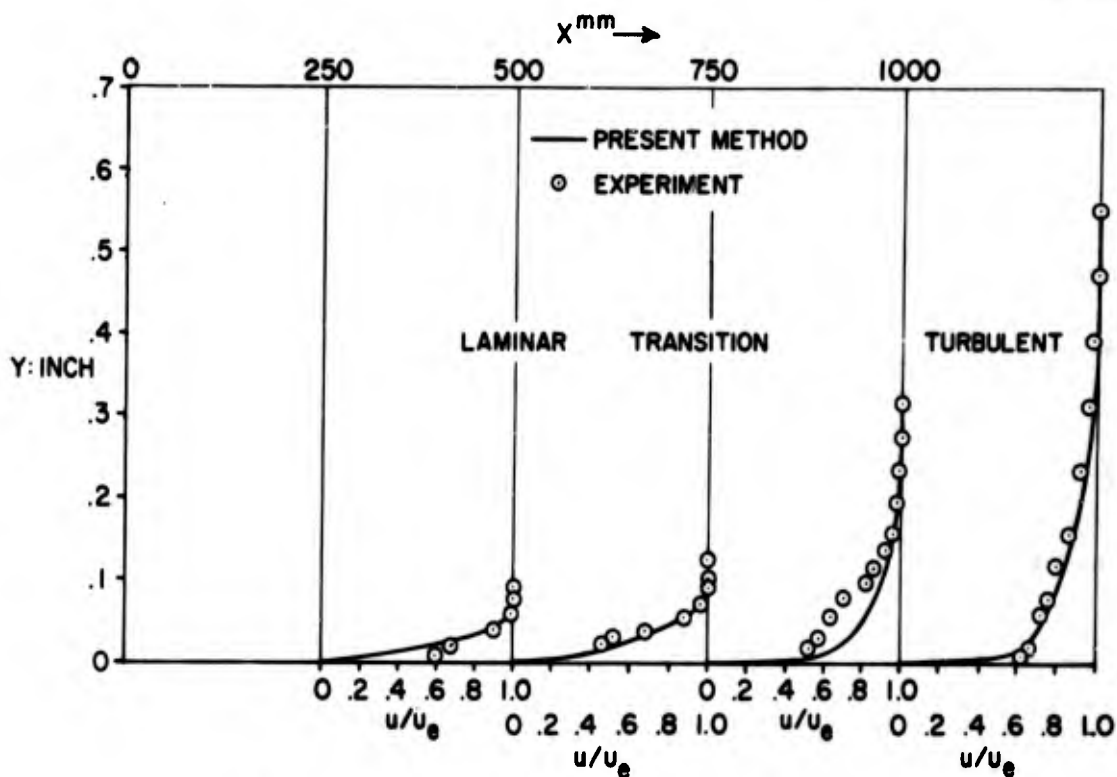
(U) FIG. 10. Comparison of Calculated and Experimental Velocity Profiles on a 2-Inch Diameter Cylinder for Incompressible Turbulent Flow.



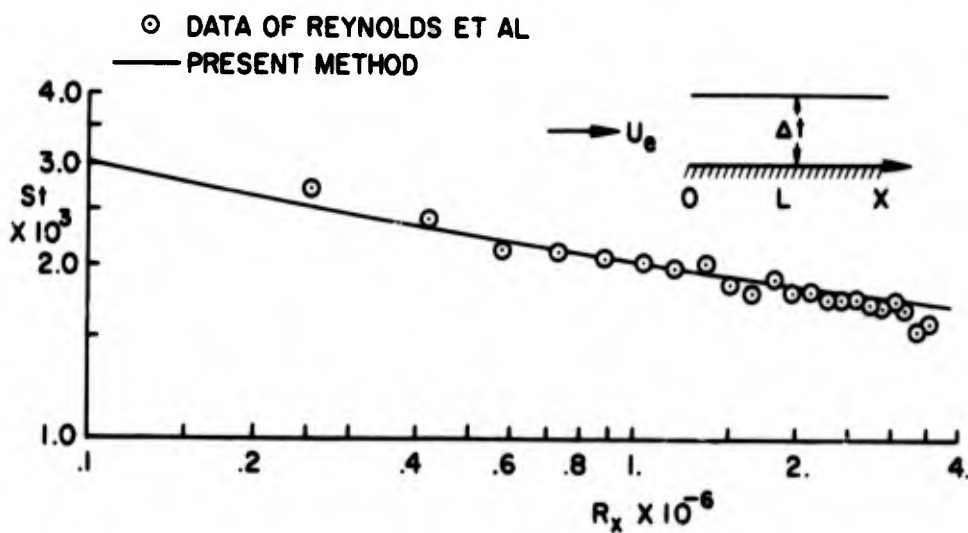
(U) FIG. 11. Comparison of Calculated and Experimental Velocity Profiles on a 0.024-Inch Diameter Cylinder for Incompressible Turbulent Flow.



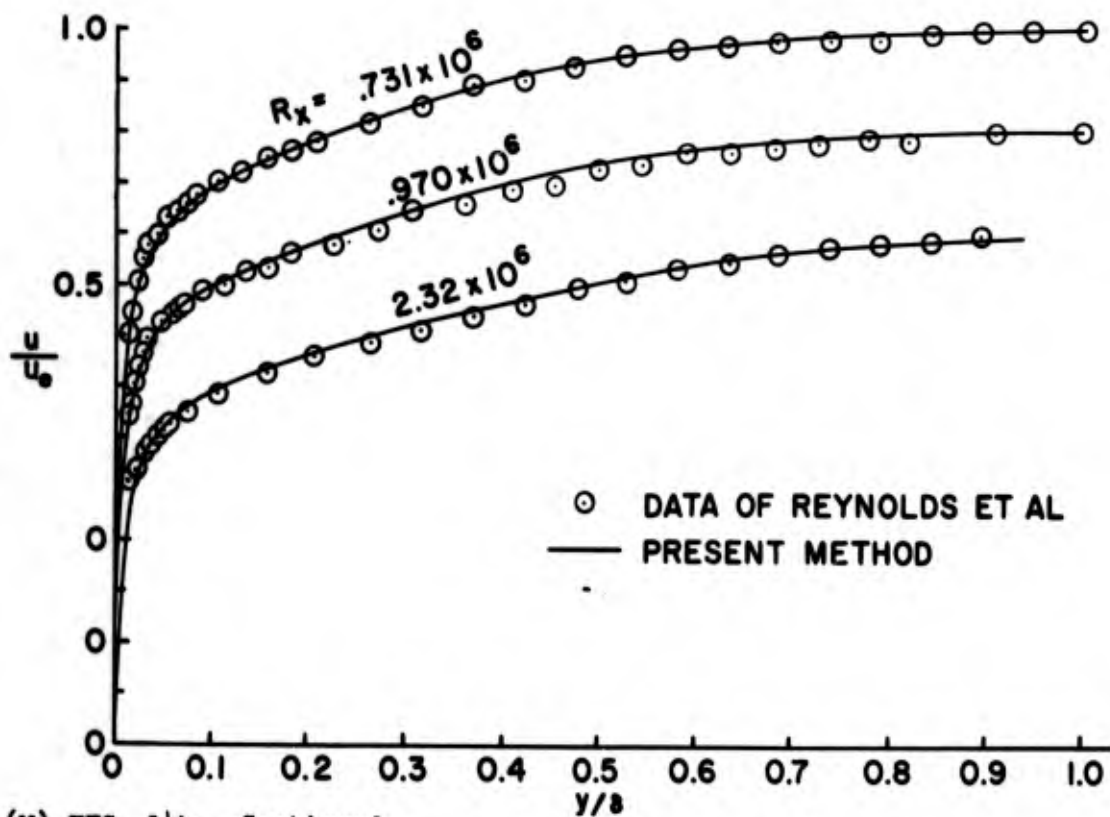
(U) FIG. 12. Comparison of Calculated and Experimental Law-of-the-Wall Profiles in an Axisymmetric Turbulent Boundary Layer.



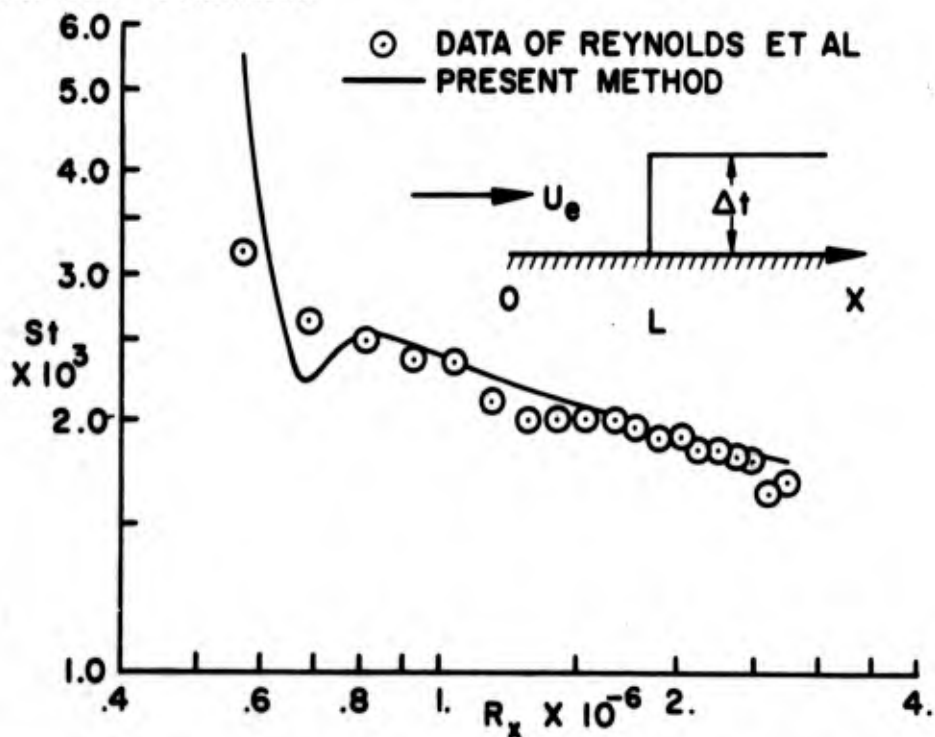
(U) FIG. 13. Comparison of Calculated and Experimental Velocity Profiles on a Slender Cylinder.



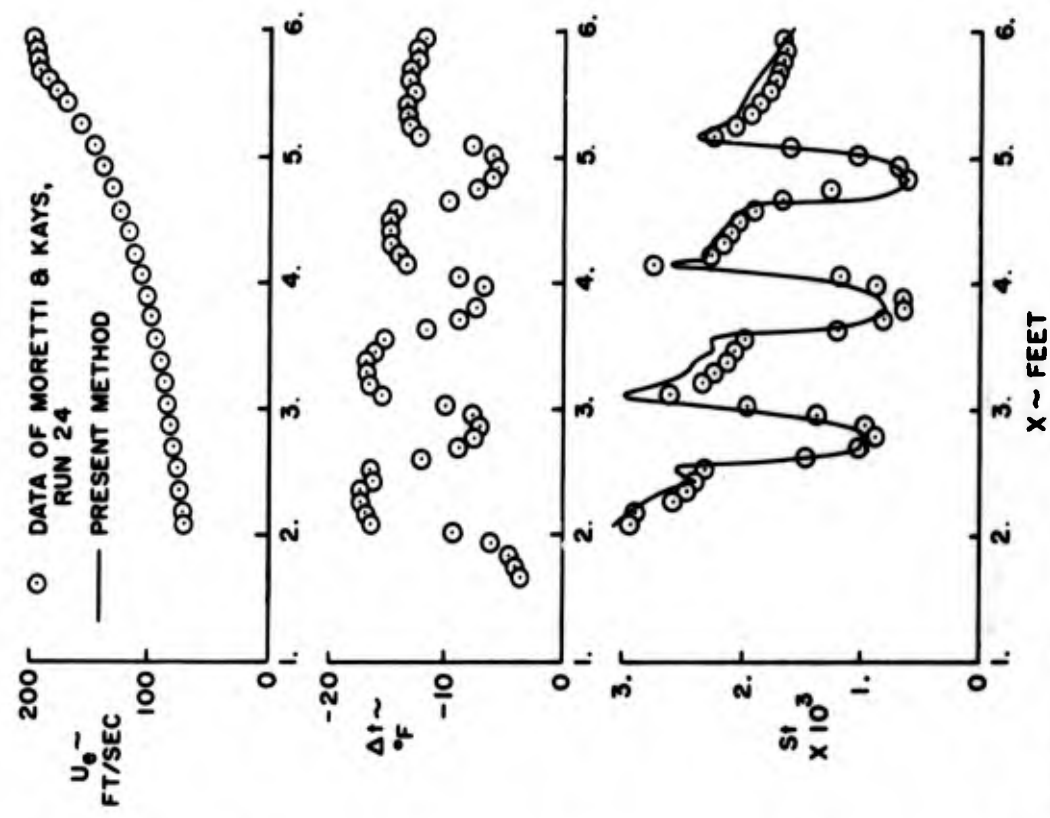
(U) FIG. 14a. Comparison of Calculated and Experimental Stanton Numbers for the Flat-Plate Boundary Layer Measured by Reynolds, Kays and Kline.



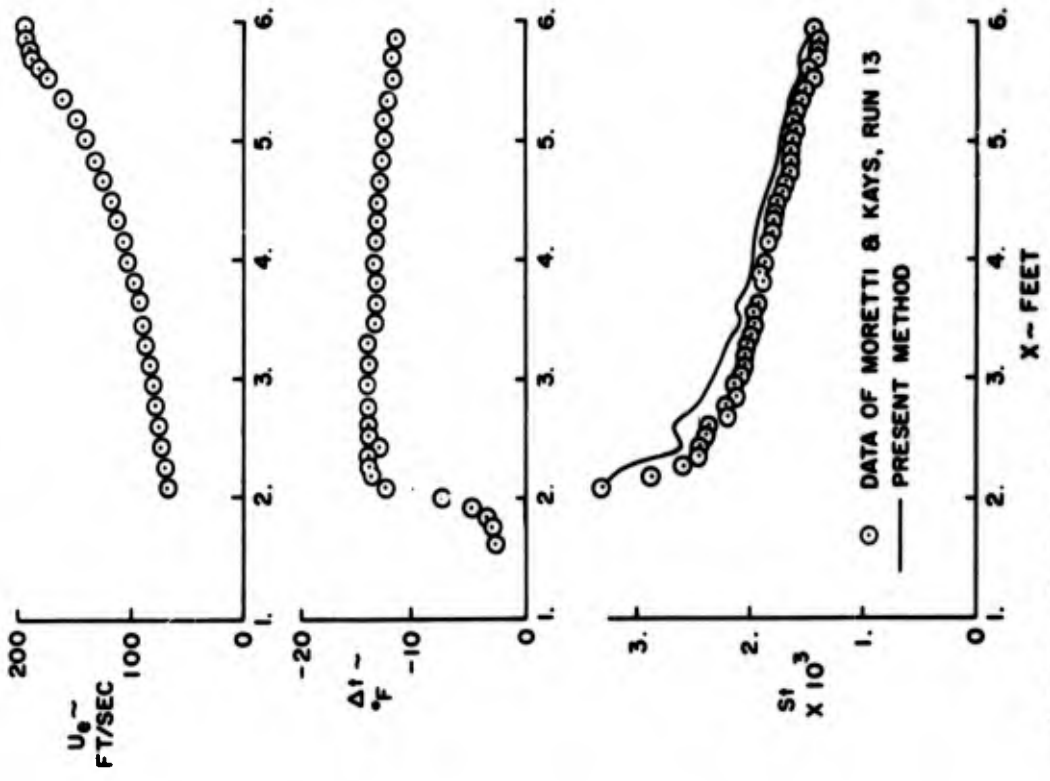
(U) FIG. 14b. Continued.



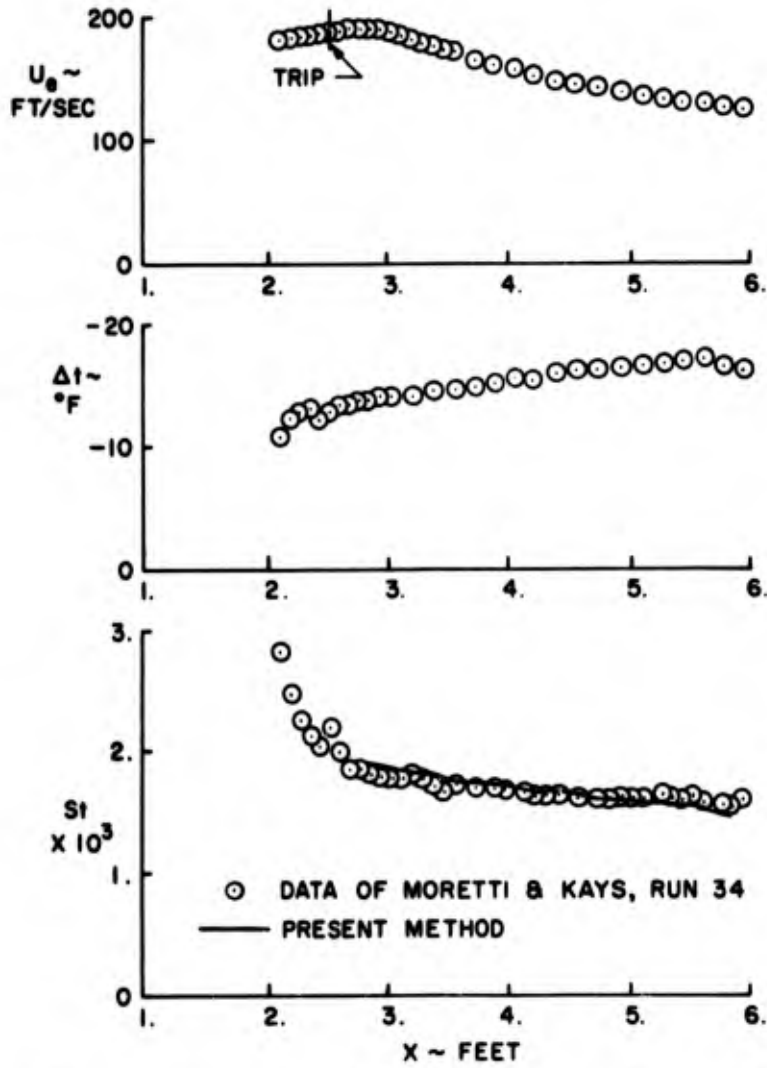
(U) FIG. 15. Results of the Flat-Plate Boundary Layer Measured by Reynolds, Kays and Kline.



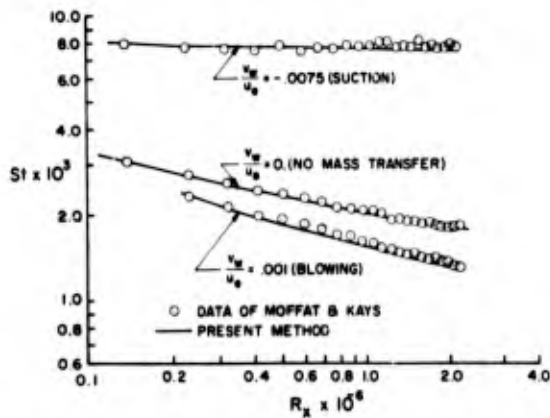
(U) FIG. 16. Results of the Accelerating Boundary Layer Measured by Moretti and Kays.



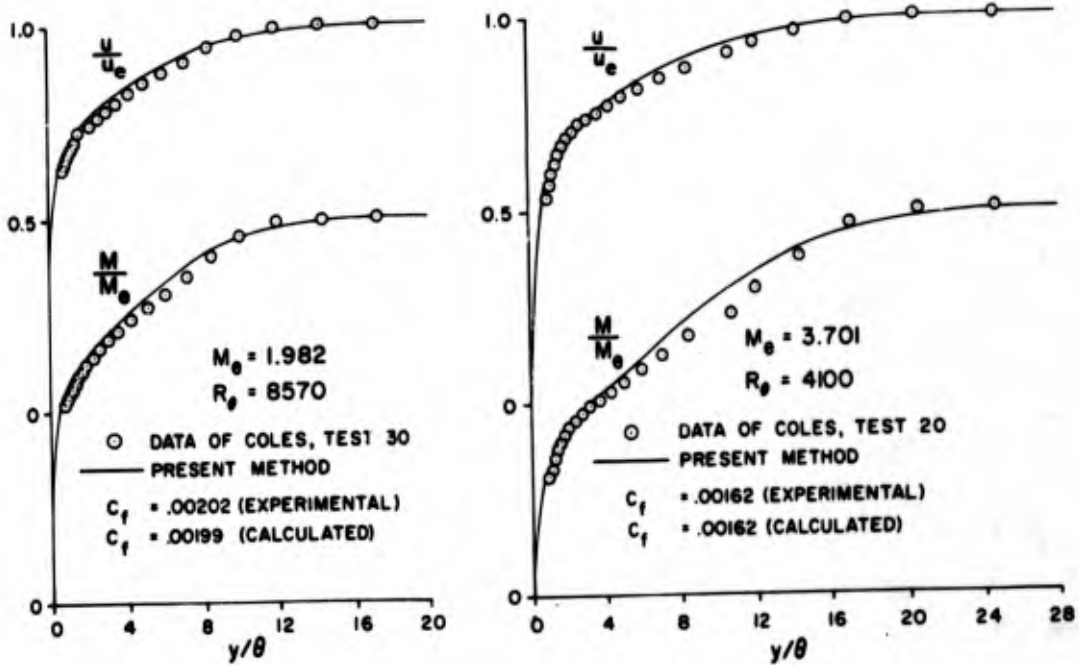
(U) FIG. 17. Results of the Accelerating Boundary Layer Measured by Moretti and Kays.



(U) FIG. 18. Results of the Decelerating Boundary Layer Measured by Moretti and Kays.

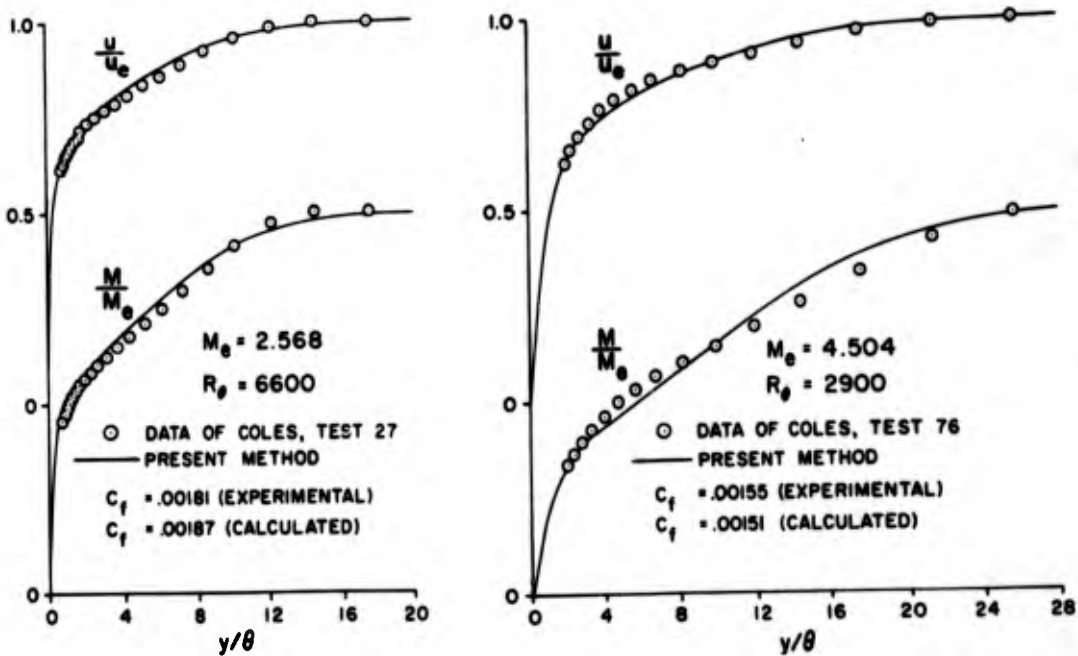


(U) FIG. 19. Results of Flat-Plate Flow With and Without Mass Transfer (Experimental Data of Moffat and Kays).



(a)

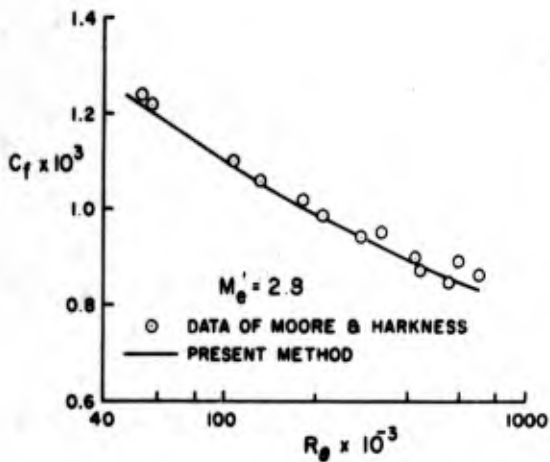
(c)



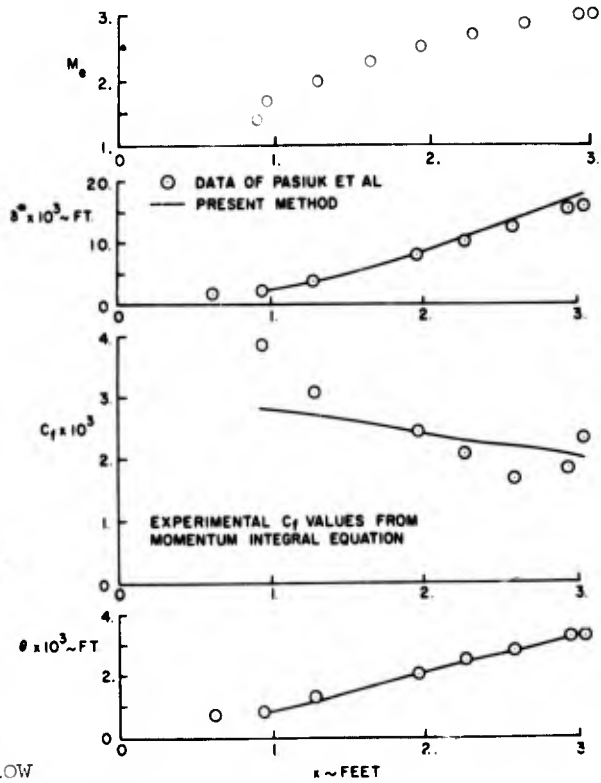
(b)

(d)

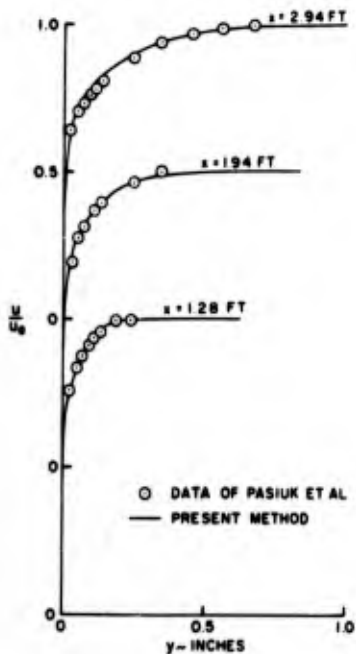
(U) FIG. 20. Comparison of Results for the Flat-Plate Flow Measured by Coles. Skin Friction was Measured by Floating Element.



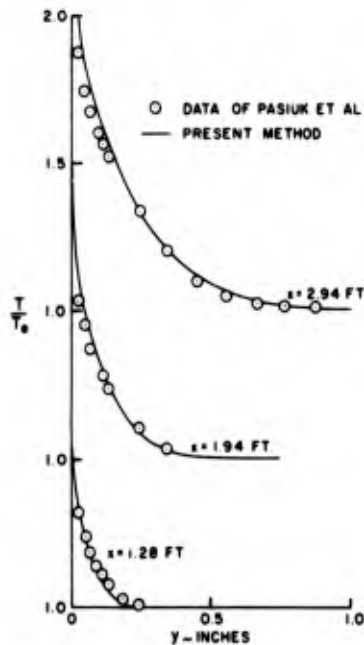
(U) FIG. 21. Comparison of Results for the Flat-Plate Flow Measured by Moore and Harkness. Skin Friction was Measured by Floating Element.



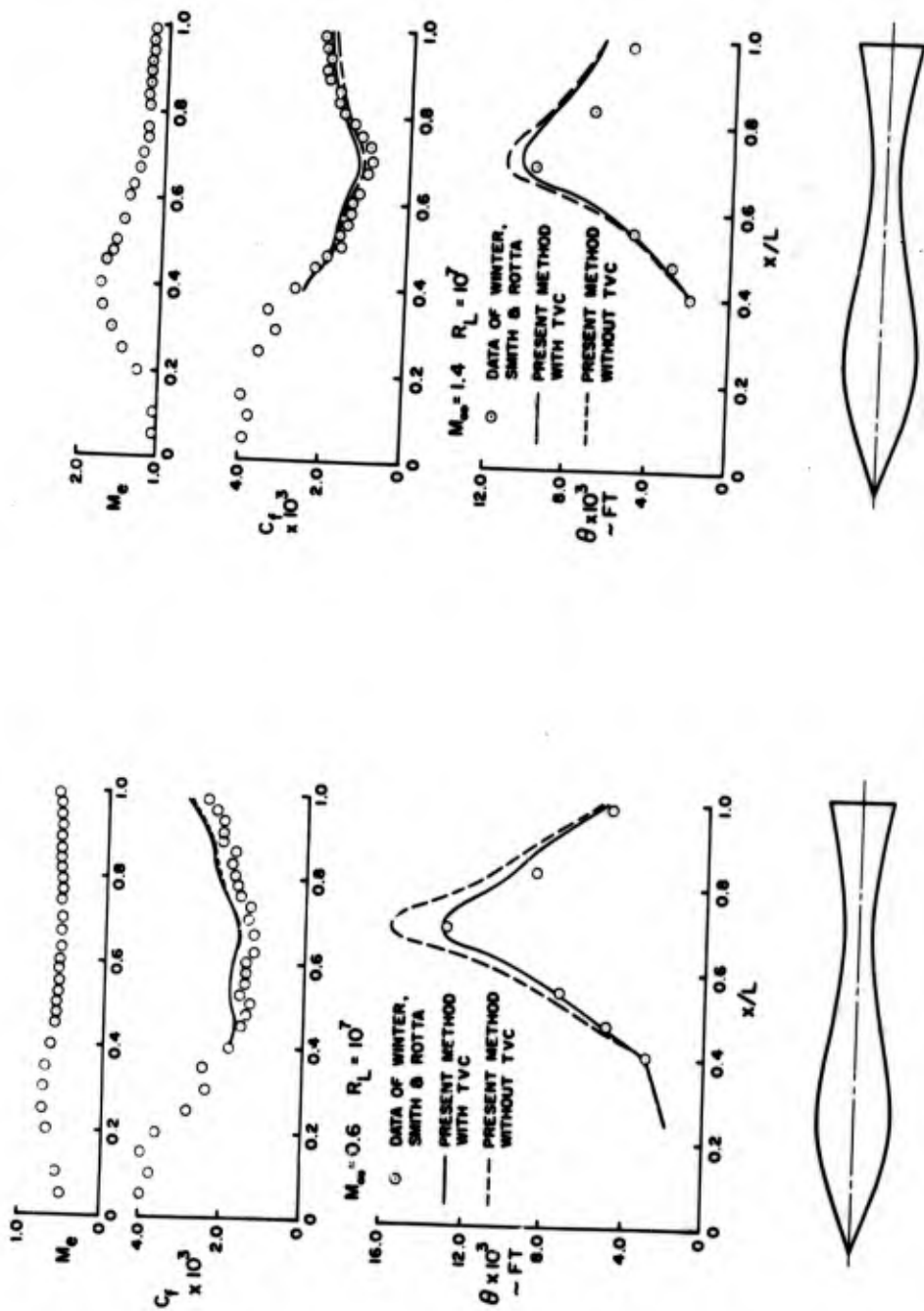
(U) FIG. 22a. Comparison of Results for the Accelerating Flow Measured by Pasiuk et al.



(U) FIG. 22b. Continued.



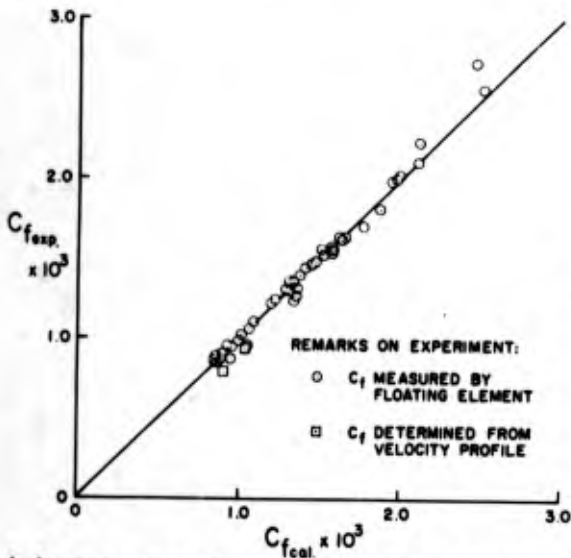
(U) FIG. 22c. Continued.



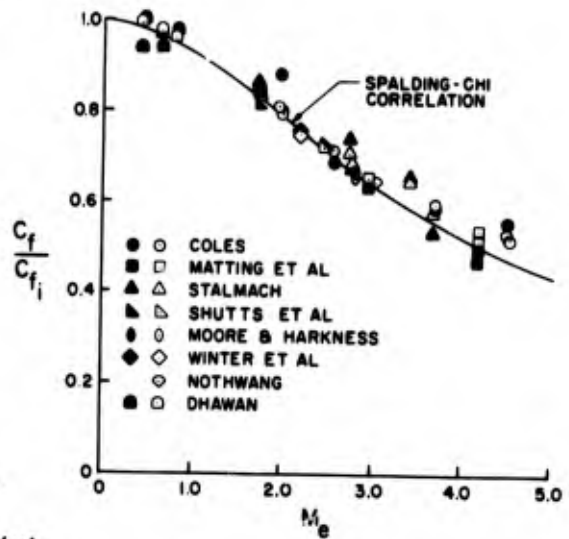
(a)

(b)

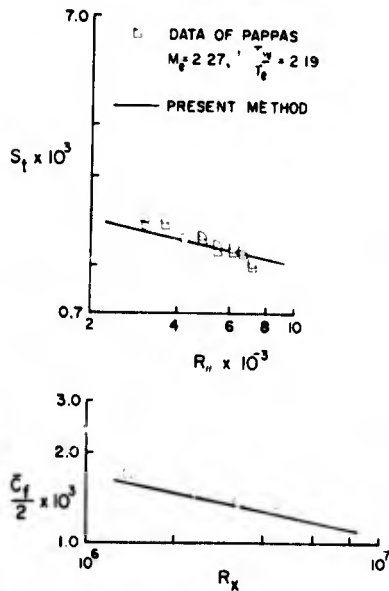
(U) FIG. 23. Comparison of Results for the Waisted Body of Revolution Measured by Winter, Smith and Rotta. The Skin-Friction Values were Obtained by the "Razor Blade" Technique.



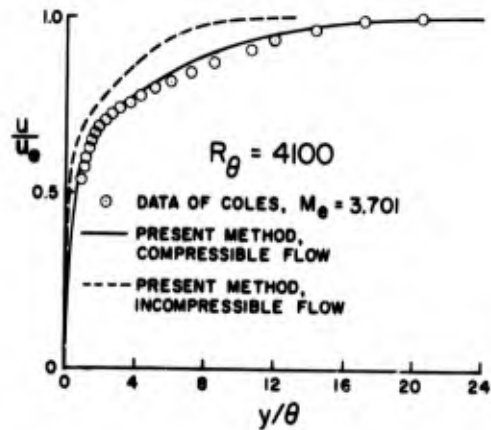
(U) FIG. 24. Comparison of Calculated and Experimental Local Skin-Friction Values. The rms Error Based on 43 Experimental Values Obtained by the Floating Element Technique is 3.5%.



(U) FIG. 25. Comparison of Skin-Friction Variation with Mach Number. Open Symbols Denote the Calculated Values and the Solid Symbols Denote the Experimental Values.



(U) FIG. 26. Comparison of Calculated and Experimental Stanton Numbers and Average Skin-Friction Values for the Flat-Plate Flow Measured by Pappas.



(U) FIG. 27. Compressibility Effect on the Velocity Profiles. Experimental Data is Due to Coles.

Paper No. 13

**AN EXPERIMENTAL INVESTIGATION OF THE COMPRESSIBLE  
TURBULENT BOUNDARY LAYER WITH A FAVORABLE  
PRESSURE GRADIENT**

(U)

(Paper UNCLASSIFIED)

by

William J. Yanta, David L. Brott,  
Robert L. Voisinet, and Roland E. Lee  
U.S. Naval Ordnance Laboratory  
White Oak, Silver Spring, Md. 20910

ABSTRACT. (U) This paper describes the results of a detailed experimental investigation of a two-dimensional turbulent boundary layer in a favorable pressure gradient where the free-stream Mach number varied from 3.8 to 4.6; the ratio of wall to adiabatic wall temperature remained constant at a value of 0.82. Detailed profile measurements were made with pressure and temperature probes; skin friction was measured directly with a shear balance. The velocity and temperature profile results are compared with zero pressure gradient and incompressible results. The skin-friction data are correlated with momentum-thickness Reynolds number and the pressure gradient parameter  $\beta = -\theta/\tau_w \frac{dP}{dx}$ . The skin friction decreases with decreasing  $\beta$  for a constant value of momentum-thickness Reynolds number.

NOMENCLATURE

- A = constant in equation (4)
- B = constant in equation (4)
- $C_f$  = skin friction coefficient
- $H_u$  = shape factor =  $\frac{\int_0^\delta (1 - \frac{u}{u_e}) dy}{\int_0^\delta \frac{u}{u_e} (1 - \frac{u}{u_e}) dy}$
- k = Karman's constant
- M = Mach number
- N = velocity profile exponent  $\frac{u}{u_e} = (\frac{y}{\delta})^{\frac{1}{N}}$
- P = pressure
- $Re_\theta$  = momentum-thickness Reynolds number
- T = temperature
- $\bar{T} = \frac{T_t - T_w}{T_{te} - T_w}$
- u = velocity
- $u_\tau$  = shear velocity =  $\sqrt{\tau_w / \rho_w}$
- $u^+ = \frac{u}{u_\tau}$
- x = distance along plate
- y = distance normal to flow

$$y^+ = \frac{u_\tau y}{\nu_w}$$

$$\beta = \text{pressure gradient parameter} = - \frac{\theta}{\tau_w} \frac{dP}{dx}$$

$\delta$  = boundary-layer thickness

$\rho$  = density

$\theta$  = momentum thickness

$\tau$  = shear stress

$\nu$  = kinematic viscosity

#### Subscripts

aw = adiabatic wall

e = free-stream conditions

o = supply conditions

w = wall conditions

t = total conditions

#### INTRODUCTION

(U) The work presented herein is part of an experimental program being carried out at the U. S. Naval Ordnance Laboratory (NOL) in which the turbulent boundary-layer flow is studied systematically and in detail with conventional pressure and temperature probes, and with a skin-friction balance. The earlier studies at zero pressure gradient and moderate heat-transfer rates were reported in reference 1. The present paper describes the results of the study of the turbulent boundary layer on the flat plate of the NOL Boundary Layer Channel<sup>2</sup> along which the free-stream Mach number varied from 3.8 to 4.6, and for moderate heat-transfer rates. Typical velocity and temperature profile data are presented along with skin-friction coefficients measured with a friction balance. The effect of the favorable pressure gradient on the boundary-layer flow structure and friction drag is discussed, and compared with supersonic zero pressure gradient and incompressible flow.

Nozzle Design

(U) The main component of the NOL Boundary Layer Channel is the two-dimensional supersonic half nozzle shown in figure 1. One wall of the nozzle is a flat plate, 8 feet long and 12 inches wide. The opposite wall is a flexible plate which may be adjusted to give a prescribed Mach number distribution along the flat plate. In the present investigation, three different calculation procedures were attempted to prescribe the free-stream favorable pressure gradient Mach number distribution along the flat plate. The first approach used the concept originally proposed by Von Doenhoff and Tetervin<sup>3</sup> for incompressible flow, in which the turbulent boundary-layer characteristics were shown to be related to the shape factor  $H_u$ . In order to see if this assumption could be made in the present investigation, the moment of momentum equation was integrated along the flat plate of the boundary layer channel for the zero pressure gradient contour described in reference 1. Poor agreement with experimentally measured  $H_u$  was obtained, and therefore this approach was dropped. The second approach was to integrate the von Karman momentum equation along the flat plate for  $du_e/dx$  equal to a constant. The nozzle contour was then determined from the Mach number distribution by the method of characteristics. This approach gave a nozzle contour which over-stressed the flexible plate. The final approach used the concept of an equilibrium boundary layer first introduced by Clauser<sup>4</sup> for incompressible flow. The von Karman momentum equation was again integrated along the flat plate, and the nozzle contour was determined by the method of characteristics. This approach yielded a satisfactory nozzle contour and was the one used in the present test.

Details of the Experiment

(U) The experiments were performed in the NOL Boundary Layer Channel at tunnel supply pressures between 1 and 10 atm, and a tunnel supply temperature of 150°C. The flexible wall of the tunnel was adjusted in the present test to give a prescribed Mach number distribution described above. The actual Mach number distribution is shown in figure 2. The impact probe survey, shown in figure 3, along the flat plate and 3 inches from the plate, indicates that the flow was shock free. The momentum-thickness Reynolds number varied in the present test from 7500 to 48,000; the ratio of wall to adiabatic wall temperature was constant at 0.82. Further details of the channel and its performance are given

in reference 2. Measurements were taken at five stations along the test plate; at 50, 60, 70, 78 and 84 inches from the nozzle throat. Typical boundary-layer thicknesses along the test section ranged from 1.3 inches to 3.0 inches.

#### Instrumentation and Nozzle Design

(U) The boundary-layer profile surveys were made by traversing a Pitot pressure probe and an equilibrium conical temperature probe across the boundary layer. Both probes were mounted in a single holder, which was designed and tested so that there was not any probe interference between the two probes. The probes were traversed from the free stream toward the plate, with maximum movement of 3 inches. The traverse was stopped at each point in the boundary layer at which data were taken, and the temperature and pressure were allowed to reach equilibrium.

(U) The profile data were recorded automatically on NOL's PADRE.<sup>5</sup> This unit provides seven channels with servo-systems and direct digital conversion to permit recording the data directly on IBM cards.

(U) Pitot pressure probes were made of 0.125-inch diameter stainless-steel tubing flattened at the tip to a rectangular cross section of 0.005 x 0.100 inch (outside dimensions). The wall static pressure was measured by the 0.032-inch ID orifices in the flat plate. The local Mach number was computed from the Rayleigh Pitot tube formula using the measured Pitot and wall static pressure.

(U) The basic design of the equilibrium conical temperature probe is described in reference 6. Essentially, the equilibrium temperature of a sharp 10-degree platinum cone was measured by a thermocouple mounted into its 0.050-inch diameter base. The measured cone temperature, together with the measured local Mach number and cone tables, provided the necessary information to calculate the local stagnation and static temperatures. A cone recovery factor equal to the square root of the Prandtl number was assumed.

(U) A fine-wire stagnation temperature probe was also used to measure the temperature profile through the boundary layer. The basic features of this probe are described in reference 7. The probe consists of a thin (0.002-inch diameter, 0.240-inch long) chromel-alumel thermocouple wire placed normal to the flow. Using the measured Mach number distribution and conventional empirical equations for predicting the heat losses to and from the probe, the local stagnation temperature and hence the local static temperature may be obtained.

(U) The static-pressure profile across the boundary layer was measured with a 0.125 inch OD static-pressure probe. The tip of the probe was a conical 10-degree cone, and the static orifices were located on the circular tubing 20 diameters from the tip.

(U) The local Mach number distribution was computed from the measured Mach number and temperature distributions. The edge of the boundary layer was selected as the location where the velocity gradient became zero.

(U) The NOL skin-friction balance is described in reference 8. The instrument measures directly the shear drag on a 0.5-square-inch surface floating element mounted flush with the flat plate. The balance was designed for measurements in flows with heat transfer and pressure gradient.

#### Experimental Results

(U) The Mach number distribution along the flat plate (see figure 2) was computed from the ratio of wall-static to tunnel-supply pressure, see figure 3. Both methods agree within 2 percent, indicating that the static pressure is constant across the boundary layer. To further verify this result, static-pressure surveys were taken through the boundary layer. The typical results shown in figure 4 indicate that the static pressure is practically constant across the boundary layer.

(U) A typical boundary-layer velocity profile is shown in figure 5. The line drawn in the laminar sublayer region was computed from the friction-balance measurement. The fact that the last two velocity-profile points do not fall along the curve computed from the friction-balance measurement is possibly due to probe-wall interference. A power profile is seen to be a good fit to the outer region of the velocity profile. In the case of pressure gradient flow, a power profile was a better fit to the outer region of the boundary layer than in the zero pressure gradient case.<sup>1</sup> A least-squares fit of the power profile exponent versus momentum-thickness Reynolds number shows a value of the exponent slightly higher than for the zero pressure gradient flow case (see figure 6). This result is due to the fact that the favorable pressure gradient makes the profiles fuller.

(U) The correlation between the shape factor  $H_u$  and momentum-thickness Reynolds number is shown in figure 7.

The favorable pressure gradient data are lower than the zero pressure gradient data and has the same general variation with momentum-thickness Reynolds number. This is consistent with incompressible results.<sup>9</sup>

(U) The effect of pressure gradient history on the temperature-velocity profile is to displace the curve from the zero pressure gradient results of Crocco.<sup>10</sup> A typical temperature-velocity correlation is shown in figure 8. Shown for comparison is Crocco's equation<sup>9</sup>

$$\bar{T} = \frac{u}{u_e} \quad (1)$$

and Walz's equation<sup>11</sup> for zero heat transfer

$$\bar{T} = \left(\frac{u}{u_e}\right)^2 \quad (2)$$

The last few points in the profile were linearly extrapolated to the wall. The data in the sublayer regions follow the zero pressure gradient adiabatic flow relation of Walz, and is fuller in the outer turbulent region. The displacement of the data from Crocco's equation is consistent with that predicted in reference 10. An inflection point in the temperature-velocity profile occurring at the lower edge of the logarithmic region of the boundary layer was observed consistently in all the data. For the data shown in figure 8 this point is located at  $u/u_e \approx 0.6$ . To insure that this point was not due to probe interference, temperature profiles were measured with a fine-wire stagnation temperature probe at the same supply conditions. These results, shown in figure 8, exhibit the same trends as those of the conical probe. Therefore, the inflection point in the temperature-velocity profile does exist.

(U) Correlation of the favorable pressure gradient results in terms of the law-of-the-wall and velocity-defect law is shown in figures 9 and 10. Supersonic zero pressure gradient and incompressible results are shown for comparison.<sup>12</sup> The favorable pressure gradient data for  $M_e = 3.87$  are seen to be below the supersonic zero pressure gradient results for  $M_e = 4.7$ , and the incompressible results for  $\beta = .267$  and for  $\beta = 0$ . The results shown in figures 9 and 10 indicate that as a result of the favorable pressure gradient, the logarithmic region of the boundary layer has increased substantially in thickness and the velocity defect in the outer part of the layer has decreased. For incompressible flow the logarithmic portion of the boundary layer can be fitted by the equation<sup>13</sup>.

$$u^+ = \frac{1}{k} \ln y^+ + 4.9 \quad (3)$$

where  $k = 0.4$  is Karman's constant. In the present investigation it was observed that the logarithmic portion of the boundary layer could be fitted by the equation

$$u^+ = \frac{1}{A} \ln y^+ + B \quad (4)$$

where  $A = 0.541$ .  $B$  was not constant in the investigation.

(U) The skin friction, obtained by a shear balance, is shown plotted against momentum-thickness Reynolds number in figure 11. Presented for comparison are the incompressible favorable pressure gradient results of Ludwig-Tillman<sup>12</sup> and Herring and Norbury.<sup>14</sup> The present supersonic data are seen to lie well below the incompressible results. A consistent correlation of the present results in terms of the shape factor  $H_u$  was not observed. These results do not agree with the incompressible results of Ludwig-Tillman<sup>12</sup> who were able to correlate the skin friction in terms of the shape factor. The measured skin friction in the present investigation was approximately 20 percent below that predicted by the combination of the Ludwig-Tillman skin-friction formula and the reference enthalpy method.

(U) A consistent trend in the present skin-friction data was observed when correlated in terms of the pressure gradient parameter  $\beta = -\frac{\theta}{\tau_w} \frac{dp}{dx}$ . For decreasing  $\beta$  and constant Reynolds number the skin friction decreases. The correlation of the skin friction in terms of  $\beta$  is consistent with the incompressible results first proposed by Buri<sup>9</sup> who found similar results.

#### CONCLUSIONS

(U) The effect of a favorable pressure gradient on supersonic turbulent boundary layers was studied in the NOL Boundary Layer Channel, for  $7500 < Re_\theta < 48,000$  and for  $T_w/T_{aw} = 0.82$ , with temperature and pressure probes and a shear balance.

(U) The structure of the turbulent boundary layer was examined in terms of velocity and temperature profiles, law-of-the-wall, velocity-defect law and incompressible form factor. The outer region of the boundary layer can be fitted with a power profile. The shape factor  $H_u$

decreases in a supersonic favorable pressure gradient. An inflection point in the temperature-velocity profile was observed to occur at the lower edge of the logarithmic portion of the boundary layer. The effect of a favorable pressure gradient is to thicken the logarithmic portion of the boundary layer and decrease the outer velocity defect portion.

(U) The effect of a favorable pressure gradient on the turbulent skin friction was correlated in terms of the pressure gradient parameter  $\beta$ . For decreasing  $\beta$  and constant Reynolds number the skin friction decreases.

## REFERENCES

1. Lee, R. E., Yanta, W. J. and Leonas, A. C., "Velocity Profile, Skin-Friction Balance and Heat Transfer Measurements of the Turbulent Boundary Layer at Mach 5," Proceedings of the 1968 Heat Transfer and Fluid Mechanics Institute, June 1968
2. Lee, R. E., Yanta, W. J., Leonas, A. C. and Carner, J. W., "The NOL Boundary Layer Channel," NOLTR 66-185, November 1966
3. Von Doenhoff, A. E. and Tetervin, N., "Determination of General Relations for the Behavior of Turbulent Boundary Layers," NACA Report 772, 1943
4. Clauser, F. H., "The Turbulent Boundary Layer," Advances in Applied Mechanics, Vol IV, Academic Press, New York, 1956
5. Kendall, J. M., "Portable Automatic Data Recording Equipment (PADRE)," NAVORD Report 4207, August 1959
6. Danberg, J. E., "The Equilibrium Temperature Probe, a Device for Measuring Temperatures in a Hypersonic Boundary Layer," NOLTR 61-2, December 1961
7. Yanta, W. J., "A Fine-Wire Stagnation Temperature Probe," NOLTR (to be published in 1969)
8. Bruno, J. R., Yanta, W. J. and Risher, D. B., "Balance for Measuring Skin Friction in the Presence of Heat Transfer," NOLTR (to be published in 1969)

**8th Navy Symposium on Aeroballistics**

---

**Vol. 2**

9. Schlichting, H., "Boundary Layer Theory," McGraw-Hill Book Co., Inc., London, 1968
10. Tetervin, N., "An Approximate Method for the Calculation of the Reynolds Analogy Factor for a Compressible Turbulent Boundary Layer in a Pressure Gradient," NOLTR 67-186, December 1967
11. Walz, A., "Compressible Turbulent Boundary Layers," The Mechanics of Turbulence, Science Publishers, Inc., New York, 1964
12. Ludwig, H. and Tillman, W., "Investigation of the Wall Shearing-Stress in Turbulent Boundary Layers," NACA TN-1285, 1950
13. Baronti, P. O. and Libby, P. A., "Velocity Profiles in Turbulent Compressible Boundary Layers," AIAA Journal, Vol 4, No. 2, February 1966
14. Herring, H. J. and Norbury, J. F., "Some Experiments on Equilibrium Turbulent Boundary Layers in Favorable Pressure Gradients," Journal of Fluid Mechanics, Vol 27, Pt. 3, 1967

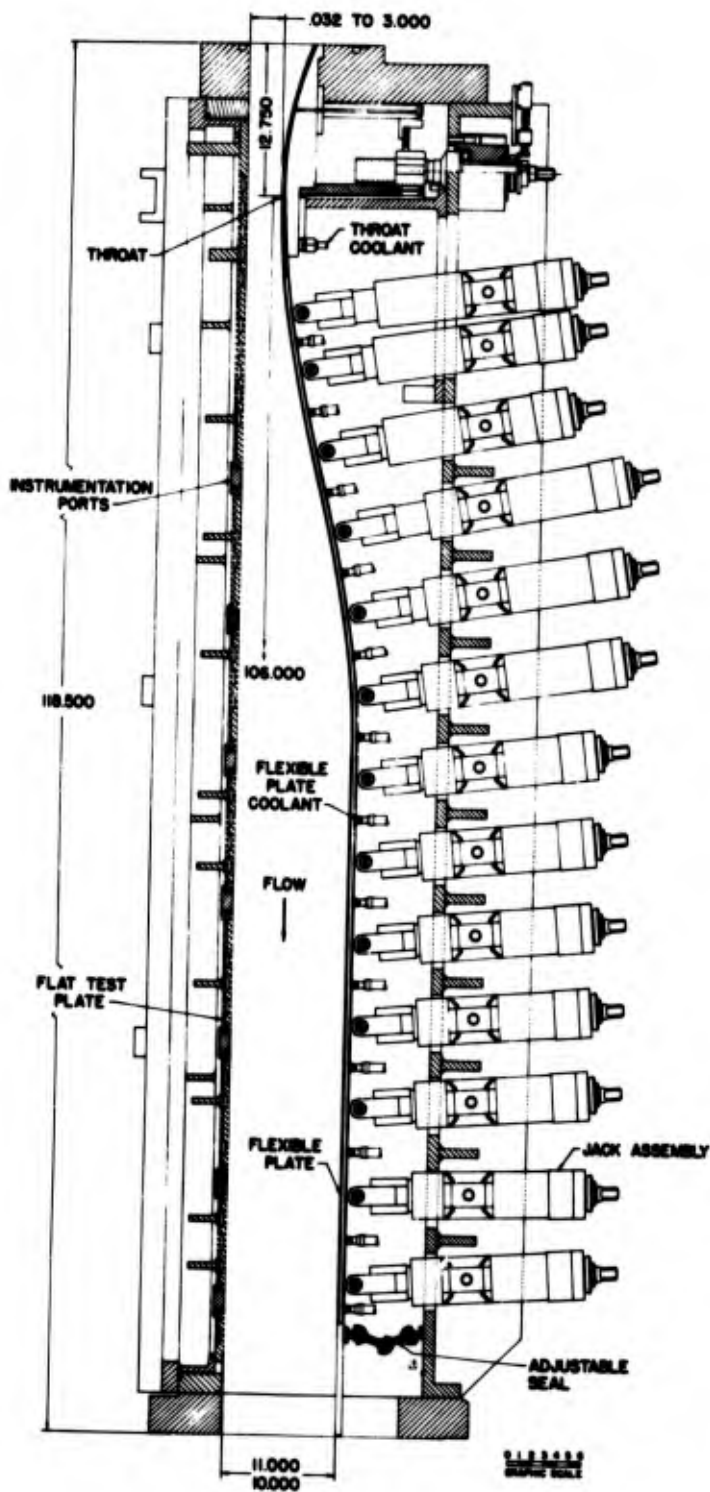


FIG. 1 BOUNDARY LAYER CHANNEL FLEXIBLE NOZZLE

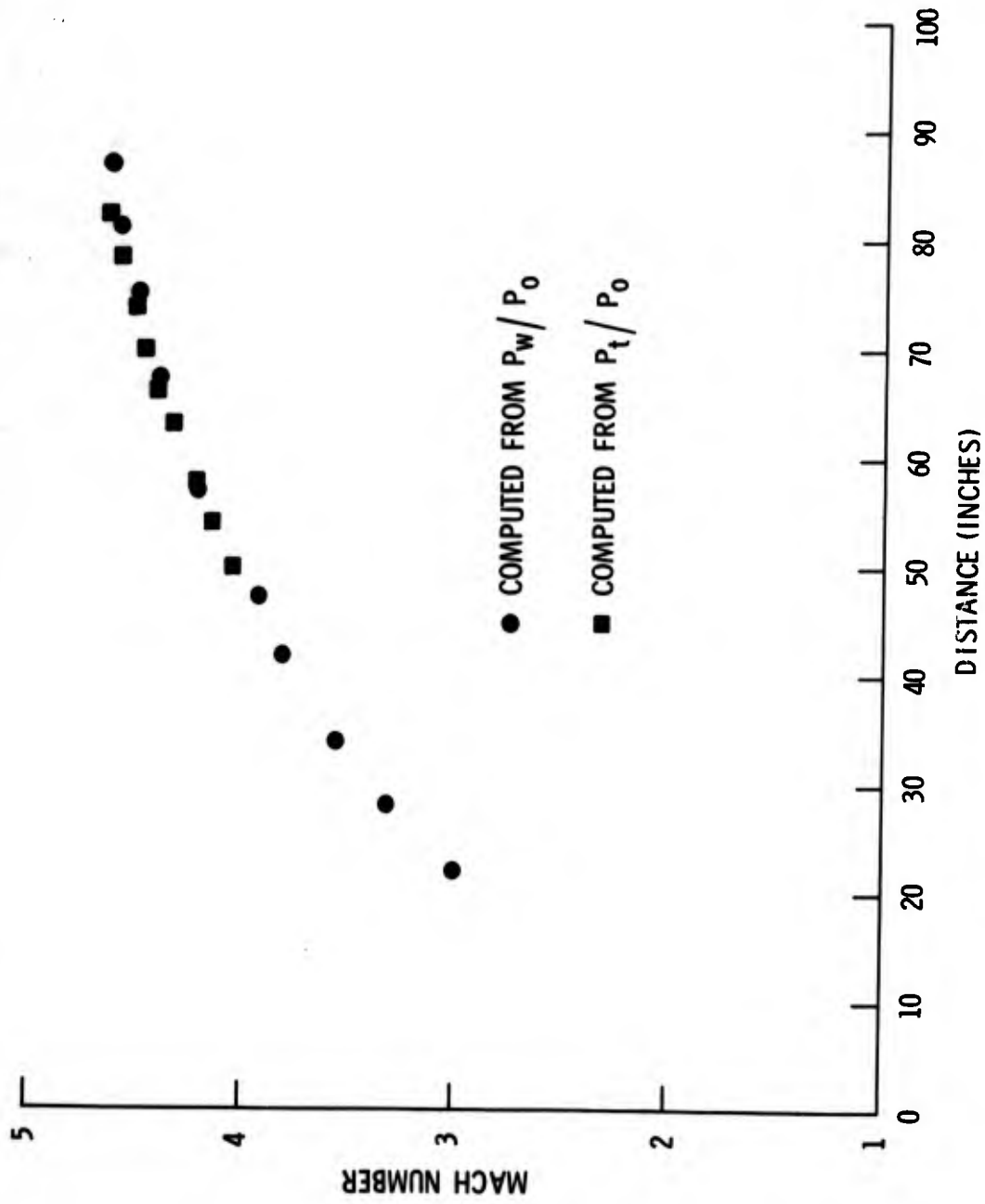
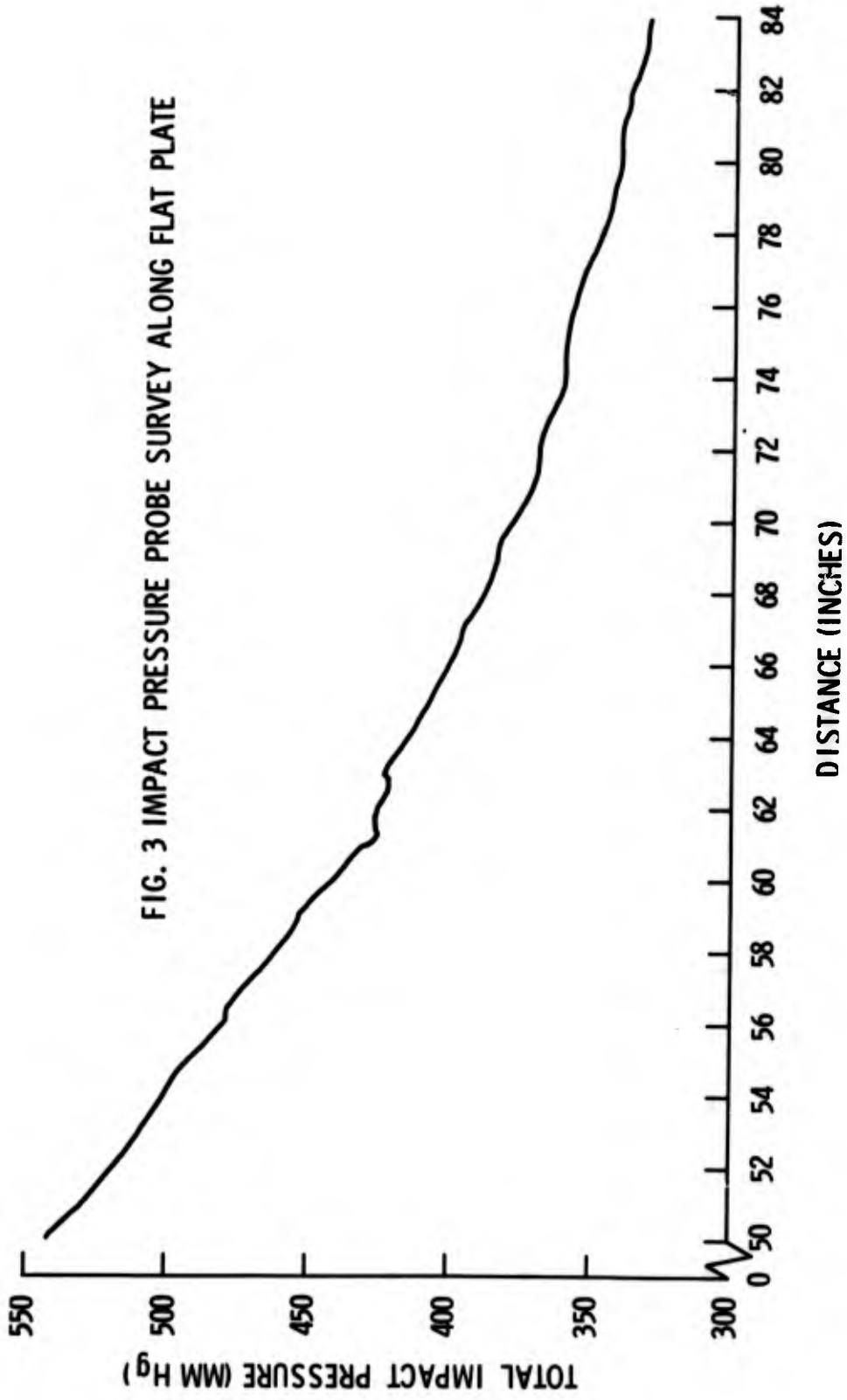


FIG. 2 MACH NUMBER VARIATION ALONG FLAT PLATE



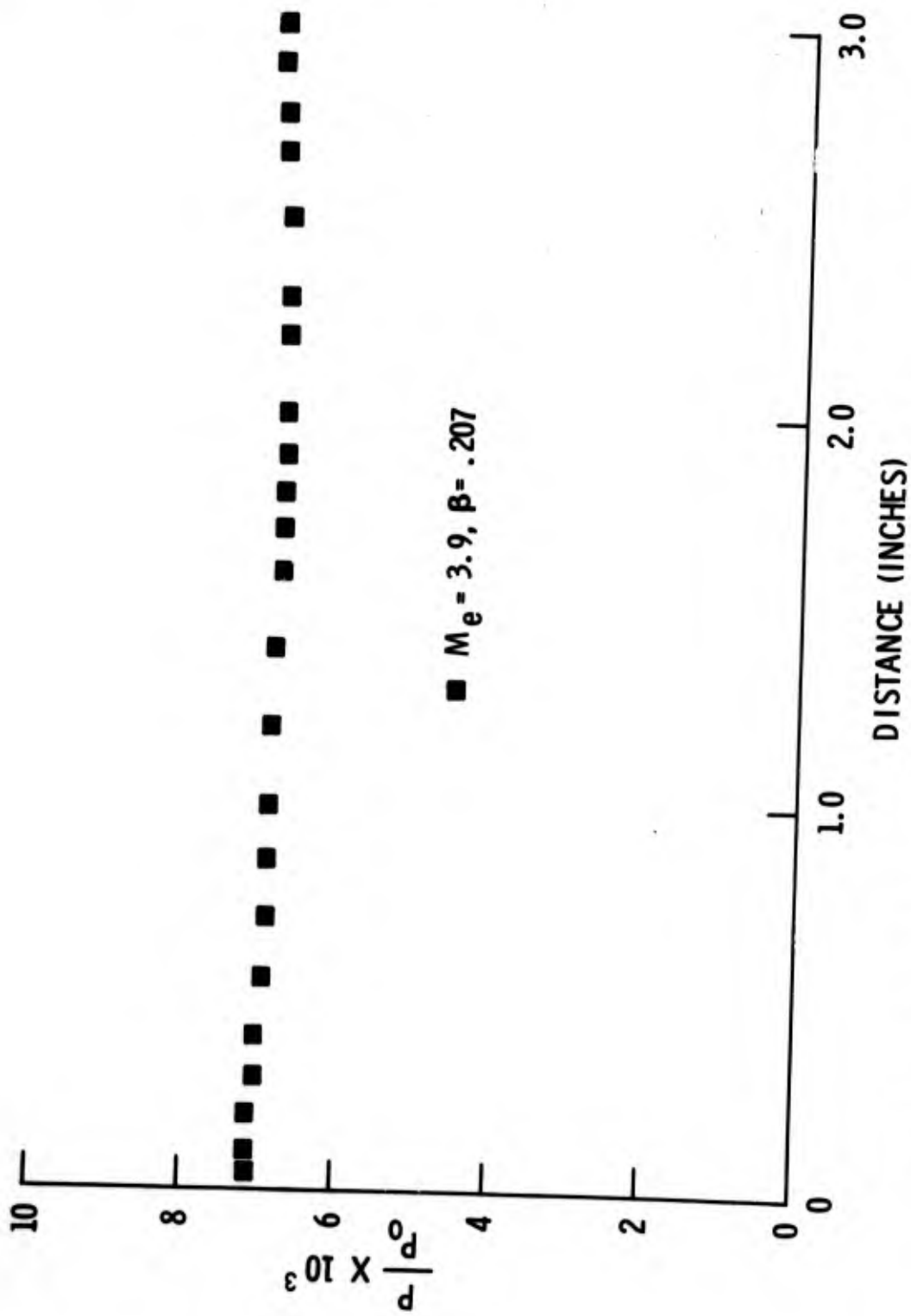


FIG. 4 STATIC PRESSURE DISTRIBUTION THROUGH THE BOUNDARY LAYER

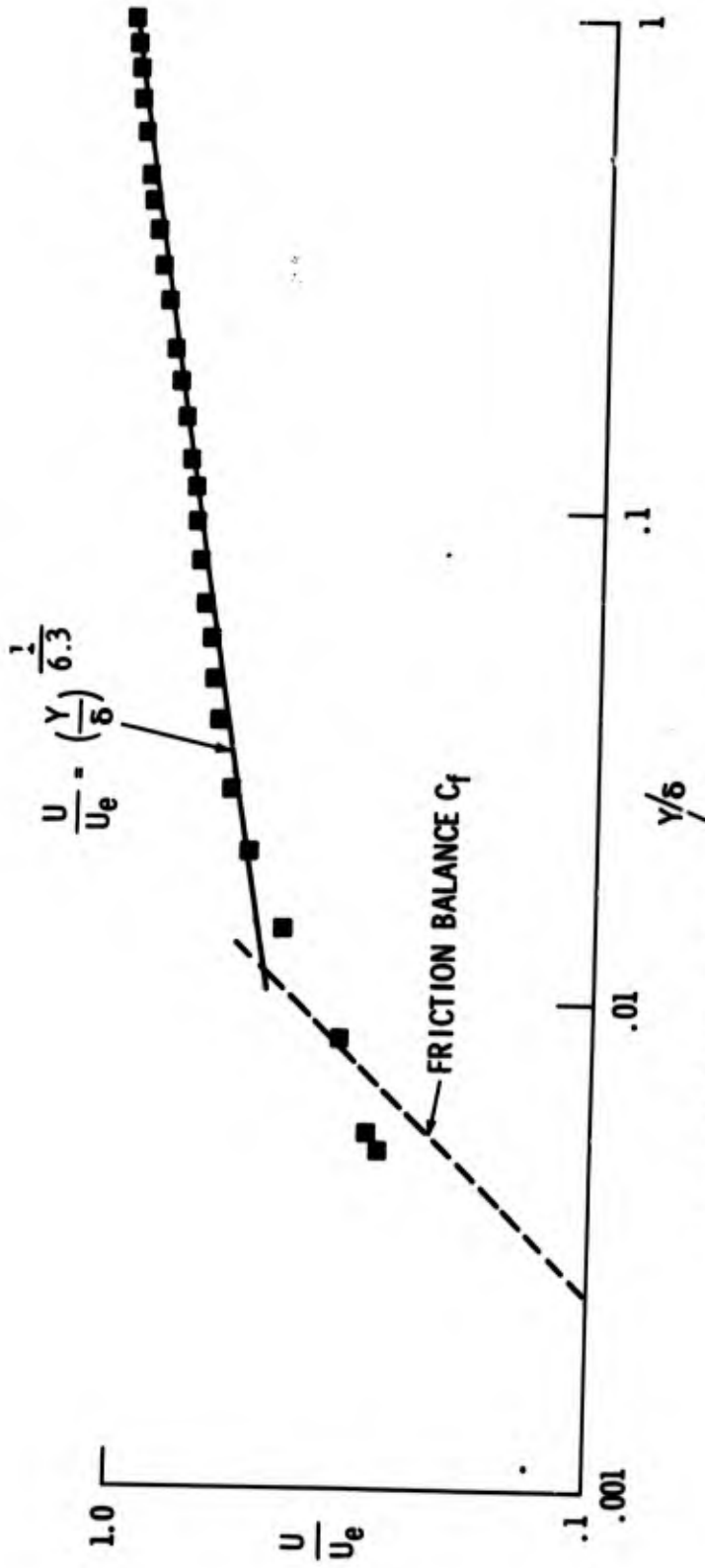


FIG. 5 VELOCITY PROFILE  $Re_\theta = 8290$ ,  $M_\theta = 3.87$ ,  $\beta = .207$

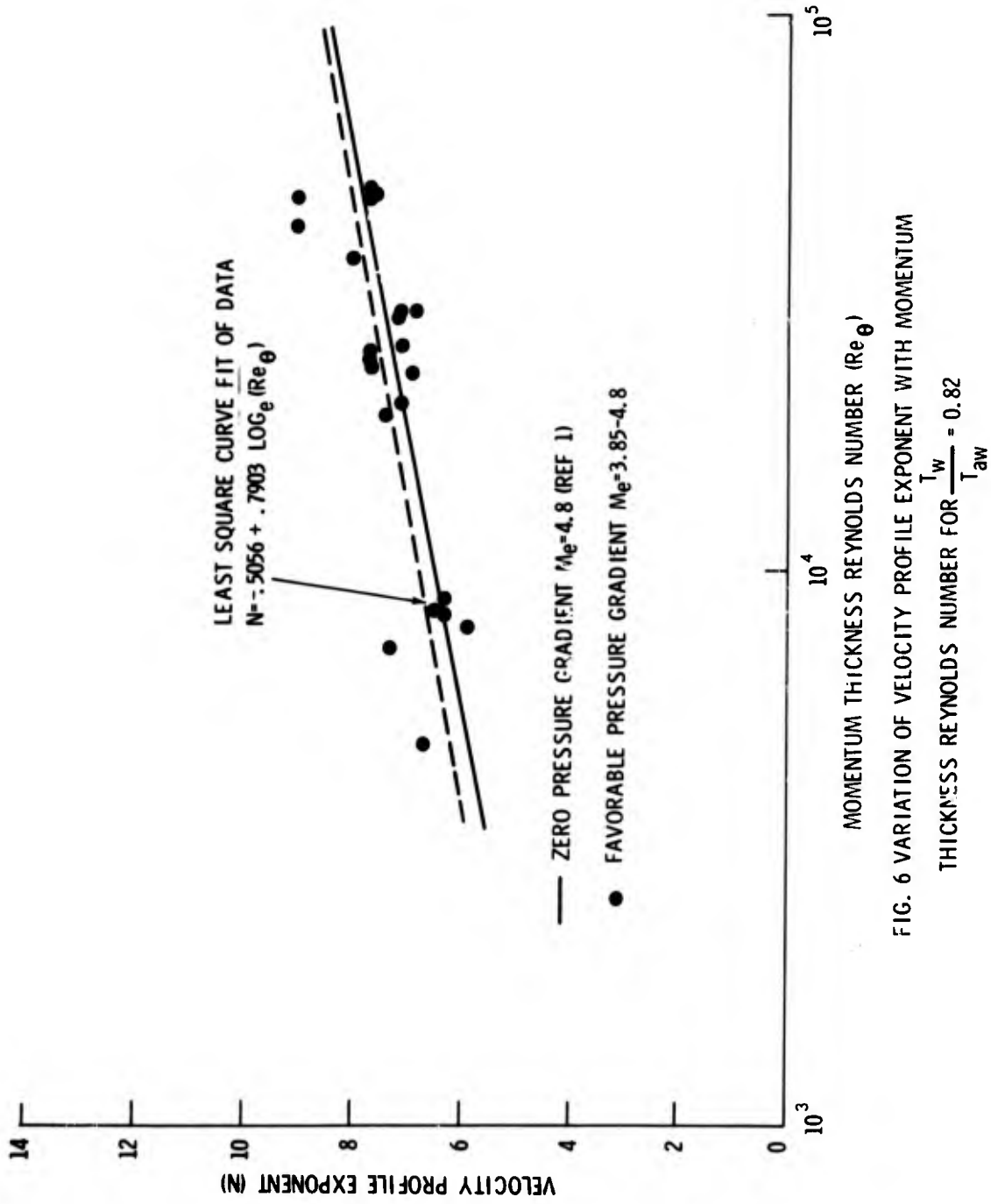


FIG. 6 VARIATION OF VELOCITY PROFILE EXPONENT WITH MOMENTUM THICKNESS REYNOLDS NUMBER FOR  $\frac{T_w}{T_{aw}} = 0.82$

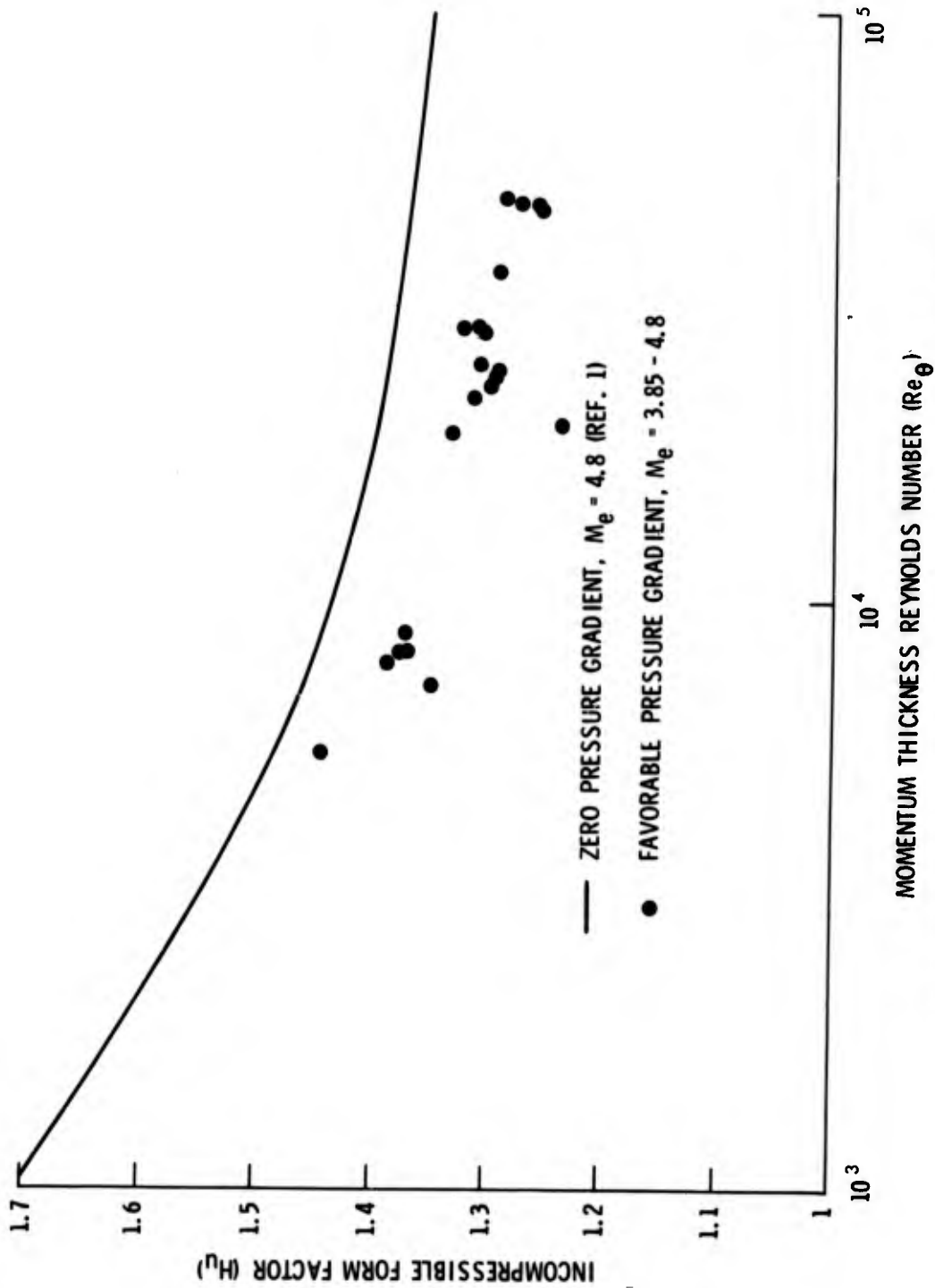


FIG. 7 VARIATION OF INCOMPRESSIBLE FORM FACTOR WITH MOMENTUM THICKNESS REYNOLDS NUMBER FOR  $T_{aw} = 0.82$

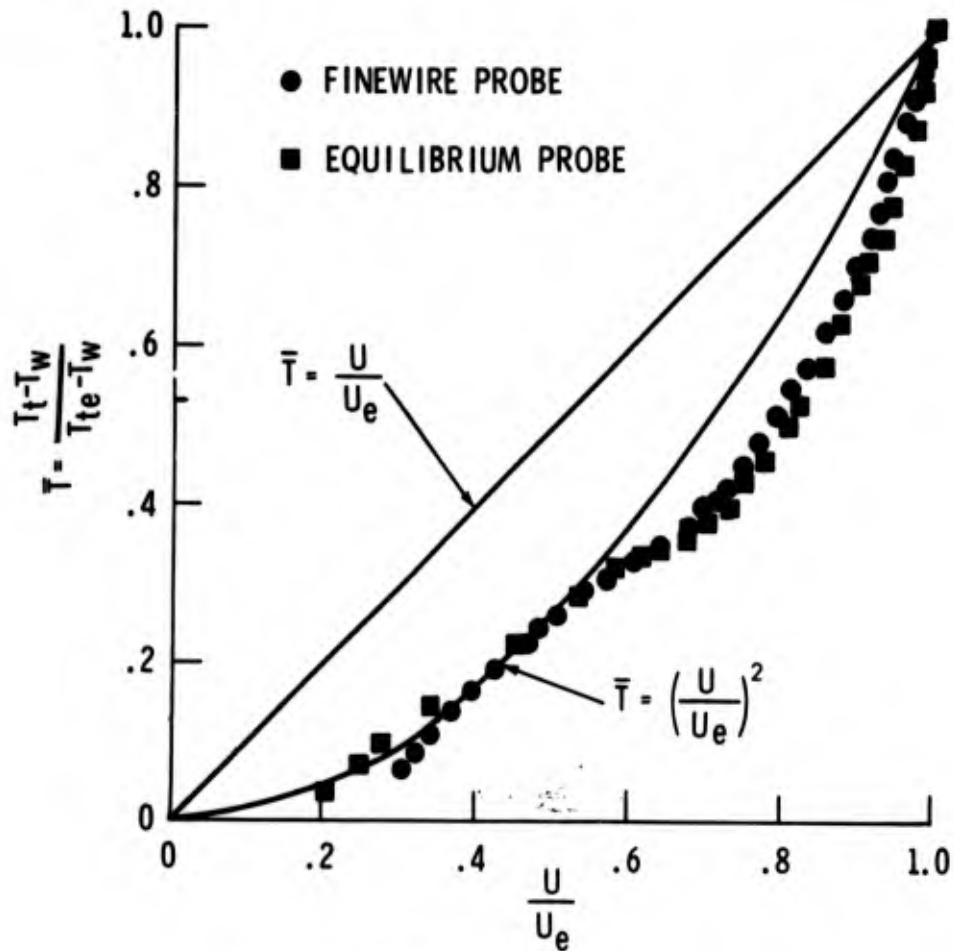


FIG. 8 TEMPERATURE -VELOCITY DISTRIBUTION

FOR  $\frac{T_w}{T_{aw}} = 0.82, Re_\theta = 8290, M_e = 3.87, \beta = .207$

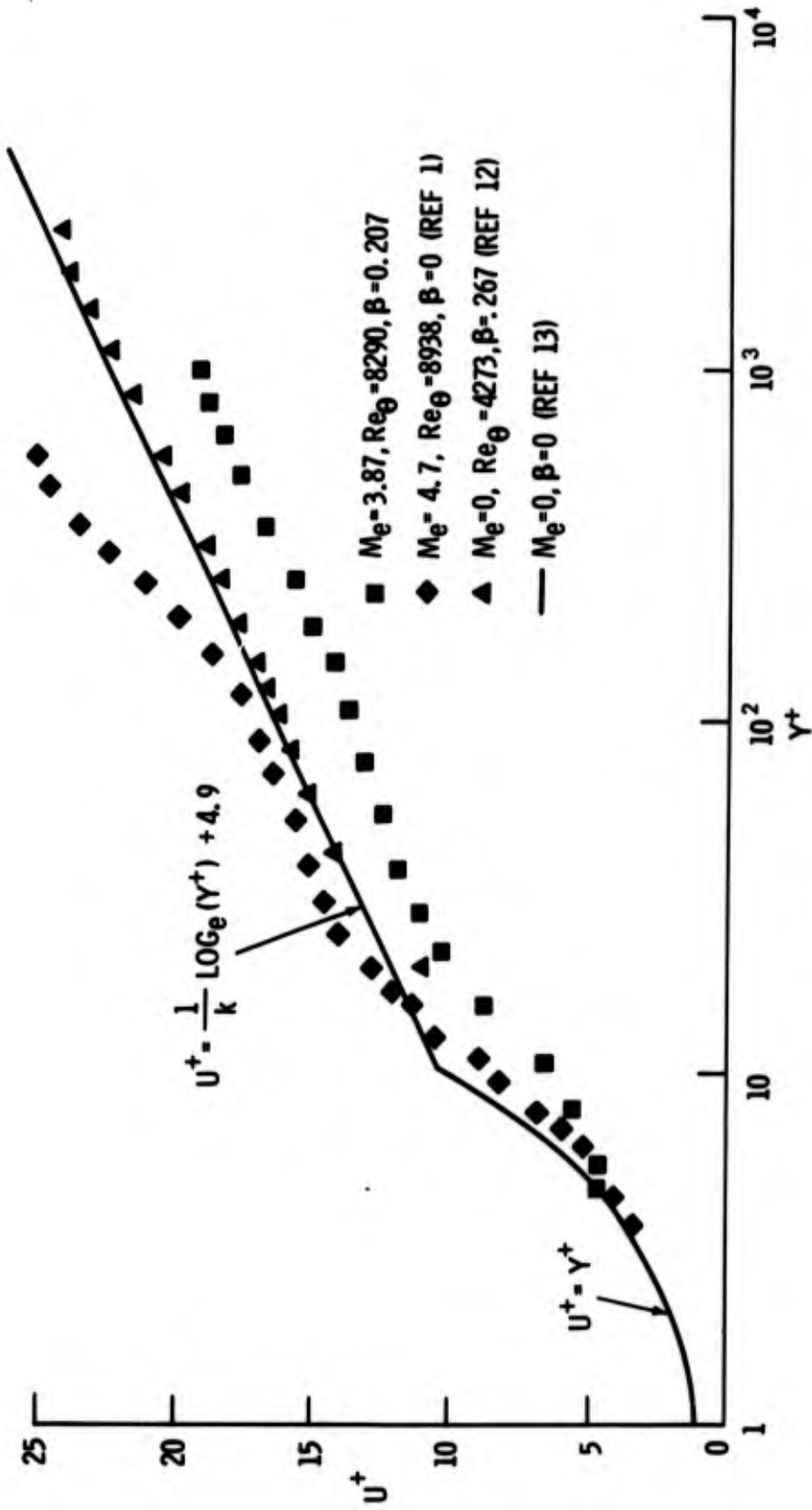


FIG 9 CORRELATION OF EXPERIMENTAL RESULTS IN TERMS OF LAW OF THE WALL

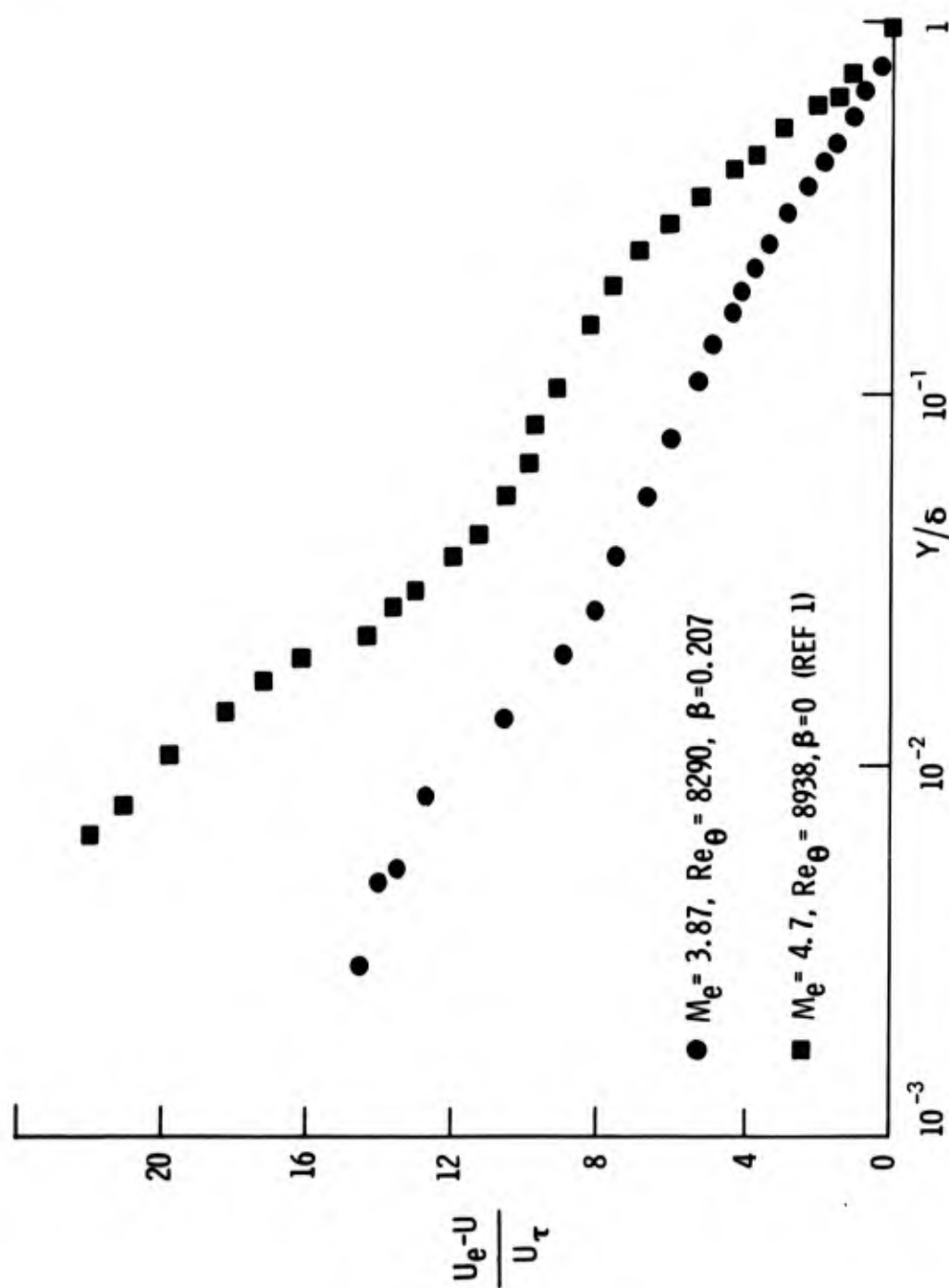


FIG 10 CORRELATION OF EXPERIMENTAL RESULTS IN TERMS OF VELOCITY DEFECT LAW

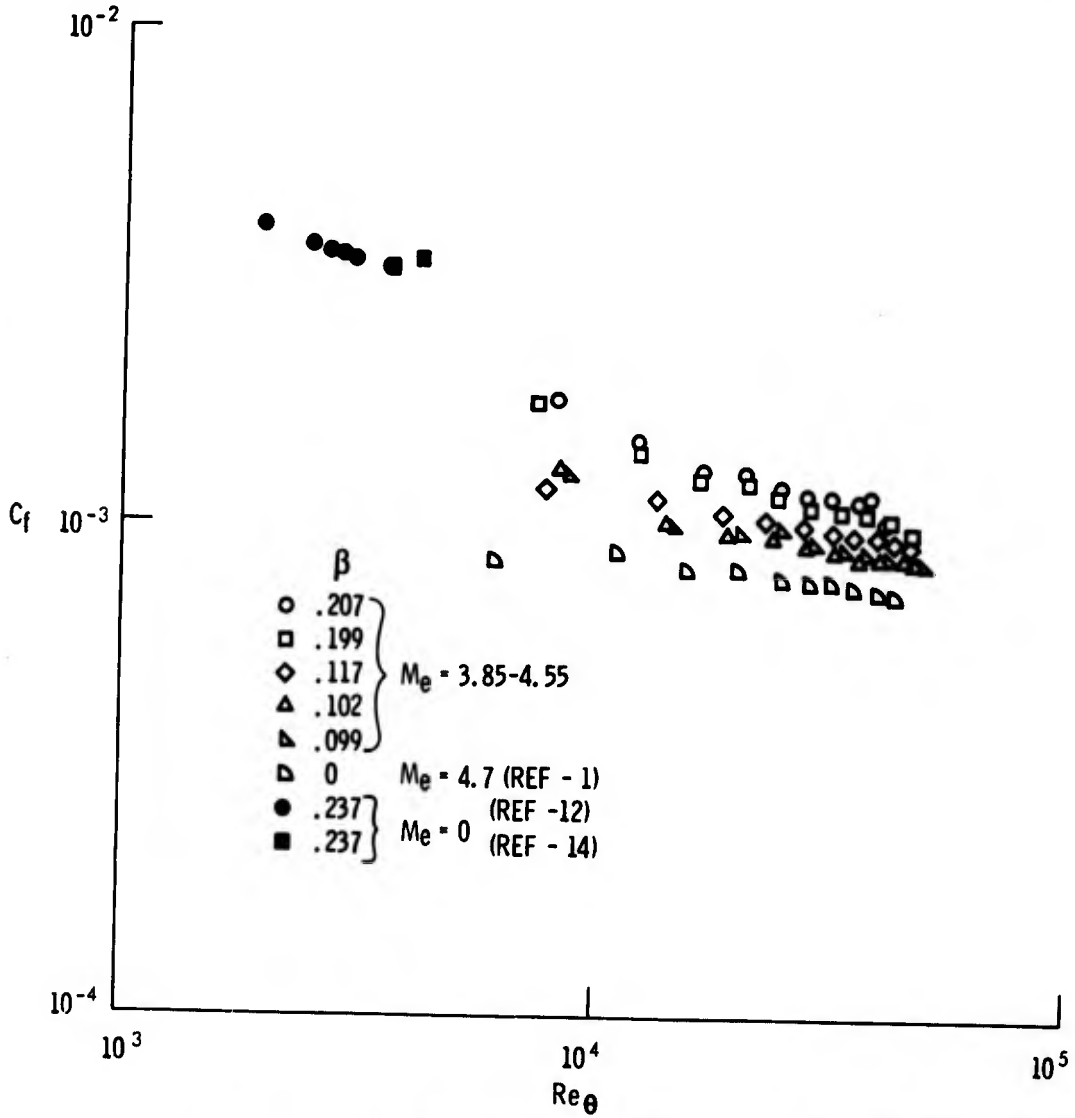


FIG. 11 SKIN FRICTION CORRELATION WITH MOMENTUM THICKNESS REYNOLDS NUMBER

**BLANK PAGE**

Paper No. 14

**AN EXPERIMENTAL REYNOLDS ANALOGY FOR THE  
HIGHLY COOLED TURBULENT BOUNDARY LAYER**

(U)

(Paper UNCLASSIFIED)

by

Donald M. Wilson  
U.S. Naval Ordnance Laboratory  
White Oak, Silver Spring, Md. 20910

**ABSTRACT.** An experimental investigation has been performed to obtain the heat-transfer and skin-friction measurements from which a Reynolds analogy for the highly cooled turbulent boundary layer could be determined. The experiments were conducted on sharp cone models at Mach number 5.0 and wall-to-stagnation temperature ratios between 0.12 and 0.80. The experimental measurements of Stanton number and average skin-friction coefficient have been compared with existing theories. These comparisons indicate that the skin friction is accurately predicted by the Sommer-Short reference temperature method, and the heat transfer, for wall-to-stagnation temperature ratios above 0.3, by the Spalding-Chi law. A direct comparison of the heat-transfer and skin-friction data indicate that Colburn's form of Reynolds analogy is valid for temperature ratios above 0.5. However, for lower ratios, the experimental Reynolds analogy decreases with decreasing wall temperature in a manner which has not been previously reported.

## SYMBOLS

As	surface area exposed to external flow
C	constant (Eq. (3))
$C_f$	local skin-friction coefficient, $\tau_w / \frac{1}{2} \rho_e U_e^2$
CF	average skin-friction coefficient, $F / \frac{1}{2} \rho_e U_e^2 A_s$
Cp	specific heat at constant pressure
d	dynamic pressure, $\frac{1}{2} \rho_e U_e^2$
F	total shear force due to skin friction
h	convective heat-transfer coefficient, $q / (T_r - T_w)$
L	total length
P	pressure
Pb	model base pressure (weighted average of 4 taps)
PB	base pressure coefficient, $(P_b - P_e) / d$
Po	supply or stagnation pressure
q	convective heat-transfer rate, per unit area
R	local Reynolds number based on length X, $\frac{\rho_e U_e X}{\mu_e}$
RL	local Reynolds number based on length L, $\frac{\rho_e U_e L}{\mu_e}$
S	Reynolds analogy factor (Eq. (7))
St	Stanton number, $h / \rho_e C_p U_e$
To	supply or stagnation temperature
Tr	recovery temperature

$T_w$	wall temperature
$U$	flow speed
$X$	distance measured streamwise along the surface from the cone tip
$y$	distance measured normal to and outward from the model surface
$\mu$	kinematic viscosity
$\rho$	density
$\tau_w$	local shear at the wall, $\mu \left. \frac{\partial U}{\partial y} \right _{y=0}$

#### Subscripts

$e$	conditions locally external to the boundary layer
$i$	incompressible flow

#### INTRODUCTION

The re-entry of a spacecraft into the atmosphere or the rapid acceleration of a high-speed aircraft is accompanied by the development of highly cooled turbulent boundary layers. Because the mechanics of turbulent flow, even for incompressible boundary layers, are not understood, there are no reliable methods available to predict the skin-friction drag or the associated aerodynamic heating of such vehicles. Historically, the solution of these problems, which involve compressible turbulent boundary layers, has depended on the use of experimental data. Examples of some of the available methods are (1) the reference temperature (or enthalpy) methods of Eckert, Ref. 1, or Sommer and Short, Ref. 2, which transform an incompressible flow to the corresponding compressible one, or (2) semiempirical theories based on the "mixing length" hypothesis such as those of Van Driest, Ref. 3, or Spalding and Chi, Ref. 4. Unfortunately, experimental data at conditions approximating the highly cooled turbulent boundary layers sometimes encountered in supersonic or hypersonic flight are very scarce. Also, an extrapolation of some of the available turbulent theories into this region will yield a widely varying result, Ref. 5.

The study of highly cooled turbulent boundary layers requires experimental data to improve prediction methods. Some quantities of interest in boundary-layer studies are the skin friction, the heat transfer and the proper Reynolds analogy relationship between them. Recent compilations of zero pressure gradient skin-friction data by Peterson, Ref. 6, and a similar heat-transfer compilation by Bertram and Neal, Ref. 7, indicated that the experimental data obtained under heat-transfer conditions cannot be accurately correlated by any single theory. However, both studies concluded that an increase in the heat-transfer rate causes an increase in the heat-transfer or skin-friction coefficient. On the other hand, heat-transfer measurements made by Gates, Noonan and Brekka, Ref. 8, and by Drougge, Ref. 9, for highly cooled turbulent boundary layers have produced some relatively low values. This indicates the opposite trend, i.e., that increases in boundary-layer heat-transfer rates will cause a decrease in the heat-transfer coefficients.

An accurate determination of the Reynolds analogy relationship between heat transfer and skin friction for the compressible turbulent boundary layer suffers from a lack of experimental data. Comparisons of heat-transfer and skin-friction data for incompressible turbulent flow were originally made by Colburn and von Karman, Refs. 10 and 11, respectively. These methods are usually assumed to be valid for the turbulent compressible problem. A few attempts have been made to obtain and compare measurements of compressible turbulent skin friction and heat transfer for similar conditions. Bradfield, Ref. 12, concluded that Colburn's Reynolds analogy was valid for adiabatic boundary layers between Mach 1 and 6, and Neal, Ref. 13, found a similar result for moderately cooled boundary layers at Mach 6.8. However, Wallace produced data for highly cooled boundary layers at Mach numbers between 6.6 and 10.7 and observed a trend to a lower-than-incompressible value for the Reynolds analogy (Ref. 14).

The behavior of highly cooled turbulent boundary layers is not understood due to the scarcity of experimental data and, in the case of heat transfer, to the existence of apparently contradictory data. Furthermore, there has been no definitive investigation to determine the Reynolds analogy relationship between skin friction and heat transfer. The need for experimental data to clarify the relationship between turbulent skin friction and heat transfer for the highly cooled boundary layer has prompted the present investigation. The results reported herein include both skin-friction and heat-transfer data for cooled, naturally

turbulent boundary layers at a free-stream Mach number of 5.0. Boundary-layer cooling was achieved by precooling the models. Wall-to-stagnation temperature ratios between 0.12 and 0.80 were obtained. A modification to Reynolds analogy was found for wall cooling rates which correspond to both a highly cooled and a moderately cooled turbulent boundary layer.

## EXPERIMENTAL EQUIPMENT AND PROCEDURE

### EXPERIMENTAL FACILITY AND TEST CONDITIONS

The tests were performed in the Naval Ordnance Laboratory's Hypersonic Tunnel. In operating this facility, the supply air is stored in separate 3000 psia and 5000 psia bottlefields and released into the tunnel through a pressure regulating valve. The air is preheated by passing it through a pebble bed heater before it enters the tunnel settling chamber and nozzle. A two-dimensional contoured nozzle, designed for operation at Mach 5.0 and used in this investigation, has an exit cross section measuring 17.25 by 17.50 inches. The tunnel was operated at supply pressures between 10 and 80 atmospheres and at supply temperatures of approximately 300°F and 750°F. All of the data were recorded by a high-speed, multi-channel, analog-to-digital data system which operates at very high sampling rates.

### MODELS

Three, 10-degree total-angle, sharp cone models were constructed, one for heat-transfer and two for skin-friction measurements. The heat-transfer cone was constructed of stainless steel. It was 10 inches long and had a nominal wall thickness of 0.020 inch. Chromel-alumel thermocouples were used to obtain temperature measurements from which Stanton numbers were reduced. Of the skin-friction models, one was used to measure total drag and the other to measure the pressure (wave) drag and the base drag. The total-drag cone was constructed of copper with a thin plating of nickel to prevent surface erosion. It contained a strain-gage balance to measure the drag (see Ref. 15). Its wall thickness was varied from 0.375 inch to 0.291 inch so that the wall temperature would increase uniformly during a test. This model also contained surface pressure taps to help align it with respect to the wind-tunnel airstream.

The second cone model was constructed of steel and contained eight surface- and four base-pressure taps. Both of the skin-friction models were 20 inches long; the extra

Vol. 2

length being needed to increase the relative magnitude of the turbulent skin-friction drag. This drag component is only about 15 percent of the total drag, and a typical measured value was about six pounds.

TEST TECHNIQUE AND DATA ACQUISITION

Prior to each test, the initial wall-to-stagnation temperature ratio was set by precooling, preheating or operating with the model at ambient temperature. Liquid nitrogen or liquid carbon dioxide provided the precooling while hot air was used for preheating. A hinged shell was built to apply the coolant or heat and to protect the model while tunnel flow was being established. This shell could be rapidly opened or closed by air pressure which was controlled by solenoid valves. The model was mounted on a pneumatically activated sting so that it could be rapidly inserted into the tunnel test section, from the cooling shell, when a test run was to be conducted.

A proven method of measuring aerodynamic heat-transfer rate for a model undergoing transient heating is the heat-pulse - or transient thin-skin - technique. The heat-transfer coefficients are customarily found by fitting polynomials through temperature-time data. Differentiating these functions yields the slope needed in the heat-pulse equation, Ref. 16. Unfortunately, this method failed for the low wall temperatures encountered in the present tests. That is, polynomials of degrees 3 through 7 were fitted through the initial 21 points but the temperature-time derivatives calculated from these curves were not consistent. This failure was blamed on the rapid decrease in model specific heat, Ref. 17, and on the decrease in experimental Stanton numbers, both for liquid nitrogen temperatures. To overcome this difficulty, a new data-reduction method was devised, Ref. 18. This method integrates the heat-pulse equation under the assumption that the model specific heat is a linear function of temperature and that the heat-transfer coefficient is a constant. The justification of these assumptions is that the integration is performed over the small time interval which corresponds to the sampling rate between two temperature recordings (0.112 seconds for these tests).

The skin-friction drag was deduced by measuring the total drag on the drag cone and subtracting the wave-drag and base-drag components which had been measured on the similar pressure cone. Only the highest supply pressure, 80 atmospheres, was used in the total-drag tests so that the

contribution of laminar skin-friction drag would be negligible in comparison with the turbulent skin-friction drag. It was discovered that the drag cone must be carefully aligned with respect to the wind-tunnel airstream because a small misalignment affects the wave drag. This is important because the wave-drag component is approximately five times as large as the turbulent skin-friction drag being sought for the 10-degree total-angle cone. The model was aligned by means of four pressure taps, located 90 degrees apart and near the base of the cone. After tunnel flow had been established, the total-drag model was pitched or yawed until the differential pressure in both the pitch and yaw planes was approximately zero. Shadowgraphs of the model were taken corresponding to pitch angles between 0 and 17 minutes. These were compared to shadowgraphs taken during the drag tests to provide a further correction for misalignment.

#### EXPERIMENTAL DATA

##### HEAT-TRANSFER DATA

Heat-Transfer data were obtained for a wide range of initial temperatures which, when run with the two supply temperatures, produced wall-to-stagnation temperature ratios between 0.12 and 0.80. The wind-tunnel supply pressure was varied to produce boundary layers on the model ranging from entirely laminar to primarily turbulent. Data for the naturally turbulent boundary layers were obtained for Reynolds numbers between 6.0 and 32.0 million.

Fig. 1 shows a representative sample of the Stanton number measurements which were made on the heat-transfer cone with a fully laminar boundary layer. It was found that, even for the lowest wall temperature ratios, the experimental data are in good agreement with the incompressible Blasius law (Ref. 19) modified by the reference temperature of Rubesin and Johnson (Ref. 20), and converted to heat transfer by Colburn's Reynolds analogy. The reference temperature method has been verified extensively by experiment and is the commonly accepted means of solving compressible laminar boundary-layer problems. General agreement of the laminar data with an accepted theory indicates that the experimental testing technique and the data-reduction method are reliable and accurate.

Fig. 2 shows some representative Stanton number measurements for those tests where transition from laminar to turbulent flow was evident. These data are compared to

Vol. 2

Young's incompressible law, Ref. 21, modified for compressibility by the Sommer-Short reference temperature method, Ref. 2, and to the Spalding-Chi semiempirical method, Ref. 4. These laws were converted to heat transfer by use of Colburn's Reynolds analogy. An examination of this figure, and a consideration of all other heat-transfer data of these tests, indicate that the Spalding-Chi law accurately represents the data for wall-to-stagnation temperature ratios between 0.3 and 0.8. These data are in general agreement with other wind-tunnel data obtained under similar conditions, for example, the data of Refs. 22 and 23. However, for severe wall cooling rates, indicated by wall temperature ratios less than 0.3, the Stanton number was observed to decrease with increased wall cooling rate. The relatively low Stanton numbers observed for a wall temperature ratio of 0.15 in Fig. 2 are in general agreement with the data of Refs. 8 and 9 but do not agree with the data of Refs. 7 and 24. The reason for this apparent discrepancy is unknown. A possible explanation is that the decrease in Stanton number may depend on other parameters in addition to the wall temperature ratio, for example, the Mach or Reynolds numbers. The amount of highly cooled wall heat-transfer data presently available is too scant to explore this possibility.

SKIN-FRICTION DATA

The turbulent skin-friction drag was deduced by subtracting the pressure drag and base drag from the measurement of total drag. Surface and base-pressure coefficients were measured in separate tests using an uncooled model. The surface-pressure coefficients were found to be in excellent agreement with values tabulated in Ref. 25. The base-pressure coefficient was computed from pressure measurements made at four base stations. These are plotted in Fig. 3 against the Reynolds number based on total cone length. The data of Fig. 3 are in excellent agreement with the base-pressure coefficients given in Ref. 26 for a 9.5-degree total-angle sharp cone.

An average skin-friction coefficient was calculated from the experimentally determined turbulent skin-friction drag. Fig. 4 shows the average turbulent skin-friction coefficient compared with Young's law and Sommer-Short reference temperature method for the Reynolds numbers which resulted from the use of the two supply temperatures. The experimental data are in excellent agreement with the modified Young's law for wall-to-stagnation temperature ratios between 0.19 and 0.73. This agreement was expected since the reference temperature method of Sommer and Short was based on data for

both supersonic and low hypersonic Mach numbers and for wall temperature ratios as low as 0.16. Furthermore, an attempt by Peterson and Monta (Ref. 27) to determine the superiority of either the Sommer and Short method or Spalding-Chi laws for skin friction was inconclusive.

## CORRELATION AND COMPARISON OF DATA

### STANTON NUMBER CORRELATION

All of the turbulent heat-transfer data have been correlated by comparing the measured (compressible) Stanton numbers with an incompressible reference value for the wall-to-stagnation temperature ratios achieved in these tests. The incompressible Stanton number was derived from Young's law and Colburn's Reynolds analogy. The resulting expression is given in Ref. 28 for cone flow. It is

$$St_i = \frac{0.026}{R^{1/6}} \quad (1)$$

Correlation of the experimental data will be based on the assumption that the compressible Stanton number variation with Reynolds number can be approximated by a one-sixth power law similar to that given by Eq. (1). Unfortunately, this assumption could not be experimentally verified due to scatter in the data. However, the assumption that incompressible and compressible flow quantities vary in a similar way with Reynolds number forms the basis for the reference temperature methods in common usage.

The data correlation was made in the following manner. First, Stanton number distributions along the model, similar to those shown in Fig. 2, are found for several wall-to-stagnation temperature ratios of each test. Secondly, least square fits are made to this data to determine an equation for Stanton number in terms of Reynolds number to the minus one-sixth power. Finally, these equations are compared with the incompressible reference value given by Eq. (1). The result is a correlation of compressible to incompressible Stanton number ratio in terms of the wall temperature ratio. A correlation of all of the heat-transfer data was made and compared with the Young and Sommer-Short law and with the Spalding-Chi law. This is shown in Fig. 5.

Fig. 5 indicates that the compressible turbulent Stanton number will increase from a relatively low value to a value predicted by the Spalding-Chi law as the wall temperature ratio is increased from 0.12 to approximately 0.30. For wall temperature ratios above 0.3, little effect of wall temperature on the Stanton number is present. The latter result is in agreement with the Spalding-Chi law and was a conclusion reached by Bertram and Neal (Ref. 7) for Mach numbers of 5.0 or greater. It should be noted that the spread in experimental data shown in Fig. 5 is due partly to scatter and partly to an effect of Reynolds number. That is, it was found that Stanton numbers corresponding to high Reynolds numbers were slightly lower than those for a lower Reynolds number, at the same wall temperature ratio. This effect causes the spread in the comparative laws used in Fig. 5 since these are also based on experimental data.

The decrease in Stanton number, with decreasing wall temperature ratio for a highly cooled turbulent boundary layer, was previously noted explicitly only in the experimental data of Ref. 9. In these experiments, the Mach number, supply temperature and model wall temperatures are remarkably close to those of the present tests. The only significant difference between the tests is that, for the data of Ref. 9, the Reynolds numbers are much lower and tripping was necessary to achieve a turbulent boundary layer. These data are correlated in a manner identical to the present correlation method, except that the turbulent Blasius law (Ref. 19) was used with Colburn's Reynolds analogy to obtain the incompressible Stanton number, and the compressible Stanton numbers were taken to vary inversely with the fifth power of the Reynolds number. Fig. 6 shows a correlation of the data of Ref. 9 and its comparison with the Spalding-Chi law and with the Blasius law and Sommer-Short reference temperature method. This correlation is in good general agreement with the correlation given in Fig. 5. The notable difference between correlations is that the decrease in Stanton number with decreasing wall temperature ratio begins at a lower value, approximately 0.2. This difference may be due to a Reynolds number effect on the point where the Stanton number can be expected to decrease.

#### SKIN-FRICTION COEFFICIENT CORRELATION

The measured average skin-friction coefficient must be converted to a local coefficient in order to directly compare the heat-transfer and skin-friction data. From their definitions, the relationship between the average and local

skin-friction coefficient for cone flow is:

$$C_F = 2 \int_0^1 C_f \cdot \left(\frac{x}{L}\right) \cdot d\left(\frac{x}{L}\right) \quad (2)$$

The local coefficients were deduced from the average coefficients in the following manner. First, the assumption was made that the local coefficient varies inversely with the one-sixth power of Reynolds number. This can be expressed mathematically as:

$$C_f = \frac{C}{R^{1/6}} \quad (3)$$

Here, the proportionality constant,  $C$ , is a function of temperature only. Eq. (3) is consistent with the heat-transfer data. Furthermore, it was shown in Ref. 28 that the one-sixth power of Reynolds number accurately represents incompressible turbulent skin-friction data. Secondly, Eq. (2) is integrated, with the help of Eq. (3), to yield an expression for the unknown proportionality constant,  $C$ . The result is:

$$C = 0.0917 \cdot C_F \cdot R_L^{1/6} \quad (4)$$

The local skin-friction coefficient can be found from Eqs. (3) and (4). However, it is more convenient to find the ratio of compressible to incompressible skin-friction coefficient since this ratio can be compared to the Stanton number ratios previously obtained. The incompressible skin-friction coefficient for cone flow, according to Young's law, is given in Ref. 28 as:

$$C_{fi} = \frac{0.0429}{R^{1/6}} \quad (5)$$

The final step is to compute the skin-friction coefficient ratio through a comparisons of Eqs. (3), (4) and (5). The result is:

$$\frac{C_f}{C_{fi}} = 2.167 \cdot C_F \cdot R_L^{1/6} \quad (6)$$

Fig. 7 presents the skin-friction coefficient ratio as calculated from the measured average skin-friction coefficients for all of the wall-to-stagnation temperature ratios realized in these tests. Note that only two Reynolds number conditions were obtained, i.e., those conditions which resulted from the use of the two supply temperatures and the single supply pressure. Also shown on Fig. 7 are Stanton number ratios which correspond to the same Reynolds numbers as the skin-friction coefficient ratios. Here the experimental data is in a form where it can be directly compared to determine a Reynolds analogy relationship.

#### EVALUATION OF REYNOLDS ANALOGY

The Reynolds analogy relating boundary-layer heat transfer to skin friction was originally formulated by Reynolds (Ref. 29) who maintained that the Stanton number was equal to one-half of the local skin-friction coefficient. The Reynolds analogy concept was successfully extended to incompressible turbulent flows by Colburn (Ref. 10) and later, von Karman (Ref. 11). Theoretical work has been done to relate compressible turbulent heat transfer to skin friction (Refs. 30 and 31). Unfortunately, their validity could not be judged due to the lack of experimental data. Furthermore, neither theory was in agreement with all of the Reynolds analogy data found below.

A Reynolds analogy factor,  $S$ , defined as the ratio of Stanton number to one-half the local skin-friction coefficient, will be sought, i.e.,

$$S = \frac{2St}{C_f} \quad (7)$$

This factor will be computed from the experimental data shown in Fig. 7. For example, let

$$S = \frac{2St/St_i}{C_f/C_{fi}} \cdot \frac{St_i}{C_{fi}} \quad (8)$$

where the ratio  $St_i/C_{fi}$  for incompressible turbulent flow will be given by Colburn's Reynolds analogy.

Fig. 8 shows an average value of the compressible turbulent Reynolds analogy factor as calculated from Eq. (8) and the curves faired through the data of Fig. 7. This figure shows that the compressible turbulent Reynolds analogy factor approaches the incompressible prediction of approximately 1.2

for wall temperature ratios above 0.5. However, for wall temperature ratios less than 0.5, the Reynolds analogy factor decreases rapidly. This behavior has not been previously defined, either theoretically or experimentally, except for the relatively low Reynolds analogy factors obtained by Wallace (Ref. 14) for wall temperature ratios between 0.09 and 0.30. The data of Fig. 8 are in good qualitative agreement with the data of Ref. 14 for wall temperature ratios between 0.20 and 0.30.

### CONCLUSIONS

An experimental investigation into the effects of extreme and moderate wall cooling on hypersonic turbulent heat transfer and skin friction has been carried out at Mach 5.0 and for wall-to-stagnation temperature ratios between 0.12 and 0.80. Based on the experimental results, the following conclusions have been reached.

1. The experimental laminar Stanton numbers are accurately predicted by the incompressible Blasius law, modified by the reference temperature method of Rubesin and Johnson, for all of the wall temperature ratios of these tests.
2. The measured turbulent Stanton numbers may best be predicted by the Spalding-Chi law for wall temperature ratios between 0.3 and 0.8.
3. For wall temperature ratios less than 0.3, the turbulent Stanton number decreases rapidly with decreasing wall temperatures. This behavior is not predicted by any available law.
4. The turbulent skin-friction coefficient is in excellent agreement with Young's incompressible law, modified by the reference temperature method of Sommer and Short, for the wall temperature ratios tested, i.e.,  $0.19 < T_w/T_o < 0.73$ .
5. The Reynolds analogy relationship for the compressible turbulent flow is adequately represented by Colburn's and von Karman's incompressible forms for wall temperature ratios above approximately 0.5.
6. For wall temperature ratios less than 0.5, the compressible turbulent Reynolds analogy factor was observed to decrease, slowly at first but rapidly for wall temperature

ratio less than 0.3. This behavior is due to the effect of extreme wall cooling on Stanton number.

7. The rapid decrease in turbulent Stanton numbers at very low wall temperature ratios was not observed when a laminar boundary layer was present. Although laminar skin-friction data were not obtained, the heat-transfer data imply that the Reynolds analogy factor for compressible laminar boundary layers can be approximated by Colburn's or von Karman's law for all of the wall temperature ratios of these tests.

#### REFERENCES

1. Journal of Aerospace Sciences. Engineering Relations for Friction and Heat Transfer to Surfaces in High Velocity Flow, by E. R. G. Eckert. August 1956. pp. 585-587. (Vol. 23, No. 8, publication UNCLASSIFIED.)
2. Journal of Aerospace Sciences. Free Flight Measurements of Skin Friction of Turbulent Boundary Layers with High Rates of Heat Transfer at High Supersonic Speeds, by S. C. Somner and B. J. Short. June 1956. 7 pp. (publication UNCLASSIFIED.)
3. Journal of Aerospace Sciences. Turbulent Boundary Layer in Compressible Fluids, by E. R. Van Driest. March 1951. pp. 145-160. (Vol. 18, No. 3, publication UNCLASSIFIED.)
4. Journal of Fluid Mechanics. The Drag of a Compressible Turbulent Boundary Layer on a Smooth Flat Plate with and without Heat Transfer, by D. B. Spalding and S. W. Chi. 1964. pp. 117-143. (Vol. 18, publication UNCLASSIFIED.)
5. U. S. Naval Ordnance Laboratory. A Digital Computer Program for Making Comparative Aerodynamic Heat Transfer and Skin Friction Drag Calculations, by D. M. Wilson. White Oak, Silver Spring, Md., NOL, August 1967. 23 pp. (NOLTR 67-137, publication UNCLASSIFIED.)
6. National Aeronautics and Space Administration. A Comparison of Experimental and Theoretical Results for the Compressible Turbulent-Boundary Layer Skin Friction with Zero Pressure Gradient, by J. B. Peterson, Jr. Langley Field, Va., NASA, March 1963. 55 pp. (TN D-1795, publication UNCLASSIFIED.)

7. National Aeronautics and Space Administration. Recent Experiments in Hypersonic Turbulent Boundary Layers, by M. H. Bertram and L. Neal, Jr. Langley Field, Va., NASA, May 1965. 22 pp. (TMX-56335, publication UNCLASSIFIED.)
8. U. S. Naval Ordnance Laboratory. Heat Transfer Measurements on a Flat Plate in the NOL Hypersonic Shock Tunnel No. 1, by D. F. Gates, B. J. Noonan and L. Brekka. White Oak, Silver Spring, Md., NOL, October 1964. 26 pp. (NOLTR 61-91, publication UNCLASSIFIED.)
9. The Aeronautical Research Institute of Sweden. Measurements of Heat Transfer in a Highly Cooled Turbulent Boundary Layer at  $M = 4.6$  and 7, by G. Drougge. FFA (Sweden), April 1965. 83 pp. (AU-120:4, DEL II, publication UNCLASSIFIED.)
10. Transactions of American Institute of Chemical Engineers. A Method of Correlating Forced Convection Heat Transfer Data and a Comparison with Fluid Friction, by A. P. Colburn. 1933. pp. 174-210. (Vol. 29, publication UNCLASSIFIED.)
11. Transactions of American Society of Mechanical Engineers. The Analogy Between Fluid Friction and Heat Transfer, by T. von Karman. November 1939. pp. 705-710. (Vol 61, No. 8, publication UNCLASSIFIED.)
12. Journal of Heat Transfer. Conical Turbulent Boundary Layer Experiments and a Correlation with Flat Plate Data, by W. S. Bradfield. May 1960. pp. 94-100. (publication UNCLASSIFIED.)
13. National Aeronautics and Space Administration. Pressure, Heat Transfer and Skin Friction Distributions over a Flat Plate having Various Degrees of Leading Edge Bluntness at a Mach Number of 6.8, by L. Neal, Jr. Langley Field, Va., NASA, April 1966. (TN D-3312, publication UNCLASSIFIED.)
14. Proceedings 1967 Heat Transfer and Fluid Mechanics Institute. Hypersonic Turbulent Boundary-Layer Studies at Cold Wall Conditions, by J. E. Wallace. La Jolla, Calif., 1967. pp. 427-451. (publication UNCLASSIFIED.)
15. U. S. Naval Ordnance Laboratory. NOL Wind Tunnel Internal Strain-Gage Balance System, by J. Shantz, B. D. Gilbert and C. E. White. White Oak, Silver Spring, Md. NOL, September 1953. (NAVORD Report 2972, publication UNCLASSIFIED.)

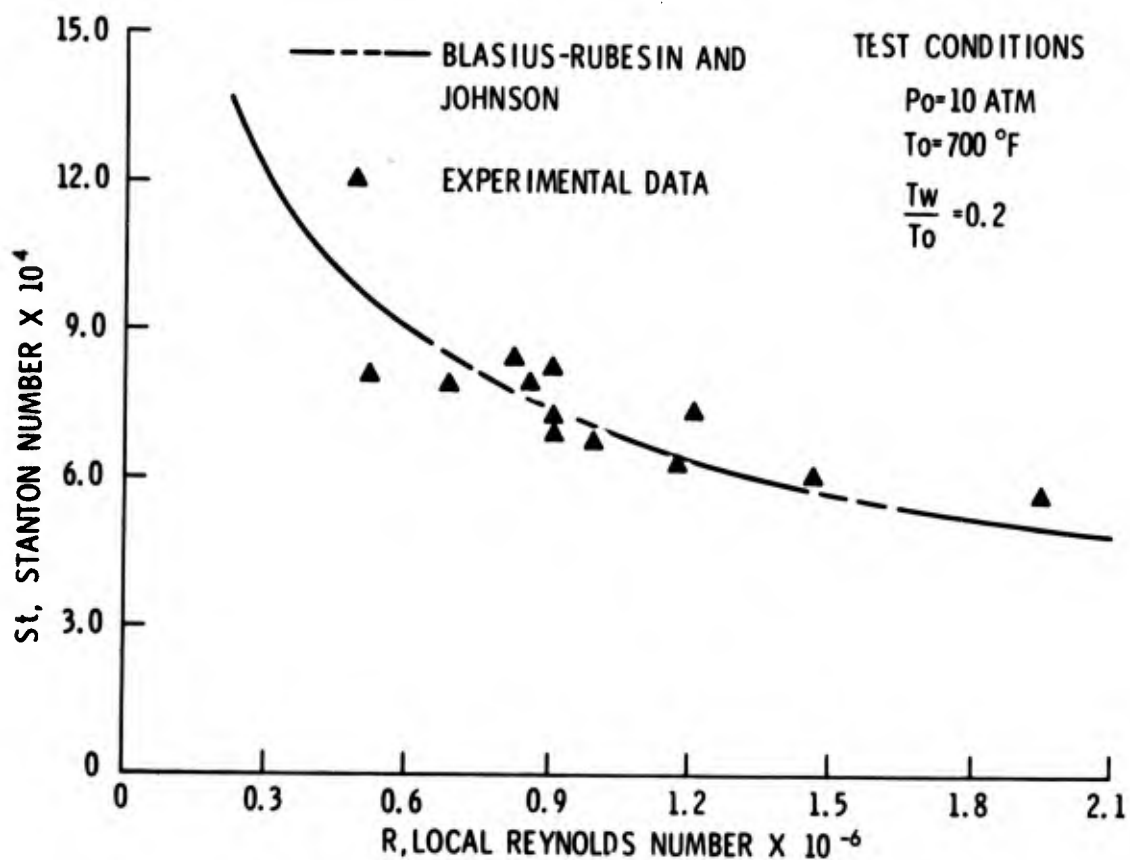
## 8th Navy Symposium on Aeroballistics

---

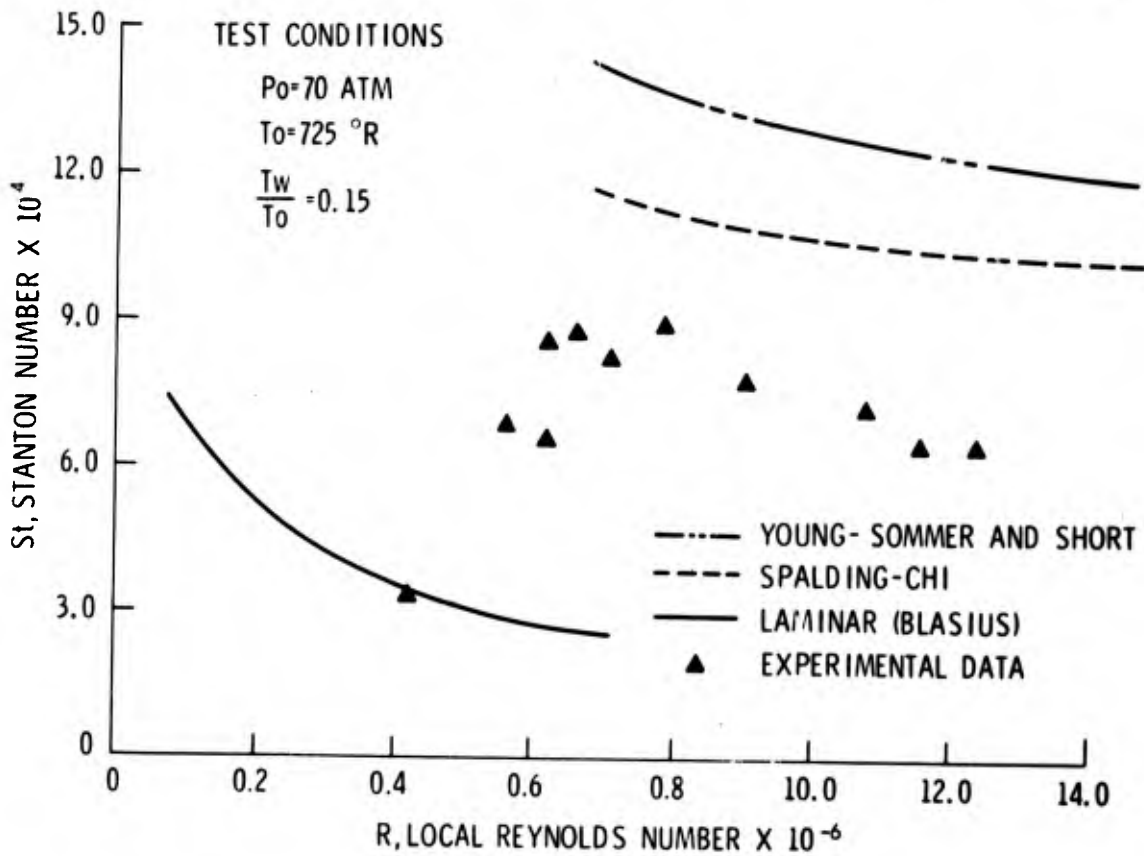
### Vol. 2

16. Aeronautical Research Council (London). Measurements of Aerodynamic Heating on a  $15^\circ$  Cone of Graded Wall Thickness at a Mach Number of 6.8, by J. G. Woodley. London, England, 1964. 26 pp. (Report No. 3357, publication UNCLASSIFIED.)
17. U. S. Naval Ordnance Laboratory. Measurements of Hypersonic Turbulent Heat Transfer on a Highly Cooled Cone, by D. M. Wilson. White Oak, Silver Spring, Md., NOL, August 1967. 34 pp. (NOLTR 67-24, publication UNCLASSIFIED.)
18. Proceedings 1966 Heat Transfer and Fluid Mechanics Institute. Measurements of Hypersonic Turbulent Heat Transfer on Cooled Cones, by D. M. Wilson and P. D. Fisher. 1966. pp. 236-252. (publication UNCLASSIFIED.)
19. McGraw-Hill. Boundary Layer Theory, by H. Schlichting. New York, 1955. pp. 123-126, 430-441. (1st ed., publication UNCLASSIFIED.)
20. Transactions of Society of Mechanical Engineers. A Critical Review of Skin-Friction and Heat Transfer Solutions of the Laminar Boundary Layer of a Flat Plate, by M. W. Rubesin and H. A. Johnson. May 1949. p. 383. (Vol. 71, No. 4, publication UNCLASSIFIED.)
21. Aeronautical Research Council (London). Calculation of the Profile Drag of Aerofoils and Bodies of Revolution at Supersonic Speeds, by A. D. Young. London, England, 1953. (Report 15970, publication UNCLASSIFIED.)
22. National Aeronautics and Space Administration. Effects of Mach Number and Wall Temperature Ratio on Turbulent Heat Transfer at Mach Numbers from 3 to 5, by T. Tendeland. NASA, 1959. 16 pp. (TR R-16, publication UNCLASSIFIED.)
23. National Aeronautics and Space Administration. Experimental Investigation of the Heat Transfer Rate to a Series of  $20^\circ$  Cones of Various Surface Finishes at a Mach Number of 4.95, by J. J. Jones. NASA, June 1959. 26 pp. (Memo. 6-10-59L, publication UNCLASSIFIED.)
24. Eighth Aerospace Sciences Meeting, AIAA. An Experimental Investigation of Heat Transfer from a Highly Cooled Turbulent Boundary Layer, by R. M. Nerem and R. A. Hopkins. New York, N. Y., January 1968. 13 pp. (Paper 68-43, publication UNCLASSIFIED.)

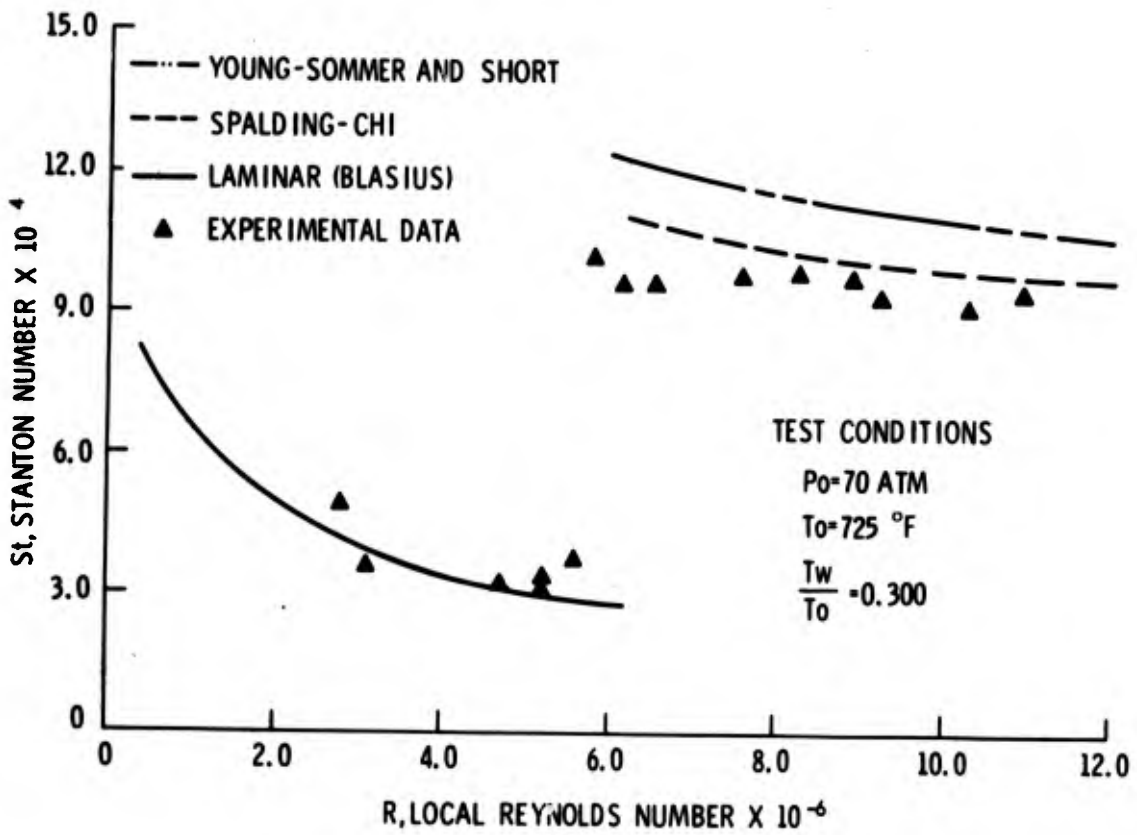
25. National Aeronautics and Space Administration. Tables for Supersonic Flow around Right Circular Cones at Zero Angle of Attack, by J. L. Sims. NASA, 1964. (SP-3004, publication UNCLASSIFIED.)
26. Ballistics Research Laboratory. Base Pressure Measurements on Sharp and Blunt  $9^\circ$  Cones at Mach Numbers from 3.50 to 9.20, by N. A. Zarin. Aberdeen Proving Ground, Md., BRL, November 1965. 36 pp. (Memo Report No. 1709, publication UNCLASSIFIED.)
27. National Aeronautics and Space Administration. Considerations Regarding the Evaluation and Reduction of Supersonic Skin Friction, by J. B. Peterson, Jr. Langley Field, Va., NASA, October 1966. (TN D-3588, publication UNCLASSIFIED.)
28. U. S. Naval Ordnance Laboratory. A Correlation of Heat Transfer and Skin Friction Data and an Experimental Reynolds Analogy Factor for Highly Cooled Turbulent Boundary Layers at Mach 5.0, by D. M. Wilson. White Oak, Silver Spring, Md., NOL, March 1969. (NOLTR 69-51, in publication, publication UNCLASSIFIED.)
29. Proceedings of Manchester Literary and Philosophical Society. On the Extent and Action of the Heating Surface for Steam Boilers, by O. Reynolds. 1874. (Vol. 14, publication UNCLASSIFIED.)
30. U. S. Naval Ordnance Laboratory. A Semi-Empirical Derivation of Friction Heat-Transfer, and Mass-Transfer Coefficients for the Constant Property Turbulent Boundary Layer on a Flat Plate, by N. Tetervin. White Oak, Silver Spring, Md., NOL, July 1963. (NOLTR 63-77, publication UNCLASSIFIED.)
31. National Advisory Committee for Aeronautics. A Modified Reynolds Analogy for the Compressible Turbulent Boundary Layer on a Flat Plate, by M. W. Rubesin. Moffett Field, Calif., NACA, March 1953. 23 pp. (TN 2917, publication UNCLASSIFIED.)



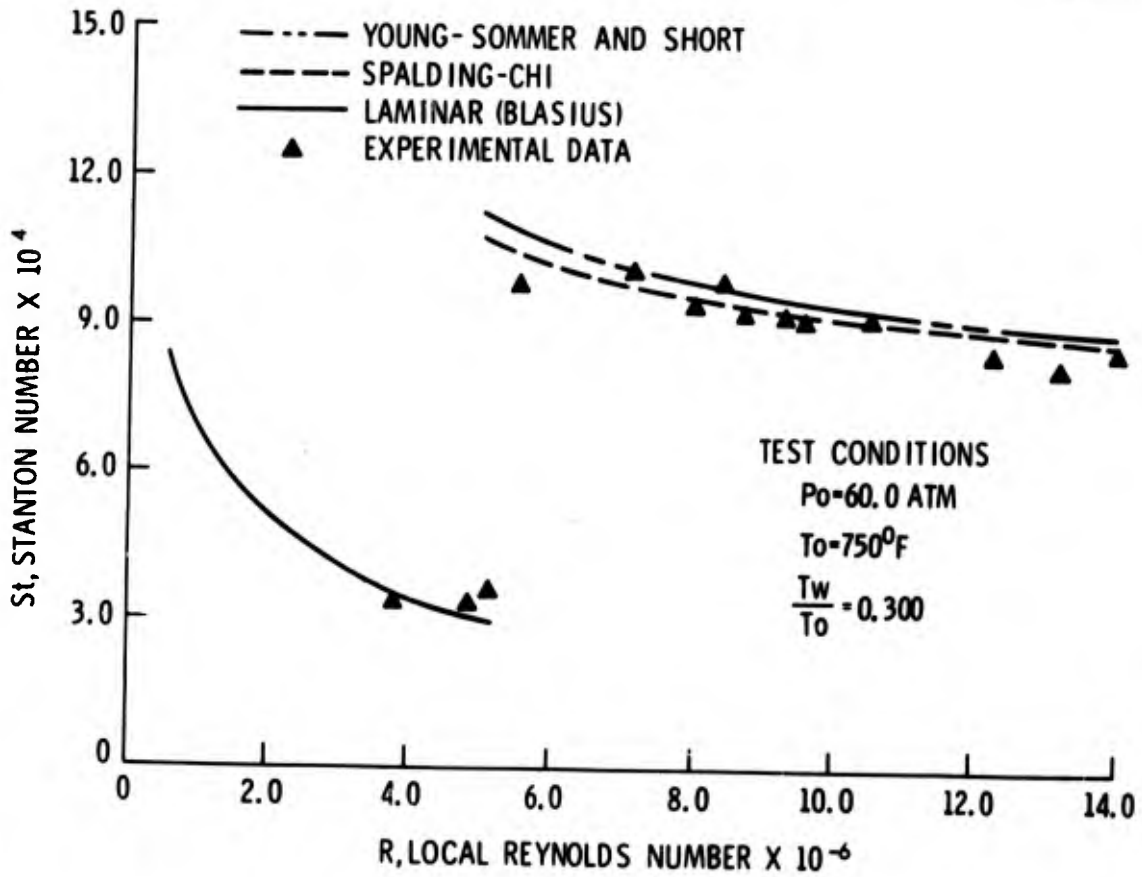
(U) FIG. 1 Heat Transfer Measurements for a Laminar Boundary Layer



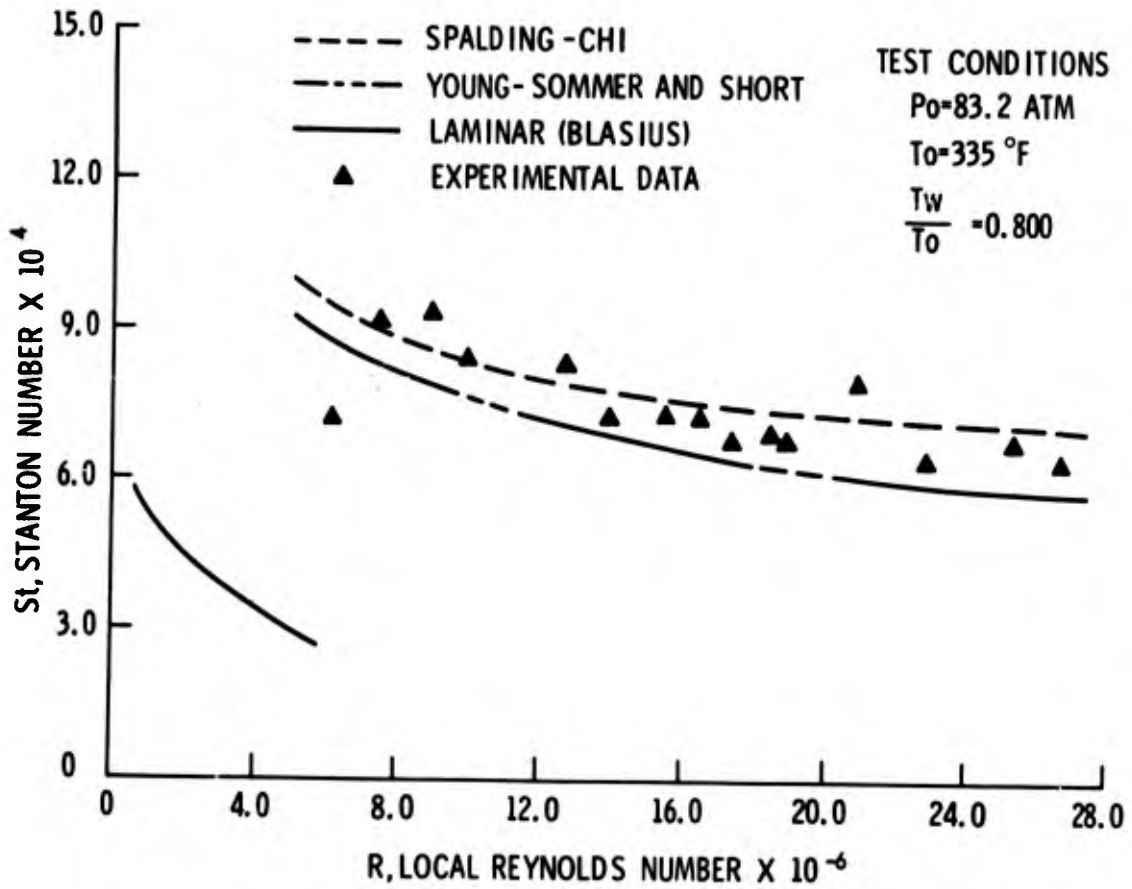
(U) FIG. 2a Turbulent Heat Transfer Measurements for a Wall to Stagnation Temperature Ratio of 0.15



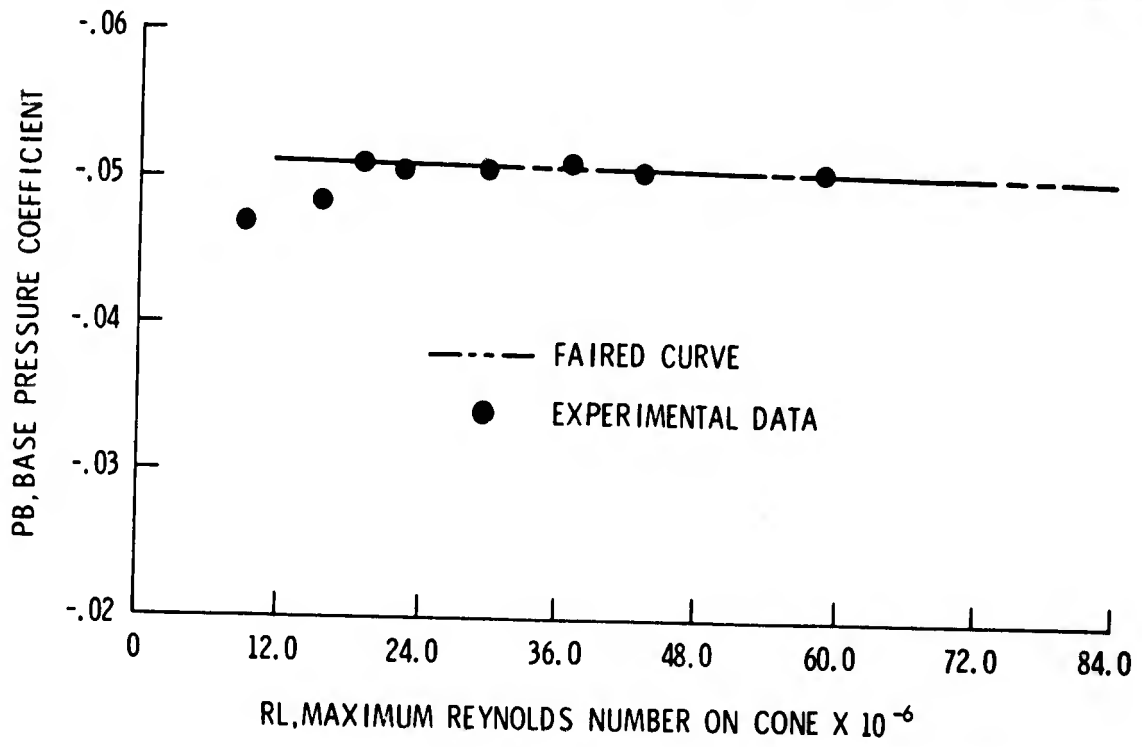
(U) FIG. 2b Turbulent Heat Transfer Measurements for a Wall to Stagnation Temperature Ratio of 0.30



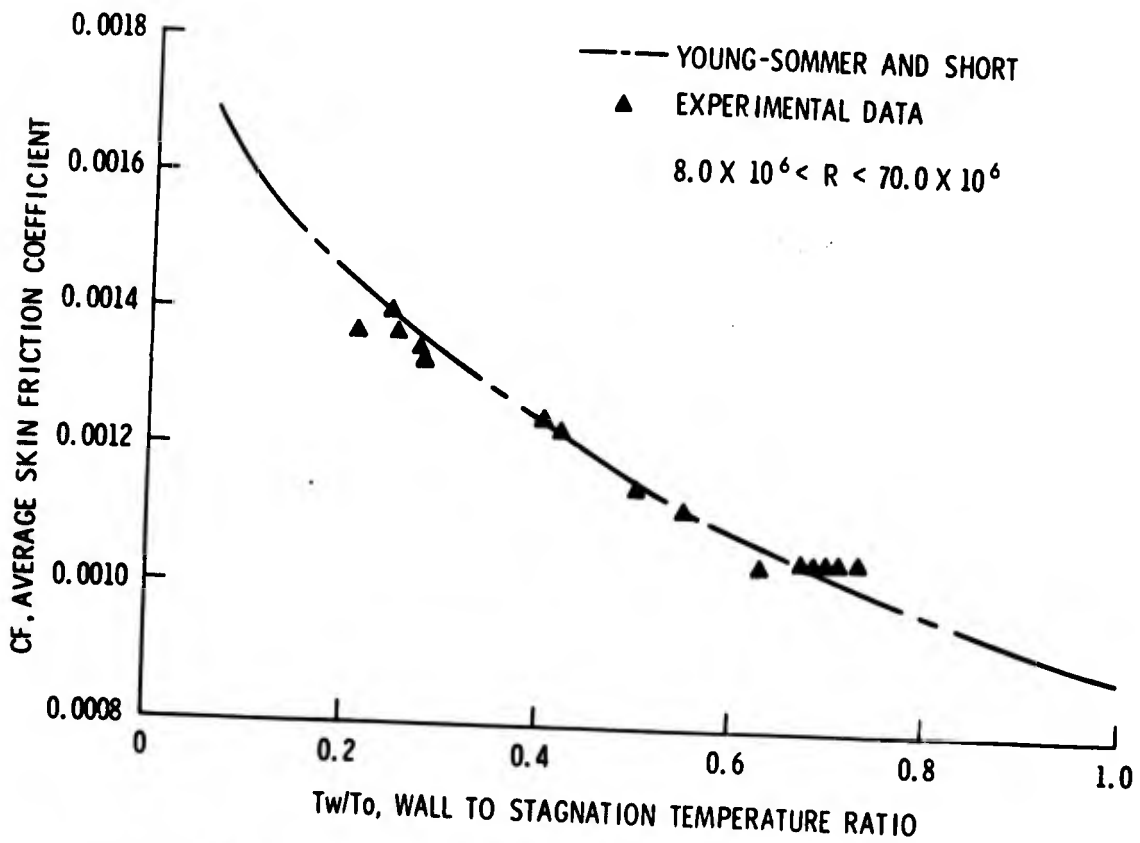
(U) FIG. 2c Turbulent Heat Transfer Measurements for a Wall to Stagnation Temperature Ratio of 0.50



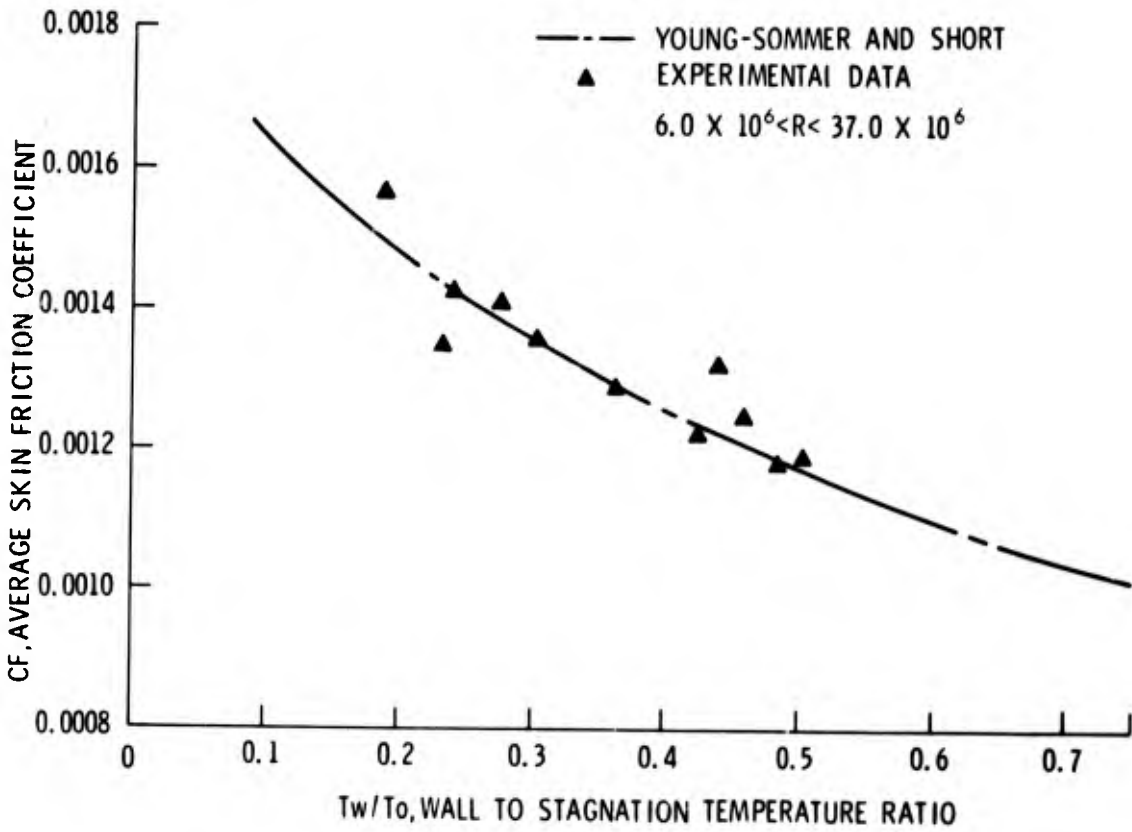
(U) FIG. 2d Turbulent Heat Transfer Measurements for a Wall to Stagnation Temperature Ratio of 0.80



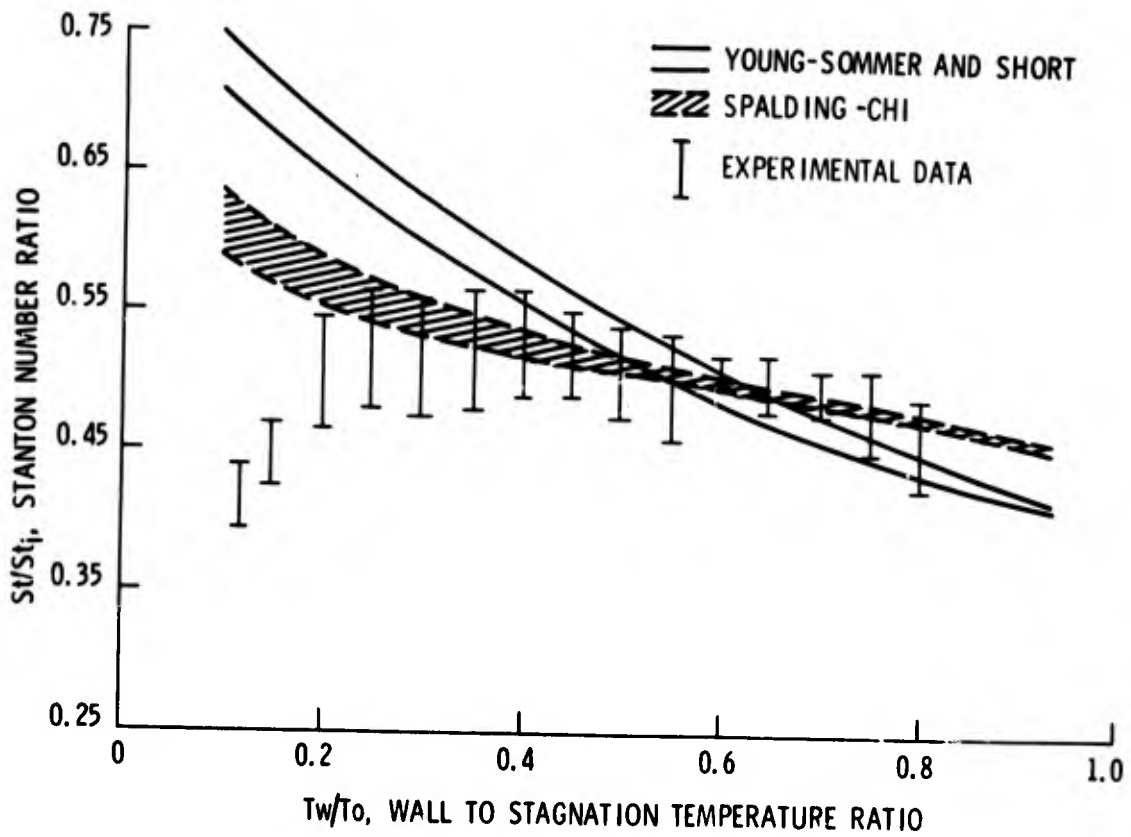
(U) FIG. 3 Base Pressure Coefficient versus Maximum Reynolds Number



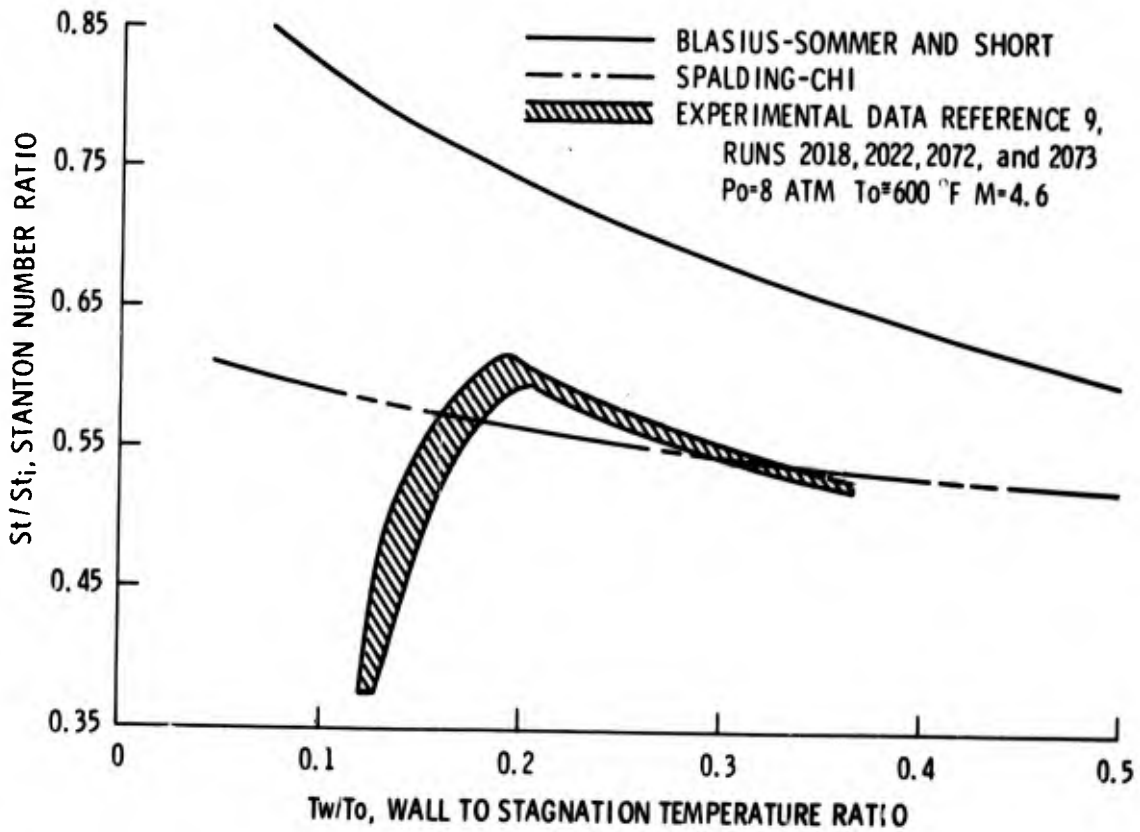
(U) FIG. 4a Average Turbulent Drag Coefficient for the 350 °F Supply Temperature



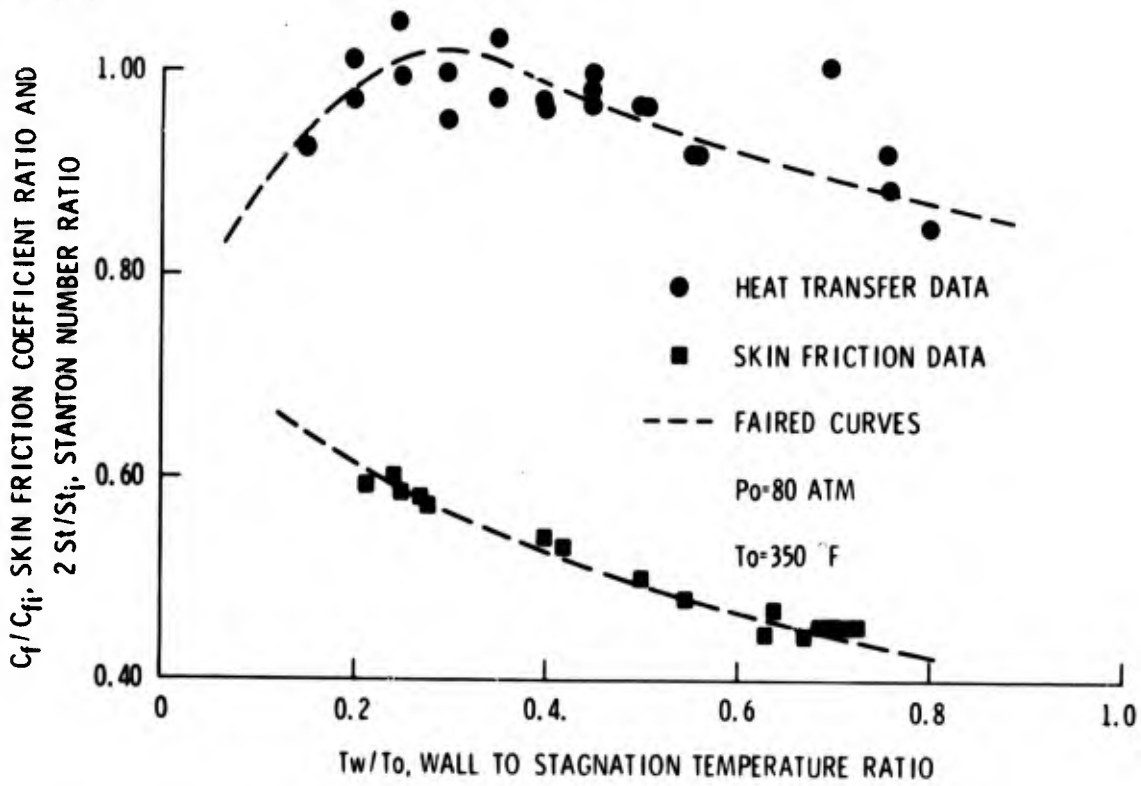
(U) FIG. 4b Average Turbulent Drag Coefficient for the 750 °F Supply Temperature



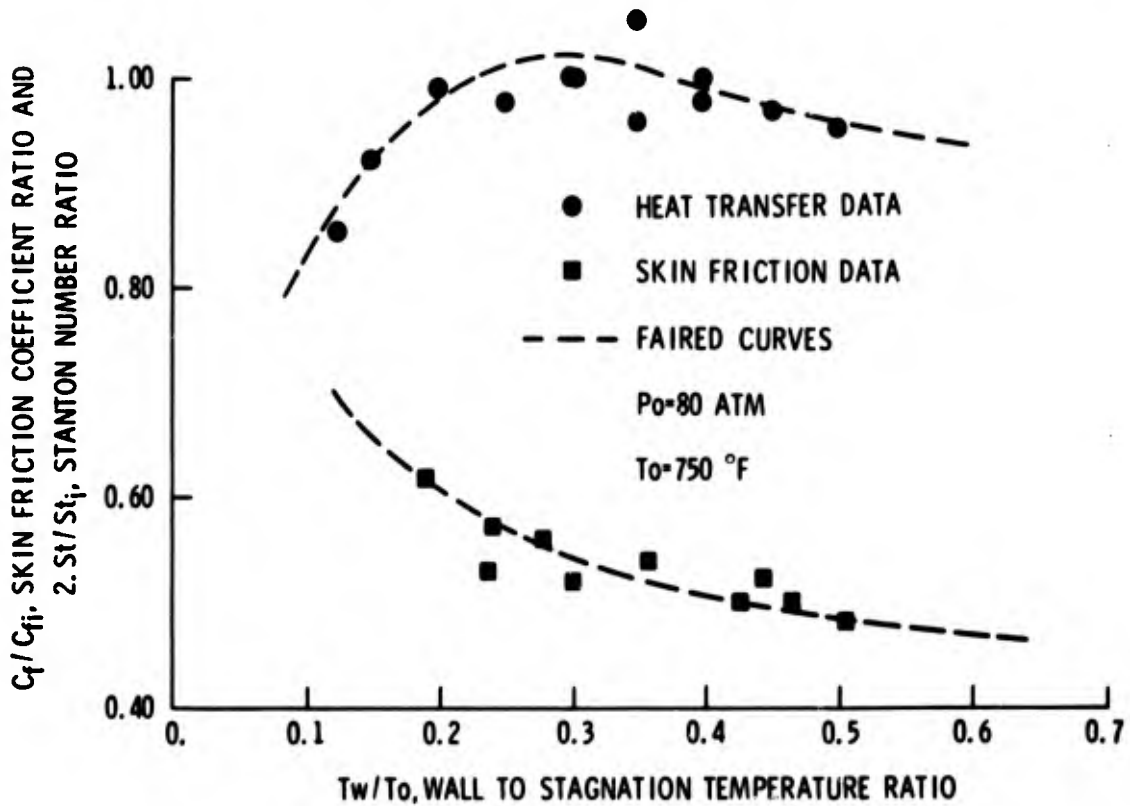
(U) FIG. 5 A compilation of all Experimental Heat Transfer Data



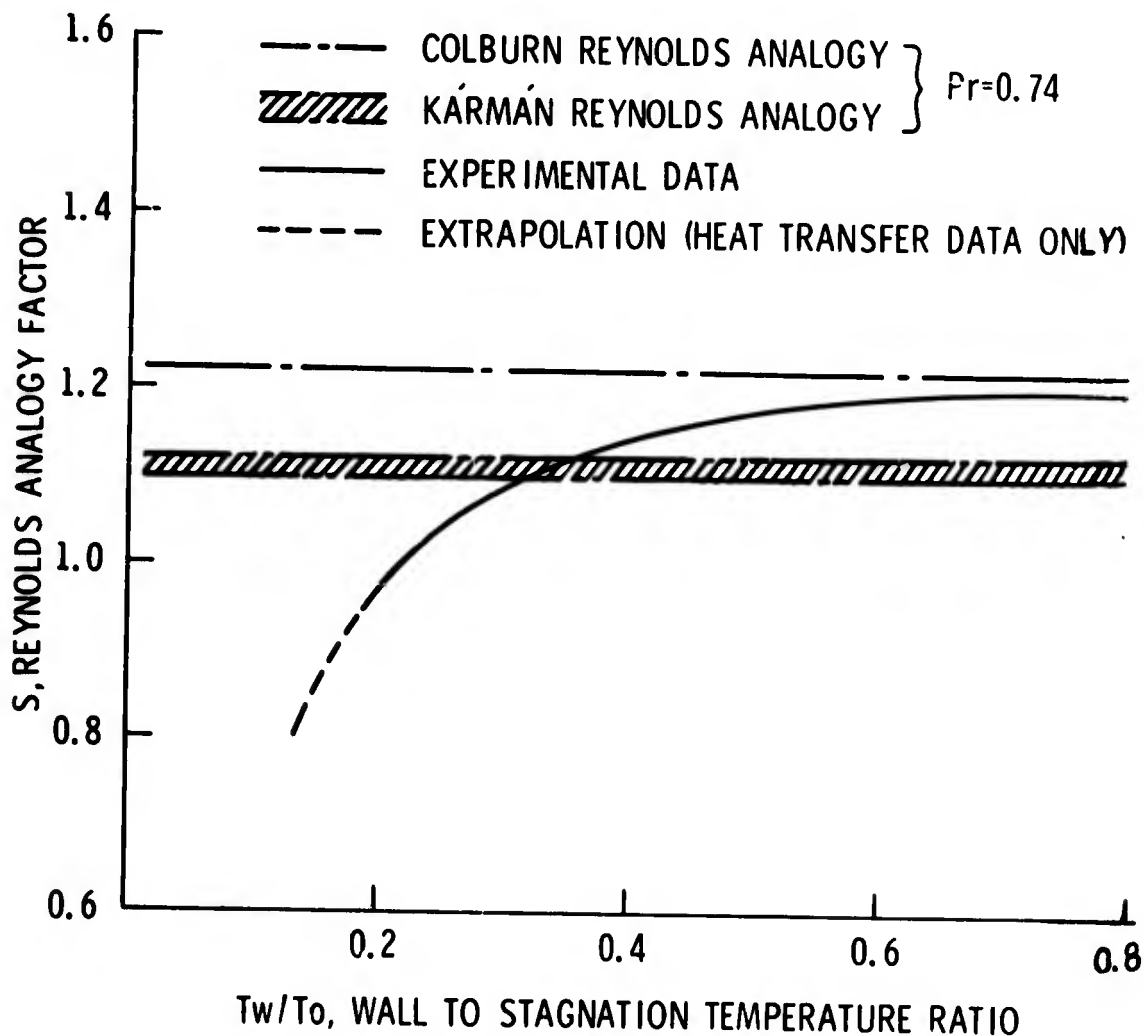
(U) FIG. 6 Correlation of the Heat Transfer Data Given in Reference 9



(U) FIG. 7a Comparison of Heat Transfer and Skin Friction Data for the 350 °F Supply Temperature



(U) FIG. 7b Comparison of Heat Transfer and Skin Friction Data for the 750 °F Supply Temperature



(U) FIG. 8 Experimental Reynolds Analogy Factor

Paper No. 15

**THE EFFECT OF FLOW FIELD IRREGULARITIES ON  
SWEEP LEADING EDGE HEAT TRANSFER**

(U)

(Paper UNCLASSIFIED)

by

Albert F. Gollnick  
M.I.T. Aerophysics Laboratory  
Cambridge, Mass. 02139

ABSTRACT. (U) Stagnation line heat transfer distributions were obtained on blunt swept leading edges at Mach 3.66 and a unit Reynolds number of  $2.1 \times 10^5$  per foot. Pressure distributions were obtained for comparable test conditions. The results illustrate the effects of various flow nonuniformities on leading edge heat transfer and pressure, including those arising from: finite span and nonuniform leading edge sweep, free stream nonuniformity induced by the bow shock of a typical blunt body, boundary interaction near the leading edge root, and impingement of a trailing tip vortex. At present none of these effects can be predicted analytically and all may lead to significant deviation from the levels based on infinite cylinder theory. The importance of the individual results are discussed and, where possible, appropriate design criteria are presented.

INTRODUCTION

(U) It is well known that the heat flux to the wing leading edge can produce severe burdens on the adjacent structure as vehicle operating speeds are increased into the high supersonic regime. Ideally the problem can be alleviated by selecting a suitable combination of leading edge bluntness and sweep angle, based on predicted heat transfer levels. However both of these techniques can adversely affect vehicle performance, so it is most important that the aerodynamic heating analysis be very accurate and also be applicable to a wide range of vehicle geometries and flight conditions. In the case of a laminar leading edge boundary layer, a two-dimensional analysis has been used, based on an idealized model of the flow, corresponding to that on an infinitely long cylinder of constant sweep (Ref. 1,2). Recently a number of potentially fruitful analyses of the full three-dimensional boundary layer problem have been published (Ref. 3-7), which focus attention on the leading edge stagnation line, where the highest heat flux will normally occur. The limits on the applicability of the infinite cylinder analyses, in terms of Mach and Reynolds number; sweep angle and wing angle of attack are fairly well defined (Ref. 8,9), based on experimental data obtained on the idealized model. This has not yet been accomplished for the newer theories, due in part to the lack of suitable experimental data.

(U) Perhaps more important from the design standpoint is the fact that on practical vehicle configurations various phenomena actually do occur which can adversely affect the stagnation line heat transfer to the leading edge and that these are essentially three-dimensional in nature. Some attention has been given to the effects of high angles of attack (Ref. 9) and to shock impingement (Ref. 10,11). To this list may be added various types of wing/body interference, as well as nonisothermal and non-uniform sweep effects. Often these occur in combination. Presently neither existing theory nor available experimental data provides a satisfactory basis for establishing reliable design criteria for minimizing adverse effects of these phenomena on leading edge heat transfer.

(U) As part of an extended study of leading edge aerodynamic heating, sponsored by the Naval Weapons Center at

China Lake, the M.I.T. Aerophysics Laboratory has measured the effects on heat transfer of some of the above phenomena (Ref. 12,13,14). The study includes the effect of leading edge curvature (i.e. nonuniform sweep), wing/body interference and vortex impingement. In this paper the results are compared with infinite cylinder predictions, and their significance discussed with reference to design considerations.

### TEST PROGRAM

(U) The tests were carried out in the M.I.T. Naval Supersonic Facility continuous flow closed circuit wind tunnel. The heat transfer measurements were obtained using the so-called hot core installation (Ref. 15) which provides a 6x6 inch region of high temperature ( $T_0 \sim 600^\circ\text{F}$ ) uniform Mach 3.66 flow. The core is established within the standard Mach 3.5 nozzle blocks, so the balance of 18x18 inch wind tunnel test section is filled with a cool ( $T_0 \sim 70^\circ\text{F}$ ) flow at about Mach 3.5. The two flow regimes are separated by a shear layer approximately 1 1/2 inches thick, across which the static pressure is balanced. A splitter plate (Fig. 1) was located at the inner edge of the shear layer and parallel to the core axis. The half span models (Fig. 2) were mounted perpendicular to the splitter plate on a movable pylon driven by a pneumatic piston. With the pylon retracted the wing was immersed in the cool peripheral flow behind the splitter plate. Upon injection the model passed through an appropriately contoured slot in the plate and into the core flow, the penetration distance being varied by adjusting the piston stroke. There resulted a step increase in the leading edge recovery temperature and hence in heat flux. Between data runs the pylon was retracted and the model cooled to a uniform temperature preparatory to the next data run.

(U) The isothermal heat transfer distribution was obtained from the temperature responses of small heat gages mounted along the leading edge stagnation line. Each gage consisted of a small cylindrical ceramic plug mounted with its axis perpendicular to the leading edge and insulated from the rest of the model. The plug temperature response was measured by a thermocouple located in the center of the exposed surface. Design, calibration and use of the heat gage is described in detail in Ref. 16. During the data recording interval the gage temperature rise was small compared to  $(T_{aw} - T_i)$ , where  $T_{aw}$  is the adiabatic wall temperature for the leading edge in the hot core, and  $T_i$  is the

initial leading edge temperature prior to model injection. Using one-dimensional analysis the isothermal heat transfer coefficient corresponding to  $T_i$  may be computed (Ref. 17).

(U) Pressure data was obtained on separate models at Mach 3.55 with the hot core removed and the models mounted on the splitter plate. In addition some data was obtained with the splitter plate removed and Models A, B and C sting-mounted. Thus the leading edge shock shape could be observed and photographed through the Facility's 30 inch diameter single pass schlieren system. A small amount of pressure data was also recorded at Mach 3.66 on Model S<sub>1</sub> in the hot core.

(U) The test configuration used during the vortex impingement study is shown in Fig. 1. The generator consisted of a rectangular stub wing having a double wedge airfoil section ( $11^\circ 25'$  included angle) and an aspect ratio of 2.30 (chord = 2.10 ins). Since it is not possible to accurately predict the location of the vortex generator with respect to the plane of the model necessary to ensure impingement of the tip vortex on the leading edge, this was determined experimentally. The generator pitch angle was preset and a vapor screen established by running the wind tunnel at a high dew point with the hot core removed. A luminous "screen" of vapor was created using an illuminated slit (Fig. 1). The vortex core appeared as a dark hole in the screen. By remotely adjusting the vertical location of the generator with respect to the plane of the model, the vortex could be caused to impinge on the leading edge. Since the normalized downwash velocity ( $w/u_\infty$ ) and hence the vertical displacement of the vortex ( $z/c$ ) is dependent on the total lift coefficient ( $C_L$ ) only (at a fixed streamwise location  $l/c$ ), it was possible to determine the proper settings for the vortex generator in this manner, and use the same settings in the hot core at Mach 3.66; even though the vortex strengths are much different, due primarily to the different  $T_o$  (Ref. 14). The small error in  $C_L$  due to the change in  $M_\infty$  could be neglected in this case.

(U) All models had cylindrical leading edges of either 0.063 or 0.125 inch radius. Of the models shown in Fig. 2, S<sub>1</sub>, which was tested first, was a full scale production version of the Sidewinder I canard, supplied by the U.S. Naval Weapons Center and instrumented and modified for the test program. The leading edge radius was 0.063 inches. One canard was cropped to three-quarter span and used to study wing/body interference effects in conjunction with a blunt ogive-cylindrical half-body having the same contour as that tested in Ref. 18. This configuration is denoted S<sub>1</sub>B. A twice scale, half span model of the canard (Model S<sub>2</sub>)

was used to investigate Reynolds number effects in lieu of varying the wind tunnel conditions. The Sidewinder canard planform consists of a constant radius root section ( $R_p = 1.00$  inches) which fairs tangentially into a constant (66.7 degree) sweep outboard section. This same outboard sweep angle was used on the subsequent models, in order to provide data comparable to that obtained on Models S<sub>1</sub> and S<sub>2</sub>. Models A, B and C consisted of blunt slab wings with one-eighth inch radius leading edges. Model C was the constant sweep model used as a basis of comparison for the variable sweep data, and for the interference and vortex impingement studies. Models A and B were formed by adding root sections of either 0 degrees and 30 degrees sweep respectively to the root of Model C, thus providing a leading edge configuration incorporating a step increase in sweep angle.

## RESULTS

(U) Both heat transfer and pressure distributions were obtained along the leading edge stagnation line of the various models at zero angle of attack. The pressure data was used to determine the local recovery temperature ( $T_{aw}$ ) as described below, and also to provide additional information concerning the effects of the various flow phenomena studied.

(U) At present the most commonly used and straightforward method for computing stagnation line heat transfer coefficients is based on infinite swept cylinder theory. Data obtained on straight cylindrical leading edges indicates that, at low Reynolds numbers and angles of attack, and for moderate sweep angles, this theory gives heat transfer coefficients which are accurate to  $\pm 15\%$ . It is thus of particular importance to determine what errors result from applying the available theory to wing configurations and flow fields such as those treated in this report. Therefore the results presented herein have been normalized with respect to the theoretical values based on either the constant, outboard sweep angle ( $\lambda_0$ ) or on the local sweep angle.

## FREE STREAM CONDITIONS

(U) Free stream conditions in the hot core were held constant throughout the program, giving a test Mach number ( $M_\infty$ ) of 3.66, at a stagnation pressure ( $p_0$ ) and temperature ( $T_0$ ) of 5.00 psia and 600°F, respectively. This corresponds to a unit Reynolds number of  $2.1 \times 10^5$  per foot, and a Reynolds number based on leading edge radius ( $Re_r$ ) of

$1.1 \times 10^3$  and  $2.2 \times 10^3$  for Models S<sub>1</sub> and S<sub>2</sub>, A, B and C respectively. The pressure data was obtained with  $1.6 < Re_r \times 10^{-3} < 12$  at a Mach number of 3.48 to 3.51 (depending on Reynolds number). The boundary layer was assumed to be laminar, consistent with the results of the literature review contained in Ref. 12, which gives a critical Reynolds number of  $Re_r \approx 5 \times 10^4$  for moderate sweep angles.

## RECOVERY TEMPERATURES

(U) In order to obtain the heat transfer coefficient from the heat gage responses, it was necessary to determine the recovery temperature ( $T_{aw}$ ) based on the Mach number ( $M_\ell$ ) adjacent to the stagnation line boundary layer:

$$\frac{T_{aw}}{T_o} = \frac{1 + \frac{\gamma-1}{2} r M_\ell^2}{1 + \frac{\gamma-1}{2} M_\ell^2} \quad (1)$$

The laminar value of the recovery factor ( $r = \sqrt{Pr}$ ) was taken as 0.85 throughout. The Mach number distribution was computed from isentropic flow relations, using the static-to-stagnation pressure ratio ( $p_w/p_{o\ell}$ ). Measured values of  $p_w$  were used, but  $p_{o\ell}$  had to be approximated, since details of the flow field downstream of the leading edge bow shock were unknown. Two methods were used, both of which assume that the inviscid flow between shock and boundary layer is irrotational in the plane of the stagnation line. This is a valid assumption at zero angle of attack, provided both leading edge and shock planforms are straight. It is only approximately true in other cases, and may be grossly in error at high pitch angles or in regions where, either due to pronounced leading edge curvature or flow interferences of various kinds, the flow near the leading edge is strongly three-dimensional. However, this approach is characteristic of infinite swept cylinder theory, which calculates both  $p_w$  and  $p_{o\ell}$  on the basis of the shock being parallel to the leading edge (Ref. 2). The surface pressure in this case is taken as the stagnation pressure downstream of a normal shock whose strength corresponds to the free stream flow component perpendicular to the leading edge. The stagnation pressure is computed from the oblique shock relations for isentropic flow, using the sweep angle ( $\Lambda$ ). On this basis  $T_{aw}/T_o$  may be computed directly from the following expression:

$$\frac{T_{aw}}{T_o} = \frac{1 + \frac{\gamma-1}{2} M_\infty^2 (\cos^2 \Lambda + r \sin^2 \Lambda)}{1 + \frac{\gamma-1}{2} M_\infty^2} \quad (2)$$

(U) The simpler of the two methods used in reducing the data differs from the above approach in one respect only: the local Mach number is computed explicitly using the measured surface pressure values, while computing the stagnation pressure  $p_{o\ell}$ , based on the local sweep angle, as before.

(U) The second method can be used when the actual shock shape is known (e.g. from a schlieren photograph). In this case the downstream flow properties and streamline directions can once again be obtained using oblique shock relations and the shock angles as measured from the photograph. By extrapolating the streamlines from shock to leading edge (assuming them to be straight) points of correspondence on shock and wing could be found and the leading edge stagnation pressure distribution determined. The distributions of  $p_{o\ell}$ ,  $M_\ell$  and  $T_{aw}$  along the leading edge can then be computed, using the measured values of  $p_w$ . In practice the mapping of the downstream flow sometimes lead to intersecting streamlines originating from different points on the shock - due to pronounced shock (and leading edge) curvature on Models S<sub>1</sub>, A and B. This is a clear indication of the limitations of this approach. In such a case the dilemma was resolved by fairing the best curve through the computed  $p_{o\ell}$  versus  $s$  distribution.

(U) Both of the above methods were used during the program, together with the usual infinite cylinder technique described above.

(U) It is shown in Ref. 12 that  $T_{aw}/T_o$  is quite insensitive to errors in  $M_\ell$ . Indeed, for  $M_\ell \approx 1$ , a 1% error in Mach number produces a 0.015% error in  $T_{aw}$ . At  $M_\ell \approx 3$  this figure is 0.025%. Thus it is not surprising that the various values of  $T_{aw}/T_o$  for the 66.7 deg. sweep portion of the wings are in close agreement. The method of Ref. 2 gives a value of 0.913; those based on measured  $p_w$  and a known shock shape give 0.909. If the leading edge were relatively "hot" this discrepancy could be significant, but during the present program the wings were always cold, i.e.  $T_w/T_o \leq 0.5$ , so the error in computing the heat transfer coefficient was less than 1%. In many cases, therefore, use of Eq. (2)

Vol. 2

combined with the local sweep angle will give reasonably accurate predictions of  $T_{aw}$ .

HEAT TRANSFER COEFFICIENT

(U) The details of the data reduction procedures for Models  $S_1$ ,  $S_1B$  and  $S_2$  appear in Ref. 12; those for Models A, B and C in Refs. 13 and 14. All are based on the methods contained in Ref. 17. Basically, the heat transfer coefficient ( $h$ ) was assumed to be isothermal and constant over the data time interval. It was computed from the measured heat flux ( $q$ ) using Eq. (3):

$$q = h (T_i - T_{aw}) \quad (3)$$

(U) On Models A, B and C the heat gage design and calibration technique were substantially improved. The gages on Models  $S_1$  and  $S_2$  had a repeatability of  $\pm 3\%$  and an average scatter (gage to gage) of  $\pm 10\%$ . Due to calibration difficulties, however, the uncertainty in the absolute heat flux level could be as high as 25%. The corresponding uncertainty for the later gages (i.e. those on Models A, B and C), was only  $\pm 7\%$  and the gage repeatability  $\pm 2\%$ .

EFFECTS OF LEADING EDGE GEOMETRY

(U) The leading edge data obtained during the program was effected by two model geometrical characteristics. First, the wings were of finite span, with both a root or nose and also a tip. Thus the leading edge was not really infinite. Secondly, in the case of all but Model C, the leading edge sweep was not constant, but increased, either over a curved section near the root (Models  $S_1$  and  $S_2$ ) or in a single step (Models A and B). In some instances the effects of leading edge geometry on pressure and heat flux was masked by, or combined with those arising from other phenomena (such as boundary layer separation near the wing root); however, some indication of root and tip (i.e. finite span) effects were isolated and a significant amount of data on nonuniform sweep effects was obtained.

EFFECT OF FINITE SPAN

(U) The effects of finite leading edge length can be illustrated by the data obtained at constant sweep on Model

C (Fig. 3). The heat transfer coefficient ( $\bar{h}$ ) has been normalized with respect to the theoretical value for  $\Lambda_0 = 66.7$  deg. The distance normal to the wing root ( $y$ ) has been normalized with respect to the leading edge radius ( $r$ ).

(U) Due to the presence of the splitter plate, any variation in heat transfer near the leading edge root is masked by the interaction between splitter plate boundary layer and that on the model leading edge. Stagnation line heat transfer and pressure data taken on sharp nosed, full span delta wings (Ref. 19) indicates that shock/boundary layer interaction near the apex can bring about increased pressure and heat flux levels downstream thereof. This effect was also noted in the present instance when Model C was sting-mounted. Comparison with Ref. 19 data suggests that the pressures are affected more than the heat transfer, and that the effect decays with increasing Mach number (the Ref. 19 data was obtained at Mach 9.6,  $\Lambda_0 = 70^\circ$ ,  $2.2 < Re_r \times 10^{-4} < 4.0$ ). For the Ref. 19 data the heat transfer level decays to the theoretical value within twenty leading edge radii of the apex. This is in qualitative agreement with Liu's small perturbation theory (Ref. 20).

(U) It was noted that for all models tested the bow shock was not parallel to the leading edge, even near the wing tip. This would help to explain the fact that the measured heat flux (and pressure) level is higher than theory. If the shock angle rather than the sweep angle were used in predicting  $h$ , the disagreement would be reduced by about 2% on the outboard portion of Model C. In cases where the leading edge shock shape is known, therefore, using the shock angle can improve the accuracy of the heat transfer prediction.

(U) In Fig. 3 the difference between the flagged and unflagged Model C data is that in the former case the leading edge was not isothermal prior to injection, for  $y/r > 30$ . This was also true for Models A and B (Fig. 4), due to the experimental technique used. By design the shear layer at the hot core boundary passed behind the splitter plate. It impinged on the outer portion of the wings, resulting in relatively high initial temperatures. This problem was eliminated by retracting Model C deeper into the cold peripheral flow during the pre-cooling process (unflagged data).

(U) In Fig. 4 the normalized heat transfer distribution outboard on the constant sweep section of the leading edge is presented,  $s'$  being the distance from the point at which the sweep first becomes constant, measured parallel to the stagnation line. Using the theory of Ref. 3 for

Vol. 2

large  $s'$ , together with the measured values of  $T_i$ , the isothermal and nonisothermal heat flux distributions have been computed (Ref. 21). These appear for Model A in Fig. 4. Agreement between the nonisothermal curve and the data is quite good.

EFFECT OF NONUNIFORM SWEEP

(U) All of the nonuniform sweep models tested during the program combine a root section of low sweep (and hence high heat flux) with an outboard panel of constant high sweep, on which the leading edge heat flux is relatively low. Primary interest is centered on the extent to which the high heating rates persist outboard of the point at which  $\Lambda$  becomes constant. This decay length can be inferred from the leading edge heat transfer distributions, which appear in Fig. 4. The coordinate  $s'/r$  is the distance along the stagnation line measured from the start of the constant sweep section and normalized with respect to the leading edge radius. The heat transfer coefficient ( $\bar{h}$ ) has been normalized with respect to the theoretical values for  $\Lambda_0 = 66.7^\circ$  and the appropriate free stream conditions.

(U) The shock shapes obtained on the nonuniform sweep models exhibit the same gross characteristics and, as previously noted, are similar to those observed elsewhere (Ref. 19,22). However, while the shock angle for the sharp cornered models increases monotonically, the shocks on Model  $S_1$  and the hemispherical-nosed models of Ref. 19 and 22 have an inflection some distance outboard on the constant sweep section. It would seem that the shock shape should be determined by the detailed leading edge geometry and  $M_\infty$ . In Ref. 23, however, it is shown that for a blunt nosed delta wing with  $\Lambda_0 = 80^\circ$  the shock corresponds to that on a hemisphere, so at high sweep angles the straight leading edge plays little or no part in determining the shape, and carry-over effects will persist much further outboard than at lower  $\Lambda_0$ .

(U) The heat transfer is seen to decay much more rapidly on Models A and B than on Models  $S_1$  and  $S_2$ , for which there is a carry-over at least as far outboard as  $s'/r = 50$ . The relatively low heat transfer levels obtained outboard of  $s'/r = 60$  are probably due to nonisothermal effects, as already noted. The pressure data on Models  $S_1, S_2$  and A exhibit little carry-over and agree well with theoretical predictions based on the local sweep angle. On Model B, however, there appears to be a pronounced over-expansion outboard of the corner, resulting in reduced pressures for  $s'/r < 20$ .

(U) The persistence of the high root heating rates outboard onto the constant sweep leading edge is believed to be due to rotationality induced in the inviscid flow field near the leading edge by the curved shock which, in turn, is the result of the varying leading edge sweep. It has been shown both experimentally (Ref. 24) and theoretically (Ref. 25) that properly oriented free stream vorticity can greatly increase the heat flux near the stagnation line of a yawed cylinder, while affecting the pressure level only slightly. The slight heat transfer carry-over observed on the sharp cornered models as compared with that on Models  $S_1$  and  $S_2$  can be explained in terms of the leading edge planform radius of curvature ( $R_p$ ), see Fig. 2, since the region of rotational flow should be related in extent and strength to the shock radius of curvature and hence to  $R_p$ .

(U) In order to determine the extent to which  $R_p$  is a characteristic length for nonuniform sweep effects the Model  $S_1$  and  $S_2$  data is compared with published results on other configurations with nonuniformly swept leading edges (Fig. 5). Once again,  $h$  is normalized with respect to the theoretical value for  $\Lambda_0$ . The distance from the leading edge root ( $s$ ) is measured along the stagnation line. The only other data found (Ref. 19, 23, 26) was obtained on sting mounted delta wings with hemispherical noses and straight leading edges. This configuration differs from Models  $S_1$  and  $S_2$  in two important aspects: (a) the leading edge and planform radii of curvature are equal ( $r = R_p$ ); (b) there is no boundary layer interaction near the stagnation point ( $\Lambda = 0$  deg.). Apart from the heat transfer data of Ref. 26, no measurements were taken on the model noses where  $\Lambda$  is varying. In addition very little data was taken for  $s/R_p < 6$  which, based on the  $S_1$  and  $S_2$  results, is the region where a carry-over effect might be detected. The theoretical curve for Model  $S_1$  is also shown in Fig. 5. Observations concerning the data may be summarized as follows:

(i) Even on the outboard portion of the wings ( $s/R_p > 6$ ) agreement between infinite cylinder theory and experiment is only  $\pm 20\%$ . The  $\Lambda_0 = 80^\circ$  data indicates agreement will deteriorate for  $\Lambda_0 > 70^\circ$ .

(ii) The Ref. 19 and 23 data exhibits no carry-over effect. The present data does so, for the region  $s/R_p < 6.0$ . The data of Ref. 26 at  $s/R_p = 4.7$  is consistent with the present results, especially at low Mach number. This agreement in itself lends support to using  $R_p$  as the spanwise normalizing factor.

(iii) The Model  $S_1$  and Ref. 26 data and that from Ref. 10 with  $\Lambda_0 = 70$  deg. show a peak in  $\bar{h}$  near  $s/R_p = 10$ . The Ref. 19 and 23 data does not contain such a peak, and the

Vol. 2

Ref. 10 data for  $\Lambda_0 = 60$  deg. shows no such effect. It should be noted that in Fig. 4 the Model A and B data agrees with the  $S_1$  data in this respect.

(iv) The Ref. 26 data, which was obtained at constant  $Re_r$ , suggests that any carry-over effect and any local peaking in  $\bar{h}$  will decrease with increasing  $M_\infty$ . The Ref. 23 results ( $\Lambda_0 = 80$  deg.) also suggest a decrease in  $\bar{h}$  with increasing Mach number. The relative levels of the Mach 6.8 and 9.6 data (Ref. 19) agrees with this conclusion, but excepting at  $Re_r = 12 \times 10^4$  their results are substantially lower than those obtained in Ref. 26 at comparable Mach numbers.

(v) The Models  $S_1$  and  $S_2$  data are in quite good agreement at  $s/R_p$  equals 0.4 and 1.35, indicating that the heat transfer is inversely proportional to  $rl/2$ , and hence to  $Re_r^{1/2}$ , as theory predicts. The discrepancy at  $s/R_p = 0.2$  is due to the splitter plate boundary layer. No explanation has been found for the high heat flux level obtained on Model  $S_2$  at  $s/R_p = 4.1$ .

(vi) There is no clear cut trend with Reynolds number. Even the data obtained in Ref. 19 and 23 at relatively high  $Re_r$  (that is  $12 \times 10^4$  and  $18.5 \times 10^4$ , respectively) is in fair agreement with the laminar theory.

(vii) The poor agreement between the predicted heat transfer distribution for Model  $S_1$ , based on local sweep angle and the data for  $s/R_p < 0.5$  can be attributed to boundary layer interaction in this region.

(U) In summary the present shortage of data for non-uniformly swept leading edges makes it difficult to draw definite conclusions. In spite of the apparent contradiction between the Ref. 19 results and the  $S_1$  data, the possibility of a pronounced heat transfer carry-over exists. It can only be speculated whether the presence or absence of such an effect is dependent on a particular combination of Mach number and sweep angle, or whether the ratio of leading edge to planform radii has some special significance. It is possible that the boundary layer interaction near the root of Models  $S_1$  and  $S_2$  may be a contributing factor. This could produce a much thicker boundary layer along the wing leading edge which, by making the skin friction and heat transfer less sensitive to leading edge curvature, could lead to a slower rate of decay, but in that event the agreement with the Ref. 26 data (for which no such interaction can occur) should not occur.

(U) It seems clear that where a carry-over effect does exist, it is related to the planform curvature, and therefore may be minimized by making  $R_p$  as small as possible.

(U) The possible existence of a locally high  $\bar{h}$  outboard on the constant sweep leading edge is cause for some concern. Once again, the available data is too sparse to enable either the cause or the severity of this problem to be defined. It would seem that its location on different models can be correlated on the basis of  $R_p$ . This suggests that it is related once again to the presence of the highly heated inboard section.

#### EFFECTS OF WING-BODY FLOW INTERFERENCE

(U) A review of the literature reveals that while considerable effort has been devoted to measuring pressure and heat transfer distributions on swept cylinders and blunt leading edges of delta wings, little attention has been paid to more practical configurations in which the wing is tested in combination with typical missile and aircraft components. Yet the blunt nosed missile body or aircraft fuselage and protuberances such as stub antenna and control canards can alter the flow over the wing leading edge in a variety of ways, thus affecting the stagnation line heat transfer and pressure distributions to an extent which, for the most part, cannot presently be predicted with any degree of accuracy.

(U) Two general categories of interference can be discerned. In the first of these the entire inviscid flow field upstream of the leading edge is affected, while in the second the initial impact is localized to small regions within the leading edge boundary layer or the adjacent flow field between the leading edge and the shock. If a wing is mounted on a blunt nosed body, the body bow shock may produce both types of interference. By modifying the flow conditions upstream of the leading edge it can affect the entire heat transfer and pressure distribution. The shock can also cause interference of the second type if it should impinge on the leading edge. The body itself can produce changes near the leading edge root, due to interaction between the two boundary layers (one on the body, the other on the leading edge). Similarly the wake of a canard mounted upstream of the wing can affect a large portion of the leading edge, while the tip vortex and shock can produce localized changes further outboard. It is to be expected that usually two or more different types of interference will be present simultaneously, making it difficult to isolate the individual effects of each, and causing possible mutual interaction which could produce additional changes.

(U) This was to some extent the case during the present program, which studied the effects of the body bow shock and boundary layer and of vortex impingement on heat transfer and pressure along the stagnation line of the various models. The results of these studies are discussed in the following paragraphs.

#### EFFECT OF BODY BOW SHOCK

(U) The test configuration for the wing/body interaction studies is shown in Fig. 6. The half-body was mounted 5.9 ins. downstream of the splitter plate leading edge, and was a twice scale version of the hemispherical nosed ogival cylinder tested in Ref. 18. The nose radius was 1.40 ins. The axial distance from the nose to the wing leading edge was 9.3 ins. (6.6 nose radii). The bow shock shape was taken from a schlieren photograph (Ref. 18) and as such does not show the effect of the splitter plate boundary layer near the nose. The leading edge shock contour is only approximate. It is taken from a schlieren of the wing alone at Mach 3.55 (Ref. 12) and does not show the effect of the bow shock nor of the boundary layer interaction near the root.

(U) The Model S<sub>1</sub> and S<sub>1</sub>B heat transfer data appears in Fig. 7, normalized with respect to the theoretical value with  $\Lambda_0 = 66.7$  deg. The theoretical curve for Model S<sub>1</sub> is also shown. No comparable data has been found in the literature. The heat transfer is significantly reduced in the presence of the body for  $20 < s/r < 110$ , the average being 19%. The relatively slow decay in heat flux observed on Model S<sub>1</sub> (Fig. 4) is also present on S<sub>1</sub>B. Based on the body pressure data and Mach number distributions in Ref. 18, the upstream Mach number at the leading edge root ( $s = 0$ ) is 2.4, for  $M_\infty = 3.66$ . Assuming the flow has passed through the normal portions of the bow and leading edge shocks, infinite cylinder theory gives  $h = 58.1$  BTU/ft<sup>2</sup>hr°F, or  $\bar{h} = 1.83$ , which agrees well with the measured values on S<sub>1</sub>B. In Fig. 6 the streamline which would just clear the three-quarter span wing has been traced, using oblique shock relationships. The flow inclination and Mach number are 11.3 deg. and 2.72 respectively. The effective sweep angle is therefore 78 deg., and the theoretical heat transfer is 28.1 BTU/ft<sup>2</sup>hr°F ( $\bar{h} = 0.87$ ). The relatively good agreement near the root between the data and the predicted heat transfer using local flow conditions, combined with the similarity in data trends on the straight leading edge sections of both models, indicates that in this case at least the reduction in heat transfer level is primarily due to the change in free stream conditions on the low sweep inboard section of

the wing. This implies that the outboard portion of the bow shock has relatively little effect on the leading edge heat transfer and in most cases its shape need not be known in detail. The significant portion of the shock therefore is largely determined by the hemispherical body nose. It should be noted that the theoretical heat flux at the root for Model S<sub>1</sub>B is 68% of that on S<sub>1</sub>. If this value were used to predict outboard heat transfer rates in the presence of the body, it would underestimate them significantly. Neglecting the bow shock entirely and using infinite cylinder theory would be more satisfactory, but as can be seen in Fig. 7, for  $s/r < 80$  this approach will also underestimate the heat transfer by as much as 20%.

(U) One consideration of great importance from a design standpoint is whether or not the bow shock actually impinges on the leading edge. Heat fluxes up to four times the normal level have been measured near the impingement point (Ref. 10,11).

#### EFFECT OF BOUNDARY LAYER INTERACTION

(U) The effect of the splitter plate boundary layer is apparent on all of the heat transfer measurements obtained near the model root. In Fig. 3 the data from the root sections Models S<sub>1</sub>, S<sub>2</sub>, A and B, and from all of Model C is presented, normalized with respect to the theoretical value for the local sweep angle (not  $\Lambda_0$ ). A data point obtained at zero sweep during a heat gage calibration run is also included. The spanwise coordinate  $y$  is measured normal to the wing root (Fig. 1). The Model C data exhibits the usual low heat flux levels corresponding to a separated region, followed by a rapid increase to a peak at the point where the separated boundary layer attaches to the leading edge. Outboard of this the heat flux decays to the normal, undisturbed level. The peak in the case of  $\Lambda = 66.7^\circ$  is nearly 50% higher than the theoretical level. The data on the other models is in general agreement with the Model C results, but is insufficient to determine any effect of varying sweep angle on the magnitude or location of the peak heating rate. In Ref. 10, however, data was obtained over a range of  $\Lambda$  which while exhibiting the same general characteristics as Fig. 3, also indicates that the peak heating level decreases markedly with increasing sweep while the peak location is hardly affected. It is probable that in the present case and in Ref. 10 the splitter plate boundary layer was laminar. Reference 27 indicates that a turbulent boundary layer would be much less likely to separate, particularly at low sweep angles, and that the peak heat flux levels on the leading edge would be substantially

Vol. 2

lower than for a laminar layer and occur closer to the root. Thus while it is not presently possible to predict the magnitude or level of the peak heat fluxes, the problem can be minimized by ensuring that the wing is located where the body boundary layer is turbulent. It may also be assumed that the peak will occur within the region  $0 < y/r < 10$ .

EFFECT OF VORTEX IMPINGEMENT

(U) Investigations of the effect of free stream vorticity on heat transfer have shown that, with proper orientation, the vortex filaments can be stretched and their effects amplified by a boundary layer, and severe local heating result (Ref. 24,25). In the case of the vortex shed from the tip of a stub antenna or canard inclined to the local flow, the orientation is not such as should result in increased heating, but it may significantly alter the local flow field. Normally the spacing between canard and wing would be such that the vorticity would be concentrated in the trailing vortex shed from the canard tip.

(U) The test configuration appears in Fig. 1. Data was obtained at vortex generator pitch angles ( $\phi$ ) of 5 and 10 deg., thus ensuring the flow did not separate from the leeward surface. The corresponding vortex strengths ( $\Gamma$ ) as computed from Ref. 28 are 26.5 and 53.0 ft<sup>2</sup>/sec. The spanwise location of the vortex impingement on the Model C leading edge was computed (Ref. 28) to be 2.27 ins. ( $y/r = 18.2$  or  $s/r = 46$ ). The diameter of the completely rolled up vortex core was estimated as 0.75 ins. For low aspect wings the vortex sheet is essentially rolled up into two concentrated cores within a few chord lengths ( $c$ ) of the trailing edge. For the Mach numbers of the present test the average distances were  $l/c = 8.4$  for  $\phi = 5$  deg.;  $l/c = 4.4$  for  $\phi = 10$  deg. (Ref. 28). Since for the impingement point  $l/c = 5.24$ , it is concluded that for  $\phi = 5$  deg. the vortex was not completely rolled up when it impinged on the leading edge.

(U) The heat transfer data appears in Fig. 8, normalized in the usual way. The displacement of the generator axis from the model plane ( $z$ ) has been normalized with respect to the generator chord ( $c$ ). The first two settings are those corresponding to impingement. For  $z/c$  of 0.238 the core axis was significantly above the plane of the leading edge. The location of the vortex impingement point is at  $s/r = 46$ . Inboard of this point the leading edge lies within the generator wake, resulting in wide variations in heat transfer (and pressure). However the very pronounced and localized reduction in  $\bar{h}$  at the impingement point can be

discerned, especially for  $\phi = 10^\circ$ . This effect decays rapidly beyond the limits of the core ( $40 < s/r < 52$ ).

(U) The variation of the heat transfer coefficient with vortex strength appears in Fig. 9. The measured values are those recorded at Station 5, and have been normalized with respect to the experimental level with no vortex present. Also shown is the local Reynolds number under the vortex,  $Re_w$ , defined as  $\rho_w u_{\infty} s / \mu_w$ , and likewise normalized to the undisturbed free stream value. Since, in the above definition,  $s$ ,  $T_w$  and hence  $\mu_w$  are constant and independent of the local free stream conditions,  $Re_w / (Re_w)_{\Gamma=0}$  is simply  $p_w / p_w \Gamma=0$  times the local velocity ratio. In this treatment the latter is assumed equal to one, so the Reynolds number ratio is also the normalized pressure for the different vortex strengths.

(U) Using the linear fit to the Reynolds number data, it is shown in Fig. 9 that a Reynolds type analogy may be used to predict the heat transfer reduction due to vorticity. Agreement between the square root curve and the heat transfer data is good. Beyond this there is little that can be said as far as predicting the effects of vortex impingement. The effect of varying the streamwise distance  $l/c$ , for example cannot be determined from the present data, nor can possible effects of sweep angle and free stream conditions be found.

(U) From a practical standpoint vortex impingement offers a design problem only insofar as the large heat flux gradient may induce thermal stresses in the leading edge structure. The inboard wake effects in general do not produce heating rates higher than those measured in the absence of the generator. There may be important effects, however, on the aerodynamic performance of the wing.

### CONCLUSIONS

(U) In general it must be said that the results obtained during the present program, even when combined with data published previously in the literature, do not completely define the magnitude of the changes in leading edge heat transfer which may be brought about by the various phenomena treated herein. It is possible to confirm whether or not unacceptably high deviations from the theoretical heat flux levels may occur and, in some cases, to suggest steps appropriate to minimizing these effects during the design of a high speed missile or aircraft. None of the various effects investigated - finite span, nonuniform sweep, wing/body and boundary layer interactions and vortex impingement - can be treated analytically at present. The

Vol. 2

alternate approach is to experimentally determine the effects of varying the free stream conditions and such geometrical parameters as sweep, planform radius of curvature, etc. in an effort to develop semi-empirical methods for predicting the size and extent of the changes produced by each of the different phenomena. This indeed should be done. Free stream conditions, especially Mach number, were almost constant during this program, as was the basic sweep angle on the outboard leading edge. Extension of the data to both higher and lower Mach and Reynolds numbers, for larger and smaller sweep angles and different combinations of chord-wise and planform radii of curvature is recommended.

REFERENCES

1. Sears, W.R., "The Boundary Layer of Yawed Cylinders", J.A.S., Vol. 15, No. 1, p. 49, January 1948.
2. National Advisory Committee for Aeronautics, Low Pressure Laminar Boundary Layer over a Yawed Infinite Cylinder with Heat Transfer and Arbitrary Prandtl Number, by E. Reshotko and I.E. Beckwith, Washington, D.C., NACA, 1958, (NACA Report 1379).
3. Massachusetts Institute of Technology, Department of Aeronautics and Astronautics, Heat Transfer Near the Stagnation Line of a Swept Wing, by A.M. Piermatteo, Master of Science Thesis, Cambridge, Mass., August 1965.
4. Massachusetts Institute of Technology, Aerophysics Laboratory, The Effects of Shock Wave Curvature on Heat Transfer in Three-Dimensional Supersonic Flow over Bodies, by V.S. Avdyevskii, in Investigation of Heat Exchange in Liquid and Gas Flows, pp. 29-54, Moscow, Russia, 1965, Translation in Cambridge, Mass., M.I.T. (AL TN 116).
5. North Atlantic Treaty Organization, Advisory Group of Aeronautical Research and Development, "Resultats Experimentaux et Theoriques sur le Transfert de Chaleur au Bord d'Attaque des Ailes a Forte Fleche en Hyper-sonique", by J. Valensi, R. Michel and D. Geoffroy in Recent Developments in Boundary Layer Research, Paris, France, May 1965 (AGARDograph 97).

6. U.S. Air Force Flight Dynamics Laboratory, Laminar Heat Transfer to a Swept Leading Edge in Hypersonic Flow, by M.C. Fong and C.G. Freeman (North American Aviation, Inc.), Wright-Patterson AFB, Ohio, AFFDMG, April 1967, (AFFDL-TR-66-208).
7. Fannelop, T.K., "A Method of Solving the Three-Dimensional Laminar Boundary-Layer Equations with Application to a Lifting Re-entry Body", AIAA Journal, Vol. 6, No. 6, pp. 1075-1084, June 1968.
8. National Aeronautics and Space Administration, Local Heat Transfer and Recovery Temperature on a Yawed Cylinder at a Mach Number of 4.15 and High Reynolds Number, by I.E. Beckwith and J.J. Gallagher, Washington, D.C., NASA, 1961 (NASA TR R-104).
9. National Aeronautics and Space Administration, Analysis of Hypersonic Pressure and Heat Tests on Delta Wings with Laminar and Turbulent Boundary Layers, by A.L. Nagel and others, (The Boeing Airplane Company), Washington, D.C., NASA, August 1966, (NASA CR-535).
10. Arnold Engineering Development Center, Effect of Shock Impingement on the Heat-Transfer and Pressure Distributions on a Cylindrical-Leading-Edge Model at Mach Number 19, by L.G. Siler and H.E. Deskins, Arnold Air Force Station, Tenn., AEDC, November 1964, (AEDC-TDR-64-228).
11. Arnold Engineering Development Center, An Investigation of Shock Impingement on a Blunt Leading Edge by A.D. Ray and R.L. Palko, Arnold Air Force Station, Tenn., AEDC, July 1965, (AEDC-TDR-65-153).
12. U.S. Naval Ordnance Test Station, An Experimental Study of Heat Transfer Rates and Recovery Temperatures on a Nearly Triangular Fin, by T.E. Chamberlain, E.E. Covert and others (Massachusetts Institute of Technology), China Lake, California, NOTS, May 1967, NAVWEPS Report 8978, NOTS TP3944).
13. U.S. Naval Ordnance Test Station, Heat Transfer Measurement on Blunt Leading Edges of Nonuniform Sweep Angle, by A.F. Gollnick, Jr. (Massachusetts Institute of Technology), China Lake, California NOTS, November 1966, (NOTS TP4220).

## 8th Navy Symposium on Aeroballistics

### Vol. 2

14. U.S. Naval Weapons Center, Heat Transfer and Pressure Distributions on a Blunt Swept Leading Edge Including the Effects of Upstream Vorticity, by A.F. Gollnick, Jr. (Massachusetts Institute of Technology), China Lake, California NWC, January 1968, (NWC TP4479).
15. Massachusetts Institute of Technology, Naval Supersonic Laboratory, A High Temperature Stream Tube for a Supersonic Wind Tunnel, by R.H. Adams, Cambridge, Mass., M.I.T., May 1958 (TR 303).
16. Covert, E.E. and Gollnick, A.F., Jr., "Design and Calibration of a Small Heat Transfer Gage and Its Application", Proceedings of the 23rd Annual ISA Conference, New York, N.Y., 1968, Instrument Society of America, Pittsburg, Pa., (ISA Paper No. 68-535).
17. Wright Air Development Center, Some Heat Conduction Solutions Involved in Transient Heat Transfer Measurements, by R.J. Cresci and P.A. Libby, Wright-Patterson Air Force Base, Ohio, WADC, September 1957 (WADC TN 52-236).
18. Massachusetts Institute of Technology, Naval Supersonic Laboratory, Experimental Measurements of Aerodynamic Heat Transfer at 700°F,  $M = 3.6$ , to a Blunted Ogival Cylinder, by F.E. Fahrenholz and E.E. Covert, Cambridge, Mass., October 1960, (NSL TR401).
19. National Aeronautics and Space Administration, An Experimental Study of the Pressure and Heat Transfer Distribution on a 70° Sweep Slab Delta Wing in Hypersonic Flow, by M.H. Bertram and P.E. Everhart, Washington, D.C., December 1963, (NASA TR R-153).
20. Liu, J.T.C., "On Laminar Heat Transfer to the Stagnation Line Region on a Highly Yawed Cylinder", published in Proceedings of the Sixth Midwestern Conference on Fluid Mechanics, pp. 34-46, University of Texas, Austin, Texas, 1959.
21. Piermatteo, A.M., Gollnick, A.F. and Covert, E.E., "Stagnation Line Heat Transfer to a Blunt Leading Edge of Nonuniform Sweep", Presented at the Seventh Navy Aeroballistics Symposium, U.S. Naval Missile Center, Pt. Mugu, California, June 7-9, 1966.

22. Aeronautical Research Laboratory, The Flow About the Leading Edge of a Swept Blunt Plate at Hypersonic Speeds, by C.C. Horstman and I.E. Vas (Princeton University), Wright-Patterson AFB, Ohio, AFARL, August 1962 (ARL 62-405).
23. National Aeronautics and Space Administration, A Study of Pressure and Heat Transfer Over an 80° Sweep Slab Delta Wing in Hypersonic Flow, by A.H. Whitehead, Jr. and J.C. Dunavant, Washington, D.C., March 1965, (NASA TN-D-2708).
24. Kestin, J., Maeder, P.F. and Sogin, H.H., "The Influence of Turbulence on the Transfer of Heat to Cylinders Near the Stagnation Point", Journal of Applied Mathematics and Physics (ZAMP), Vol. 12, No. 2 (1961), pp. 115-132.
25. Suter, S.P., Maeder, P.F. and Kestin, J., "On the Sensitivity of Heat Transfer in the Stagnation Point Boundary Layer to Free Stream Vorticity", J. Fluid Mech., Vol. 16, (1963), pp. 497-520.
26. Wright-Patterson Air Force Base, Experimental Heat Transfer Data Made Available by the Air Force Flight Dynamics Laboratory (FDMG), Wright-Patterson AFB, Ohio.
27. National Aeronautics and Space Administration, Heat Transfer and Pressure Distribution at a Mach Number of 6.8 on Bodies with Conical Flares and Extensive Flow Separation, by J.V. Becker and P.F. Korycinski, Washington, D.C., April 1962, (NASA TN D-1260).
28. Spreiter, J.R. and Sacks, A.H., "The Rolling Up of the Trailing Vortex Sheet and its Effect on the Downwash Behind Wings", Jour. of the Aeronautical Sciences, Vol. 18, No. 1 (1951), pp. 21-32.

## LIST OF SYMBOLS

$C_L$	wing lift coefficient
	vortex generator root chord
$h$	isothermal heat transfer coefficient
$\ell$	distance measured downstream from vortex generator centerline
$M$	Mach number
$p$	pressure
$R_p$	leading edge planform radius of curvature
$Re$	Reynolds number based on free stream conditions
$Re_r$	Reynolds number based on leading edge radius
$Re_w$	local Reynolds number = $\frac{\rho_w u_\infty \ell}{\mu_w}$
$r$	leading edge chordwise radius of curvature
$s$	distance along stagnation line
$s_c$	distance from root to start of constant sweep section
$s'$	distance along constant sweep section = $s - s_c$
$T$	temperature
$T_i$	initial temperature for heat transfer tests (= $T_w$ )
$T_{aw}$	adiabatic wall temperature
$u$	velocity
$w$	downwash velocity
$Y$	spanwise distance, normal to wing root
$z$	vortex generator displacement from plane of wing

- $\Gamma$  vortex strength  
 $\Lambda$  leading edge sweep angle  
 $\Lambda_o$  outboard (constant) sweep angle  
 $\phi$  vortex generator pitch angle

Superscripts

- quantity normalized with respect to infinite swept cylinder theory

Subscripts

- $l$  local value external to leading edge boundary layer  
 $w$  value on leading edge stagnation line  
 $o$  stagnation value  
 $\infty$  free stream value

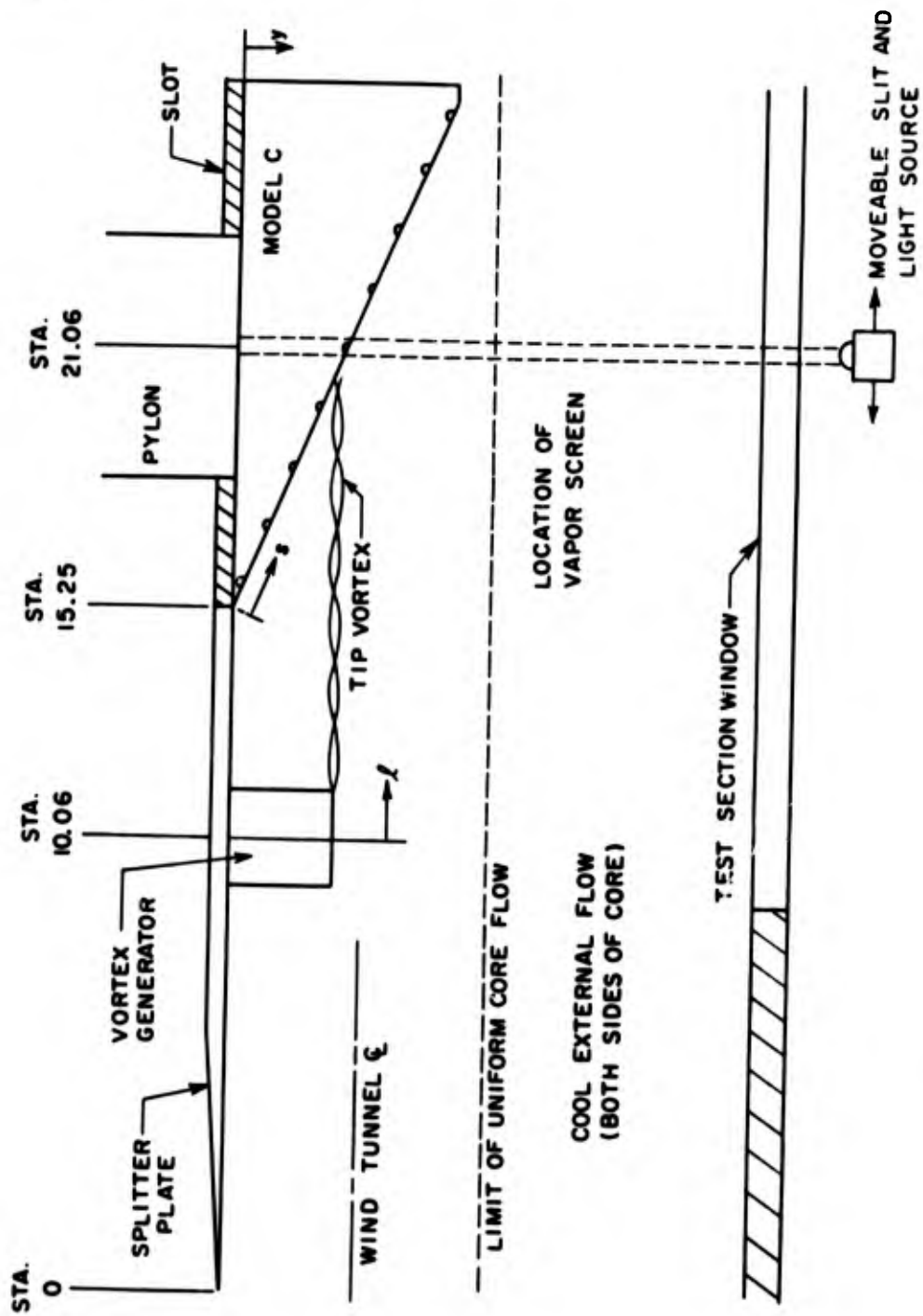


Figure 1. Wind tunnel test installation including vortex generator

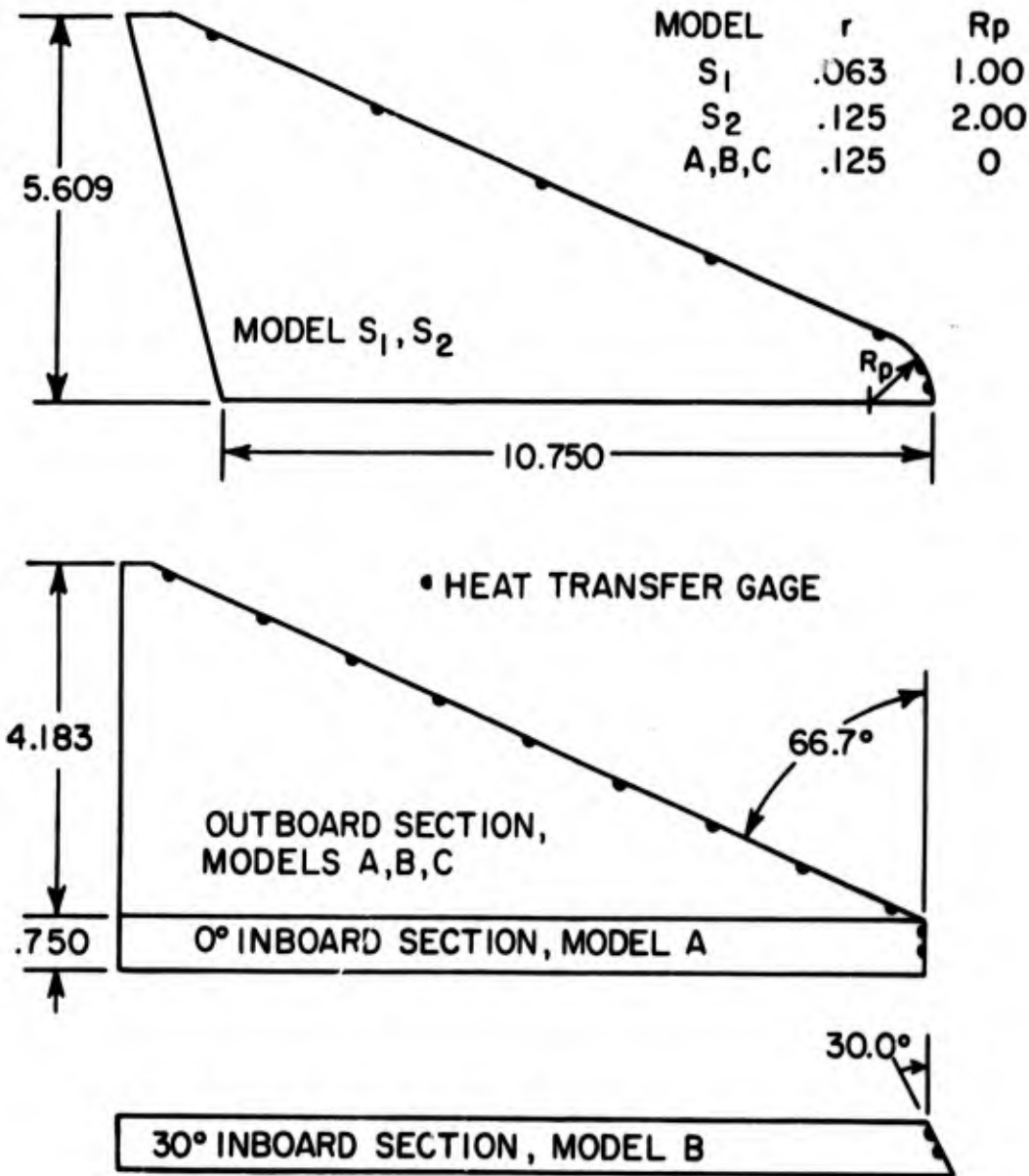


Figure 2. Model geometries

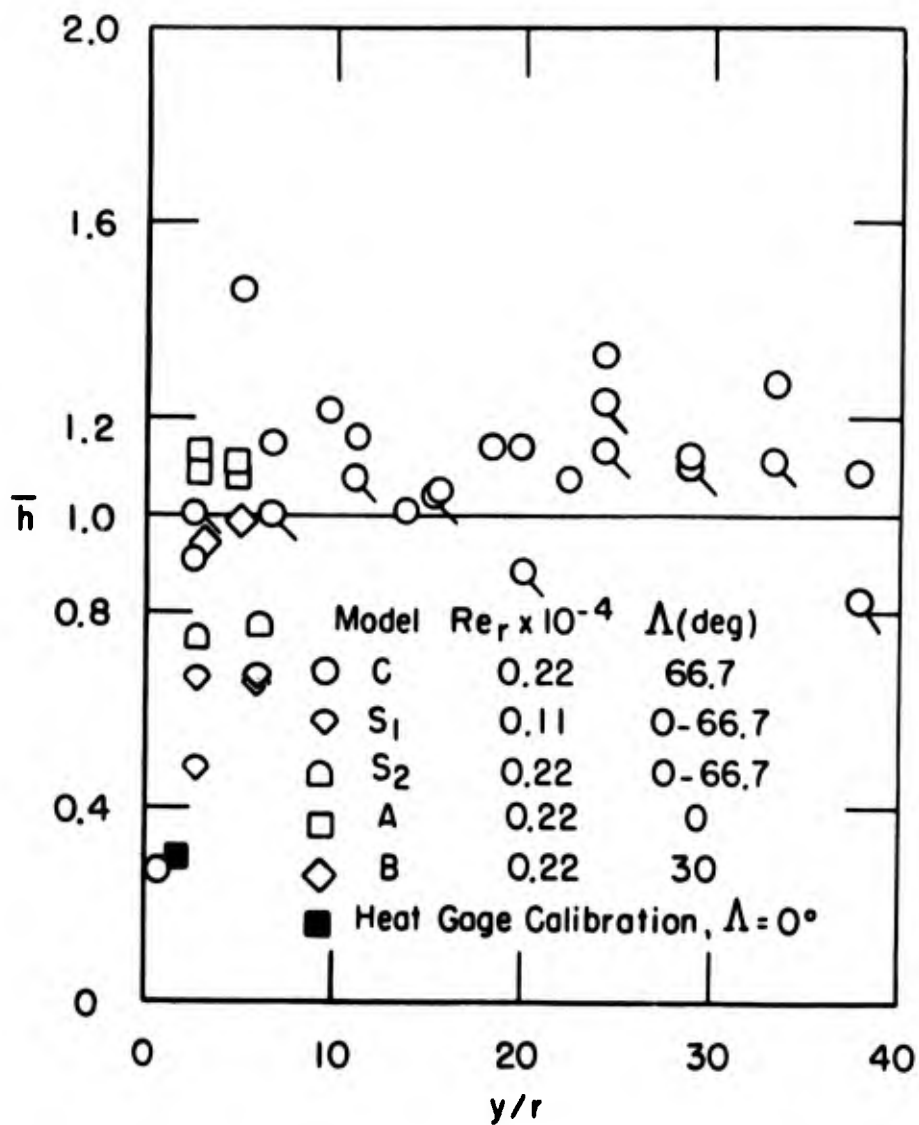


Figure 3. Effect of body boundary layer on stagnation line heat transfer

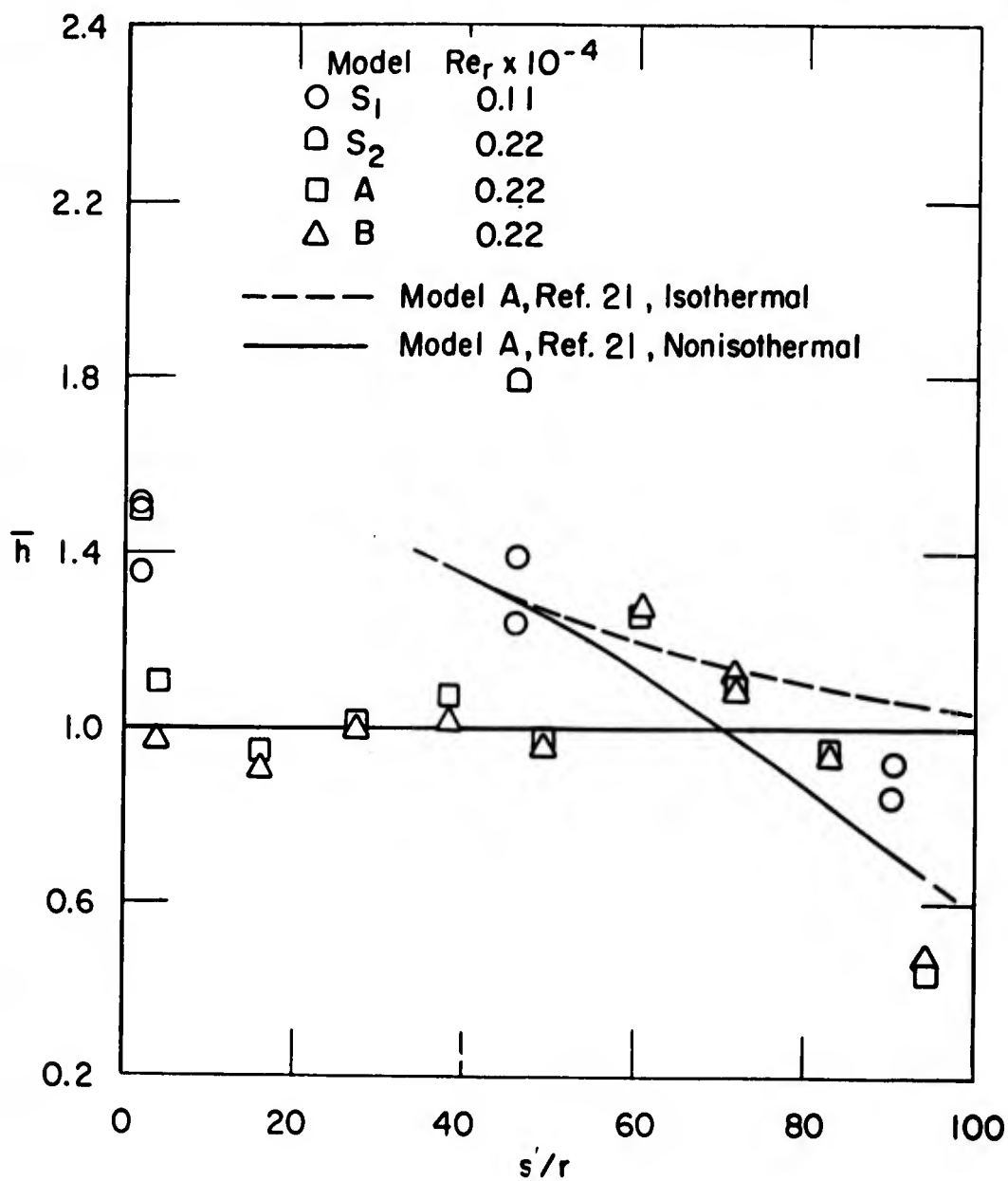


Figure 4. Outboard heat transfer distribution on stagnation line of nonuniformly swept leading edge

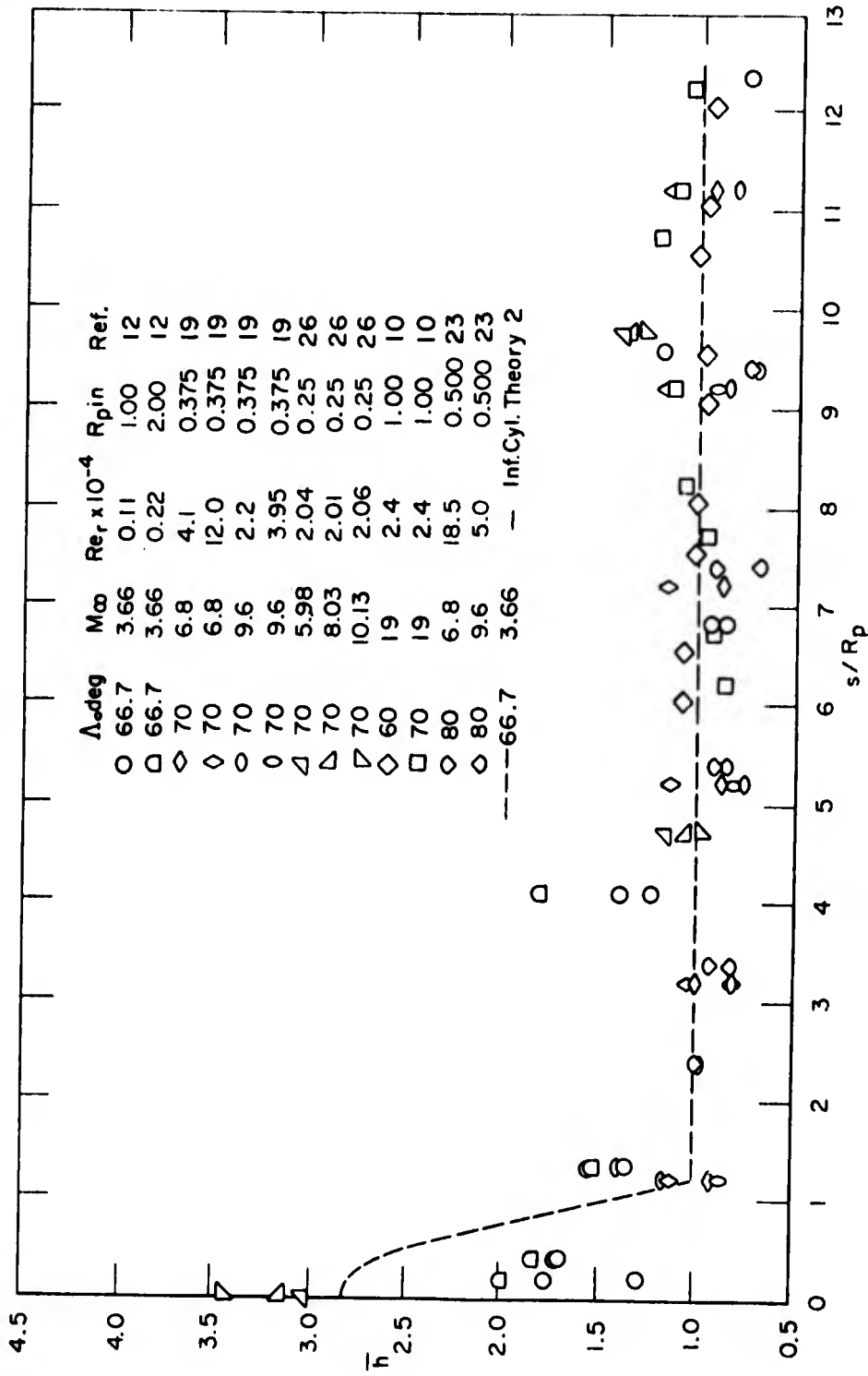


Figure 5. Stagnation line heat transfer on nonuniformly swept leading edges with curved root sections

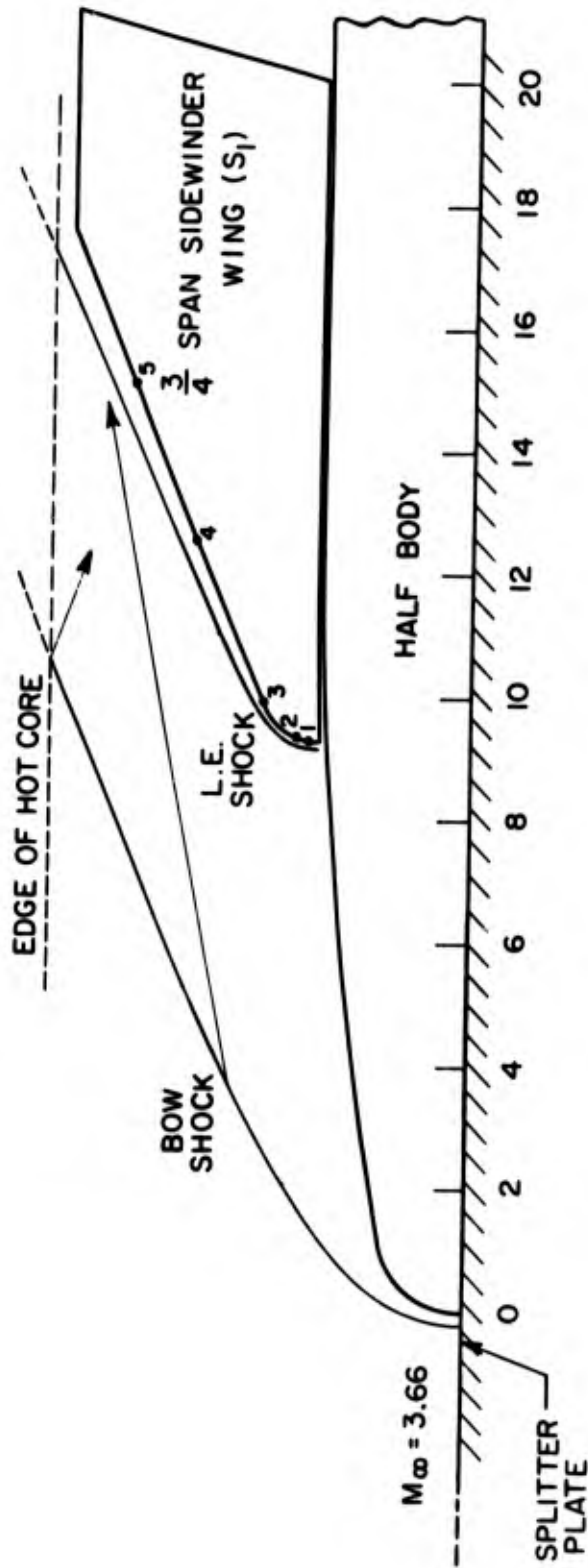


Figure 6. Model and shock configuration for wing/body interaction study

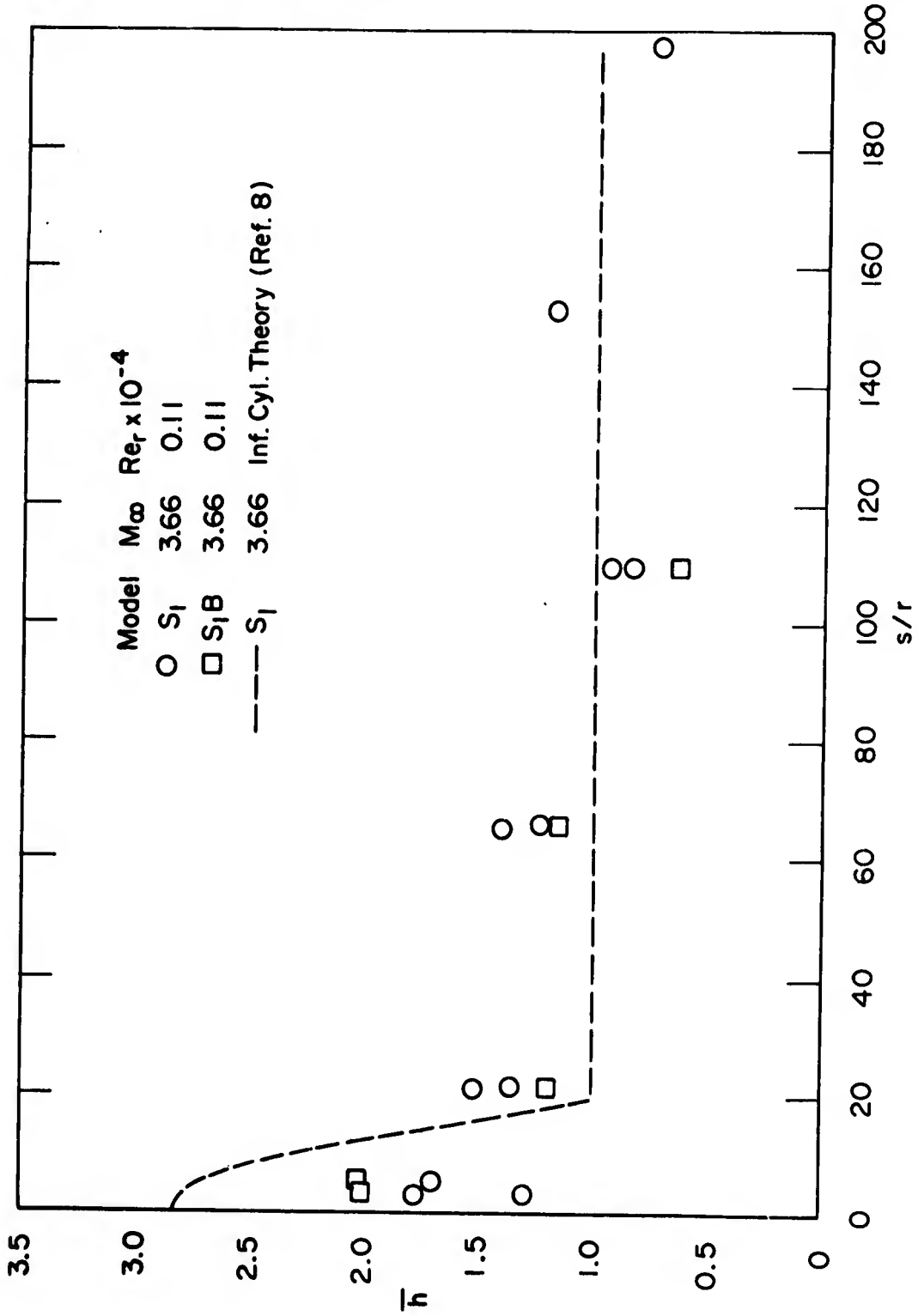


Figure 7. Effect of wing/body interaction on leading edge heat transfer

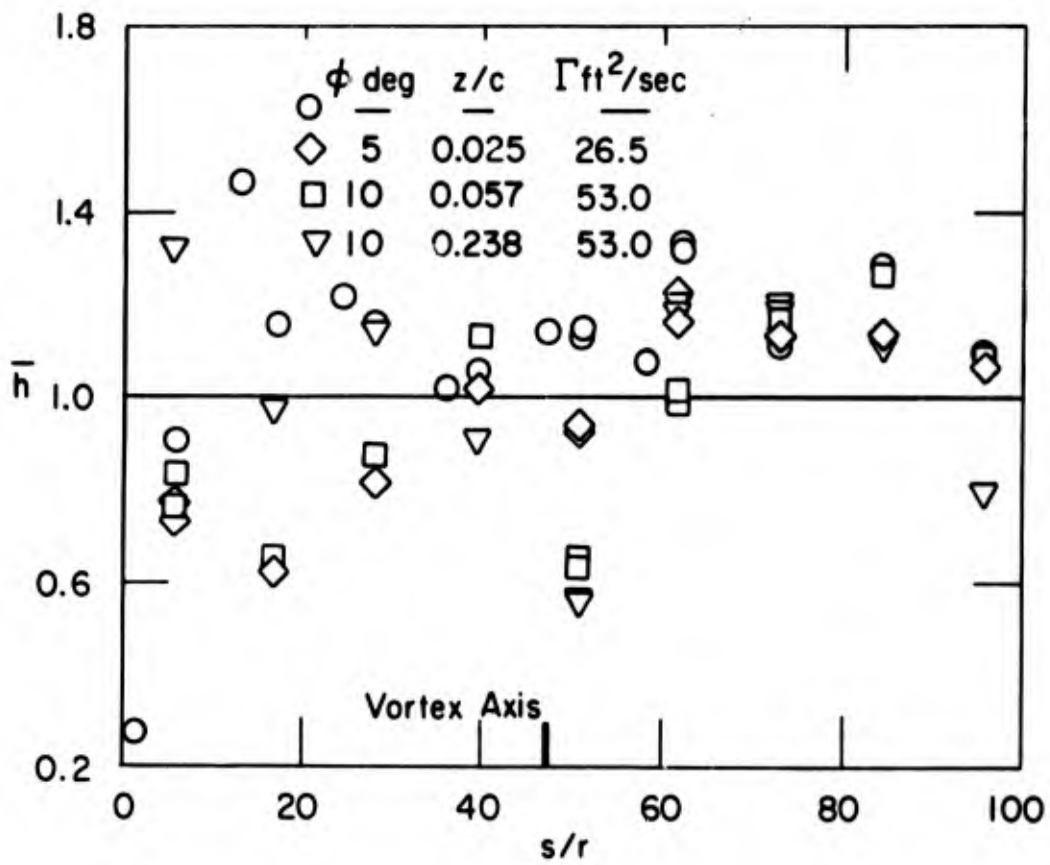


Figure 8. Effect of vortex impingement on leading edge heat transfer

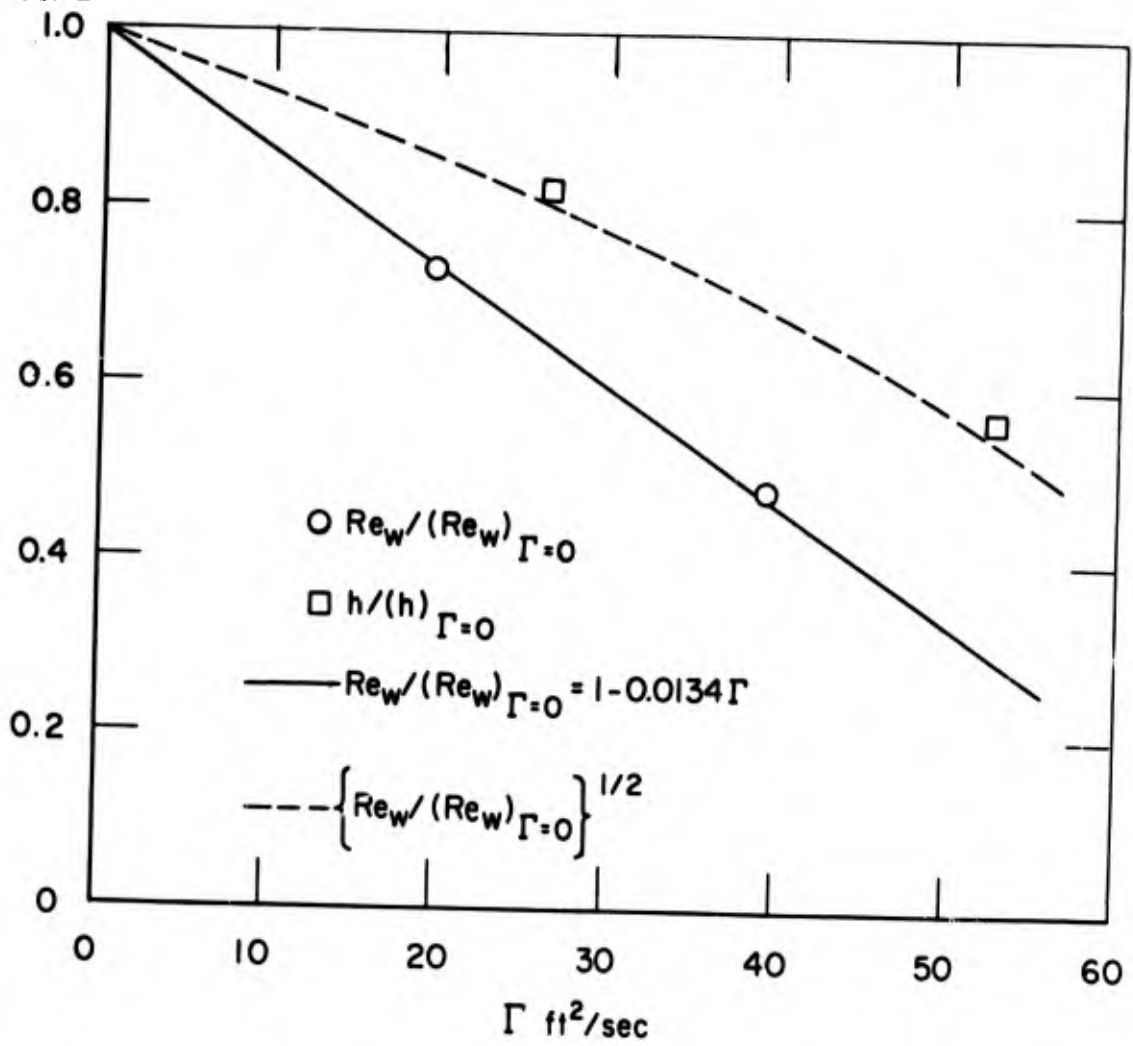


Figure 9. Correlation of leading edge heat transfer and Reynolds number as a function of vortex strength

Paper No. 16

AN EXPERIMENTAL STUDY OF MASS  
ADDITION EFFECTS IN THE NEAR WAKE\*

(U)

(Paper UNCLASSIFIED)

by

Norman G. Paul, H. J. Unger, F. K. Hill,  
and J. M. Cameron  
Applied Physics Laboratory  
The Johns Hopkins University  
Silver Spring, Md. 20910

ABSTRACT. (U) The effects of mass addition on static temperatures in a two-dimensional laminar near wake have been investigated in an arc-tunnel setup using infrared spectroscopy. Both ablating models and models with base injection of reacting and non-reacting gases have been used. Arc test conditions of 300 psia pressure and 1900 Btu/lbm enthalpy resulted in flow environments of 9000 ft/sec velocity, 5500°R stagnation temperature and 8500 for Reynolds number referred to model base height. The wake flows were examined with a duplex-scanning infrared spectrometer using spatial and wavelength scanning modes; measurements were taken at 5 vertical wake locations of  $y/h = 0$  to 0.5 over the 4 - 6 $\mu$  wavelength range. Axial locations of  $x/h = 1$  and 4 were used. Static temperature levels were determined from shifts in the P- and R-branches of the NO band at 5.35 $\mu$ ; checks on these values were made using other molecular species. Thus, the results obtained in the 1200-2400°R range, from rotational-vibrational molecular data, are accurate with an error of less than  $\pm 70^\circ\text{R}$  and are in agreement with conventional determinations based on translational kinetic temperatures.

\* This work supported by the Naval Ordnance Systems Command, Dept. of the Navy under Contract N0w 62-0604-c.

## INTRODUCTION

(U) It is well known that wakes occur behind an object moving in a fluid medium and have characteristics that result from the manner of dissipation of the kinetic energy lost by the body from drag mechanisms. For re-entry vehicles in the earth's atmosphere, these wakes or trails can extend for distances of up to hundreds and thousands of body diameters. High temperature and high velocity wakes have been of especial significance in the past few years due to the Department of Defense's interest in the detection, tracking and discrimination problems associated with re-entry vehicles. In respect to detection and tracking, the altitude regime of 100,000 to 150,000 ft is important due to the onset of significant ablation and the characteristic state of the wake flow. The essential problem in discrimination concerns the determination of the weight of the body and this can be related to the kinetic energy loss by means of wake temperatures. Analyses of the infrared radiation from common molecular species can furnish the wake temperature information.

(U) Various phenomena associated with "clean air" wakes behind high-speed objects have been extensively investigated; the efforts expended have resulted in significant progress in many areas. A number of excellent reviews exist which deal with the various problem areas of the high-velocity wake (Refs. 1-5). However, the complexities of the various problems involved have precluded a thorough examination of one of the areas of significant practical interest, i.e., wakes with mass addition. With any high-velocity, slender re-entry vehicle, heat fluxes in the nose region become extremely high and the necessary thermal protection must include either controlled injection by transpiration-type modes or self-regulated injection by ablative mechanisms. This mass, added to the boundary layer, causes changes in the thermal, chemical and flow-field characteristics of the entire wake. The effects caused by mass addition can be order of magnitude in level when concerning the wake observables and thus affect the radar and optical signatures. On a practical basis, normal mass transfer in the wake, for either wake enhancement or suppression, affects the heat shield material, body design, penetration aids requirements, and the sophistication of the radar and optical systems.

(U) At APL/JHU, exploratory Mach 6 arc-tunnel tests have been conducted using infrared spectroscopy for static temperature determinations. The purpose of these experiments has been to explore the effects of mass addition in the near wake under conditions which would provide results complementary to those obtained by others utilizing different facilities.

### EXPERIMENTAL SETUP & TEST CONDITIONS

#### MACH 6 ARC-TUNNEL

(U) Arc-unit tests were carried out at the Propulsion Research Laboratory at APL/JHU; general facility capabilities, operating characteristics, and information on instrumentation and controls are given in some detail in Refs. 6 and 7. The Mach 6 arc-tunnel is composed of an arc-heater, contoured nozzle, test section and exhaust system. Figures 1 and 2 show a view of the experimental setup and a schematic of the components. Air for the arc-tunnel operation is compressed, dried and stored in tanks at 2000 psia prior to the tests; blowdown operation is used during the tests. The air from the storage tanks is metered to the arc-heater through a standard ASME-contoured nozzle. The arc-heater consists of a thick-walled chrome-copper pressure vessel (electrically floating) with split-ring type electrodes. Heated air from the arc unit passes through a flow straightening section and then through a Mach 6.15 ( $\gamma = 1.4$ ) water-cooled nozzle. In order to provide a parallel flow field downstream, the Mach 6 nozzle was designed for the test conditions using a real-gas, method of characteristics computing program with boundary layer corrections (Ref. 8). The nozzle has a 5.4" exit diameter with an inviscid core of approximately 5 inches. The test section downstream of the nozzle, in which the model and wake are observed, is 8" in length and completely enclosed. An aft diffuser, connected to the test section and the air-stream ejector exhaust system, maintains the test section pressure level at 0.1 - 0.2 psia during the tests and aids in establishing the correct jet flow conditions. The total length of the tests has been 40-50 seconds and is a function of expected equipment durability, power requirements, air flow rate, high-pressure cooling water requirements, and steam consumption in the 2-stage ejector vacuum system. All tests are pre-programmed using auto-sequencer controls and appropriate interlocks; thus all functions of the test are carried out essentially automatically and at the correct times.

(U) The instrumentation used during the tests included, in addition to that normally employed by the arc-units, a multi-channel, magnetic-tape data recording system, a high-speed CEC oscillograph, and dual-channel strip chart recorders. Pace transducers were used for the low pressure measurements and CEC transducers for atmospheric conditions and above.

INFRARED SPECTROMETER

(U) In order to obtain non-interference static temperature measurements in the gas flow fields, as well as information on the molecular species present, a duplex scanning infrared spectrometer was utilized in the current test series. This instrument was designed and developed specifically for rugged use in emission and absorption work in high temperature arc-jet and rocket tunnels (Refs. 9,10). A complete description of the spectrometer, its operating principles, and typical data obtained under such conditions, are given in Refs. 9, 10 and 11.

(U) Briefly summarizing, the spectrometer consists of a Perkin-Elmer Model 83 Universal Monochromator modified in a number of ways including high-speed reversible scanning in both wavelength and geometric modes, and mechanical-optical synchronization in the monitoring and recording systems. A schematic of the set-up is shown in Fig. 3. The spectrometer is mounted on a heavy adjustable carriage to insure stability during the measurements; observations of the flow are made through a  $\text{CaF}_2$  window in the test section. The light path in the spectrometer is flushed continuously with super-dry nitrogen to minimize atmospheric absorption effects. The schematic in Fig. 3 shows some of the plane, elliptical and parabolic mirrors which are used to direct the light beam internally. A synchronous cam-driven mirror changes the focal position in the wake in conjunction with the wavelength and spectrometric slits. A  $\text{CaF}_2$  prism disperses the incoming light and a cam-driven rotating Littrow mirror sweeps the spectrum over a liquid nitrogen cooled PbSe detector. The high impedance detector is matched to a low impedance line with a field effect transistor amplifier of unity gain. Remote recording of the spectra is accomplished with a cathode ray tube, a 35 mm strip film camera, and, for quick post-run analyses, a CEC oscillograph is used. The spectra are also visually monitored on a 21" scope during the tests. All operations are programmed by the facility sequencer control system.

(U) The IR measurements were taken in the free stream and in the wake behind the model both with and without mass addition. Two axial positions were investigated in the present test series: at  $x/h = 1$  and  $x/h = 4$ . In the first mass addition test series (Ref. 12), the spectrometer slit was oriented perpendicular to the wake flow and focused on the center line. Scanning was done only in wavelength (2 -  $6\mu$  in 0.85 seconds). In the present test series, the 4 -  $6\mu$  wavelength region was selected for a more rapid scan rate and because all significant radiating air molecules are in this range ( $\text{CO}_2$  @  $4.25\mu$ ;  $\text{CO}$  @  $4.67\mu$ ; and  $\text{NO}$  @  $5.35\mu$ ). The flow was scanned in 0.417 sec at each of five vertical positions in the flow field from the center line outward (Fig. 4). Continual scanning was carried out in the tests so that up to 80 frames of spectral data were obtained

over the chosen wavelength range. The present wake gradient tests utilized the spectrometer slit oriented parallel to the flow. An oscillating mirror was tilted in steps of 0.0086" with a rotating sector-stepped cam so that measurements were made in the wake at ~ 0.060" intervals from the center line. A traversing mechanism, with a microscope mounted on a rectilinear stage, was used to check the location of the optical axis for each observation position. A Nernst glower was also used to determine values of the focal volumes. The gas volume in focus in the center of the flow field was a parallelepiped of 0.060" x 0.50" x 1.0" dimensions. The 0.060" is the dimension in the y-plane and corresponds to the slit opening at 5.3 $\mu$ ; the 0.50" is in the x-plane and corresponds to the length of the slit and the 1.0" refers to the depth of focus in the z-plane. The size of the focal volume was generally quite acceptable; although some problems with the data interpretation have been encountered at the  $x/h = 1$  location where different flow fields are present in a small space. The difficulties in interpretation arise in this situation because the spectroscopic measurements tend to give the highest temperature present in the focal volume. Quite obviously, a change in the internal optics in the spectrometer, which involves a change in the magnification, could aid in obtaining a reduced focal volume.

(U) Temperature levels in the flow were determined from measurements of the shifts in the P- and R-branches of the NO band (5.35 $\mu$ ). Checks on the levels were also made using the CO<sub>2</sub> (4.25 $\mu$ ) and CO (4.67 $\mu$ ) spectra. Unger (Ref. 11) discusses the theory and shows the relatively simple relationships existing between the temperature and the rotational line of maximum intensity:

$$T_{\text{NO}} = 0.1055 (\Delta\nu)^2$$
$$T_{\text{CO}} = 0.0931 (\Delta\nu)^2$$

The measurements were analyzed by magnification (20 x) and projection of the film strips using theoretically determined overlays for temperature level analyses. The general techniques are discussed by Unger (Ref. 11) and he shows typical spectra and comparisons of temperature determinations from absorption spectra of a number of diatomic molecules.

#### MODELS

(U) The models were all slender wedges, completely spanning the 5.4" jet, and were held by adjustable trunnion mountings and a heavy metal yoke. Two-dimensional models were chosen to avoid model support effects on the wake. The models were injected quickly into the stream (0.50" downstream of the nozzle) by use of a hydraulic system in the test cabin; after a pre-determined exposure time to the flow, the models were retracted. Sufficient run time was allowed for thermal stabilization before the model was injected for wake measure-

Vol. 2  
ments.

(U) The wedge models had 0.50" base heights, 0.040" nose radii, wedge half angles of  $6^\circ$ , and overall lengths of approximately 2.0". The ablating materials used were phenolic-silica (Fiberite MX-2625), ATJ grade graphite, and standard stock Teflon. The base injection models (Fig. 5) were constructed of Amsulf copper and were highly water-cooled; on the base of the models was a 1/4" x 5" strip of 20 $\mu$  sintered porous copper (1/16" thick) as the injection media. Bench tests and preliminary analytical work by Wagner and Cameron (Ref. 13) showed this material to have a porosity of 41% and a permeability in the order of  $10^{-11}$  to  $10^{-12}$  ft<sup>2</sup>. The injection velocities were believed to be uniform due to the high ratio of the effective distance to the square root of the permeability (Ref. 13); tests at low base pressure ratios confirmed this. However, high base pressure ratio data were not available and due to the uncertainties in the permeability at our test conditions, a precise value of exit velocity could not be determined; but, it was estimated to be high subsonic. Behind the porous strip was a plenum in the base of the model. High purity grade bottled gases, at ambient temperature conditions, were metered through an orifice and into the plenum. The gases used in the base injection studies were helium (He), nitrogen (N<sub>2</sub>), carbon monoxide (CO), and acetylene (C<sub>2</sub>H<sub>2</sub>). Gas injection rates were varied from 1-1/2 - 3% of the air flow rate based on model base dimensions.

TEST CONDITIONS

(U) Tables I - III show test conditions, typical levels of the flow variables, and the range of parameters involved. Table I shows the arc unit data and general test conditions for the ablator and base injection tests. Typical results are shown since data from a number of the tests are still being evaluated. The test conditions were somewhat similar to those used in earlier mass addition experiments (Ref. 12).

(U) Typical values of the flow and heat transfer parameters are shown in Table II. Most of these values were calculated from the basic measured arc-unit inputs (of Table I) using conventional energy, momentum, continuity and state equations with real gas properties based on JANAF thermochemical data (Ref. 14). In general, the calculated values shown are based on assumptions of chemical equilibrium to the nozzle throat, freezing downstream of the throat to the wedge shock, equilibrium conditions behind the normal portion of the shock, and frozen flow over the face of the body (Ref. 15). Some preliminary non-equilibrium calculations by Perini (Ref. 16) also indicate frozen flow conditions exist over the sides of the model. For comparison purposes, and to obtain the limiting bounds on the parameters, calculations were also carried out assuming complete equilibrium,

(E) - in Table II, or a completely frozen (F) state at all the flow points. The (E-F) values are for the most physically realistic combination of equilibrium and frozen flows described previously. All flow calculations were carried out on the IBM 7094 computing machine.

(U) Table III shows the range of the variables encountered in this test series; the results are divided into two sections based on arc-unit setup conditions. The results show good reproducibility and a low level of variation between the tests.

### EXPERIMENTAL RESULTS & DISCUSSION

(U) With the previously noted stable and reproducible arc-tunnel flow conditions as a base, investigations were carried out on the free stream and wake. Usually 15 - 30 measurements were taken in the free stream and 4 - 5 at each vertical location in both the wake flows. With the high temperature ablators (ATJ graphite & phenolic-silica), 8 - 10 spectral frames were obtained at each y/h location. However, for Teflon models, only 2 - 3 spectra per location could be obtained due to rapid nose blunting and erosion. The measured static temperatures were then averaged and maximum deviations of  $\pm 70^{\circ}\text{R}$  were found over a 1100 - 2400 R range of free stream and wake values; generally, the deviation was less than half the maximum.

(U) In respect to the free stream, spectroscopic observations confirmed the frozen nature and level of the flow. Observed amplitudes of the NO and CO<sub>2</sub> were consistent considering the species concentrations and radiative properties. While the CO concentration was always finite in the free stream and wake, little or no radiation at 4.67 $\mu$  was observed in these flows; at equivalent concentrations, its radiating intensities are two orders of magnitude below CO<sub>2</sub>. However, with the ablators and base injection studies, CO was observed in the wake and temperatures were determined from it. Tables IV and V show comparisons between measured and calculated values of both free stream static temperatures and also model stagnation pressures. Calculated limiting values (for the all equilibrium or all frozen stream) are also given. Values of the free stream temperature were frequently determined both before and after the mass addition experiments. As can be seen from Table IV, the variation in the free stream temperature with time was not large. The results also agree with prior test data (Ref. 12) where the data were taken and analyzed in a slightly different manner.

(U) It is well known that most arc units have some contamination in the stream. The Mach 6 arc unit had copper and boron nitride from the electrode and insulator decomposition. A slight amount of water vapor could also be noticed spectroscopically at 6.0 $\mu$  and may have come from either some slight component seepage at the high pressure

and temperature conditions or possibly from condensed moisture in the air lines from the storage tank field. However, even though the amounts were small, there were no problems in respect to the temperature determinations since the technique is essentially independent of concentration and manner of production of the species. The band width, produced by the rotational motion, is the significant characteristic and the temperature is related to spectral profiles of the rotational level population (Ref. 11). Preliminary calculations by Wagner (Ref. 17) showed little effects of the contaminants on the  $\text{CO}_2$  and NO concentrations and this was also noted spectroscopically from test to test observations. A by-product of this, though, has been the intermittent appearance of an unidentified species in the wake flows at  $\sim 5.0\mu$ ; the specie must be formed at the particular environment existing in the model stagnation region, or it has an extremely short radiative lifetime, since it is only seen in the wakes. The band or branch at  $\sim 5.0\mu$  also, apparently, has its P-branch overlapping the R-branch of the NO band. Comparisons with other spectral measurements and repeated efforts to identify this radiating compound have not been successful. Both BO ( $1861$  and  $1915\text{ cm}^{-1}$ ) and CN ( $2042\text{ cm}^{-1}$ ) are the most likely possibilities; although neither has the correct center ( $1997\text{ cm}^{-1}$ ) and the latter can be possibly eliminated due to an insufficient concentration under these conditions.

(U) For the wake-type flows, pictures of both the clean air wake, and that with 3% nitrogen added from the base, are shown in Figs. 7 and 8. Figure 9 shows a highly luminous Teflon wake. The spectrometer viewing port can be seen in the background. The differences in the base recirculation zone and shock waves can be seen (Ref. 18). Figures 10 - 12 show wake static temperature results at the  $x/h = 1$  axial position with 1-1/2 and 3%  $\text{N}_2$  and 1-1/2% CO base injection. The gas temperature at the model stagnation point (total) is used as a convenient non-dimensionalizing factor; from Table III, the values of  $T_{\text{STAG}}$  are seen to be  $5500 - 5800^\circ\text{R}$ . All wake test results are cold wall ( $T_{\text{WALL}}/T_{\text{STAG}} \approx 0.1 - 0.2$ ) with the exception of the ablators. For the wake without injection, the results differ from Muntz and Softley (Ref. 19) in level by almost a factor of two and show agreement with Batt and Kubota (Refs. 20,21) to approximately 25%. The general trends in the gradient, to  $y/h \approx 0.25$  also show agreement. In Fig. 13, a plot is given of the data of Batt and Kubota at  $x/h = 1$  and 1-1/2 using static enthalpy ratios; assuming constant specific heats these could be converted to stagnation temperature-type plots by division of the abscissa by  $\sim 8.5$ . The overall quantitative differences with Batt & Kubota and the qualitative differences at  $y/h > 0.25$  may be due to two factors. First, the temperatures determined spectroscopically are the maximum ones occurring in the focal volume; our measuring points are shown on Batt & Kubota's data (Fig. 13). Further, at the opening of the slit at  $5.3\mu$  (NO), the edges of the focal volumes essentially touch. The length of the slit determines the fact that the focal volumes

extend from  $x/h = 0.5$  to  $x/h = 1.5$ . From Batt & Kubota's mapping of this early region of the near wake, it can also be seen that our focal volumes at  $y/h > 0.25$  probably encompass a portion of either the lip and/or wake shock or the so-called "hot spot" from the boundary layer as it moves downward and aft. The fact that we are overlapping these regions can be seen from the apparent increase in NO concentration as  $y/h$  is increased. Initially, regions of the base recirculation zone are covered by the focal volume. The cooler equilibrium gas here has essentially zero NO concentration. Moving upward encompasses more of the shear layer and the regions behind the shocks and also the boundary layer "hot spot" thus giving increased amplitudes.

(U) Generally, in the clean wake, the amplitude of the  $\text{CO}_2$  band is reduced by a factor of 2 - 3 compared to its free stream value while that of the NO band remains essentially constant. This is consistent both with conditions in the stagnation region, where calculations show dissociation of  $\text{CO}_2$  to approximately one-half its free stream mass fraction and where the NO is affected only slightly (10 - 15% change) and in respect to the frozen nature of the flow over the body (Ref. 16) and in the wake. At both  $x/h = 1$  and 4 in the clean wake, the amplitude of the  $\text{CO}_2$  band is essentially a constant for all  $y/h$  values. However, for the NO band, at  $x/h = 1$  there is, as previously noted, a gradual increase in amplitude from the center line outward. At  $x/h = 4$ , the amplitude is essentially constant across the stream.

(U) Figures 14 and 15 show the clean wake at  $x/h = 4$  and mass addition with both 3% CO and  $\text{N}_2$ . The clean wake levels are essentially the same as at  $x/h = 1$ , agreeing again with Batt & Kubota (Ref. 22). The gradient is qualitatively in agreement with Muntz and Softley (Ref. 19) and indirectly supports Batt & Kubota (Ref. 21) concerning the disappearance of the boundary layer "hot spot" which has moved into the wake. It can also be noted that the maximum temperatures seen in the wake at  $x/h = 4$  are consistent with the prior measurements of Ref. 12 where the spectrometer viewed a vertical thin slice of the entire wake width at  $x/h$  values of 4-1/2 - 5.

(U) Figures 10 - 12 and 14 - 15 also show the effects of base injection on the near wake temperature profiles at  $x/h = 1$  and 4, respectively. Injection occurs from the base over the region  $y/h = \pm .25$  and the results at  $x/h = 1$  qualitatively confirm a high injection velocity (Ref. 24). The 1-1/2% CO temperature data at  $x/h = 1$  were somewhat surprising in comparison with the 1-1/2 and 3%  $\text{N}_2$  results; considering the residence time and the molecular weights of the two gases, it was expected that the results would be similar. Considerable noise was present in the spectra in this early CO test but the data appeared consistent. The results showed the CO band amplitude to be high for the first two  $y/h$  positions and then decrease to almost zero at  $y/h = .5$ . The  $\text{CO}_2$  amplitude was low at the center line and gradually increased to its normal wake level at  $y/h = 0.5$ ;

Vol. 2

the NO band had the same trend but not so pronounced. With the 1-1/2 and 3% N<sub>2</sub> injection, similar effects were noted for the CO<sub>2</sub> and NO. At x/h = 2, nitrogen injection (3%) effects still persist while some slight oxidation has occurred with the carbon monoxide. Figures 16 & 17 summarize the temperature as compared to the local value in the wake. The results show that up to 15 - 30% reductions are possible at x/h = 1 for these small flow rates and approximately 10% at x/h = 4.

(U) For the ablators, heat transfer levels to the stagnation region of the models was not high (typical of the higher altitude environments simulated) and thus, where onset of ablation occurs, significant mass losses to effect wake cooling were not present. However, some qualitative aspects of the tests were interesting. Figure 18 shows a comparison between a Teflon wake at x/h = 1 and those from non-ablating bodies. As can be seen, both the temperature levels and gradients are the same even though mass addition occurs in the stagnation region of the Teflon body. Further, the temperature levels of the surfaces of the two model types are not too different and the mass loss rate from the Teflon is of a comparable level to that used in the base injection studies. It can be concluded that, at x/h = 1, the effectiveness of the stagnation region is quite low in respect to wake static temperature changes as compared to base injection.

(U) Figure 19 shows the wake temperatures from three types of ablating bodies, compared to a non-ablating one, at the x/h = 4 axial location. Some caution must be exercised in using the center-line data for Teflon. It consists of only one data point; two others were lost due to the unexpected amplification (off-scale) of the NO band in this region. The Teflon results imply also that little changes have occurred except perhaps that the additional residence time at the lower center line velocities have allowed for the endothermic dissociation and resultant oxidation mechanisms to occur. Heicklen (Ref. 23) and Cresswell (Ref. 25) discuss the problems in the chemistry of C<sub>2</sub>F<sub>4</sub> oxidation.

(U) For the high surface temperature (3000 - 4000°R) graphitic-type ablators, ATJ graphite and phenolic-silica, the mass loss rate is comparatively small and the effects noted in the wake could be due almost entirely to surface temperature. Muntz (Ref. 19) has pointed out the almost linear increase as a function of surface temperature at the lower  $T_w/T_{STAG}$  conditions. The present results tend to show this. However with all the ablators, and especially these latter two, there were significant changes in the amplitudes of the spectra. Figures 20 to 22 show this as a function of the ratio of the species to the value existing in the cold wall wake.

Figure 23 shows the typical spectra from the phenolic-silica tests at  $x/h = 4$ .

(U) During the tests, some blunting of the ablator models occurred; the nose radius for Teflon went from 0.035 to 0.050; phenolic-silica had the most significant changes, from .040 to .080 (due to the typical solidification of the molten glass); and no change occurred with the graphite models. No changes in wake temperatures were noted for either the Teflon or phenolic-silica cases as a function of nose radius. The amplitudes of both the NO and CO increased with time for both the ATJ and phenolic-silica models. Little effect on wake temperature, due to the transient heating of the graphite, could be seen. On all ablation tests, base heating was very low and with the phenolic-silica and ATJ models only a slight change in base material conditions could be noted.

(U) In conclusion, the results show that the use of infrared spectroscopy for static temperature determinations in high temperature and velocity flows is not only advantageous from a non-interference viewpoint in a chemically reacting flow, but also is useful in obtaining information concerning radiating species and relative concentration changes. The IR measurements may be made utilizing any of the bands of the nonhomopolar molecules (NO, CO, CO<sub>2</sub>) in air but the NO band has particular advantages due to its concentration-radiation characteristics and to the clear-cut separation of its branches.

(U) TABLE 1. Test Conditions

Test No.	$P_t$ (arc) (psia)	$H_t$ (arc) (Btu/lbm)	$\dot{w}_a$ (lbm/sec)	Total Test Time (sec)	Power (MW)	Current (amps)	Model Type
51	286	1850	0.723	31	7.9	13,700	ABL - TEF.
52	294	1950	.728	50	7.4	13,800	BI - N <sub>2</sub>
53	291	1890	.730	45	7.4	13,800	BI - N <sub>2</sub>
54	288	1840	.730	45	7.2	13,700	BI - CO
55	292	1820	.743	45	7.5	14,000	BI - He
56	292	1830	.741	45	7.6	13,800	BI - C <sub>2</sub> H <sub>2</sub>
57	290	1870	.731	35	7.1	14,100	BI - N <sub>2</sub>
58	310	2010	0.759	47	7.4	11,200	BI - N <sub>2</sub>
59	318	2070	.768	52	7.9	12,400	BI - N <sub>2</sub>
60	314	2040	.765	52	7.3	11,600	BI - N <sub>2</sub>
61	315	2030	.767	52	7.8	12,400	BI - CO
62	298	2050	.725	52	7.2	12,000	BI - CO
63	294	1950	.728	52	7.7	12,600	BI - CO
64	300	2060	.726	52	7.5	12,500	BI - N <sub>2</sub>
65	297	2020	.725	52	7.5	12,500	BI - N <sub>2</sub>
66	311	2070	.753	53	7.7	11,600	ABL - P-S
67	308	2070	.746	54	8.0	12,200	ABL - ATJ
68	318	2110	.764	53	8.1	12,500	ABL - P-S
70	315	2070	.761	52	8.1	12,400	ABL - ATJ
71	316	2080	.762	35	8.1	12,400	ABL - TEF.

BI - base injection  
ABL - ablator

(U) TABLE II. Typical Calculated Flow Properties

	Test No. 52					
	Arc Chamber (E)	Nozzle Throat (E-F)	Nozzle Exit (E-F)		Model (E)	Stag. Point (F)
P (psia)	294.	154.	0.317	0.281	10.2	9.83
T (°R)	6120.	5530.	1410.	1210.	5630.	6120.
H (Btu/lb) <sup>OR</sup>	1950.	1690.	346.	426.	1950.	1950.
s (Btu/lb <sup>OR</sup> )	2.14	2.14	2.14	2.14	2.38	2.38
ρ (lbm/ft <sup>3</sup> )	0.128	.0744	.000608	.000623	.00469	.00415
Mol. wt (-)	28.48	28.70	28.97	28.70	27.86	28.48
u (ft/sec)	0.	3620.	8970.	8740.	0.	0.
<u>Species Concentrations (Mass Percent)</u>						
NO	6.66	5.00	0.0002	5.00	4.86	6.66
CO <sub>2</sub>	0.0279	0.0352	0.0462	0.0352	0.0175	0.0279
CO	0.0117	0.0070	0.	0.0070	0.0182	0.0117
O	1.86	1.02	0.	1.02	4.40	1.86
N	0.0013	0.0003	0.	0.0003	0.0015	0.0013
O <sub>2</sub>	17.74	19.46	23.14	19.46	16.17	17.74
N <sub>2</sub>	72.42	73.19	75.53	73.19	73.26	72.42

Stagnation Heat Flow: 500 - 1000 Btu/ft<sup>2</sup>-sec

8th Navy Symposium on Aeroballistics

Vol. 2

(U) TABLE III. Range of Variables in Arc-Tunnel Near Wake Tests

		Test Series I (Runs 50-57)	Test Series II (Runs 58-71)
$P_t$	(psia)	286 - 294	294 - 318
$H_t$	(Btu/lbm)	1830 - 1950	1950 - 2110
$\dot{w}_a$	(lbm/sec)	0.723 - 0.741	0.725 - 0.768
$u$	(ft/sec)	8510 - 8740	8930 - 9050
$T_\infty$	(°R)	1070 - 1210	1160 - 1270
$P_3$	(psia)	0.21 - 0.28	0.22 - 0.30
$P_{STAG}$	(psia)	8.1 - 9.8	8.4 - 10.6
$T_{STAG}$	(°R)	5470 - 5670	5720 - 5880

(U) TABLE IV. Comparison of Measured &amp; Calculated Free Stream Static Temperatures

Test NO.	Measured Temperatures (Before)(After) * ( $^{\circ}$ R)	Calculated Temperature Range ( $^{\circ}$ R)	Maximum & Min. Calculated Temperatures $^{\circ}$ R (E) (F)	Experimental Variation in Measured $T_{\infty}$ ( $^{\circ}$ R)
50	1143 - 1172	1070 - 1150	1300 - 1000	$\pm 34$ , $\pm 27$
51	1170 - 1129	1080 - 1150	1310 - 1010	$\pm 25$ , $\pm 32$
52	1166 - 1166	1130 - 1210	1410 - 1040	$\pm 31$ , $\pm 18$
53	1125 - 1168	1100 - 1170	1350 - 1020	$\pm 27$ , $\pm 36$
54	1159 - 1165	1080 - 1150	1300 - 1000	$\pm 20$ , $\pm 25$
61	1206 - 1170	1160 - 1240	1480 - 1070	$\pm 40$ , $\pm 0$
62	1143	1190 - 1270	1550 - 1080	$\pm 29$
66	1179 - 1116	1180 - 1260	1520 - 1080	$\pm 29$ , $\pm 40$
67	1132 - 1120	1180 - 1260	1520 - 1080	$\pm 49$ , $\pm 29$
68	1195 - 1213	1190 - 1270	1560 - 1090	$\pm 31$ , $\pm 34$
70	1177 - 1201	1180 - 1240	1520 - 1080	$\pm 34$ , $\pm 34$
71	1181 - 1157	1180 - 1260	1530 - 1080	$\pm 34$ , $\pm 34$

\* Values for Before &amp; After Model Injection

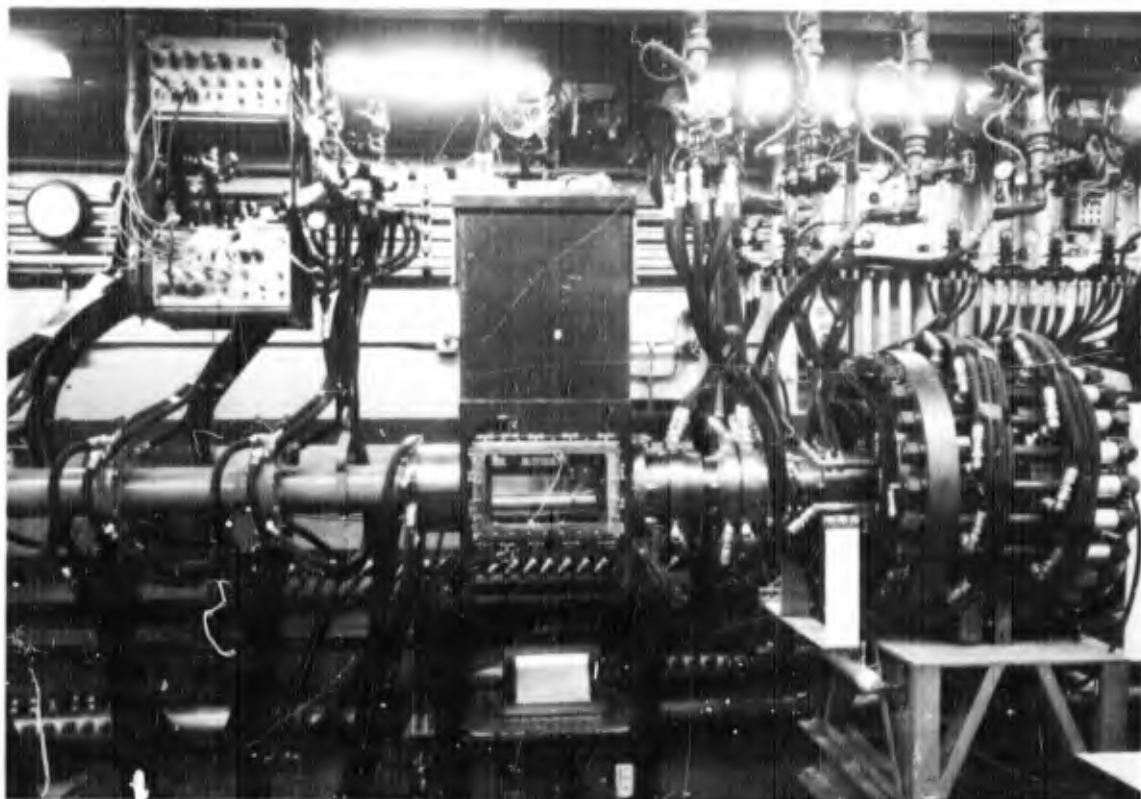
8th Navy Symposium on Aeroballistics

Vol. 2

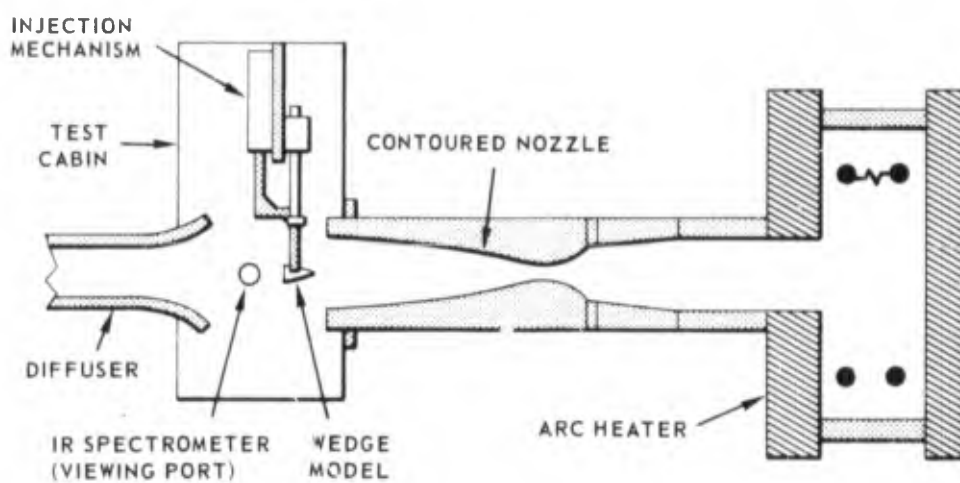
(U) TABLE V.

Comparison of Measured & Calculated Model Stagnation Pressures

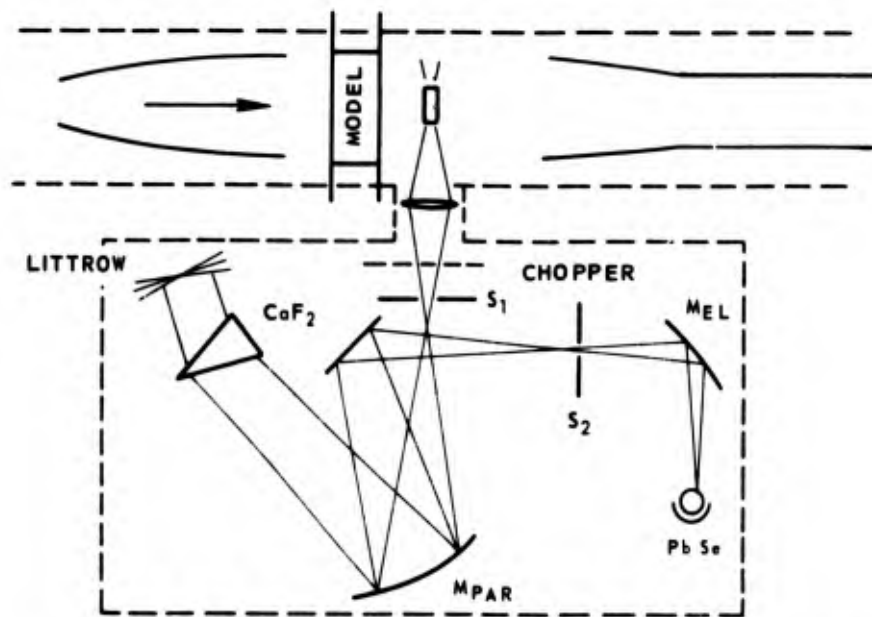
TEST No.	Measured Pressures	Calculated Pressures (E-F)	Maximum & Minimum Pressures (E) (F)
	(psia)	(psia)	(psia)
53	9.30	8.23 - 9.72	10.0 - 8.02
54	9.31	8.15 - 9.62	9.89- 7.95
55	9.70	8.27 - 9.76	10.0 - 8.07
56	9.65	8.25 - 9.74	10.0 - 8.05
57	9.55	8.22 - 9.70	9.99- 8.01
58	9.92	8.78 - 10.4	10.7 - 8.53
59	10.20	8.99 - 10.6	11.0 - 8.72
60	10.30	8.89 - 10.5	10.9 - 8.63
61	10.30	8.90 - 10.5	10.9 - 8.65
62	9.62	8.44 - 9.96	10.4 - 8.19
63	9.56	8.46 - 9.98	10.4 - 8.20
64	9.56	8.48 - 10.0	10.4 - 8.22
65	9.48	8.41 - 9.92	10.3 - 8.16



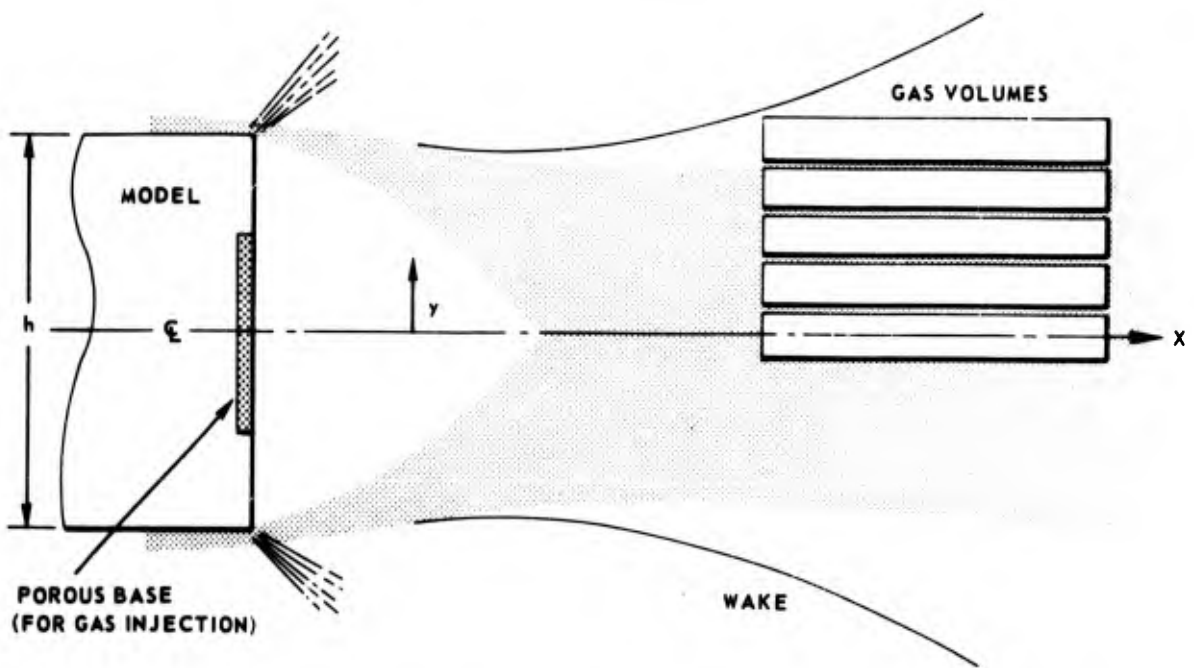
(U) Fig. 1 MACH 6 ARC TUNNEL



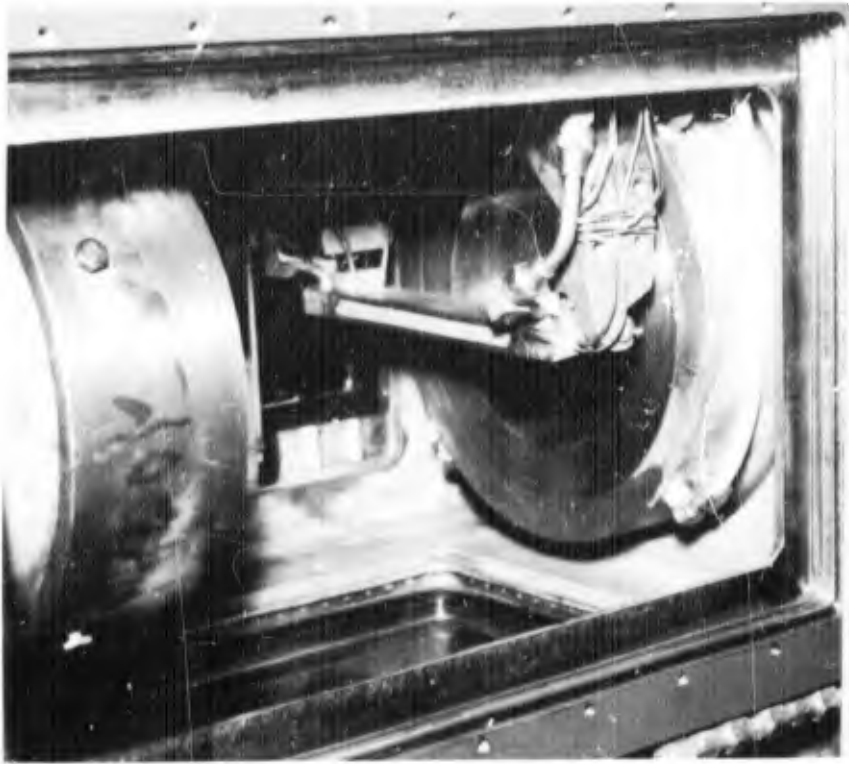
(U) Fig. 2 SCHEMATIC DIAGRAM OF TEST SETUP



(U) Fig. 3 SCHEMATIC OF SPECTROMETER AND ARC TUNNEL

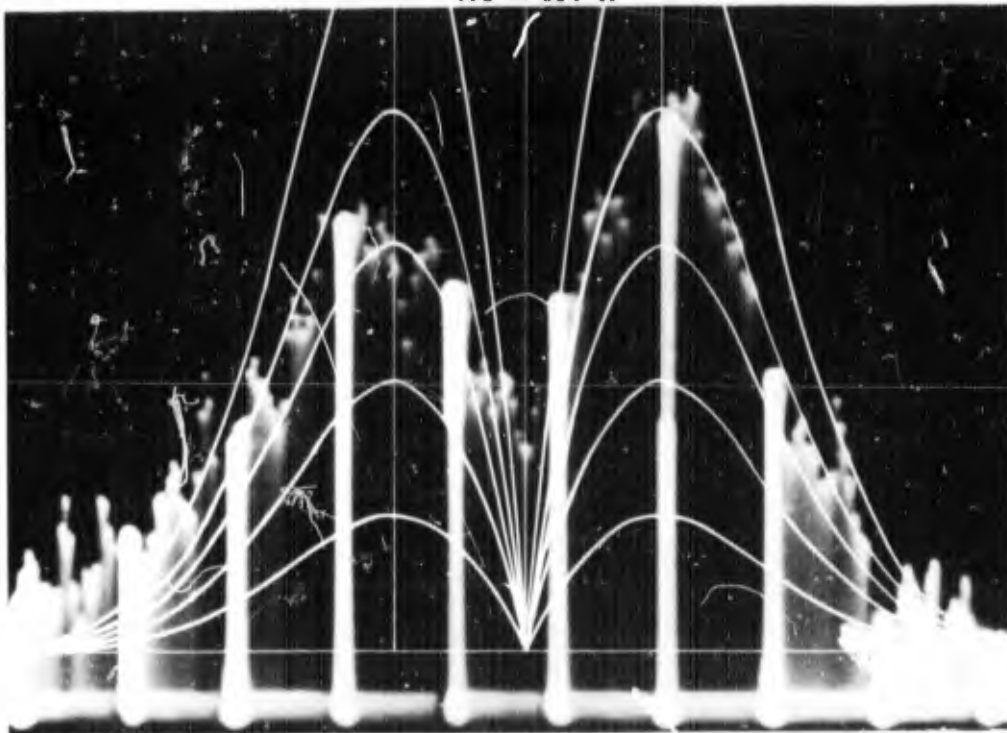


(U) Fig. 4 MODEL AND FOCAL GAS VOLUMES FOR SPECTROSCOPIC MEASUREMENTS

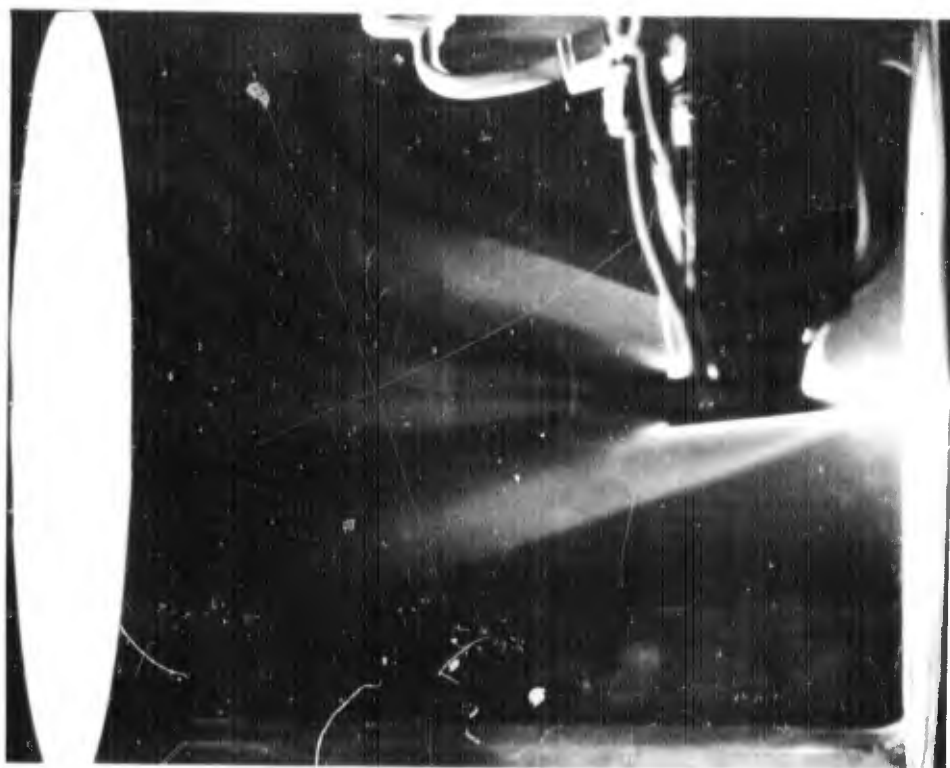


(U) Fig. 5 BASE INJECTION MODEL

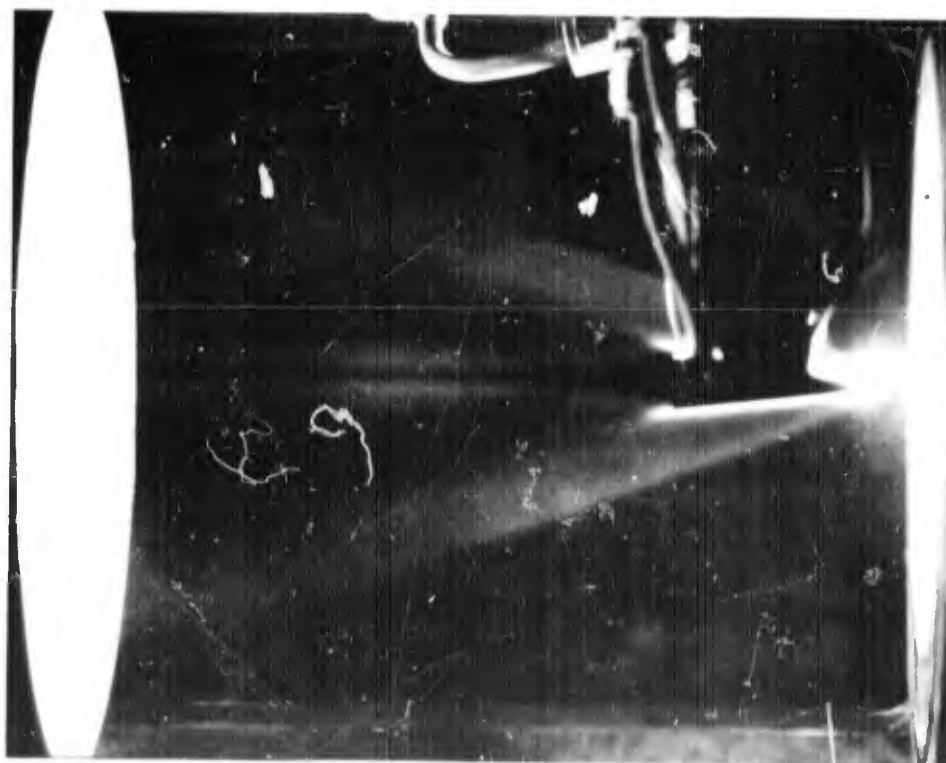
NO at 650° K



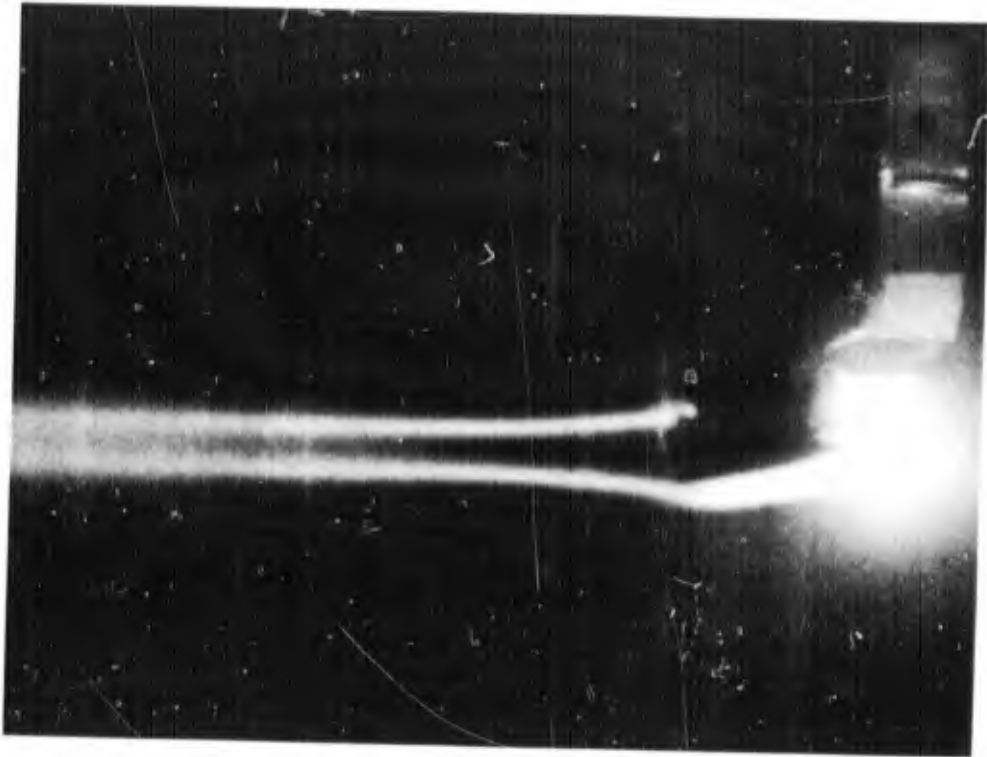
(U) Fig. 6 FREE STREAM NO-BAND SPECTRA



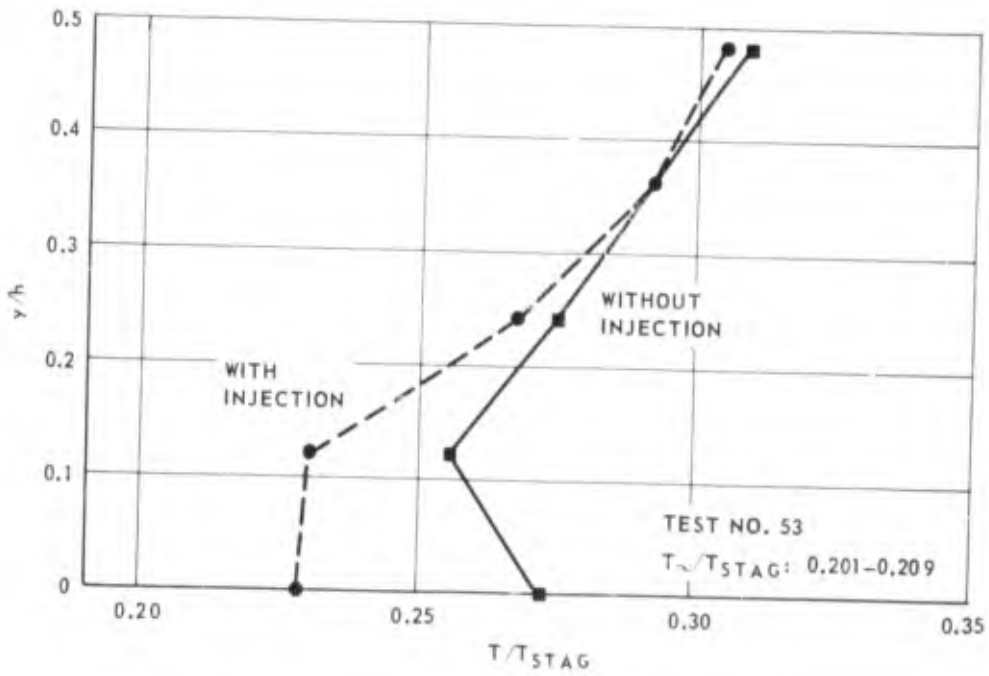
(U) Fig. 7 CLEAN AIR WAKE



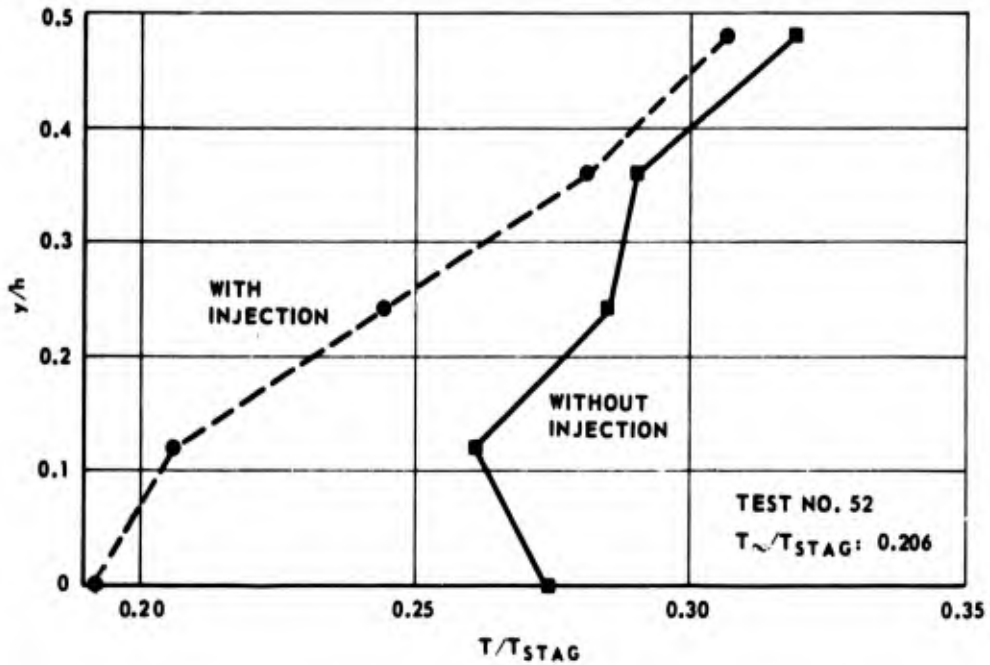
(U) Fig. 8 WAKE WITH 3% N<sub>2</sub> (BASE INJECTION)



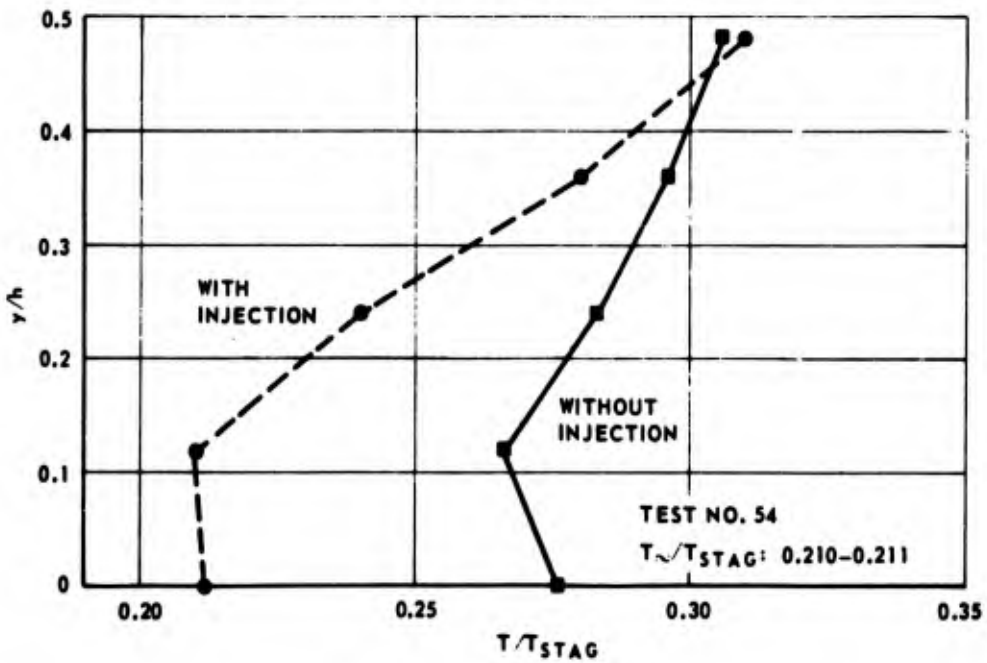
(U) Fig. 9 TEFLON WAKE



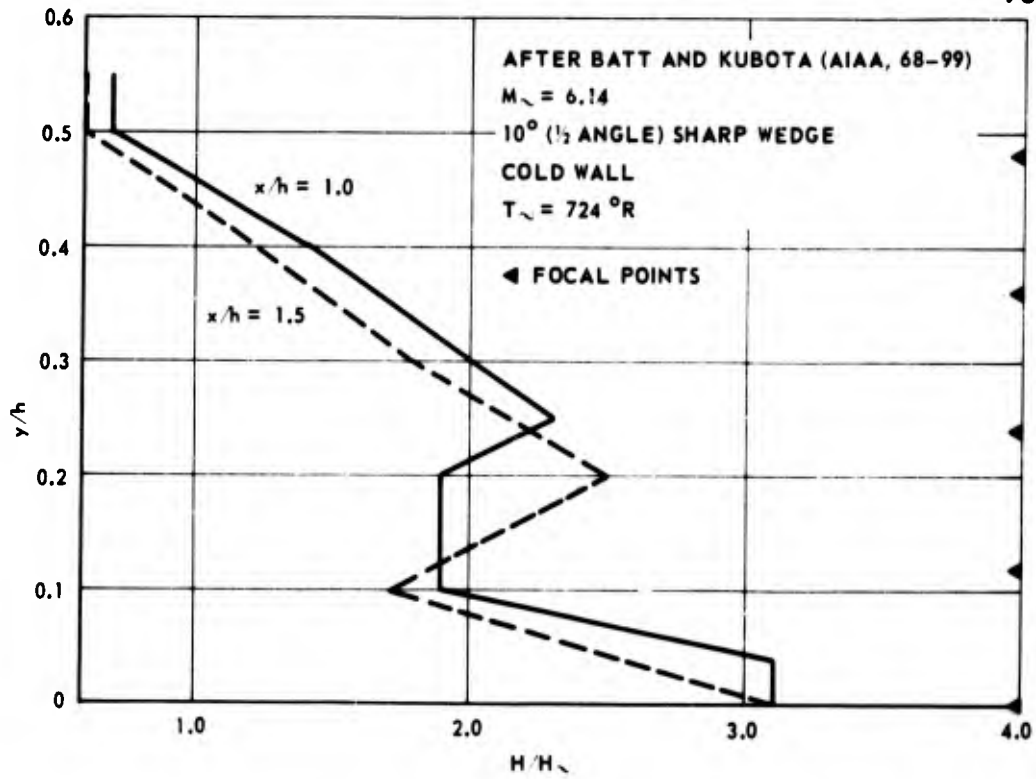
(U) Fig. 10 NEAR WAKE STATIC TEMPERATURE LEVELS  
 (WITH BASE INJECTION OF 1½% N<sub>2</sub>)  $x/h = 1$



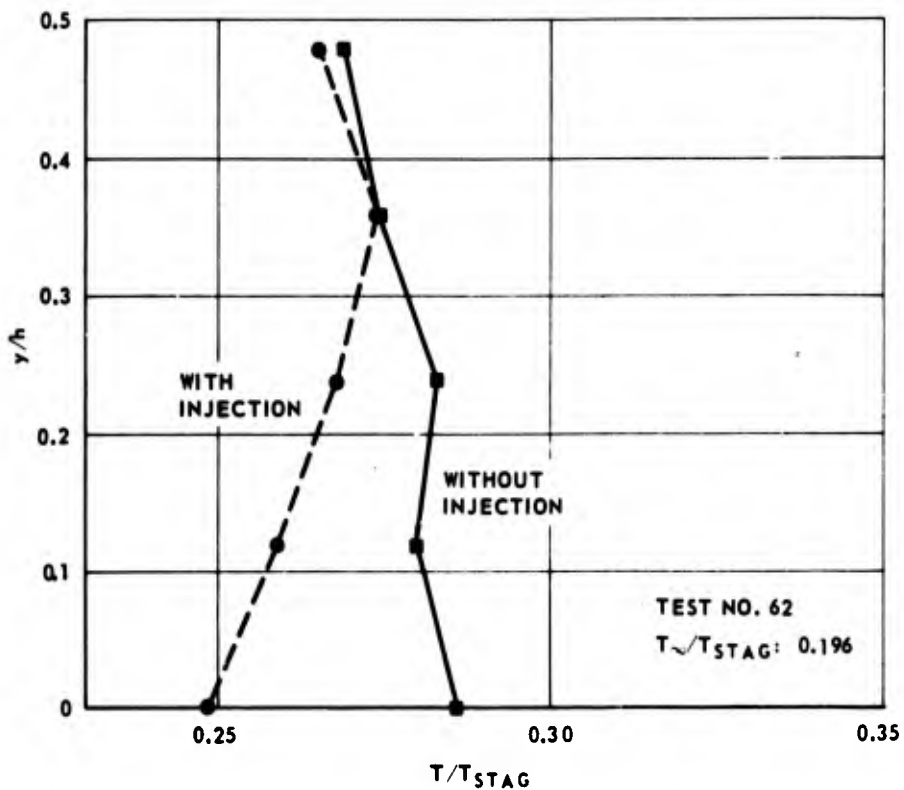
(U) Fig. 11 NEAR WAKE STATIC TEMPERATURE LEVELS (WITH BASE INJECTION OF 3% N<sub>2</sub>) x/h = 1



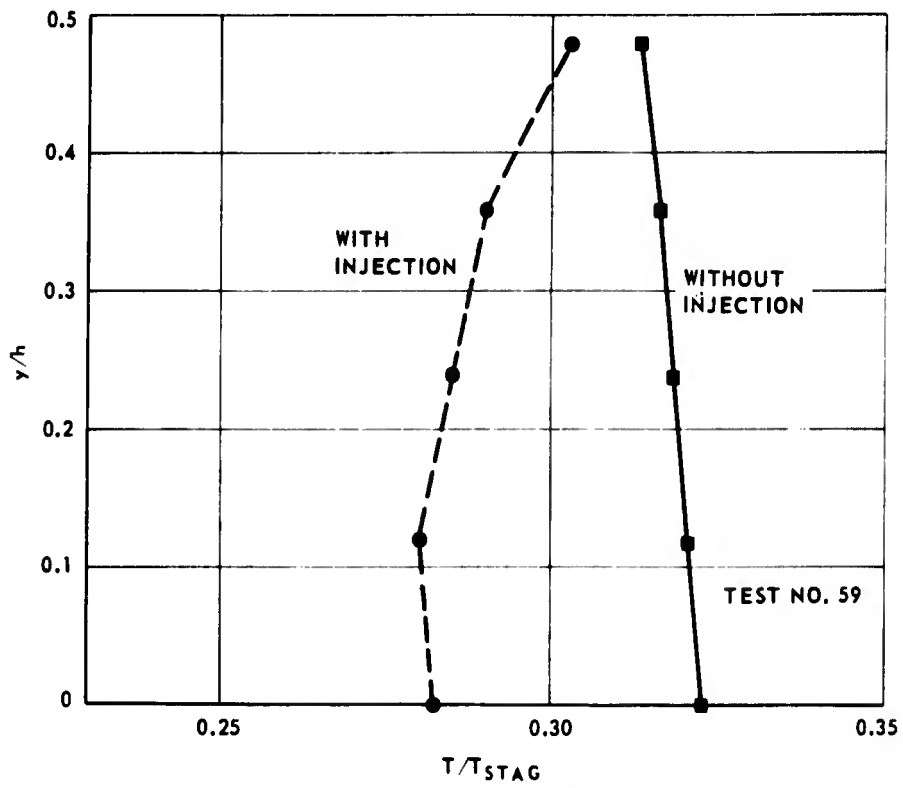
(U) Fig. 12 NEAR WAKE STATIC TEMPERATURE LEVELS (WITH BASE INJECTION OF 1 1/2% CO) x/h = 1



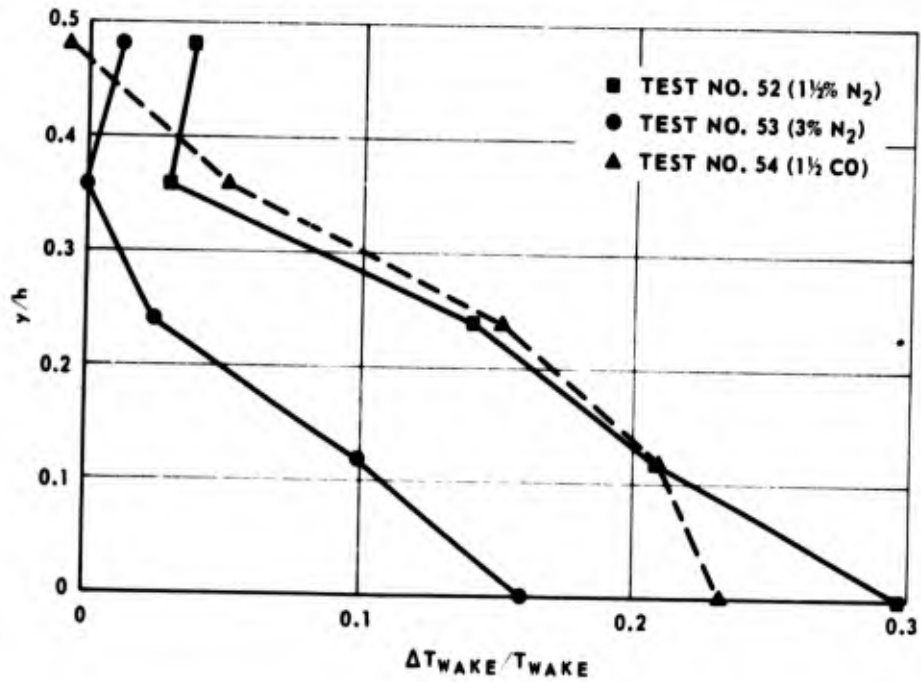
(U) Fig. 13 STATIC ENTHALPY IN THE NEAR WAKE AT  $x/h = 1.0, 1.5$



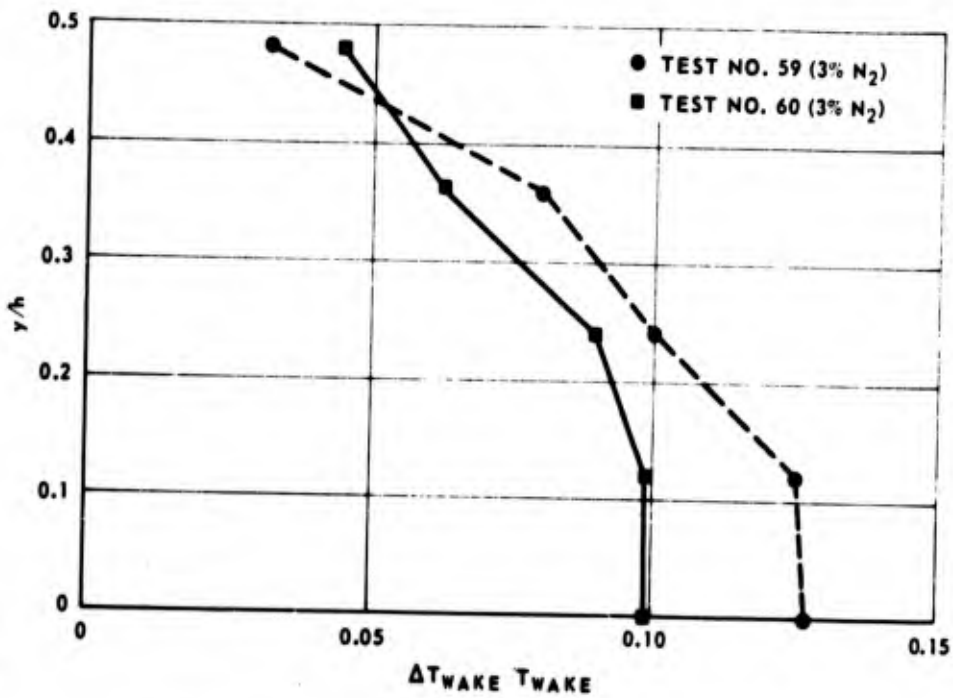
(U) Fig. 14 NEAR WAKE STATIC TEMPERATURE LEVELS (WITH BASE INJECTION OF 3% CO)  $x/h = 4$



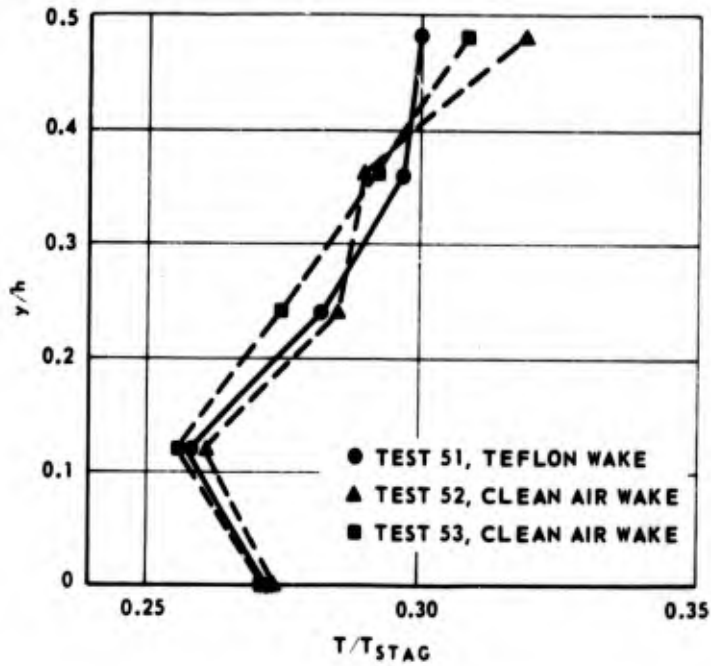
(U) Fig. 15 NEAR WAKE STATIC TEMPERATURE LEVELS  
(WITH BASE INJECTION OF 3%  $N_2$ )  $x/h = 4$



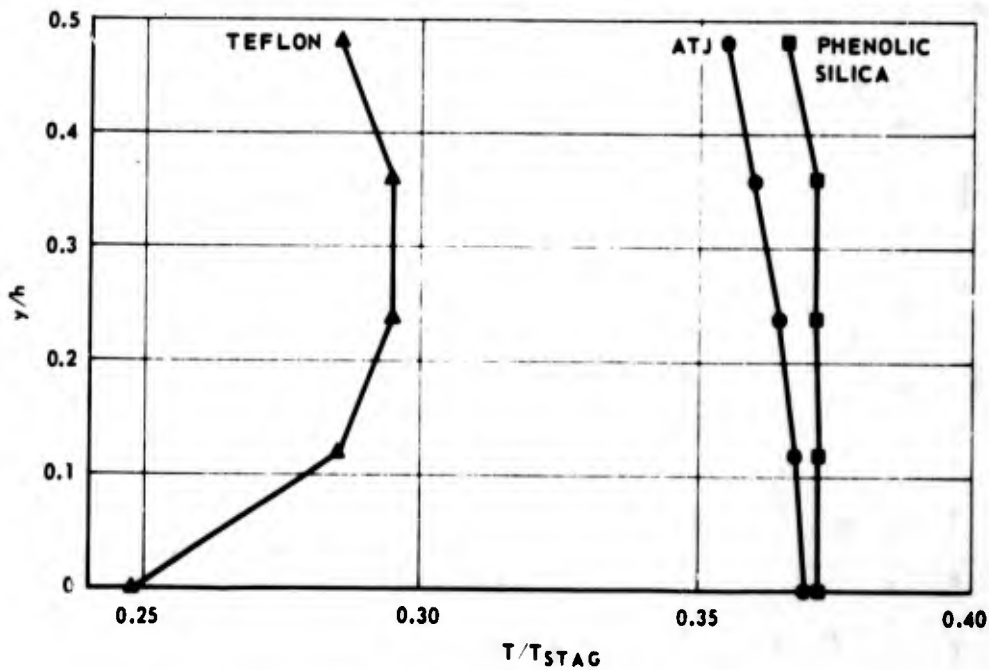
(U) Fig. 16 EFFECT OF BASE MASS ADDITION ON REDUCTION OF STATIC TEMPERATURE LEVELS (GASES: N₂, CO)  $x/h = 1$



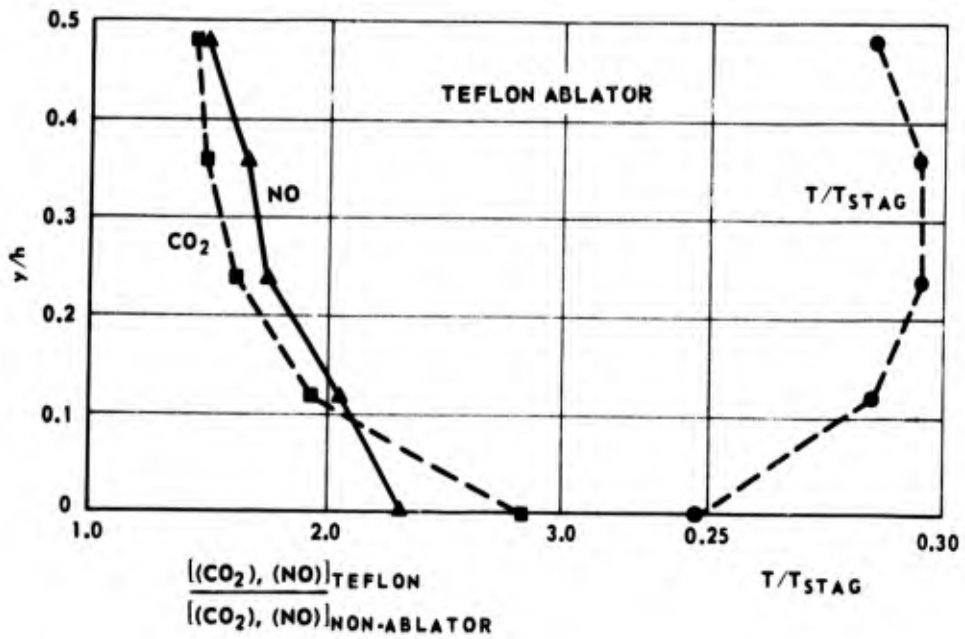
(U) Fig. 17 EFFECT OF BASE MASS ADDITION ON REDUCTION OF STATIC TEMPERATURE LEVELS  $x/h = 4$



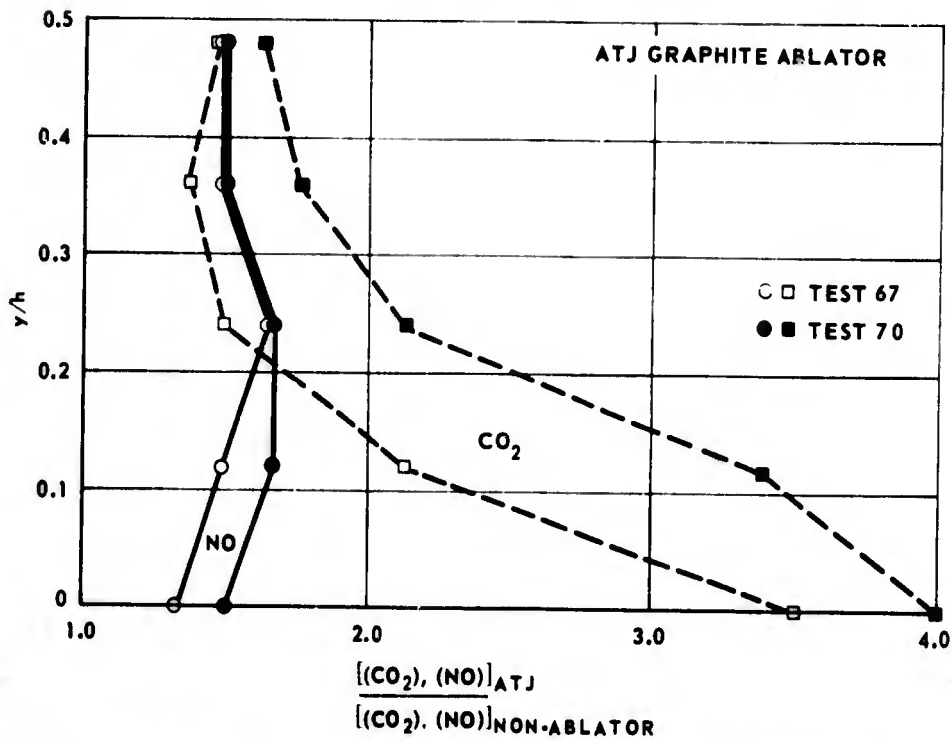
(U) Fig. 18 COMPARISON OF TEFLON AND CLEAN WAKES AT  $x/h = 1$



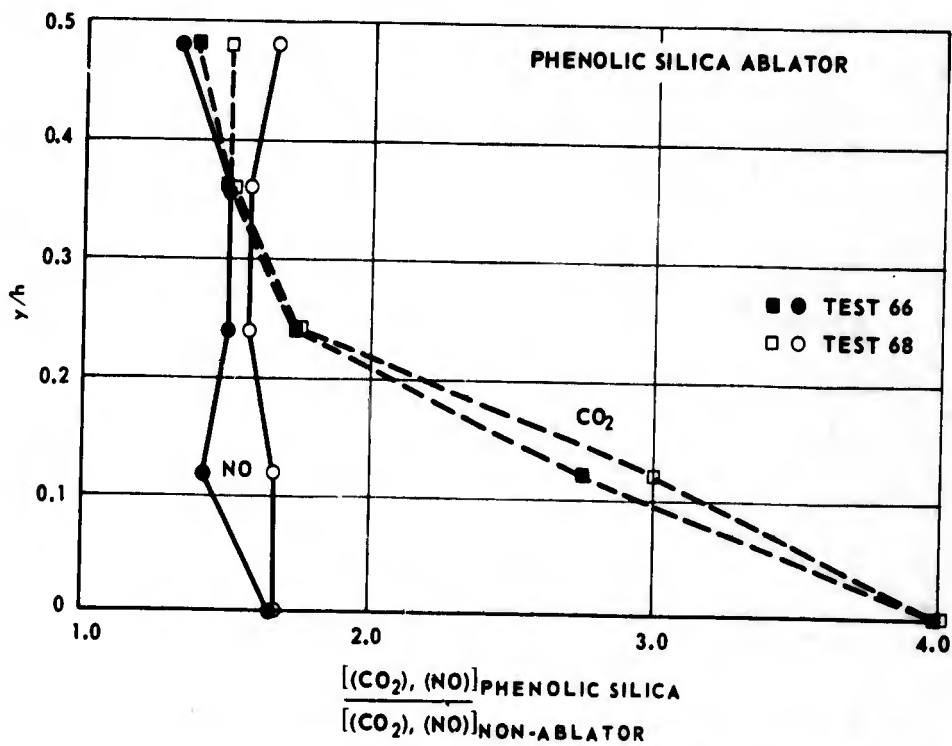
(U) Fig. 19 NEAR WAKE STATIC TEMPERATURE LEVELS AT  $x/h = 4$



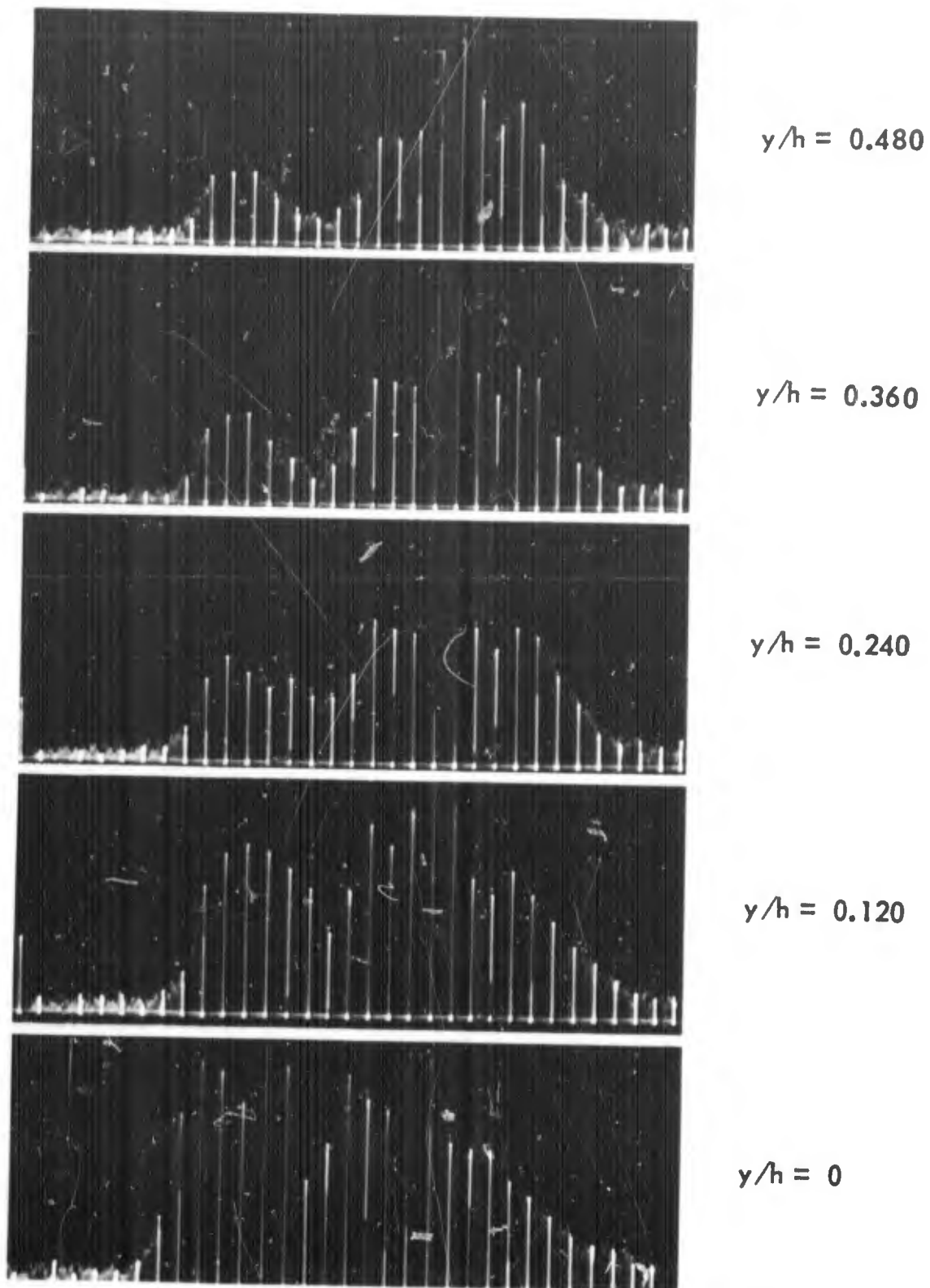
(U) Fig. 20 INCREASE IN IR SPECTRAL AMPLITUDES DUE TO MASS ADDITION  $x/h = 4$



(U) Fig. 21 INCREASE IN IR SPECTRAL AMPLITUDES DUE TO MASS ADDITION  $x/h = 4$



(U) Fig. 22 INCREASE IN IR SPECTRAL AMPLITUDES DUE TO MASS ADDITION  $x/h = 4$



(U) Fig. 23 TYPICAL SPECTRA-PHENOLIC SILICA WAKE ( $x/h=4$ )

## (U) REFERENCES

1. Lykoudis, P.S., "A Review of Hypersonic Wake Studies," AIAA Journal, Vol. 4, No. 4, April 1966, pp. 577-590. (See also: Rand Corp. Report RM-4493-ARPA, May 1965). (U)
2. Lykoudis, P.S., "Recent Developments in the Fluid Mechanics of Hypersonic Wakes," Rand Corp. Report P-3451, Nov. 1966. (Presented at XVIIth International Astronautical Congress, Madrid, October 10-15, 1966). (U)
3. Eschenroeder, A.Q., "Kinetic Processes in Hypersonic Wakes," presented at AGARD Specialists' Meeting on Fluid Physics of Hypersonic Wakes, Colorado State Univ. Fort Collins, Colorado, May 10-12, 1967 (AGARD CP No. 19 and the Supplement). (U)
4. Steiger, M., "A Review of Hypersonic Re-entry Wakes and Auxiliary Studies - Part I: Base Flow and Near Wake Fluid Dynamics," Heliodyne Corp. Res. Note 40, July 1967. (U)
5. Lees, L., "Hypersonic Wakes and Trails," AIAA Journal, Vol. 2, No. 3, March 1964, pp. 417-428 (Presented as Preprint 2662-62 at ARS 17th Annual Meeting, Los Angeles Calif. Nov. 13-18, 1962). (U)
6. Bunt, E.A., Cusick, R.T., Bennett, L.W. and Olsen, H.L., "Design and Operation of the Battery Power Supply of a Hypersonic Propulsion Facility," APL/JHU TG-660, Feb. 1965. (U)
7. Raezer, S.D., Bunt, E.A. and Olsen, H.L. "Development of Hypersonic Propulsion Tunnels Using D.C. Plasma Arc Heating," presented at AIAA/ASME Ramjet Propulsion Conference, NOL, White Oak, Maryland, April 25, 1963. (U)
8. Makofski, R.M. (APL/JHU) private communication.
9. Hill, F.K., Unger, H.J. and Dickens, W.P., "Spectroscopic Measurements of Combustion Gas Composition in Supersonic Flow," AIAA Journal, Vol. 5, No. 5, May 1967, pp. 873-881.
10. Unger, H.J., Hill, F.K. and Dickens, W.P., "Spectrographic Analysis of Rocket Nozzle Flow," APL/JHU Report TG-877, Jan. 1967. (U)

## 8th Navy Symposium on Aeroballistics

### Vol. 2

#### (U) REFERENCES (Cont'd)

11. Unger, H.J., Hill, F.K., Paul, N.G., "Spectroscopic Determination of High Velocity Flow Field Static Temperatures," to be presented at IEEE 3rd International Congress on Instrumentation in Aerospace Simulation Facilities, New York, May 1969. (U)
12. Paul, N.G., Unger, H.J., Kauffman, L.O. and Hill, F.K., "Arc-Tunnel Wake Investigations Using Scanning Infrared Spectrographic Measurements, Paper 68-704, AIAA Fluid and Plasma Dynamics Conference, Los Angeles, Calif., June 1968. (U)
13. Wagner, J.P. and Cameron, J.M., "Controlled Gaseous Injection in Re-Entry Studies," Section VII/lb, Research and Exploratory Development Quarterly Report, October-December 1968, APL/JHU AQR/68-4. (U) (publication CONF.)
14. "JANAF Thermochemical Data," Dow Chemical Co., Midland, Mich. (U)
15. Perini, L.L., "Chemical Effects in a High Enthalpy Nozzle and Shock Shape Estimate for a Highly Blunted Slender Wedge." APL/JHU BHP-67-27, September 1967. (U)
16. Perini, L.L. and Melnick, W.L., "Non-Equilibrium Hypersonic Flow Past Smooth Symmetric Bodies." J. Spacecraft & Rockets, Vol. 5, No. 3, pp. 309-313, March 1968.
17. Wagner, J.P., "The Presence of Contaminants in Wake-Type Arc-Jet Experiments," APL/JHU BFM-104, April 1968. (U)
18. Chapkis, R.L., Fox, J., Hromas, L. and Lees, L., "An Experimental Investigation of Base Mass Injection on the Laminar Wake Behind a 6-Degree Half-Angle Wedge at  $M = 4.0$ ," presented at AGARD Specialists' Meeting on Fluid Physics of Hypersonic Wakes, Colorado State University, Fort Collins, Colorado, May 10-12, 1967 (AGARD CP No. 19 and the Supplement). (U)
19. Muntz, E.P. and Softley, E.J., "A Study of Laminar Near Wakes," AIAA Journal, Vol. 4, No. 6, June 1966, pp. 961-968. (U)
20. Batt, R.G., "Experimental Investigation of Wakes Behind Two-Dimensional Slender Bodies at Mach Number Six," Ph.D. Thesis, California Institute of Technology, Pasadena, Calif., 1967. (U)

## (U) REFERENCES (Cont'd)

21. Batt, R.G. and Kubota, T., "Experimental Investigation of Laminar Near Wakes Behind  $20^\circ$  Wedges at  $M_\infty = 6$ ," AIAA Paper 68-99, AIAA 6th Aerospace Sciences Mtg. New York, Jan. 22-24, 1968. (U)
22. Batt, R.G. and Kubota, T., "Experimental Investigation of Far Wakes Behind Two-Dimensional Slender Bodies at  $M_\infty = 6$ ," AIAA Paper 68-700, AIAA Fluid and Plasma Dynamics Conf., Los Angeles, Calif., June 1968. (U)
23. Heicklen, J., "Gas-Phase Chemistry of Re-Entry," AIAA Journal, Vol. 5, No. 1, January 1967, pp. 4 - 15. (U)
24. Hill, J.A.F. and Luce, R.W., "Wind Tunnel Measurements of Turbulent Wake Cooling With Base Injection," Mithras, Inc. Rept. MC 64-85-R3 (AFOSR 66-1929), August 1966. (U)
25. Cresswell, J., Kaplan, B., Porter, R., Sarkos, C., "Material Effects of Low Temperature Ablators on Hypersonic Wake Properties of Slender Bodies," (Presented at a Specialists' Meeting of the Fluid Dynamics Panel of AGARD on "The Fluid Physics of Hypersonic Wakes," at Colorado State University, Fort Collins, Colo., May 10-12, 1967; AGARD CP-19). (U)
26. Wilson, L.N., Hayami, R.A., Evans, E.W., Robillard, P.E. and Liu, I., "Effect of Ablation Material on Observables from a Slender Cone in a Free Flight Range," General Motors Corp. DRL Rept. CTN64-09, October 1964. (U)

**BLANK PAGE**

Paper No. 17

**ISOTHERMAL LEADING EDGES**  
(U)

(Paper UNCLASSIFIED)

by

Bertram K. Ellis  
Naval Ship Research and Development Center  
Washington, D.C. 20007

**ABSTRACT.** A mathematical model is developed to simulate a two-dimensional wick-vapor chamber cooling device for application to the hypersonic leading edge heating problem. The principle involved is basically that of the heat pipe and the intent is to show how the combination of this high conductivity device and surface radiation can be employed to alleviate the high temperatures usually associated with a sharp leading edge.

The model simulates a molybdenum skin material with a fictitious underlying material of high conductivity. The fictitious material is assigned a conductivity value equivalent to the effective conductivity of an operating sodium heat pipe. Surface heating conditions in the form of convection and radiation in conjunction with internal conduction is considered for two Mach numbers. The isothermal conditions brought about by the wick-vapor chamber are clearly demonstrated.

INTRODUCTION

Aerodynamic heating can be classified among the foremost technical problems confronting the development of hypersonic vehicles. This problem is probably most apparent within the first few inches along a wing or fin leading edge where the heat transfer coefficient becomes asymptotically large (varies as  $\frac{1}{\sqrt{x}}$ ). The combination of large heating flux and the poor material area distribution of the sharp hypersonic leading edge results in temperatures at the tip approaching the recovery temperature. (Since the sharp leading edge has definite performance advantages, a means of alleviating the excessive tip temperature would be highly beneficial). Under the same high temperature tip conditions, the aft section of the leading edge (beyond a few inches) experiences equilibrium temperatures which can be of the order of hundreds of degrees lower. Fig. 1, from Ref. 1, shows the temperature distributions which would occur along the leading edges of a typical hypersonic vehicle at a Mach number of 8.

These extreme leading edge temperatures pose serious oxidation, strength, stiffness and creep problems for the most promising metallic leading edge materials. Fig. 2 shows the relative structural limitations of the coated refractory metals (molybdenum, columbium, tantalum and tungsten) and the super alloys (nickel or cobalt base) at extreme temperatures over a period of exposure time.

Although the coated refractory metals have superior stiffness qualities up to 2300°F, they could not effectively be used at this temperature for any extended length of time since the worn coatings would result in the metal rapidly oxidizing. Reduction in leading edge tip temperatures would greatly enhance the suitability of the refractory metals over the extended time periods.

The super alloys on the other hand are highly resistive to oxidation but have strength, stiffness and creep restrictions imposed at about 1600°F. Both sets of metals could be used as hot leading edge materials over the economic life of a reusable hypersonic vehicle in the Mach number 6-8 flight regime if an effective means could be found to reduce stagnation tip temperatures.

The intention of this paper is to numerically show that a heat pipe configured in the form of a sharp  $10^\circ$  leading edge would be capable of appreciable leading edge tip temperature alleviation for steady state hypersonic heating. Prior to discussing the numerical

approach, it is appropriate here to first review some of the very basic heat pipe principles.

### HEAT PIPE PRINCIPLES

The heat pipe was the result of research into high heat transfer devices for space applications (Ref. 2). It chiefly consists of a sealed metal tube enclosing a fluid saturated porous wick (Fig. 3). A steady state heat pipe operating under radiation cooling can be described as follows: Heat addition at one end of the pipe will cause the adjacent fluid contained in the wick to vaporize and travel with its acquired heat of vaporization (under the influence of a small pressure gradient) toward the unheated end. The energized vapor will continually release its latent heat on the cooler surfaces while condensing slowly back into the wick. The condensed liquid would then under the action of capillary pressure forces travel back through the wick toward the heated end, thereby continuing the heat exchange cycle. This combined heat and mass transfer process is governed by the equation,

$$Q(x) = \dot{M}_v(x) L \quad (1)$$

For steady state operation, the rate of vapor evolution equals the rate of vapor condensation. If the unheated end of the pipe is undergoing radiation, the entire pipe will be brought to a nearly isothermal temperature. The pipe's temperature at the heat source is considerably lower than that temperature which would have occurred there in the absence of the wicking fluid. The degree of temperature reduction is strongly dependent on the heat rejection capacity (emmissivity) of the unheated end.

Heat pipes are ideally suited for space applications since the capillary forces circulating the wicking fluid are only opposed by the frictional forces arising from viscosity. In an environment where G forces are present, the wicking fluids density must be sufficiently low to enable the capillary forces under the specified heating conditions to fully saturate the wick. For steady state operation, a heat pipe must satisfy the internal pressure drop criterion,

$$\left[ \begin{array}{l} \text{capillary} \\ \text{pressure} \end{array} \right] \geq \left[ \begin{array}{l} \text{viscous liquid} \\ \text{pressure drop} \end{array} \right] + \left[ \begin{array}{l} \text{viscous + inertial} \\ \text{pressure drop in} \\ \text{vapor} \end{array} \right] + \left[ \begin{array}{l} \text{G Loads} \\ \text{Pressure} \\ \text{drop} \end{array} \right] \quad (2)$$

Vol. 2

This criterion allows the capillary pressure forces to continue the fluid circulation throughout the volume of the wick under the imposed heating conditions. Relative magnitudes of the influence of G and capillary pore radius on pressure head for several candidate fluids are shown in Fig. 4 (courtesy of Westinghouse, Ref. 3). The derivation of the capillary pore data in reference 3 is based on a mean cylindrical pore radius. These data are representative of the magnitudes of capillary pressure heads developed by more realistic wicks of the same mean pore radius. Capillary pressure heads for the alkali metals at mean pore radii below .01 inches, are shown in Fig. 4 to be large compared to corresponding gravitational pressure heads. Hence, the use of heat pipe cooling on a small leading edge structure under near steady state hypersonic heating conditions may be very practical. Prior to the construction of a working model, a more detailed experimental assessment must be made into the magnitudes of the terms in Equation (2), and the special transient conditions which are characteristically different for liquid metal heat pipes (Refs. 4 and 5).

The general requirements for heat pipe fluids are: high latent heat, high thermal conductivity, low viscosity, high surface tension, high wetting ability and a suitably high boiling point. Properties of some high temperature heat pipe fluids are given in Table I.

(U) TABLE 1 - PROPERTIES OF HIGH TEMPERATURE HEAT PIPE FLUIDS

FLUID	MELTING PT. (°F)	BOILING PT. (°F)	DENSITY #/FT <sup>3</sup> @ MP	SURFACE TENSION @ MP × 10 <sup>+4</sup>	LATENT HEAT BTU/#
LITHIUM	354	2403	31.8	39.9	8440
POTASSIUM	147	1400	51.0	10.6	893
SODIUM	208	1621	58.0	19.1	1810
CESIUM	84	1301	112.0	5.5	263

For the present we will assume that an effective heat pipe can be constructed in the form of a sharp 10° two-dimensional leading edge.

We would like to determine the temperature field through the volume of this structure for Mach numbers of 6 and 8 at an altitude of 150,000 feet.

#### HEAT PIPE MODEL

A two-dimensional heat pipe (or vapor chamber) used for leading edge temperature reductions would have the same features as the cylindrical heat pipe (of Fig. 3) except for a triangular cross-sectional shape, see Fig. 5. This leading edge structure would have a wick material (probably sintered metal or metal screening) snugly lining its interior surface. Relatively sharp leading edges could be used since the heat pipe conduction mechanism is expected within the fluid wicking limits to be capable of absorbing the high heating loads on small radius leading edges. The temperature in the wick region would be sensibly isothermal due to the presence of the evaporating and condensing vapor. In a fashion similar to the cylindrical heat pipe, the high heating loads near the vertex of the leading edge would be conducted in the vapor (as latent heat) and recondensed nearly at constant temperature on the downstream wick surfaces. For the purpose of predicting surface temperatures on the outer skin, the wick-vapor region could then be considered as an artificial material of very high conductivity placed flush against the interior of the skin.

The heat pipe model considered for steady state skin temperature determination under simulated hypersonic flight conditions consists of a  $10^\circ$  half angle wedge (Fig. 5 concluded). A triangular grid field was used for the finite difference treatment since it exactly fits the wedge's geometry. The wedge is divided into five nodal rows. The first two rows lie in a given real material (molybdenum) having a conductivity of  $.0194 \frac{\text{BTU}}{\text{Ft sec}^\circ \text{R}}$ ; the last three nodal rows lie in a fictitious wick-vapor region which is assumed to have a conductivity of  $209 \frac{\text{BTU}}{\text{Ft sec}^\circ \text{R}}$ . This latter value is quoted in reference 2 and is representative of the magnitude of sodium heat pipe conductivities in the range of  $1900^\circ \text{R}$ .

#### ANALYTICAL PROCEDURE

The convective heat transfer coefficient distributions at 150,000 feet for simulated Mach numbers of 6 and 8 on a  $10^\circ$  leading edge are shown in Fig. 6. These laminar coefficients were determined with the reference temperature heat transfer equation,

$$H(x) = 9.22 \frac{K}{\sqrt{X}} \left( \frac{\rho^* V_\infty}{U^*} \right)^{\frac{1}{2}} P_r^* x 10^{-5} \quad (3)$$

where  $K^*$ ,  $\rho^*$ ,  $\mu^*$  and  $P_r^*$  are evaluated at the reference temperature given as,

$$T^* = .28 T_\infty + .50 T_w + .22 T_r \quad (4)$$

The specific equations for  $K$ ,  $\rho$ ,  $\mu$  and  $P_r$  are well known and can be found in most heat transfer texts.

Equation (3) and the supporting property value equations were programmed at the specified flight conditions.

Fourier nodal heat transfer equations incorporating Dusinberre's half-cotangent rule for triangular grids (Ref. 6) are written for the special interior nodal forms. The Fourier equation for a rectangular nodal form is,

$$Q = C a \frac{\Delta T}{\Delta l} \quad (5)$$

where (a) is the differential nodal heat transfer area between nodes,

$$a = \Delta A \quad (\text{unit depth normal to nodal cross-section}) \quad (6)$$

For a triangular grid, Equation (5) becomes

$$Q = C \Delta T \frac{\Delta A}{\Delta l} \quad (7)$$

where  $\frac{\Delta A}{\Delta l}$  is Dusinberre's conduction path coefficient. This coefficient can be shown for any grid path to be equal to the sum of the half cotangents of the angles bridging that path.

The nodal equations for interior nodes (which are influenced only by the temperature of adjacent nodes,  $T_n$ ) are of the form,

$$\sum C (T_n - T) \frac{\Delta A}{\Delta l} = 0 \quad (8)$$

A typical interior nodal equation for the interfacial boundary (of the form of Equation (8) written in terms of nodal indices (i,j), is,

$$\begin{aligned} & (T_{i-1,j+1} - T_{i,j}) CC(C_1) + (T_{i+1,j-1} - T_{i,j}) CC(C_2) + (T_{i,j-1} + T_{i,j+1} - 2T_{i,j}) \\ & BB \frac{C_1 + C_2}{2} + (T_{i-1,j} - T_{i,j}) C_1 + (T_{i+1,j} - T_{i,j}) C_2 (BB) = 0 \end{aligned} \quad (9)$$

where the values CC and BB are Dusinberre's conduction path coefficients. Along the interfacial boundary the respective conductivities  $C_1$  and  $C_2$  of the skin and fictitious material are averaged. This assumption seems plausible. A further description of the heat balance at an interfacial point, 3,7, is shown in Fig. 7.

A similar typical interior nodal equation for the adiabatic boundary is given as,

$$(T_{i,j-1} + T_{i,j+1} - 2T_{i,j}) AA + (T_{i-1,j+1} + T_{i,j}) CC + (T_{i-1,j} - T_{i,j}) BB = 0 \quad (10)$$

where AA is a Dusinberre constant, (see Fig. 7 continued).

For the surface nodes which are influenced by convection and radiation, the general form of the heat balance equation is,

$$H(T_{i,j}) \Delta A (T_{aw} - T_{i,j}) - \epsilon (T_{i,j}^4 - T_{\infty}^4) \Delta A + \text{sum of Fourier conduction terms} = 0 \quad (11)$$

where the first two terms (from the left) are attributed respectively to surface convection and radiation (Fig. 7 concluded). The last term consists of the Fourier conduction influence of adjacent nodes explained above. The nodal equations applied to the surface nodes assume a constant surface emissivity of .5; they also take into account first-order changes in convective heat transfer coefficients with wall temperature variations. Hence, the  $H(T)$  value shown in these equations is equal to,

$$H(x) + (T_w - B) \text{ Slope} \quad (12)$$

where it is understood that  $H(x)$  is the heat transfer distribution evaluated at a wall temperature, B (3000°R). Since the heat transfer coefficient is not a strong function of wall temperature, the slope term represents a mean sensitivity of heat transfer coefficient with wall temperature over the length of the plate. The nodal equations were solved for temperature distribution on a SDS 930 machine using a Gauss-Siedel numerical solution. A Newton-Raphson method is applied to the surface nodal equations in order to speed the convergence. A total of 17 nodal equations were necessary to define all the cases in the 341 node field. Convergence was assumed when the integrated radiation and convection over the surface of the wedge were equal to within  $.01 \frac{\text{BTU}}{\text{sec}}$ . Although the results are very reasonable, additional programming is being conducted to determine node size

influence and initial h influence on the near stagnation temperature field.

## RESULTS

The preliminary numerical results for the cooled and uncooled leading edge at the simulated flight conditions are shown in Figs. 8 and 9. The influence of the highly conductive vapor region is very apparent for both Mach number cases. As a result of radiation influences the overall temperature gradient at Mach 8 exceeded that obtained at Mach 6. Hence, the larger heat pipe influence on temperature shown at Mach 8, is attributed to its greater effectiveness at the higher Mach numbers where radiation is more significant. The integrated heat flux ( $\frac{\text{BTU}}{\text{sec}}$ ) for the cooled and uncooled cases were shown to be identical in each Mach number case. This is significant since stagnation region temperatures are reduced (at the expense of slightly higher temperatures downstream) without having to accept any additional heat input over the entire leading edge structure.

The leading edge tip temperature gradient retained by the cooled wedge is attributed to the high Q loads imposed over the long horizontal conduction paths extending from the wedge's vertex to the high conductivity region. Details of the temperature distributions for the heat pipe model near the stagnation points for both Mach numbers are shown in Figs. 10 and 11. The influence of the vertex material distribution on temperature distribution can be eliminated through shortening the vertex conduction paths and providing more heat pipe area in the vertex region. Hence, the use of a small (.2' to .25" radius) cylindrically conformed leading edge having constant metal thickness in the vertex region would be appropriate. This arrangement is also shown in Figs. 10 and 11. If we assume that a leading edge structure containing a perfectly conformed skin-wick vertex region could be fabricated then isothermal temperature distributions across the structures surface would be possible, see Figs. 8 and 9. The temperature increase over the entire surface attributed to further temperature reductions at the conformed tip would be on the order of 60°F. for the cases shown. This is a welcome trade off at the higher Mach numbers for the rather large reduction obtained in edge temperature.

## CONCLUDING REMARKS

The numerical results demonstrate the ability of cooling methods based on the heat pipe principle to significantly reduce stagnation

tip temperatures. The results are preliminary since node size influence on accuracy (especially in the vertex region) has not been determined. Nevertheless, the initial results are encouraging and strongly indicate that through proper leading edge design (a minimum of conformed nose blunting) isothermal leading edge temperature distributions are achievable in the hypersonic flight domain.

The application of heat pipe cooling to minimize the current practice of extreme nose blunting to reduce stagnation point Q loads  $\left(\frac{\text{BTU}}{\text{sec ft}^2}\right)$  could pay additional dividends in appreciable form drag reductions. In such instances where drag reductions can be achieved, the conformed leading edge radius must be less than the original blunt body radius.

Finally, a minimum drag design would be subjected to the inherent physical limitations imposed on the fluid-wick system by stagnation point Q loads. This means that sufficient fluid must circulate in the stagnation point region to continually absorb the stagnation Q loads under the specified flight conditions. Low density fluids with high latent heat, surface tension, and boiling temperature are those of interest. In this category the alkali metals are the most promising.

#### REFERENCES

1. NASA Langley Research Center. Structural Prospects for Hypersonic Air Vehicles (U), by R. R. Heldenfels. Hampton, Va., Sept. 1966. p. 561 (Aerospace Proceedings), publication UNCLASSIFIED.
2. Los Alamos Scientific Laboratory. Structures of Very High Thermal Conductance (U), by G. M. Grover and T. P. Cotter. Los Alamos, New Mexico, 1964. p. 1990, Vol. 35. (Journal of Applied Physics, publication UNCLASSIFIED).
3. Westinghouse Electric Corp. Heat Pipe Analysis (U), by G. H. Parker. Miami, Fla., August 1968. p. 847 (ASME Intersociety Energy Conversion Engineering Conference) publication UNCLASSIFIED.
4. Los Alamos Scientific Laboratory. Theory of Heat Pipes (U), by T. P. Cotter. Los Alamos, New Mexico, 1965. LA-3246-MS (publication UNCLASSIFIED).
5. Los Alamos Scientific Laboratory. Heat Pipe Startup Dynamics (U), by T. P. Cotter. Palo Alto, Calif., Nov 1967. p. 344 (IEEE Thermionic Conversion Specialist Conference) publication UNCLASSIFIED.

**8th Navy Symposium on Aeroballistics**

---

**Vol. 2**

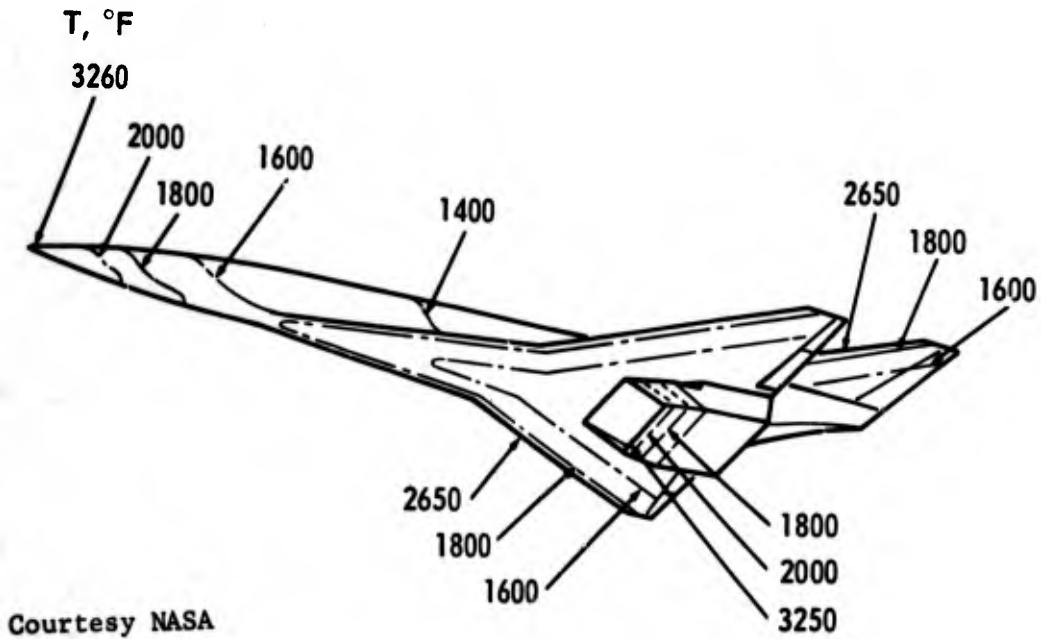
6. International Textbook Company. Heat Transfer Calculations by Finite Differences (U), by George Dusinberre. Scranton, Pa., 1961 (publication UNCLASSIFIED).

## SYMBOLS

$\Delta A$	node spacing on surface
B	calibration temperature for H
$C_1$	conductivity in skin material
$C_2$	conductivity in heat pipe region
$C_p$	specific heat of air
H	convective heat transfer coefficient
K	conductivity of air
L	latent heat of heat pipe fluid
M	Mach number
$\dot{M}_v$	Rate of vapor evolution
$\Delta P$	pressure drop in wick
Pr	Prandtl number
Q	heat transferred in heat pipe
$r_c$	mean pore radius of wick
$R_x$	Reynolds number
Slope	temperature sensitivity of heat transfer coefficient
T	temperature
V	air velocity
x	distance along surface of leading edge
$\epsilon$	emmissivity
$\phi$	angle of inclination
$\sigma$	Stefan Boltzman constant
$\theta$	wetting angle
$\mu$	viscosity of air

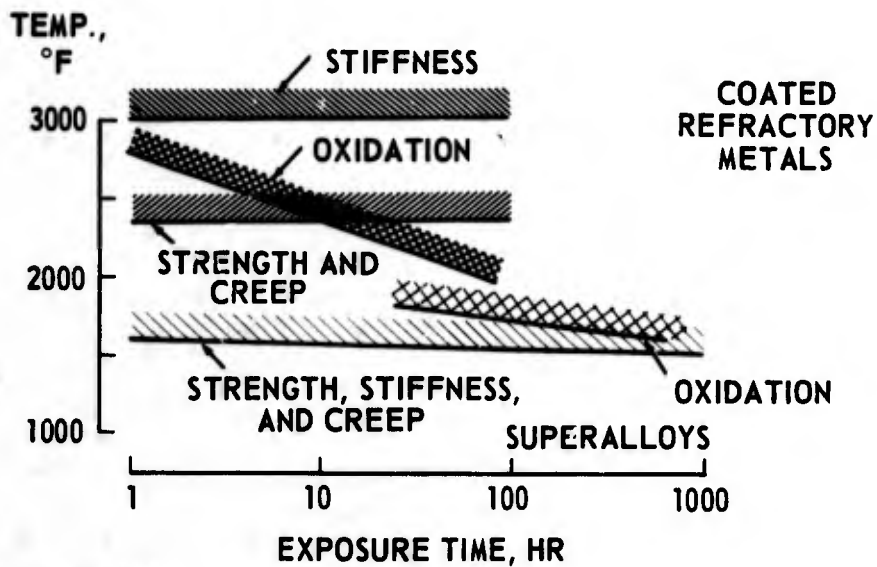
## Subscripts

w	evaluated at wall conditions
$\infty$	evaluated at infinity
*	evaluated at reference temperature conditions



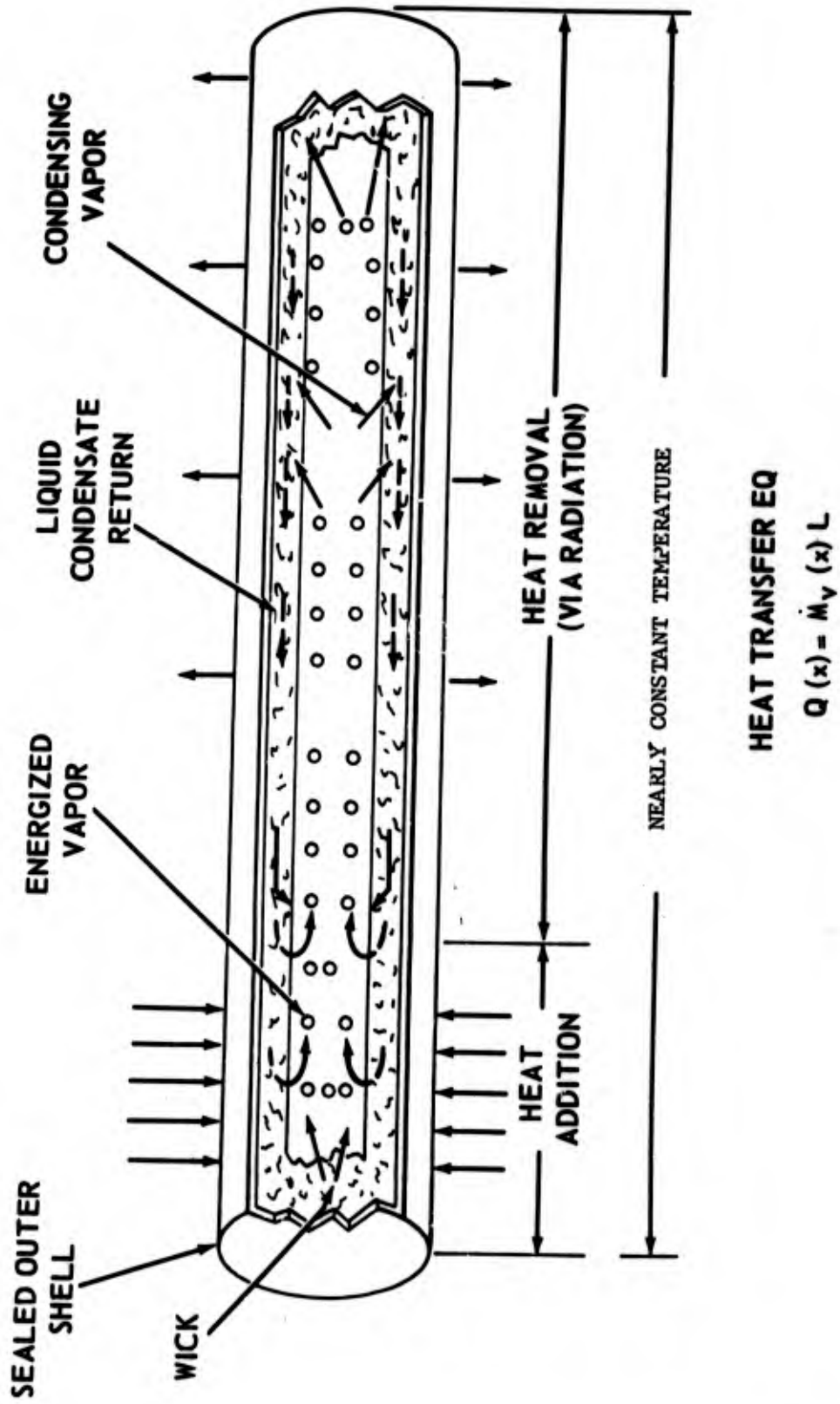
Courtesy NASA

(U) Fig. 1. - Equilibrium Surface Temperatures During Sustained Flight at Mach 8.0 at 88,000 Feet

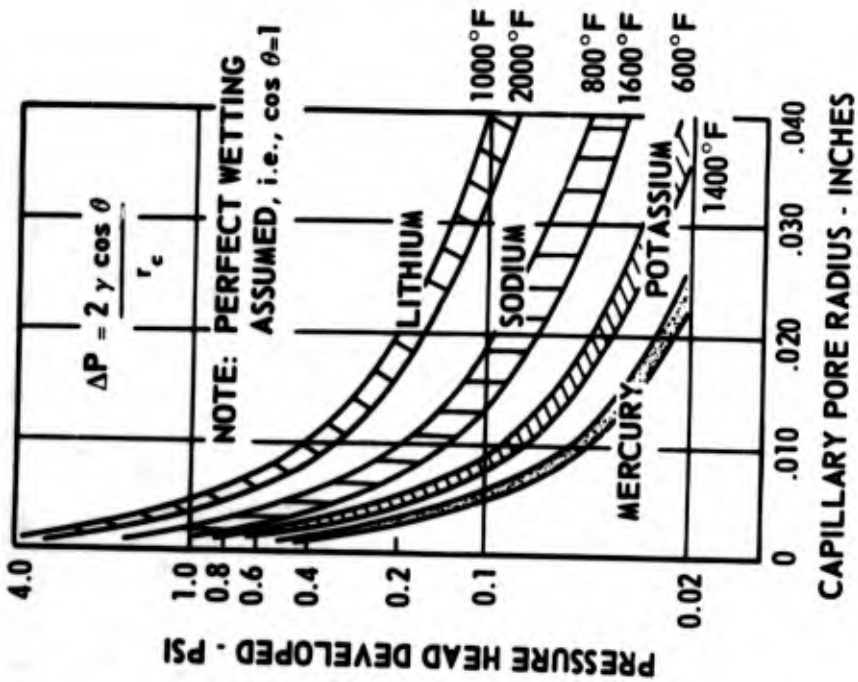
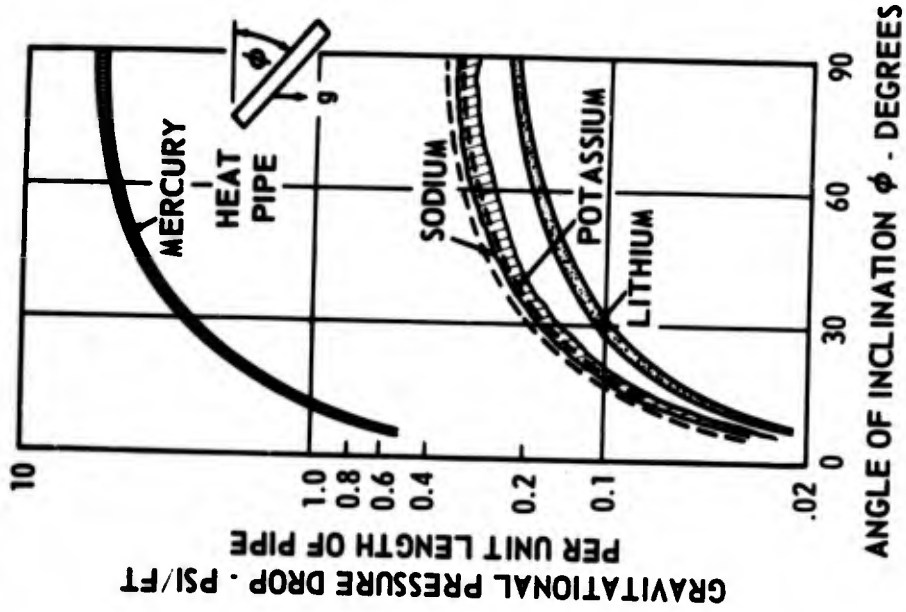


Courtesy NASA

(U) Fig. 2.- High-Temperature Structural Material Limitations

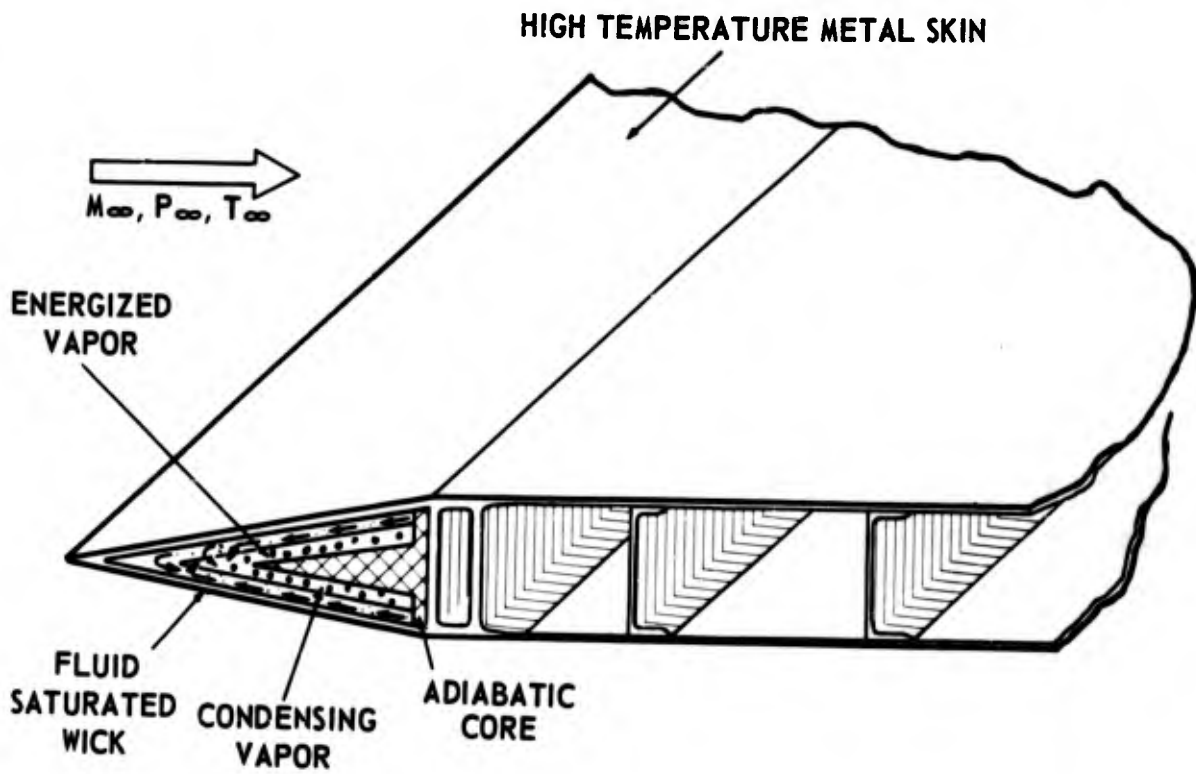


(U) Fig. 3. - Basic Heat Pipe Radiation Configuration

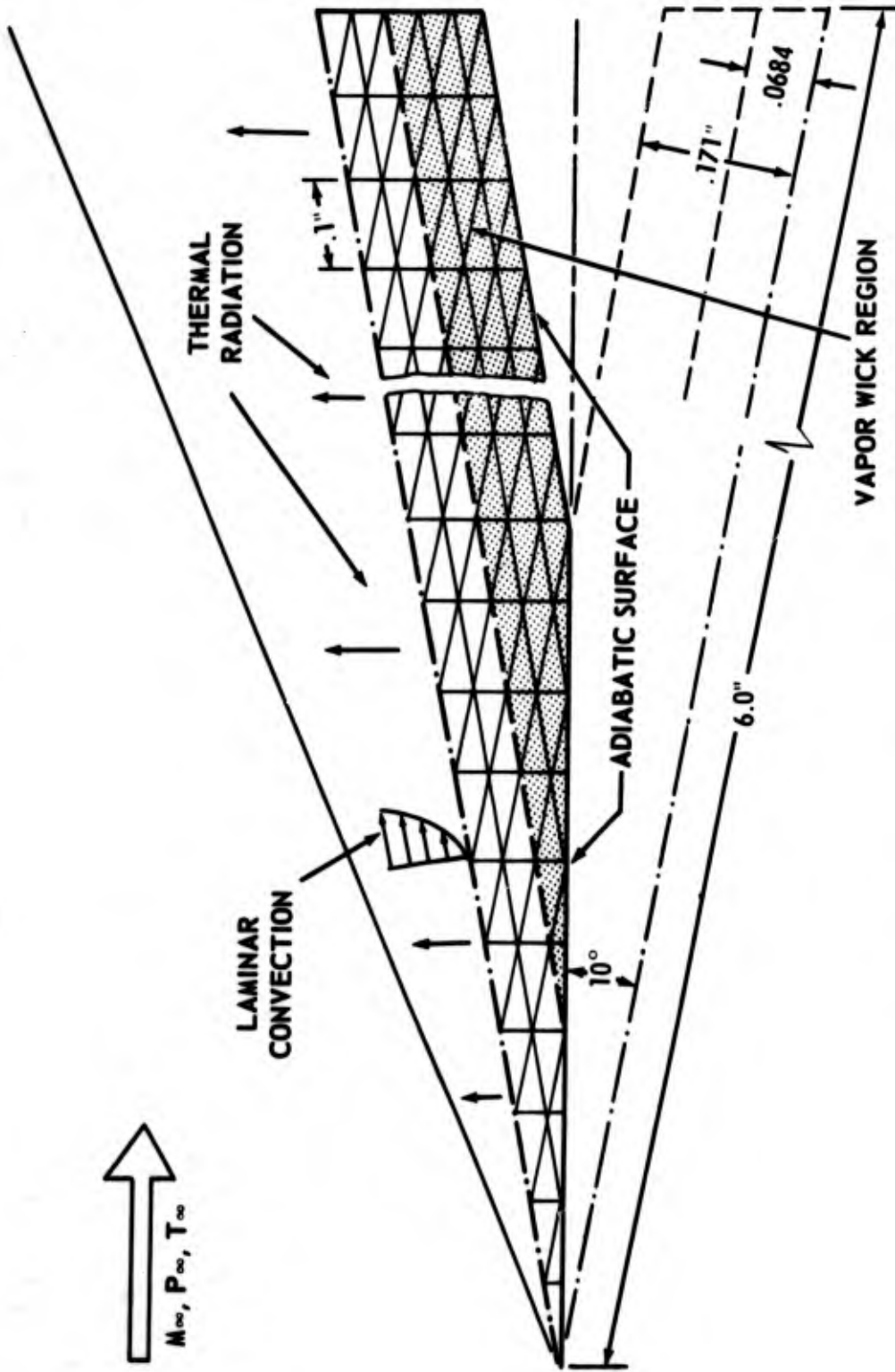


Courtesy Westinghouse

(U) Fig. 4. - Influence of Capillary Pore Radius and Inclination Angle on Liquid Pressure Drop for a Cylindrical Heat Pipe

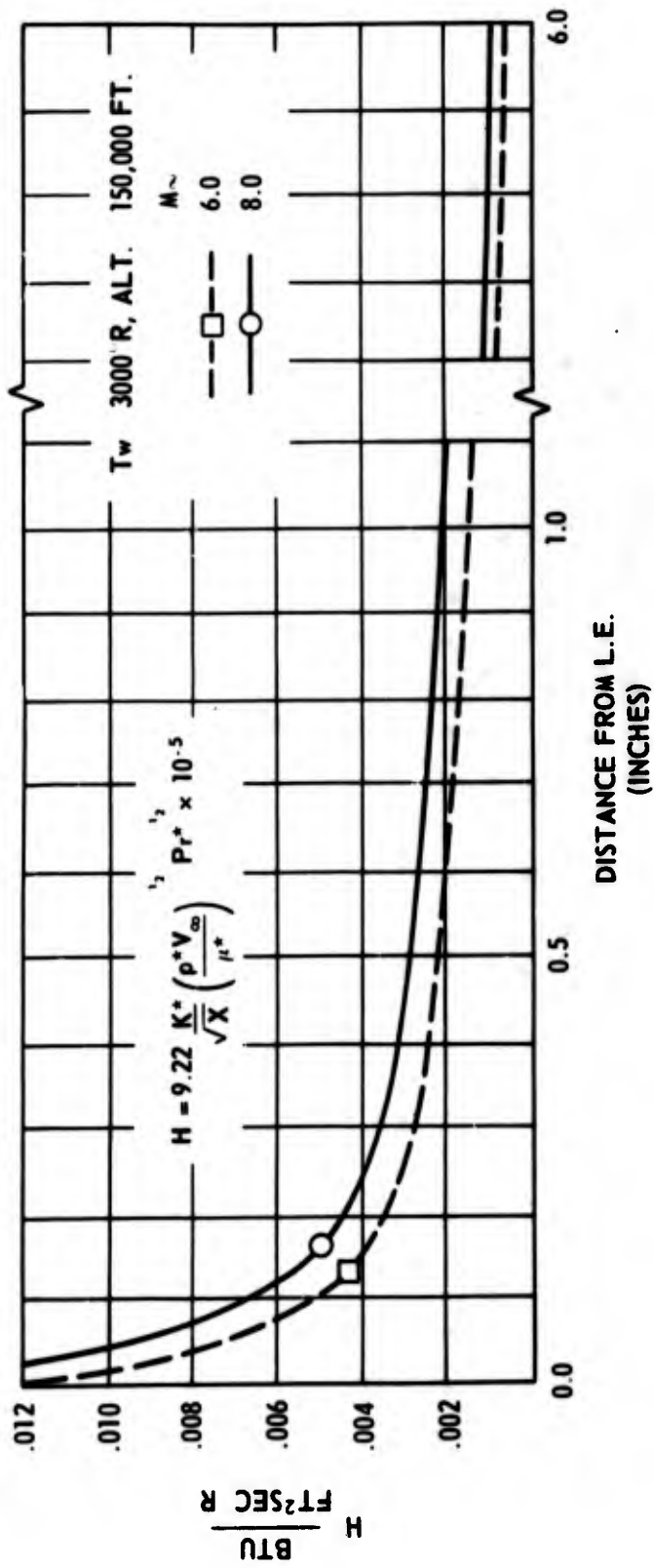


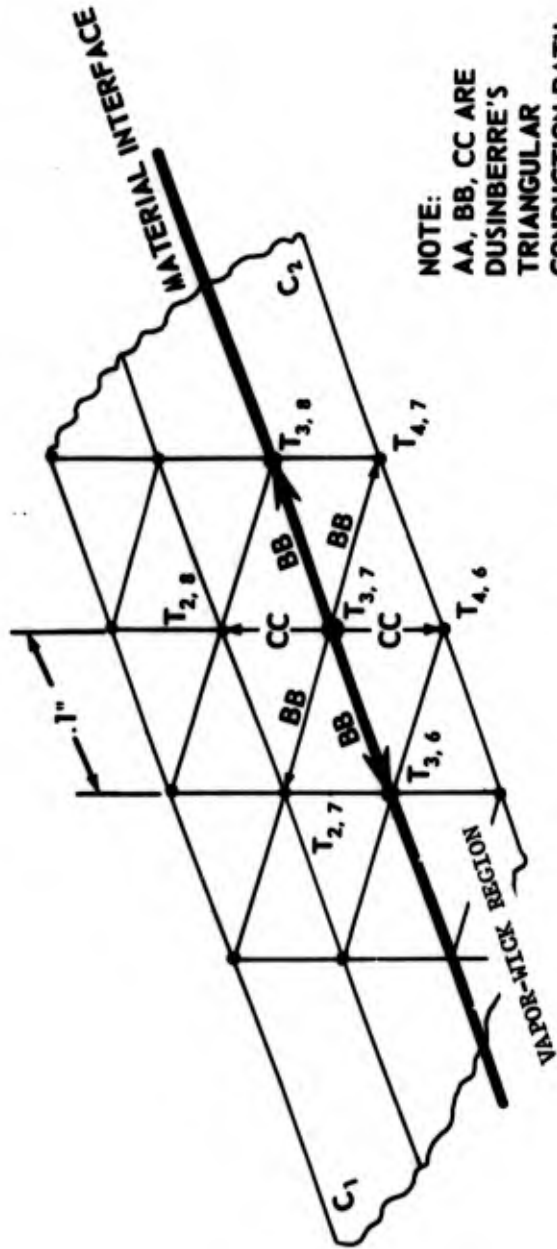
(U) Fig. 5.- Heat Pipe Leading Edge Structure



(U) Fig. 5 (Concluded)

(a) Heat Pipe Leading Edge Model

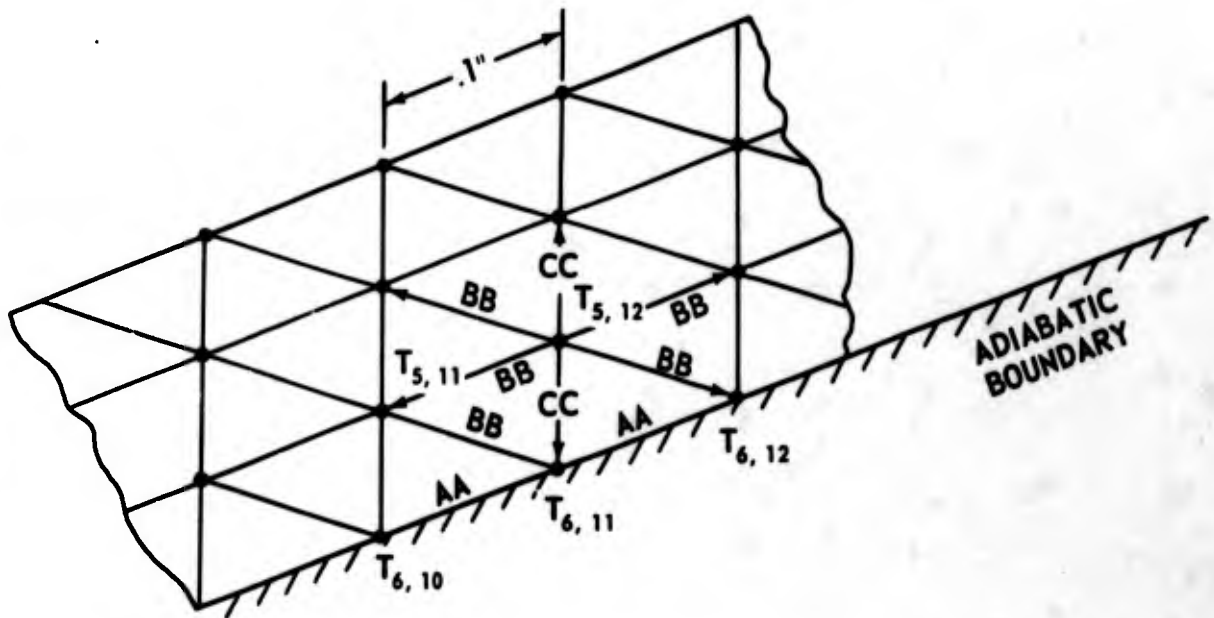




NOTE:  
AA, BB, CC ARE  
DUSINBERRE'S  
TRIANGULAR  
CONDUCTION PATH  
COEFFICIENTS

NET CONDUCTIVITY OUT OF POINT 3, 7 = 0

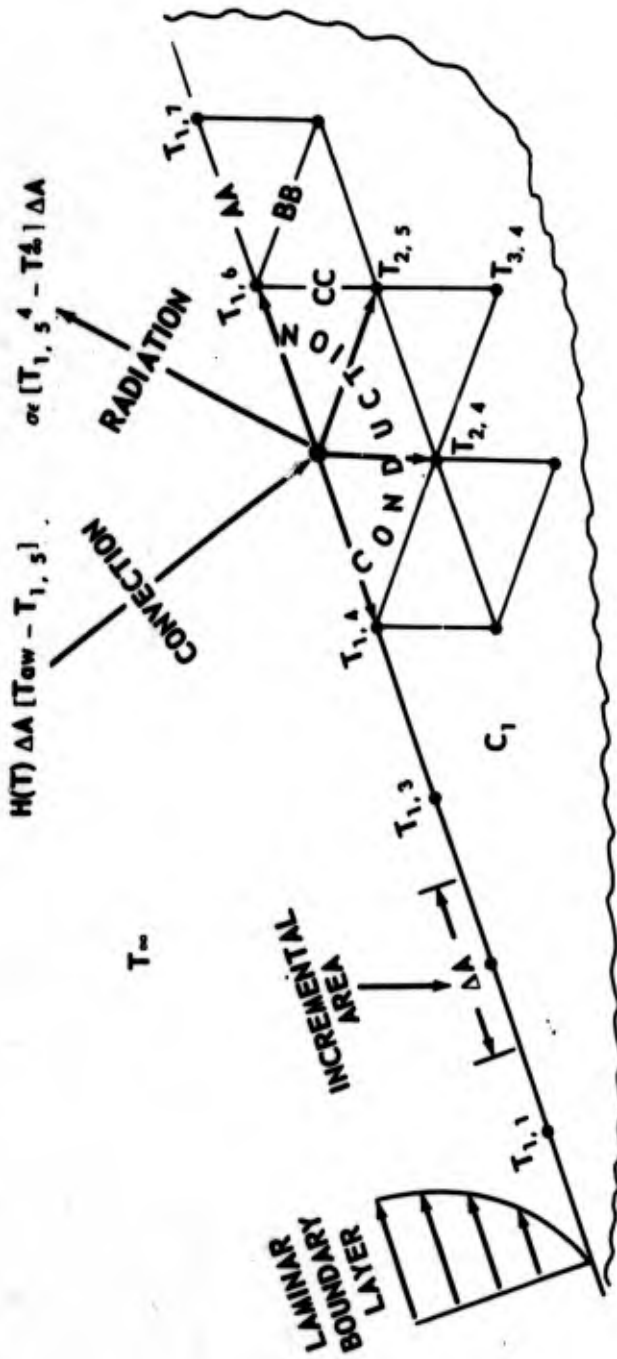
$$(\pi_{2,8} - T_{3,7}) CC(C_1) + (\pi_{4,6} - T_{3,7}) CC(C_2) + (\pi_{3,6} - T_{3,7} + T_{3,8} - T_{3,7}) BB \left( \frac{C_1 + C_2}{2} \right) + (\pi_{2,7} - T_{3,7}) (C_1) BB + (\pi_{4,7} - T_{3,7}) (C_2) (BB) = 0$$



NET CONDUCTIVITY OUT OF POINT 6, 11 = 0

$$(T_{6,10} - T_{6,11} + T_{6,12} - T_{6,11})AA + (T_{5,12} - T_{6,11})CC + (T_{5,11} - T_{6,11})BB = 0$$

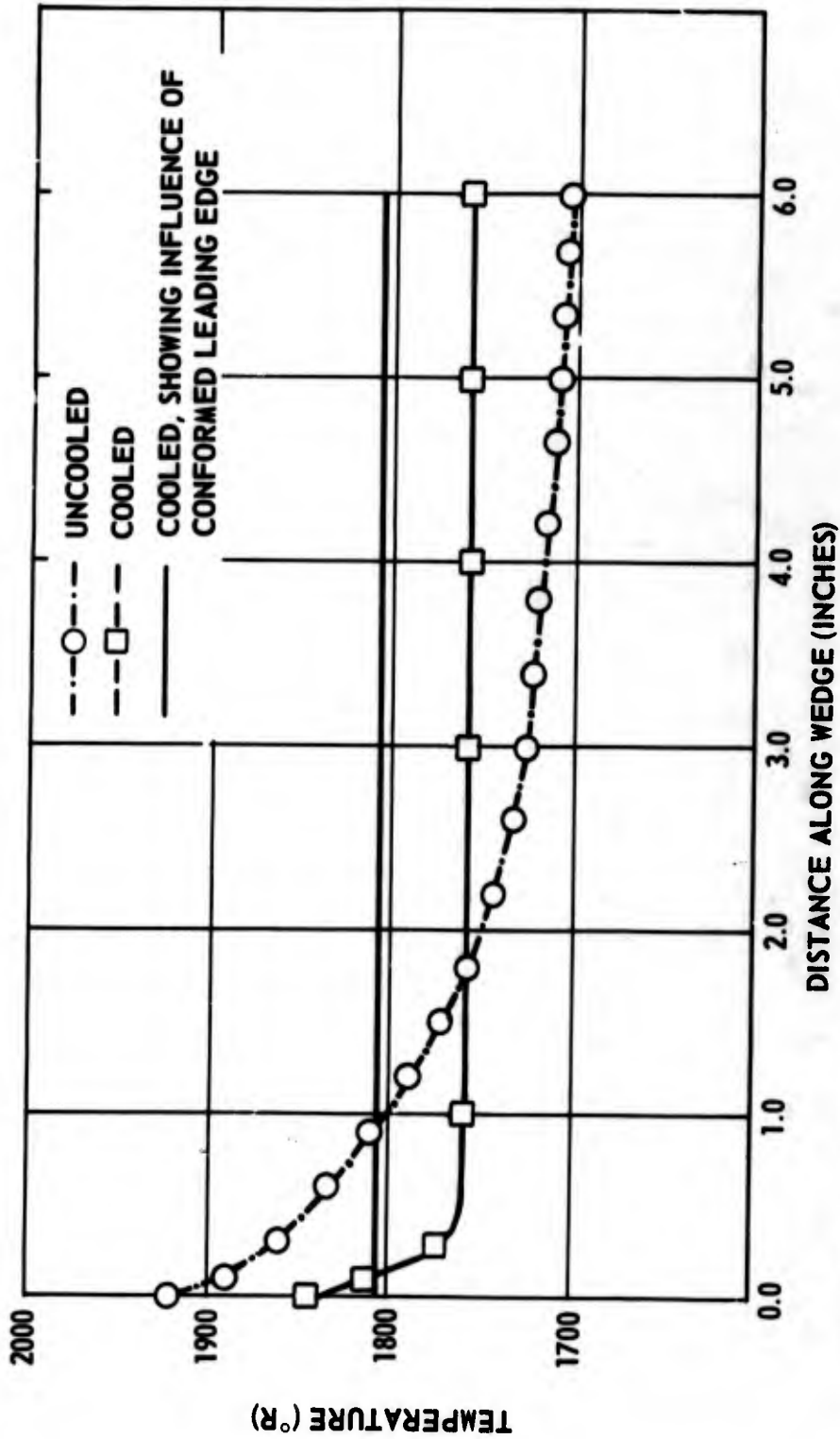
(U) Fig. 7 (Continued)  
 (a) Adiabatic Boundary Node



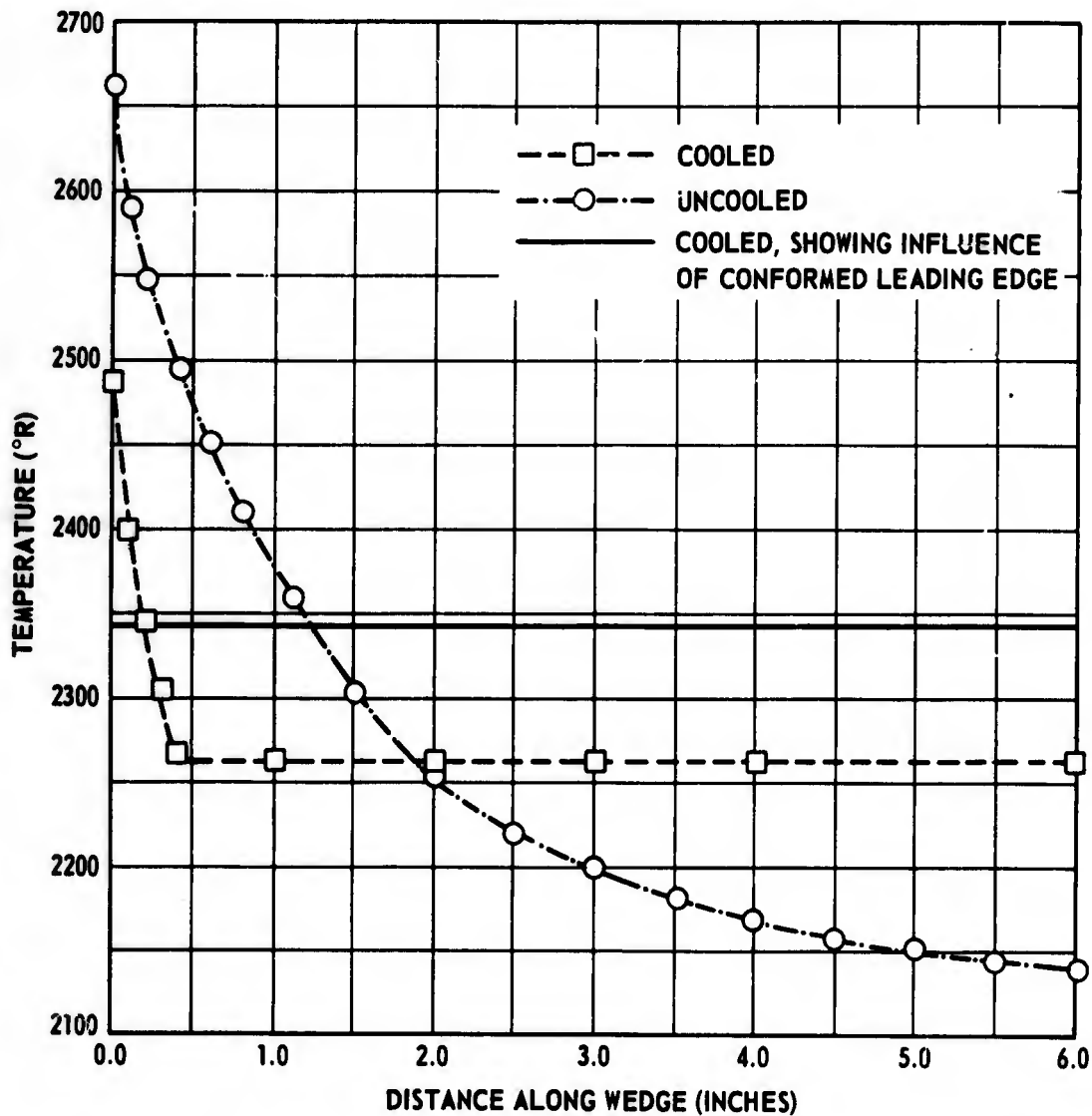
$$\underbrace{\text{CONVECTION IN}} + \underbrace{\text{RADIATION OUT}} + \underbrace{\text{CONDUCTION OUT}}$$

$$H(T) \Delta A [T_{\infty} - T_{1,1}] - \sigma \Delta A [T_{1,1}^4 - T_{\infty}^4] + \{ (T_{1,4} - T_{1,3}) AA + (T_{2,4} - T_{1,3}) CC + (T_{2,5} - T_{1,3}) BB + (T_{1,6} - T_{1,3}) AA \} (C_1)$$

(U) Fig. 7 (Concluded)  
(b) Surface Node



(U) Fig. 8.- Surface Temperature Distributions Along a 10° Wedge Showing the Effects of Heat Pipe Cooling ( $M_\infty = 6.0$ , Altitude = 150,000 ft.)



(U) Fig. 9.- Surface Temperature Distributions Along a 10° Wedge Showing the Effects of Heat Pipe Cooling ( $M_{\infty} = 8.0$ , Altitude = 150,000 ft.)





Paper No. 18

**SPIKES AS A MEANS OF REDUCING DRAG AND RAIN EROSION  
OF BLUNT BODIES AT SUPERSONIC SPEEDS**

(U)

(Paper UNCLASSIFIED)

by

Isidor C. Patapis  
Naval Ship Research and Development Center  
Washington, D.C. 20007

ABSTRACT. (U) The use of spikes as a means of reducing drag and rain erosion at supersonic speeds is appraised. A description of results of recent spike studies conducted at the Naval Ship Research and Development Center is included. These results show that spikes can significantly reduce both drag and rain erosion. The scope of future work, to include heat transfer, is also discussed.

## INTRODUCTION

(U) The radome of an aircraft or missile is most effective in a blunt body configuration. This assures the greatest uniformity in skin thickness allowing for the uniform transmission and reception of signals. A hemisphere is ideal. Other nose shapes, such as a one-one tangent ogive, can also be used.

(U) Both of these radomes present certain aerodynamic problems which tend to compromise the weapons system. That is their pressure drag and impact momentum exchange with oncoming rain particles is high because of the high body tangent angles relative to the body axis.

### THE EFFECTS A SPIKE HAS ON A BLUNT BODY

(U) Placing a spike in front of these bodies reduces both the drag and the raindrop momentum exchange. Just how this is done can be seen in the schlieren photographs showing the basic radome and two alternate flow conditions posed by using spikes: Figure 1 shows a basic radome with a detached bow shock wave indicating high pressure drag. What a spike does, essentially, is to remove the detached portion of the wave thereby diminishing its effects. A spike placed on a body that has a bow shock wave attached will not reduce drag. Figure 2 shows flow separating from the spike shank and leaving a small captured vortex bounded by a shear layer. The oncoming flow "sees" the body as formed by the spike in front of the separating flow, the shear layer and the actual body from the reattaching region rearwards. This, more slender body, shows a small reduction in drag over the actual one. Figure 3 shows flow separating from the cone, transitioning and reattaching to the body and forming a captured vortex between the shear layer and the complete spike shank. To the oncoming flow, this body is much more slender than the first two, and indeed, this is reflected in its low drag.

(U) A spike helps cause rain dispersion in a number of ways: The first is the tip shock wave. It causes compression waves to form in a rain drop passing through it. If given enough time after passing through the tip wave, the droplet may thus be dispersed to a fine vapor. The "vaporizing" process begins at about 100  $\mu$  seconds and is complete at about 700  $\mu$  seconds or so depending on the Mach number. If a droplet passes through a series of waves, it might possibly

"vaporize" very quickly. Second, the rain drop is deflected along with the oncoming flow by the conical tip and the shear layer so that when a drop finally reaches the body its impact angle is minimized. Third, if a rain drop should happen to penetrate the shear layer, it will be subjected to very high shear stresses because its size may be comparable to the shear layer thickness which is supersonic on the outside and subsonic on the inside.

#### TESTS CONDUCTED AND RESULTS

(U) In tests conducted at NSRDC the two different types of spikes shown, in Figure 4, were tested on a one-one tangent ogive and a hemisphere. The plain tip spikes were relatively ineffective giving drag coefficients not much different from the basic bodies. The blank oversize spikes caused about 35% drag reduction on the ogive and about 50% on the hemisphere. At the conclusion of these tests it was felt that more work could be done in the area of drag reduction by bleeding air from the tips into the shear layer as shown in Figure 5. The additional mass would increase the layers displacement thickness causing the bow shockwave - shear layer interaction to occur radially further from the body, thereby causing an additional reduction in pressure drag. The schlieren photographs of these tests were not clear enough to indicate a noticeable shift in the location of the interaction region, Figure 6. However, the jet does cause a shockwave to form at the exit lip which is normal to the cone in the vicinity of the lip and jet itself appears to form a layer just outside of the existing shear layer. The second shock can help amplify rain dispersion. The force data indicates two things: First, drag is reduced over the basic spikes and second, some spikes that originally had flow separation from the shank now had the flow separating from the tip. Because of this, the rain dispersion process starts further from the radome allowing for more reaction time. Apparently, this particular method of bleeding air removes an existing pressure gradient that, on some spike-body combinations, was pronounced enough to retard separation. This point may be noted in Figure 7 where, for example, an  $l/d$  of about 0.9 had shank separation and a  $C_D$  of about 0.48; with air bleed the flow separated from the tip and the drag was reduced by one unit to about 0.38. It should be pointed out that gap width,  $g_e$ , was based on a design Mach number of 2.14 and tested only at 1.55 and 3.75. The gaps show little drag reduction over the basic spikes at Mach number less than  $M$  design and greater at the greater Mach number. The effect of bleeding on the ogive is not consistent over the test Mach numbers as it is with the hemisphere, Figure 8. The hemisphere has yet to be tested with blank spikes having shank separation so that the effect of air bleeding on them is not known. From the standpoint of drag reduction, however, it would appear that the width must be designed for a low supersonic flight Mach number to be usable over the

Vol. 2

supersonic flight range. The opposite is true when determining slit width for rain erosion protection where a strong jet will help to form a strong shock at the tip and help deflect the droplets further from the cone. Calculations have shown a shift of about  $80^\circ$  in droplet direction in the vicinity of the jet. The jet strength can be said to be governed by the mass flow rate through the slit. Continuity dictates a bigger slit with Mach number increase.

(U) This contradiction between a small slit for drag reduction and a large one for rain erosion would lead one to using an intermediate flight Mach number for design. A series of spikes have been prepared to be tested at  $M = 5$ , their design Mach number, along with the existing set for temperature distribution studies. They will also be tested for force data and subsequently made into full scale products for testing on radomes on a rocket sled track in a rain environment facility.

CLOSING

(U) The work that has been done till now has provided a stimulus for the future which will center around more experiments, some of which have already been noted. Questions that have yet to be answered are:

1. What is the optimum cone angle per Mach number?
2. Can a variable geometry cone be used during a variable Mach number flight?
3. How do temperature distributions vary with blank and jet-bleed spikes?
4. How effective is the jet-bleed idea in a rain environment on full-scale radomes?

(U) After these experiments have been completed and the results digested, attempts will be made to try to formulate a mathematical model and a computer program to try to anticipate more concisely the problem of the spike-body. In the meantime, your comments and criticism are welcomed with great enthusiasm.

## REFERENCES

1. Flow Separation Ahead of a Blunt Axially Symmetric Body at Mach Numbers 1.76 to 2.10, by W. E. Moeckel. Wash., 1951. 12 p. incl. illus. (NACA RM E1I25)
2. The Effect of a Spike Protruding in Front of a Bluff Body at Supersonic Speeds, by D. Beastall and J. Turner. London, H.M.S.O., 1957. 26 p. incl. illus. (Gt. Brit. Aeronautical Research Council R&M 30007. 14,892. Gt. Brit. Royal Aircraft Est., TN 2137)
3. Study of the Pressure Rise Across Shock Waves Required to Separate Laminar and Turbulent Boundary Layers, by C. duP. Donaldson and R. H. Lange. Wash., May 1952. 20 p. incl. illus. (NACA RM L52C21)
4. Flow Separation from Rods Ahead of Blunt Noses at Mach Number 2.72, by J. J. Jones. Wash., Jul 1952. 18 p. incl. illus. (NACA RM L52E05a)
5. Exploratory Investigation of Flow in the Separated Region Ahead of Two Blunt Bodies at Mach Number 2, by H. Bernstein and W. E. Brunk. Wash., Jun 1955. 27 p. incl. illus. (NACA RM E55D07b)
6. Supersonic Wind-Tunnel Study of Reducing the Drag of a Bluff Body at Incidence by Means of a Spike, by G. K. Hunt. Farnborough, May 1958. 20 p. incl. illus. (Gt. Brit. Royal Aircraft Est. Rpt. Aero 2606)
7. Drag Reduction Studies of Tangent Ogive Radomes With Spikes at Mach Numbers 1.55, 1.90, and 2.18 (U), by I. Patapis, Wash., Mar 1967. 51 p. incl. illus. (David Taylor Model Basin, Test Rpt. AL C-37, publication CONFIDENTIAL)
8. Fragmentation of Waterdrops in the Zone Behind an Air Shock, by O. G. Engle. Wash., Mar 1960. 35 p. incl. illus. (Journal of the National Bureau of Standards, v. 60 p. 245-280)
9. The Time Required for High Speed Airstreams to Disintegrate Water Drops, by D. C. Jenkins and J. D. Brooker. London, May 1964. 51 p. incl. illus. (Gt. Brit. Royal Aircraft Est. Tech. Note Mech. Engr. 401)
10. Rain Erosion on Spike-Protected Supersonic Radomes, by J. E. Nicholson and J. A. F. Hill. Cambridge, Mass., Apr 1965. 83 p. incl. illus. (Mithras, Inc. Interim Engr. Rpt. MC-61-6R3)
11. Aerodynamic Spike for Drag Reduction and Rain Drop Disintegration at Low Supersonic Velocities, by G. J. Tatnall. Farnborough, Aug 1967. 11 p. incl. illus. (Royal Aircraft Est. Proceedings on Rain Erosion and Associated Phenomena. p. 221-232)

**8th Navy Symposium on Aeroballistics**

---

**Vol. 2**

12. Drag Reduction and Flow Studies of a One-One Tangent Ogive Radome at Supersonic Speeds, by I. Patapis (Naval Ship R&D Center. TN AL-1154. To be published)
13. On the Ability of Spikes to Reduce the Drag of Hemispherical Radomes in the Supersonic Regime, by I. Patapis. (Naval Ship R&D Center. TN AL-47. To be published)
14. Augmenting Drag Reducing - Rain Dispersing Spikes by Mass Addition, by I. Patapis. (Naval Ship R&D Center. TN AL-1163. To be published)
15. A Critical Review of Analytical Methods for Estimating Control Forces Produced by Secondary Injection: The Two Dimensional Problem, by M. J. Werle. White Oak, Md. Jan 1968. 64 p. illus. (Naval Ordnance Laboratory TR 68-5)



Figure 1 - One-One Ogive Schlieren

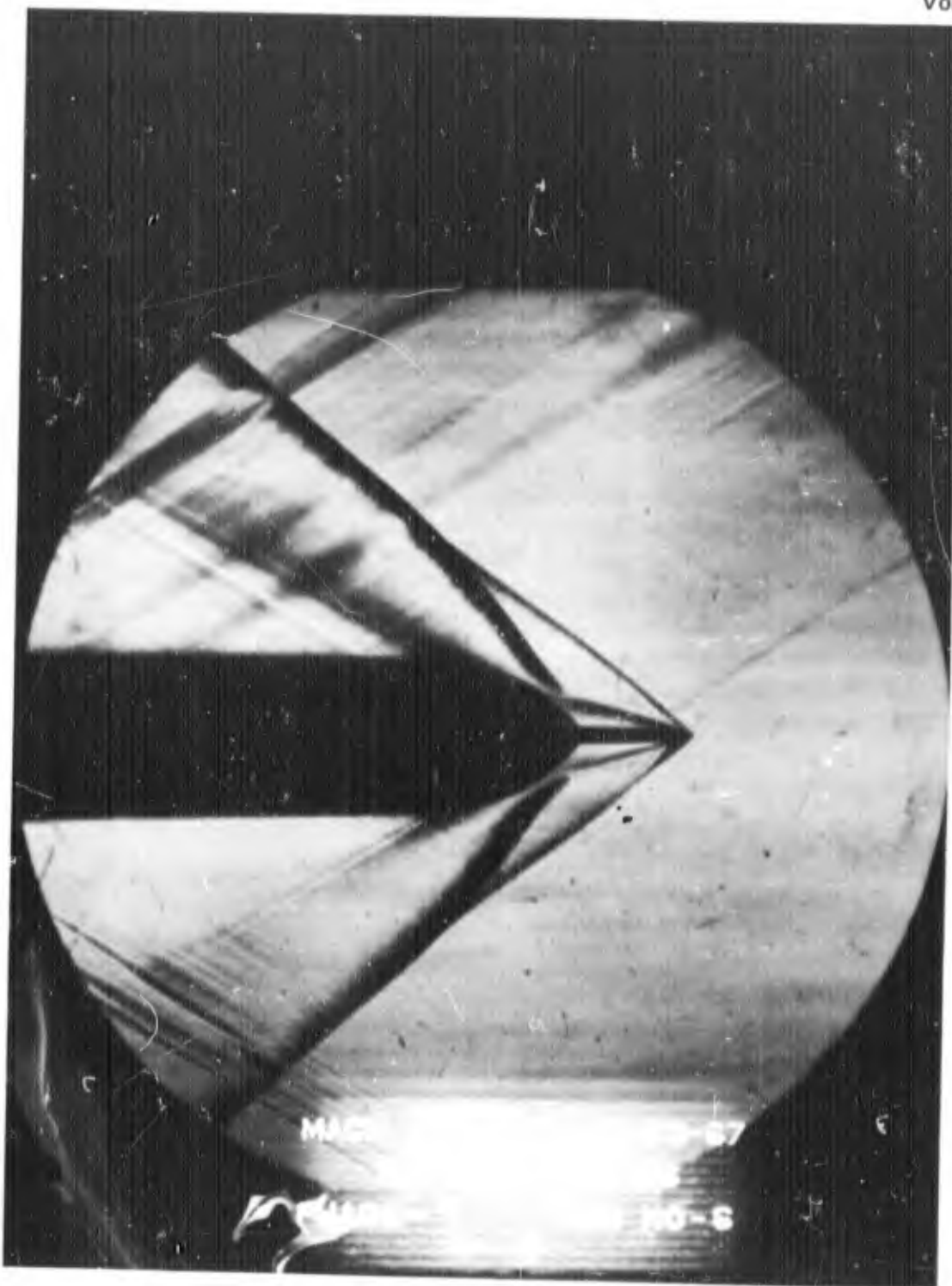


Figure 3 - One-One Ogive With Spike-Tip Separation

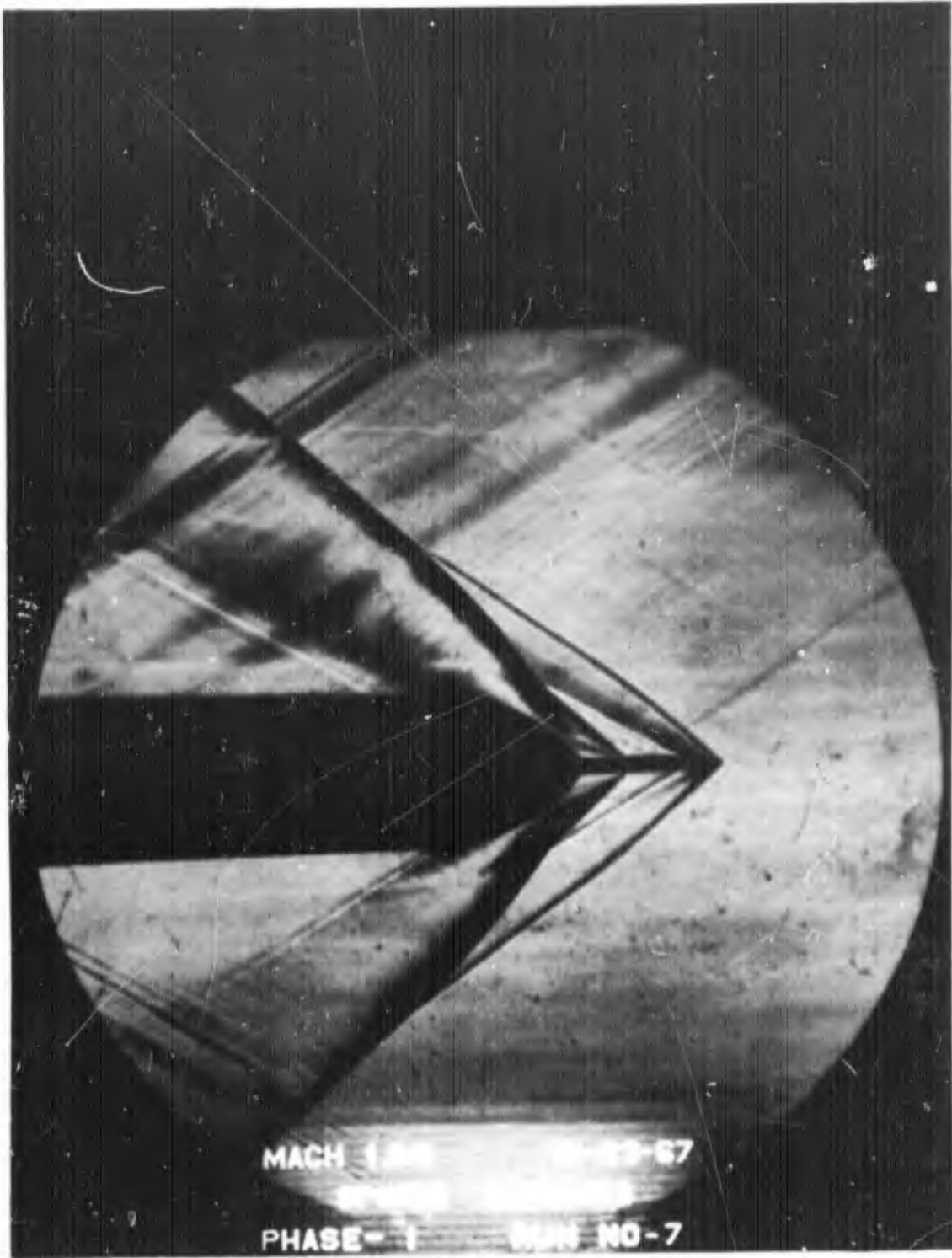


Figure 2 - One-One Ogive With Spike-Shank Separation

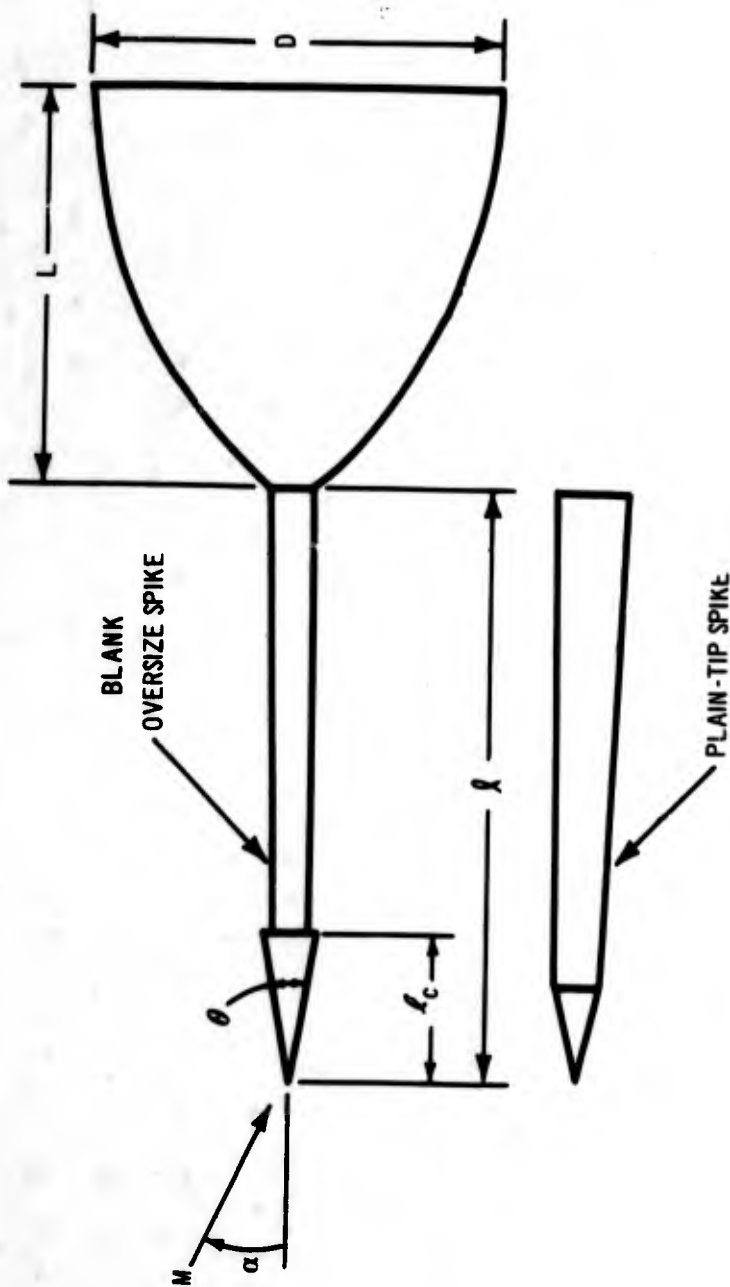


Figure 4 - The Two Different Types of Spikes Tested

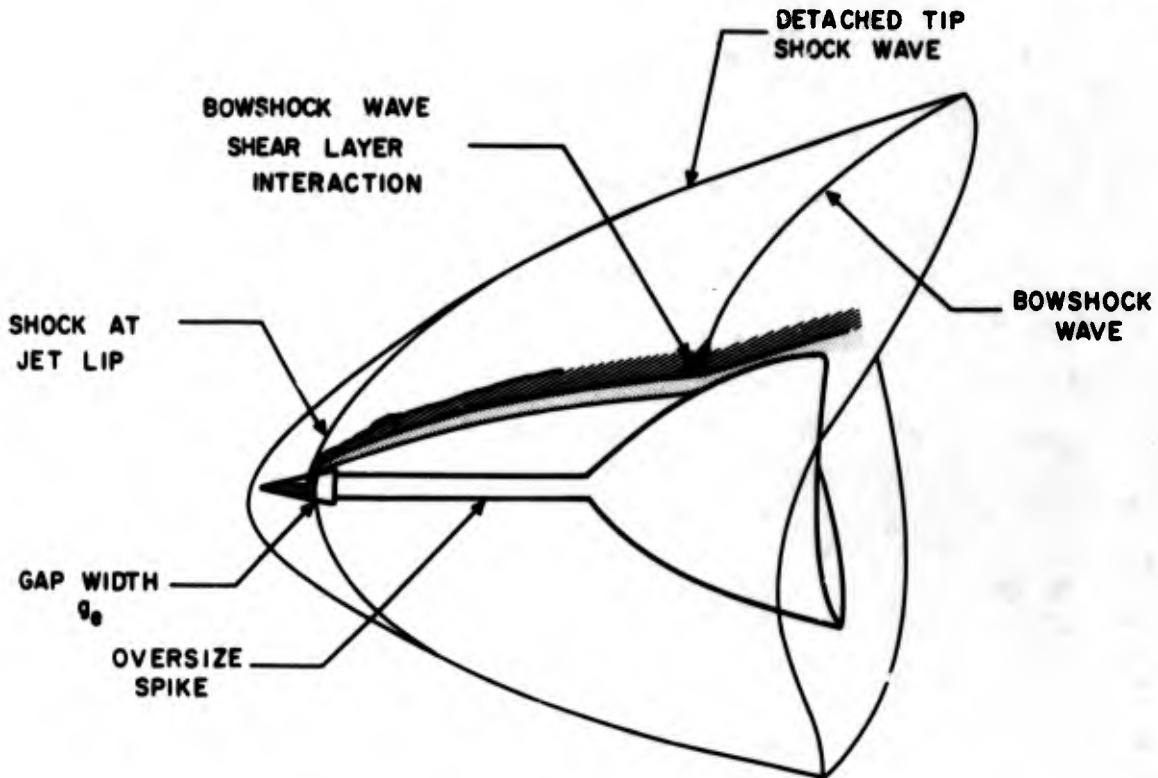


Figure 5 - A Schematic of the Jet-Bleed Principle.  
The Jetting Flow is Crosshatched

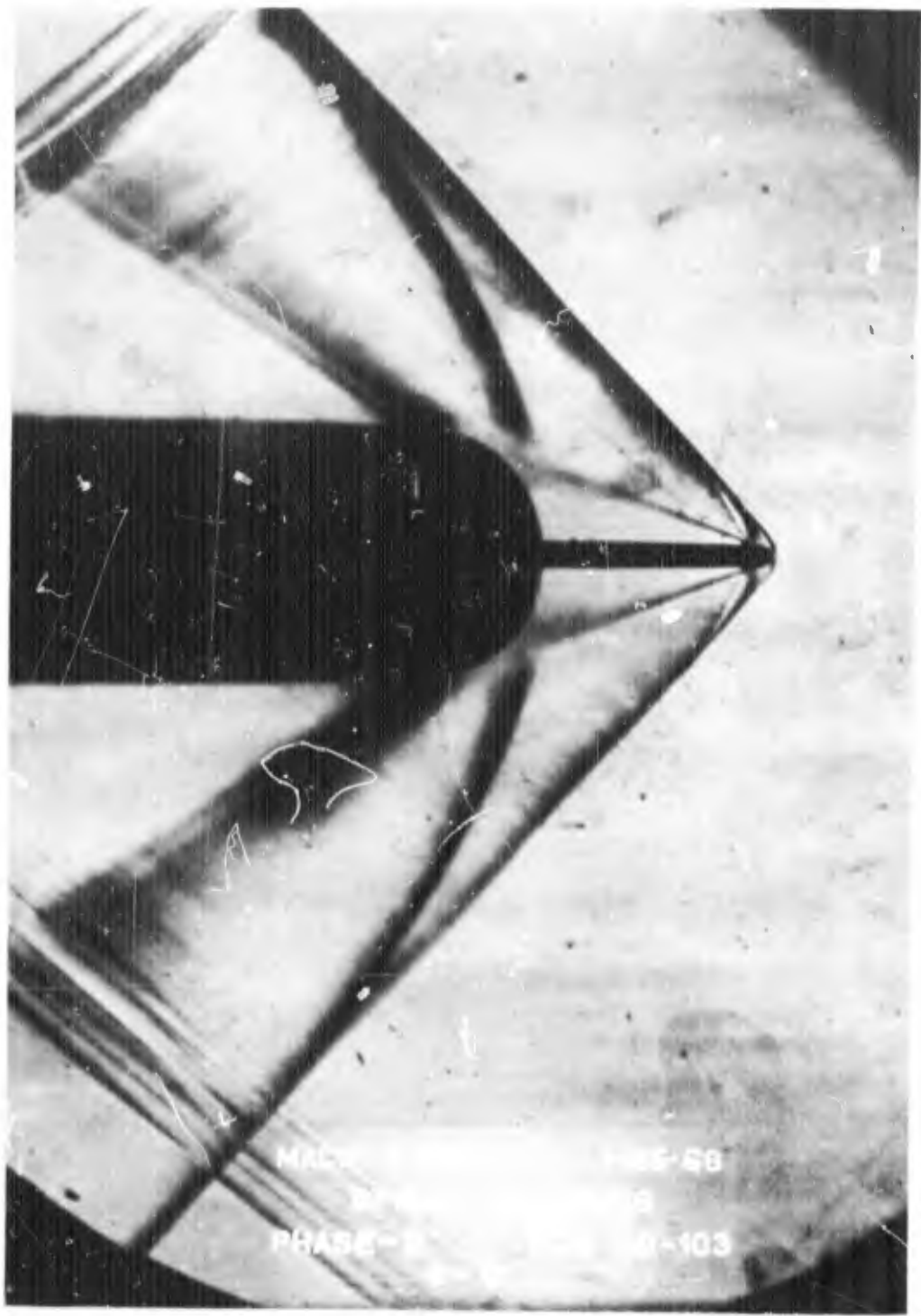


Figure 6 - Schlieren of the Jet-Bleed

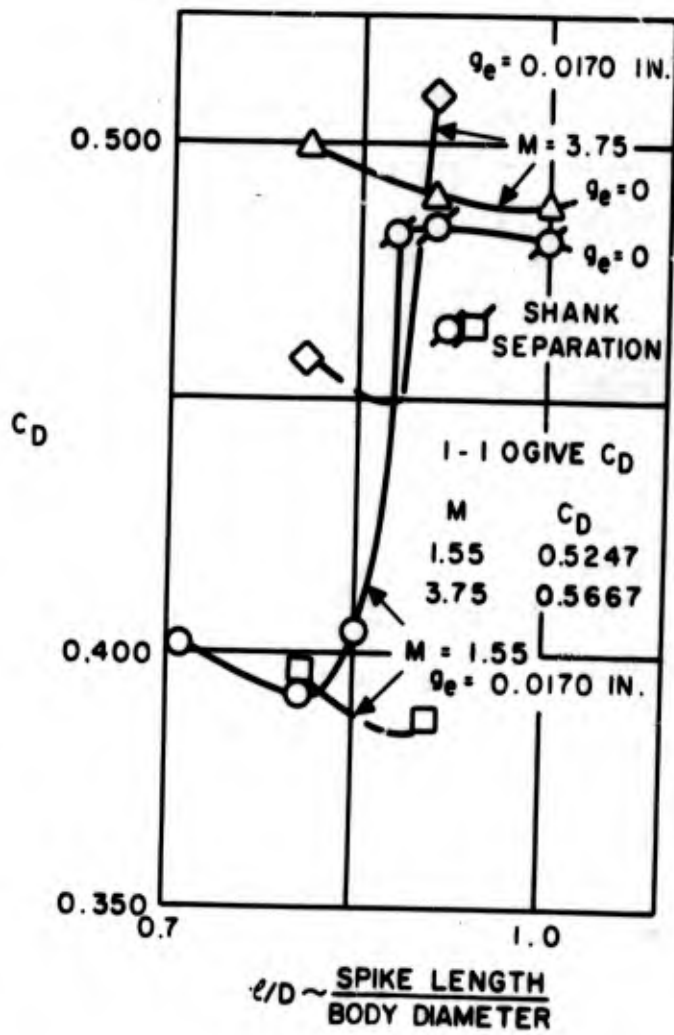


Figure 7 - The Effects of Jet-Bleed on a One-One Tangent Ogive With Oversize Spikes

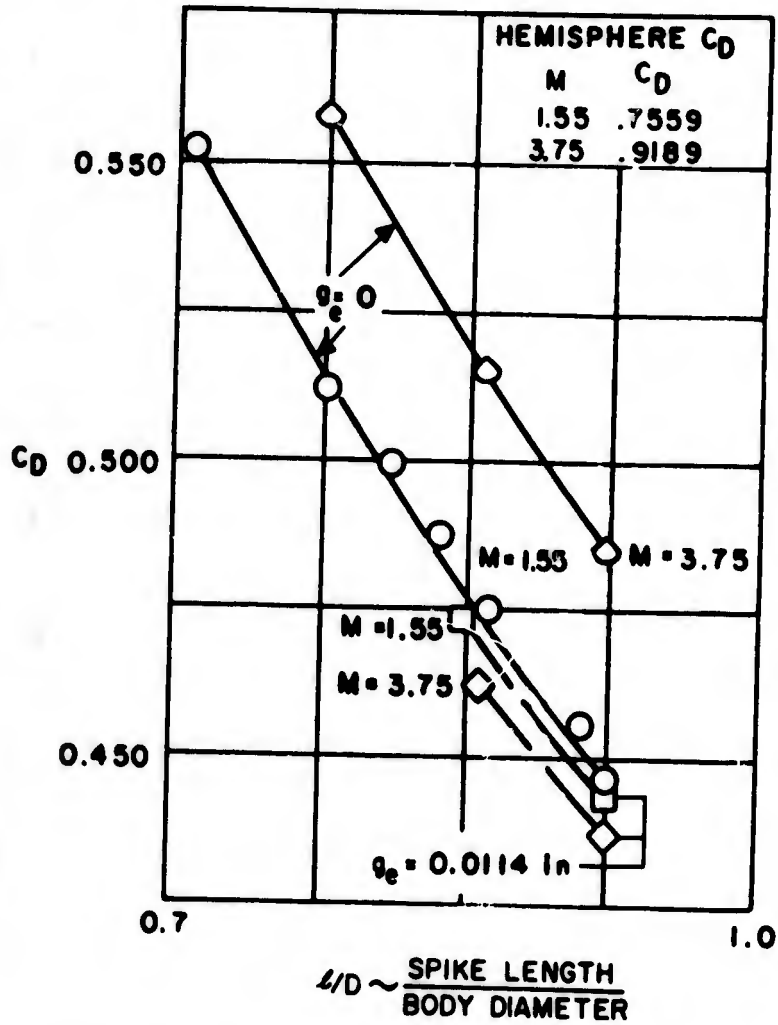


Figure 8 - The Effects of Jet-Bleed on a Hemisphere with Oversize Spikes

UNCLASSIFIED

Security Classification

DOCUMENT CONTROL DATA - R & D		
<i>(Security classification of title, body of abstract and indexing annotation must be entered when the overall report is classified)</i>		
1. ORIGINATING ACTIVITY (Corporate author)  Naval Weapons Center China Lake, California 93555		2a. REPORT SECURITY CLASSIFICATION <b>UNCLASSIFIED</b>
		2b. GROUP
3. REPORT TITLE  PROCEEDINGS OF THE 8TH NAVY SYMPOSIUM ON AEROBALLISTICS. VOLUME 2		
4. DESCRIPTIVE NOTES (Type of report and inclusive dates)		
5. AUTHOR(S) (First name, middle initial, last name)		
6. REPORT DATE  June 1969	7a. TOTAL NO. OF PAGES  306	7b. NO. OF REFS  197
8a. CONTRACT OR GRANT NO.	9a. ORIGINATOR'S REPORT NUMBER(S)  TS 69-199	
a. PROJECT NO  c.  d.	9b. OTHER REPORT NO(S) (Any other numbers that may be assigned this report)	
10. DISTRIBUTION STATEMENT THIS DOCUMENT IS SUBJECT TO SPECIAL EXPORT CONTROLS AND EACH TRANSMITTAL TO FOREIGN GOVERNMENTS OR FOREIGN NATIONALS MAY BE MADE ONLY WITH PRIOR APPROVAL OF THE NAVAL WEAPONS CENTER.		
11. SUPPLEMENTARY NOTES	12. SPONSORING MILITARY ACTIVITY Naval Air Systems Command Naval Ordnance Systems Command Naval Material Command Washington, D.C. 20360	
13. ABSTRACT		

UNCLASSIFIED

Security Classification

14. KEY WORDS	LINK A		LINK B		LINK C	
	ROLE	WT	ROLE	WT	ROLE	WT
Aeroballistics Navy Aeroballistics Symposium Flow Field Boundary Layer Nozzles Jet Effects Aerodynamic Heating Blunt Bodies						